MECHANICS OF LITHIUM-ION BATTERY ELECTRODES

BY

ELIZABETH M. C. JONES

DISSERTATION

Submitted in partial fulfillment of the requirements
for the degree of Doctor of Philosophy in Theoretical and Applied Mechanics
in the Graduate College of the
University of Illinois at Urbana-Champaign, 2015

Urbana, Illinois

Doctoral Committee:

Professor Nancy R. Sottos, Chair and Director of Research
Professor Scott R. White
Professor Andrew A. Gewirth
Assistant Professor Sameh Tawfick

Abstract

Lithium-ion battery technology has improved tremendously since it was first commercialized in the 1990s, and today lithium-ion batteries are one of the lightest and smallest rechargeable batteries commercially available [1]. While lithium-ion batteries are ubiquitous in portable electronics, limited lifetime and reliability hinder widespread adoption of the batteries in large-scale energy storage devices such as in electric vehicles. Key areas of active research that offer potential to improve lithium-ion batteries include the development of new anode and cathode materials and new electrolytes, a more complete understanding of *in situ* and artificial interfacial stabilization processes at the electrode / electrolyte interface, and strategies to mitigate combined electro-chemo-mechanical degradation of the batteries resulting from extended electrochemical cycling.

The present work touches on all three of these areas by investigating the electrochemically-induced mechanical response of lithium-ion battery anodes. First, an experimental protocol was developed to measure the strains induced in free-standing battery electrodes (i.e. unconstrained electrodes not adhered to a substrate) due to electrochemical processes. Graphite composite electrodes, similar to commercial battery anodes, were investigated first to garner baseline results. The electrodes were comprised of particles of graphite as the active material, carbon black for a conductive additive, and a polymer binder. Reversible macroscale electrode deformation was traced to nanoscale changes in graphite layer spacing as lithium was inserted into and removed from the electrodes. Irreversible electrode deformation was correlated with accumulation of electrolyte decomposition products on the surface of the electrode. Many parameters were varied, including the electrode composition (ratio of graphite

to carbon black as well as the choice of polymer binder), electrolyte composition, and cycling rate. The effect of the variation of these parameters on the strain response of graphite composite electrodes was investigated.

In situ strain measurements of free-standing graphite composite electrodes were combined with *in situ* stress measurements of electrodes adhered to a substrate. A new electro-chemo-mechanical property of the electrodes, the "electrochemical stiffness," was defined as a measure of the relative effects of stress compared to strain at any point during electrochemical cycling. Changes in the electrochemical stiffness as a function of electrode potential or capacity provided new insights into the mechanisms governing electrochemically-induced stress and strain development in graphitic electrodes.

Finally, the strain response of high-capacity silicon composite electrodes was investigated and compared to the strain response of composite graphite electrodes. The large volumetric expansion of silicon during lithiation (ca. 300 - 400 %) caused the electrodes to fracture and pulverize where they were attached to a substrate, which frustrated *in situ* strain measurements. Therefore, strain was measured only during the initial, partial lithiation of silicon-based electrodes, before the electrodes fractured. The macroscopic strain developed in the electrodes was dominated by the total amount of lithium inserted into the electrode. The type of active material (either graphite or silicon) and the ratio of electrode components (active material, conductive additive, and polymer binder) were found to be secondary influences, while the size of the active material particles had insignificant influence on the average strain response of the electrodes.

Never lose your childish enthusiasm for life.

Acknowledgments

When I was younger, I didn't have a dream or a passion to be a scientist, an engineer, or a researcher. I liked school, and I was good at math (though often only with significant effort). Those characteristics alone formed the basis of a series of circuitous (though in hindsight, fortuitous) decisions that have culminated in this thesis. From here, the possibilities are endless, and I'm looking forward to following the trail as I go, excited to see what's around the next corner. Looking back, however, I can say that there are innumerable people who have helped me get to this position, even if some of us didn't see the end goal at the time:

My parents, Pamela and Marvin Cler, who supported me in everything I have done.

My husband, Mark Jones, who has patiently waited on me while I finish not one, not two, but three degrees, who supported me financially during part of my undergrad years (and who is still waiting for the return on his investment), and who has listened to me talk enthusiastically and gripe, in nearly equal measures, about my work.

My advisors, Professor Nancy Sottos and Professor Scott White. It goes without saying that without them, I would never have become the scientist and researcher that I am today.

My committee members, Prof. Andrew Gewirth and Prof. Sameh Tawfick, for offering fresh perspectives on my work and helpful suggestions.

My collaborators, Dr. Meredith Silberstein and Dr. Hadi Tavassol. Together, we achieved things I could not have done alone.

Dr. Amanda Jones, who initially "did not work with people," but who eventually became both a great colleague and a great friend.

The battery team, for all of the useful brainstorming about the challenges that accompany working with batteries: Dr. Marta Elleby, Dr. Sen Kang, Taewook Lim, Dr. Oya Okman, and Dr. Ö. Özgür Çapraz.

My non-battery labmates, for their discussions, support, and help with all sorts of miscellaneous tasks during grad school: Dr. Jason Patrick, Dr. Andrew Hamilton, Dr. Cassandra Degen, Dr. Brett Beiermann, Ryan Gergley, Brett Krull, Kevin Hart, Stephen Pety, and Ke Yang.

Colleagues at Caterpillar's Champaign Simulation Center, especially Jeff Fullilove, Mike Henry, and Michael Lopez. These guys informally taught me as much during my internship as my professors taught me in the classroom.

All the people who selflessly helped me during my first year, when they knew they would probably get nothing useful back from a first year grad student: Dr. Brandon Long, Dr. David McIlroy, Dr. James Sobotka

All the educators who subtly and overtly influenced me to pursue a Ph.D. in engineering: Mrs. Sigler, my second grade teacher who let me build my marshmallow and toothpick tower taller than I was; Mrs. Akers and Mr. Herman, my high school math teachers; Professor Phillips, who convinced me to go to the U of I by giving me a personal tour of the 3 million pound crusher; Professor Weaver, who volunteered to advise a group of undergrads who wanted to build a non-linear spring-mass system just for fun.

And finally last, but in many ways not least, my pets, Cheech, Fitz, Hercules, and the Fool, who provided invaluable stress relief.

Table of Contents

List of Abbreviations

CB	Carbon Black
CMC	Carboxymethyl Cellulose
C/X	Charging rate (X hours to fully charge the battery)
CV	Cyclic Voltammetry
DIC	Digital Image Correlation
DMC	Dimethyl Carbonate
EC	Ethylene Carbonate
G	Graphite
G-LIC	Graphite-Lithium Intercalation Compound
GS	Galvanostatic
GUI	Graphical User Interface
PVdF	Poly(Vinylidene Fluoride)
SEI	Solid-Electrolyte Interphase
SEM	Scanning Electron Microscope
VC	Vinylene Carbonate

List of Symbols

E	Finite Strain
I	Current
f	Stress-thickness
k	Electrochemical Stiffness
σ	Stress
Q	Capacity
V	Potential or Voltage

Chapter 1

Introduction

1.1 Overview of Lithium-Ion Batteries

Lithium-ion batteries are ubiquitous in small, portable electronics such as laptops and cell phones. However, widespread adoption of lithium-ion batteries for large-scale energy storage applications, such as electric cars, requires a significant improvement in the longevity and reliability of batteries [2].

A schematic of a lithium-ion battery is presented in Fig. 1.1. Lithium-ion batteries contain an anode (negative electrode), a cathode (positive electrode), and a separator to prevent contact between the electrodes. The electrodes are comprised of a porous composite layer, 100 - 150 µm thick, on top of a metal foil current collector, 10 - 25 µm thick. The porous composite contains particles of active material ca. 5 - 20 µm diameter, a nano-size conductive additive such as carbon black, and a polymer binder. Metal oxides, such as $LiCoO_2$, $LiMnO_2$ and $Li(Ni_{1/3}Co_{1/3}Mn_{1/3})O_2$, typically serve as the active material for cathodes, while graphite, lithium titanate ($Li_4Ti_5O_{12}$), or silicon are typical active materials for anodes. A lithium salt (e.g. lithium hexafluorophosphate ($LiPF_6$)) is dissolved into carbonate-based solvents (e.g. ethylene carbonate (EC) and dimethyl carbonate (DMC)) to form the electrolyte, which resides in the pores of the electrodes and separator.

During the operation of lithium-ion batteries, lithium ions are shuttled between the two electrodes. The insertion of ions into and out of electrodes induces cyclic volumetric changes and displacements (strain) of the active material in the electrodes. Lithium interaction with electrodes also generates internal pressure (stress) within the electrode structure. These

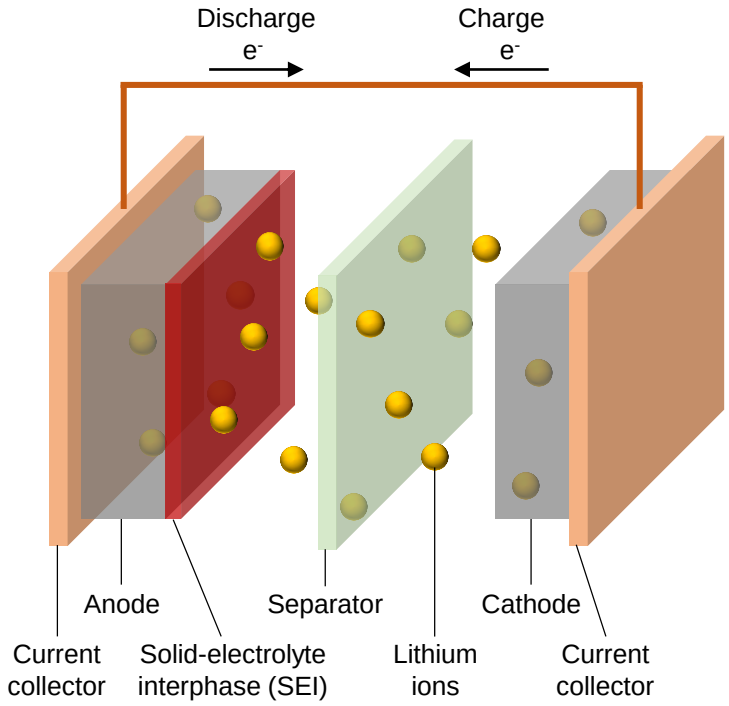

Figure 1.1: Schematic of a lithium-ion battery, depicting the main battery components. During battery charge, lithium ions diffuse from the cathode through the electrolyte and separator and insert into the anode. Electrons move in the same direction but through an external circuit. During battery discharge, or when the battery is used to power a device, lithium ions and electrons move in the opposite direction, from the anode to the cathode.

electrochemically-induced mechanical changes lead to power and capacity fade via changes in the electrode porosity and electrode fracture respectively [3]. Understanding the relationship between the electrochemically-induced mechanical response of battery electrodes and battery performance is critical for the development of high capacity electrodes and extended service life. This work focuses on characterizing the mechanical response of anodes, and specifically investigates graphite-based and silicon-based composite anodes.

1.2 Graphite-Lithium Intercalation Compounds

Graphite is currently the most common active material in commercial lithium-ion battery anodes. During battery charging, lithium ions intercalate between graphite layers, forming

a series of well-ordered graphite-lithium intercalation compounds (G-LICs): dilute stage I (LiC_x, x>24), stage IV (LiC_{24}), stage III (LiC_{18}), dilute stage II (LiC_{18}), stage II (LiC_{12}), and stage I (LiC_6) [4, 5]. The structure of the intercalation compounds are shown schematically in Fig. 1.2.

The preference for forming staged compounds instead of randomly organized compounds is due to a combination of attractive intraplanar interactions among the intercalated atoms and repulsive interplanar interactions between layers of intercalant [6]. The widely accepted model describing the mechanism of transitioning between intercalation compounds is the Daumas-Hérold intercalant-island model [7]. The model proposes that microscopic islands of intercalant form, leading to in-plane local domains of staged behavior. Neighboring domains

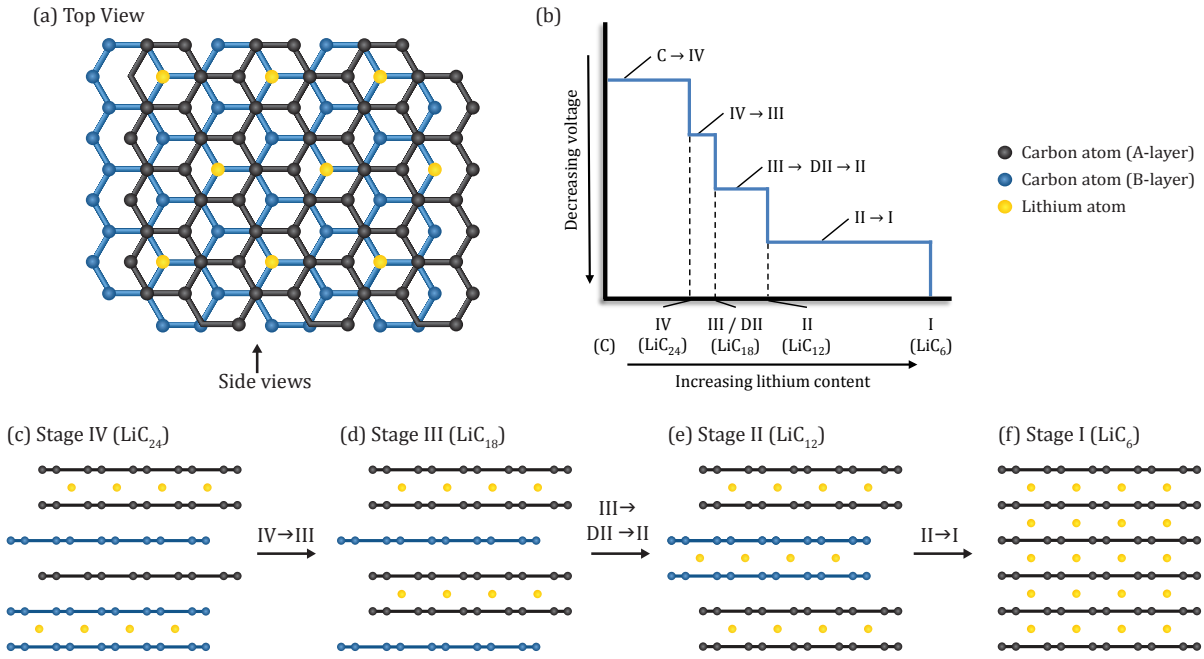

Figure 1.2: Structure of graphite-lithium intercalation compounds (G-LICs). (a) Top view showing the in-plane spatial arrangement of lithium atoms in a fully intercalated (not dilute) stage, with one lithium atom per six carbon atoms. (b) The theoretical voltage of a graphite electrode as a function of lithium content. The voltage is constant during phase transitions and drops sharply once a stage is complete. (c) - (f) Side views showing the arrangement of layers of lithium atoms between graphite layers for stage IV, stage III, stage II, and stage I G-LICs. The roman numerals refer to the number of graphite layers associated with each layer of intercalated lithium. Adjacent graphite layers adopt AB stacking while graphite layers on either side of a layer of intercalated lithium adopt AA stacking.

are similarly staged, but within different graphite galleries. Transitions between different stages of intercalation compounds occur by sliding of intercalant islands within a gallery, along with the insertion of more intercalant (to increase the total intercalant concentration associated with the new stage).

1.3 Electrochemically-Induced Strain in Anodes

Each stage of G-LICs has a characteristic graphite layer spacing [4, 5, 8, 9], and changes in the layer spacing at the atomic scale are translated through multiple length scales. At the microscale, the volumetric expansion of fully intercalated (stage I) graphite particles has been calculated as ca. 10 % from density functional theory, with experimental x-ray diffraction measurements of ca. 13 % closely agreeing [8]. At the macroscale, we measured the dilation of free-standing composite graphite electrodes, i.e. electrodes that are not adhered to a current collector [10]. We found that fully lithiated electrodes develop approximately 1.5 - 2.0 % linear strain, which corresponds to ca. 4.5 - 6.1 % volumetric expansion assuming isotropic expansion. These results are in good agreement with composite mechanics models. Constraining the electrodes on a current collector or substrate reduces the linear strain developed during lithiation to ca. 0.3 % strain [11, 12].

Silicon is a promising new anode material as it has more than 10 times the capacity as graphite. Concurrent with the high capacity, however, silicon expands more than 300 % by volume when it alloys with lithium [13], which leads to electrode fracture and even pulverization, as shown in Fig. 1.3. Using a unique nano-battery cycled inside a transmission electron microscope, Liu et al. [14] studied the expansion of individual silicon nano-wires and nano-particles during lithiation and showed that particles smaller than a certain threshold (ca. 150 nm) do not crack. Beaulieu et al. [13] adapted an atomic force microscope to study the expansion and cracking of thin films of silicon during lithiation. Moving to composite electrodes, Timmons et al. [15] observed particle motion and expansion in a composite

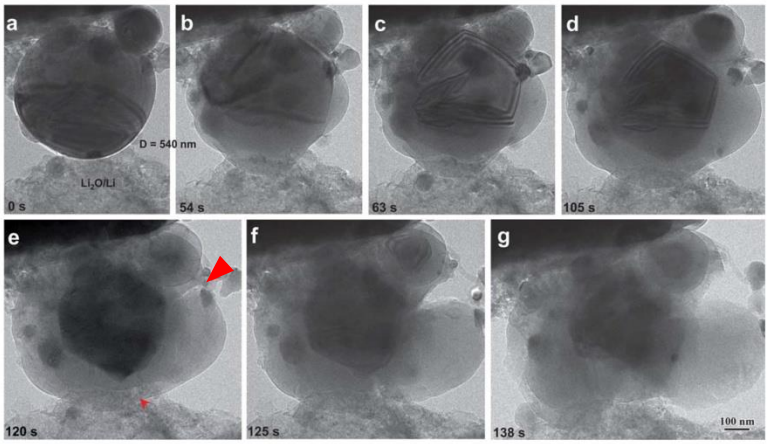

Figure 1.3: Transmission electron micrographs of the lithiation-induced fracture of a silicon particle. (a-d) As the particle is lithiated, a shell of lithiated silicon forms on the outside while a core of unlithiated silicon remains in the interior of the particle. (e) Fractures initiate at the edge of the particle, marked by the red triangles. (f) The fractures grow upon further lithiation. (g) The particle pulverizes. Image reproduced from [14].

electrode qualitatively using optical microscopy. Expanding to 3D measurements, Gonzalez et al. [16] characterized the microstructural evolution of silicon composite electrodes during the initial lithiation using x-ray computed tomography.

1.4 Electrochemically-Induced Stress in Anodes

In addition to investigating the deformation of electrodes, several studies have focused on quantifying the stress developed in electrodes during lithium insertion and removal. Sethuraman et al. [17] used a substrate curvature technique to track the stress in thin film silicon electrodes during electrochemical cycling, and showed the cyclic development of compressive and tensile stresses. They later adapted their substrate curvature technique to quantify the stresses in composite graphite electrodes harvested from a commercial battery and in composite silicon electrodes [18, 19]. Mukhopadhyay et al. [20, 21] found that electrodes comprised of graphitic carbon aligned with basal planes parallel to a substrate developed significantly less stress than electrodes comprised of graphitic carbon aligned with basal planes perpendicular to a substrate.

Complementing the experimental work, theoretical studies have been devoted to modeling the stress development in electrodes. Bower et al. [22] formulated a complete set of field equations and constitutive equations governing the coupled mechanics and electrochemistry of the lithiation and delithiation of silicon. Deshpande et al. [23] developed a mathematical model of diffusion-induced stress in nano-wire electrodes and found that surface effects can decrease diffusion-induced tensile stress, and thus reduce the probability of fracture.

1.5 Chemo-Mechanical Electrode Degradation at High Cycling Rates

The electrochemically-induced stresses and strains in battery electrodes become more significant during high rate charging and discharging [24–26]. Strain analysis of composite electrode materials has revealed that lithiation and delithiation occur through heterogeneous regimes within individual particles of active material or across the entire composite electrode [27–30]. Such heterogeneities are even more acute in high-rate exchange of lithium ions and cause sharp stress and strain gradients that ultimately lead to chemical and physical degradation of the electrodes [24, 27, 31].

1.6 Solid-Electrolyte Interphase (SEI)

After bulk lithiation / delithiation of the electrodes, the second most important set of electrochemical reactions in lithium-ion batteries is decomposition of electrolyte. Because of the low working voltage of graphite-based and silicon-based anodes (< 0.3 V vs $Li^{+/0}$), electrolyte species, including carbonate solvents, lithium salts, and impurities (e.g. water), reduce irreversibly at the anode surface when lithium-ion batteries are charged for the first time [32]. These reactions begin at ca. 0.8 V vs $Li^{+/0}$ and continue to take place down to 0 V vs $Li^{+/0}$ [33]. Electrolyte reduction products are deposited onto the surface of the

anode, forming a thin layer, ca. 10 - 100 nm thick, called the solid-electrolyte interphase (SEI) [32, 34]. A summary of the decomposition mechanisms of common electrolyte solvents is presented in Appendix A.

Ideally, the SEI passivates the electrode surface, preventing further electrolyte decomposition. However, particle fracture induced by cyclic fatigue during repeated charge / discharge cycles exposes fresh anode surfaces to the electrolyte [3, 30, 35–44]. Lithium ions consumed during continuous electrolyte decomposition is one of the primary causes of capacity fade associated with the anode. Thus, the electrochemically-induced mechanical response of the electrode (i.e. dilation, stress development, and fracture) is directly connected to the longevity and reliability of lithium-ion batteries.

Additionally, Mukhopadhyay and Tokranov et al. [45, 46] correlated irreversible stress development in oriented graphitic carbon electrodes with the formation and growth of the SEI layer. They found that the irreversible stresses in the electrode due to SEI formation were of the same order of magnitude as the reversible stresses due to lithium intercalation / deintercalation. Tavassol et al. [47] found that the SEI formed on a model gold electrode also resulted in irreversible stress generation. These results showed for the first time that surface processes at the electrode / electrolyte interface directly affect the mechanical response of the electrodes.

1.7 Overview and Outline of Dissertation

In this research, the electrochemically-induced mechanical response of lithium-ion battery anodes is investigated. Chapter 2 outlines an experimental protocol that adapts digital image correlation (DIC) to measure the strain in battery electrodes during electrochemical cycling. In contrast to previous strain measurements of anodes constrained by a current collector [11, 12], we measure the free expansion of unconstrained electrodes, i.e. electrodes that are not on a current collector or other substrate. Additionally, an analytical model based on

porous composite theory predicts the expected composite electrode expansion based on the known expansion of the active material.

In Chapter 3, the representative electro-chemco-mechanical response of graphite composite electrodes is discussed. The strain response of electrodes cycled on a current collector is compared to the strain response of free-standing, unconstrained electrodes. The expansion and contraction of free-standing electrodes is compared to the analytical model, and key parameters that influence the mechanical response of the electrode are identified through the model. Two mechanisms of deformation are identified: reversible deformation caused by the formation of different graphite-lithium intercalation compounds and non-recoverable deformation correlated with the formation and growth of the solid-electrolyte interphase.

Chapter 4 presents a systematic characterization of the strain response of free-standing composite graphite electrodes during electrochemical cycling. Specifically, the following parameters are investigated because of their importance in electrode design and their strong influence on electrode mechanics: polymer binder, carbon black content, cycling rate, and electrolyte composition. These studies provide insight into how electrode composition, electrolyte composition and cycling rate affect the mechanical response of electrodes during electrochemical cycling and SEI formation and growth.

In Chapter 5, we combine *in situ* stress and strain measurements of graphite composite electrodes during electrochemical cycling to calculate an electrochemical stiffness of the electrodes. In contrast to the elastic stiffness constants (e.g. Youngs modulus), the electrochemical stiffness reported here is a measure of the potential or capacity dependence of the stress and strain responses of the electrodes. Variations in the electrochemical stiffness as a function of electrode potential and electrode capacity reveal fundamentally different mechanisms that govern stress compared to strain induced by lithium interactions with electrodes.

Chapter 6 discusses the deformation of free-standing silicon composite electrodes. Challenges in composite electrode fabrication and attachment of free-standing electrodes to a substrate are presented and discussed. The strain response of select silicon composite elec-

trodes are compared to the strain response of graphite composite electrodes during the initial lithiation of the electrodes.

Finally, a summary of this research and directions for future work are presented in Chapter 7. In total, the research presented in this dissertation provides key information about the electrochemically-induced mechanical response of lithium-ion battery anodes, which can be used to aid in the design of more robust and reliable electrodes for the next generation of lithium-ion batteries.

Chapter 2

In Situ Strain Measurements of Battery Electrodes*

In this chapter, we describe the experimental protocol that allows strain measurements to be made on lithium-ion battery electrodes. Two custom battery cells were designed, one that utilizes an electrode on a current collector and one that utilizes a free-standing electrode. A chemically-inert, well-correlated speckle pattern for digital image correlation (DIC) was generated using fluorescent silica nano-particles. An analytical model based on porous composite theories was developed to predict the expansion of graphite-based electrodes. Finally, experimental details are presented for fluorescent particle synthesis, electrode fabrication, electrochemical cycling protocols, and strain analysis.

2.1 Custom Battery Cell

2.1.1 Initial Design

We designed and fabricated two custom battery cells to enable *in situ*, full-field strain measurements during lithiation and delithiation of lithium-ion battery electrodes. Our initial cell design is shown in Fig. 2.1. Key features of the cell included side-by-side arrangement of electrodes and a quartz window that allowed optical access to the electrodes during cycling. The working electrode, 19 mm in diameter, was a graphite-based composite electrode fabricated on a copper current collector, similar to commercial batteries. It was adhered to a

*Significant portions of this chapter were published in E. M. C. Jones, M. N. Silberstein, S. R. White, N. R. Sottos. *Exp. Mech.* (2014) 54:971-985. The analytical model presented in Sec. 2.3 was formulated primarily by Dr. M.N. Silberstein while a post-doctoral researcher at the University of Illinois at Urbana-Champaign.

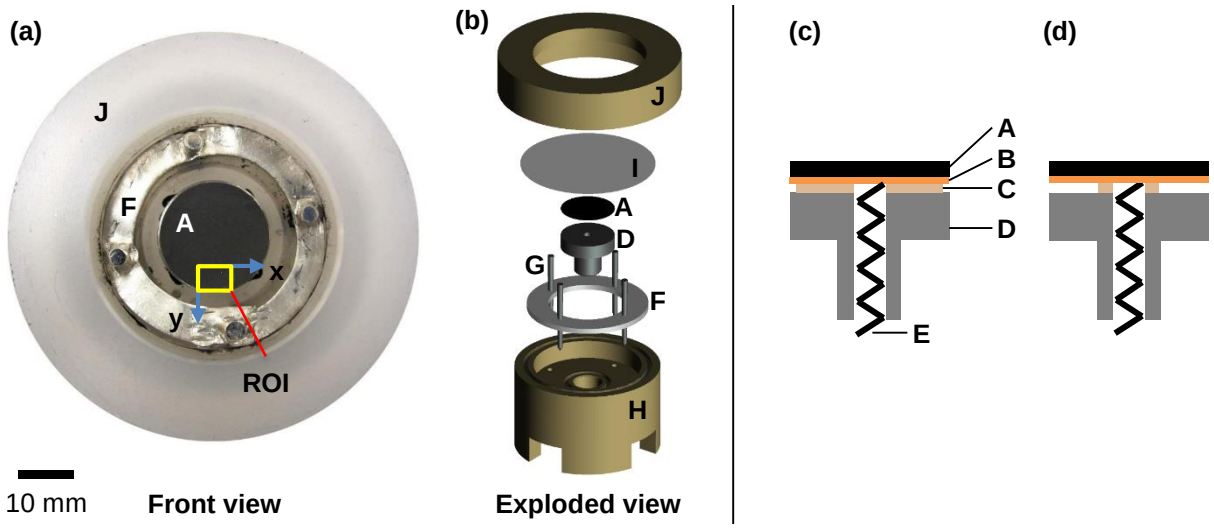

Figure 2.1: Initial design of the custom battery cell. (a) Front view of cell, (b) exploded schematic view of cell, (c) schematic cross section view of a full epoxy adhesive layer (18 mm), and (d) schematic cross section view of a small epoxy adhesive layer (5 mm). Battery cell components are: (A) working electrode, (B) current collector, (C) epoxy adhesive layer, (D) stainless steel substrate for working electrode, (E) spring for electrical connection to working electrode, (F) lithium metal counter electrode, (G) stainless steel pins for mechanical and electrical connection of counter electrode, (H) main body (insulator), (I) quartz window, (J) lid.

circular substrate with a thin layer of rigid epoxy, and electrical connection was made to the backside of the current collector by a spring placed in a hole in the substrate (Fig. 2.1c-d). The counter electrode was a ring of lithium metal surrounding the working electrode and was attached to stainless steel pins that protruded through the base of the cell.

Two different configurations were examined for the attachment of the working electrode to the substrate. In the first configuration (Fig. 2.1c), the epoxy adhesive layer was approximately 18 mm in diameter, and it completely constrained the working electrode in-plane, except at the very edge of the electrode. In the second attachment configuration (Fig. 2.1d), the diameter of the epoxy adhesive layer was decreased to 5 mm, so that only the center of the electrode was constrained.

2.1.2 Second Design

Based on the results from testing of the initial cell design (see Sec. 3.1.2), a second custom battery cell was designed that used a free-standing composite graphite electrode without a current collector (Fig. 2.2). The free-standing electrode was cantilevered from the edge of a stainless steel substrate and spot welded to the substrate at one end. Spot welds created an electrical connection between the electrode and the battery circuit and fixed the electrode to the stainless steel substrate during cycling. On the opposite free edge of the electrode, a polymer support with a thin gap (approximately 200 µm) limited the out-of-plane deflection of the electrode while allowing free in-plane expansion and contraction (Fig. 2.2c-d). Similar to the initial cell design, lithium metal was used as the counter electrode, and a quartz window provided optical access to the electrodes during cycling.

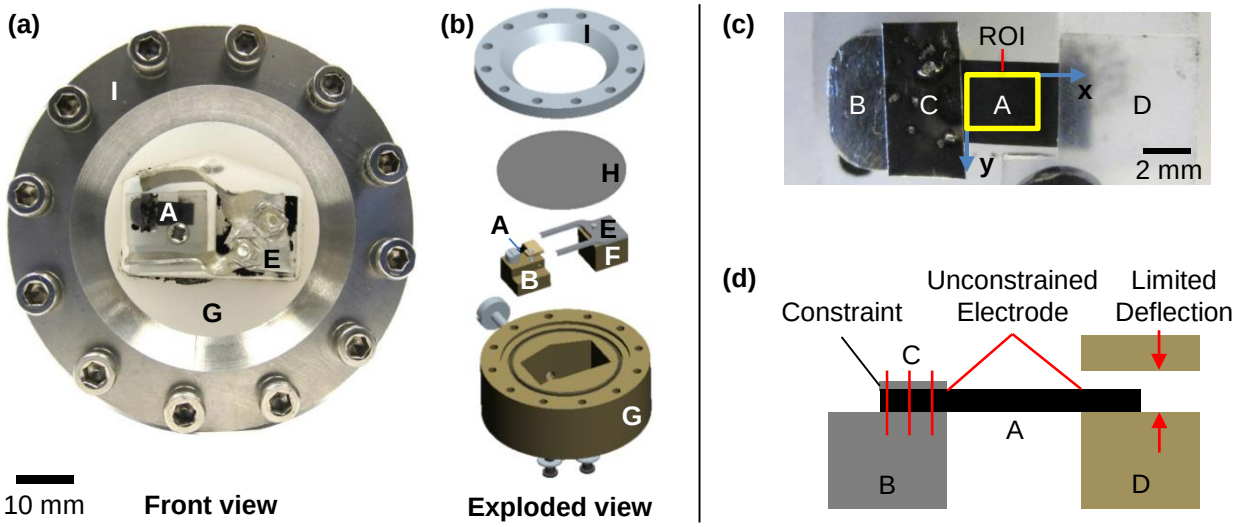

Figure 2.2: Second design of the custom battery cell. (a) Front view of cell, (b) exploded schematic view of cell, (c) magnified view of working electrode attachment configuration, (d) schematic side view of working electrode attachment configuration. Battery cell components are: (A) free-standing working electrode (i.e. without a current collector), (B) substrate for working electrode, (C) spot welds, (D) polymer support for working electrode, (E) lithium metal counter electrode, (F) substrate for counter electrode, (G) main body (insulator), (H) quartz window, (I) lid.

2.2 Speckle Pattern

Composite graphite electrodes have a natural speckle pattern appropriate for DIC at large magnifications. During cycling, however, graphite changes color as a function of lithium content (Fig. 2.3) [48], and individual speckles appear, disappear and change size and shape as particles of graphite deform and undergo rigid body motion. These changes lead to poorly-correlated speckle patterns.

To overcome the issues with the natural speckle pattern, we generated a speckle pattern by spin-casting fluorescent silica nano-particles on the electrode surface [49–51]. This method had the additional benefit of being general to electrode material and type. The particles were synthesized in house using standard particle processing techniques [52, 53], and had a core of silica coupled with a rhodamine-based fluorescent dye and a shell of pure silica to protect the dye from bleaching. During electrochemical cycling, a laser illuminated the electrode surface to excite the fluorescent particles, and the emitted fluorescent light was captured with a CCD sensor. Fig. 2.4a shows the experimental configuration of the battery cell, camera, and laser, Fig. 2.4b shows a representative speckle pattern generated by the particles on the graphite electrode, and Fig. 2.4c shows a scanning electron micrograph of a composite graphite electrode with the particles on its surface.

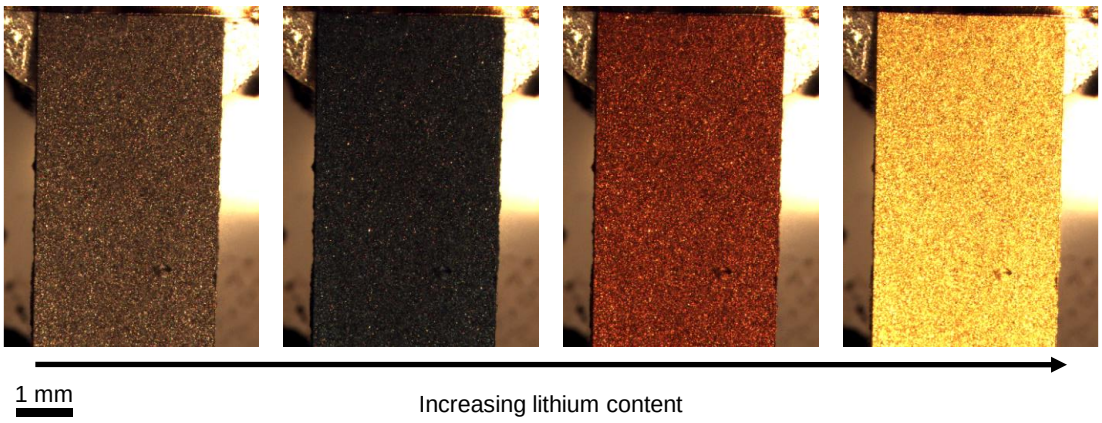

Figure 2.3: Natural color change of graphite as a function of lithium content. Electrodes transition from black (unlithiated) to dark blue, red, and finally gold (fully lithiated).

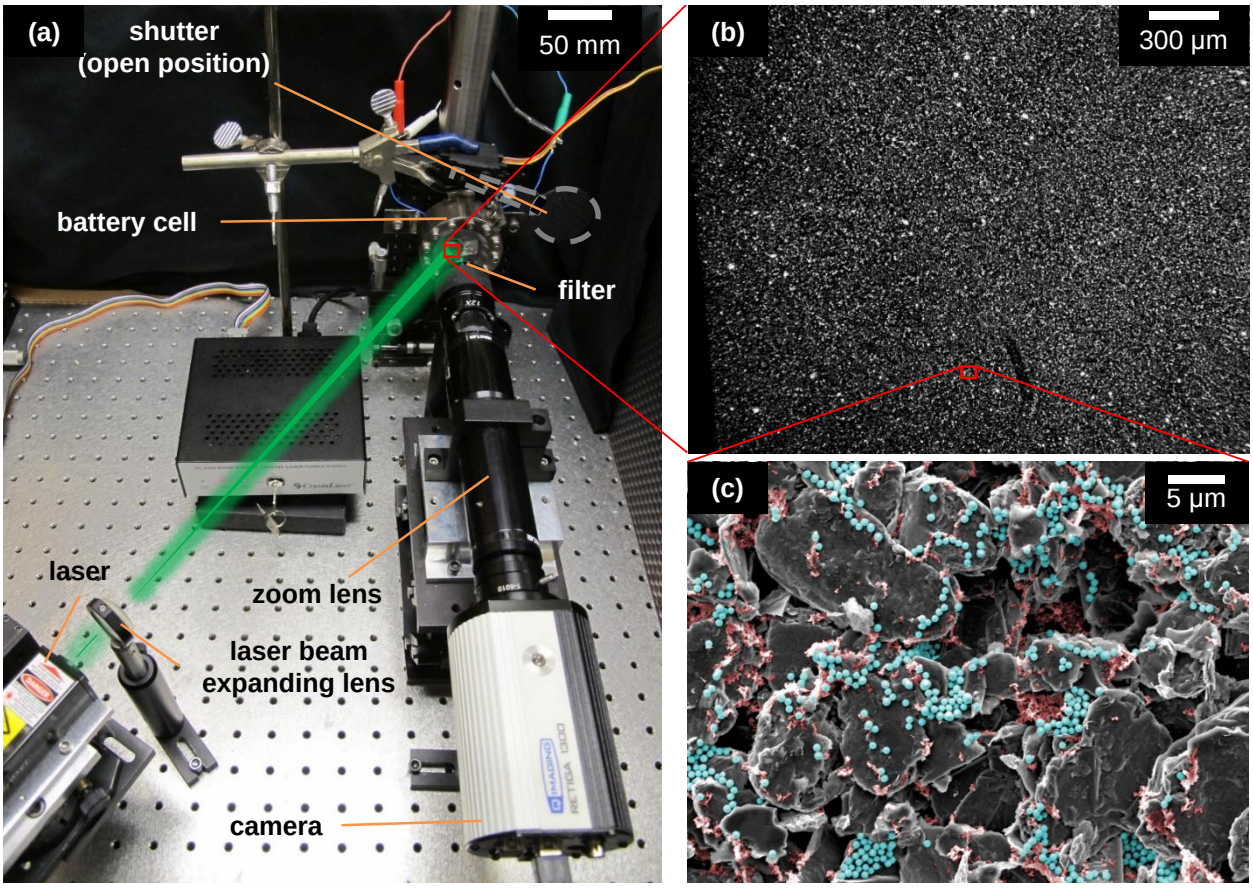

Figure 2.4: Imaging setup of the custom battery cell during electrochemical cycling. (a) A 532 nm laser excites the fluorescent particles on the electrode surface. Reflected laser light is filtered so that only the fluorescent emitted light is captured in the images. A shutter blocks the laser light during the majority of the test and opens only when an image is being captured, to minimize particle bleaching. (b) Representative speckle pattern generated by fluorescent nano-particles on the surface of a graphite composite electrode. (c) Scanning electron micrograph of a composite graphite electrode. Carbon black visible on the electrode surface is false-colored in red. Fluorescent silica nano-particles on the electrode surface are false-colored in blue.

2.3 Analytical Prediction of Composite Electrode Expansion

The elastic properties of a composite graphite electrode were estimated by treating the electrode as a graphite particulate-filled composite with a porous matrix of carbon black (CB) and carboxymethyl cellulose (CMC) polymer binder. The expansion of the composite electrode due to lithium intercalation into graphite was modeled analogously to a thermal expansion where lithium content is akin to a temperature change. Several assumptions were made to allow the problem to be analytically solvable:

- The electrode is fully unconstrained.
- The electrode undergoes only elastic, reversible deformation.
- The electrode is fully lithiated and delithiated.
- The lithiation and delithiation are spatially uniform.
- The graphite particles, though individually anisotropic, are oriented randomly within the electrode, causing the electrode to be isotropic at the length scales considered in the model.
- No electrochemical reactions occur other than the lithiation and delithiation of graphite.
- The electrolyte is free to move through the pores of the electrode without exerting significant forces on the electrode.

2.3.1 Material Properties of the Composite Constituents

As described in Chapter 1, graphite undergoes a series of smooth phase transitions between discrete, ordered graphite-lithium intercalation compounds (G-LICs) during lithiation, moving sequentially from unintercalated graphite to stage IV (LiC_{24}), stage III (LiC_{18}), dilute

stage II (LiC_{18}), stage II (LiC_{12}), and finally stage I (LiC_6) intercalation compounds [4, 5]. Qi et al. used density functional theory (DFT) simulations to predict the average volume expansion, Young's modulus and Poisson's ratio for unintercalated graphite and stage III, dilute stage II, stage II, and stage I compounds [8]. For our model, the stage III phase of the LiC_{18} composition was used instead of the dilute stage II phase in order to correlate the model with experimental results. Material properties of the intercalation compounds were linearly interpolated between the discrete phases in order to have material properties for all lithium contents.

The Young's modulus, Poisson's ratio, and density of the CB and CMC were found in the literature [8, 54–57]. The electrode porosity and volume fractions of each of the solid components were calculated from the overall density of the electrode (1.0 g cm^{-3}), the densities of the individual components, and the mass ratio of the solid components (8:1:1 wt. ratio of graphite, CB, and CMC).

The bulk and shear moduli for all of the electrode components were calculated from the Young's moduli and Poisson's ratios assuming isotropy. Additionally, the linear strain from lithium intercalation of the graphite-lithium intercalation compounds was computed from the volumetric expansion assuming an isotropic expansion. All material properties are listed in Table 2.1.

Table 2.1: Material properties of the constituents of the graphite composite electrode

	Young's Modulus (GPa)	Poisson's Ratio (–)	Bulk Modulus[a] (GPa)	Shear Modulus[a] (GPa)	Density (g cm^{-3})	Volumetric Expansion (%)	Linear Strain[a] (%)	Volume Fraction (–)	Ref.
C (graphite)	32.47	0.315	29.25	12.35	2.2	0	0	0.36	[8, 57]
LiC_{18} (stage III)	28.57	0.39	43.26	10.23	–	3.6	1.2	–	[8]
LiC_{12} (stage II)	58.06	0.34	60.48	21.66	–	4.6	1.5	–	[8]
LiC_6 (stage I)	108.67	0.24	69.66	43.82	–	10	3.2	–	[8]
CMC	1.2	0.45	4.0	0.41	1.6	0	0	0.06	[54, 56]
CB[b]	32.47	0.315	29.25	12.35	1.9	0	0	0.06	[8, 55]
porosity	–	–	–	–	–	–	–	0.52	–

[a] The bulk and shear moduli were calculated from the Young's modulus and the Poisson's ratio, and the linear strain was calculated from the volumetric expansion assuming isotropy.

[b] The Young's modulus and Poisson's ratio for carbon black are taken to be the same as unintercalated graphite.

2.3.2 Elastic Properties of the Composite Electrode

The lower bound of the effective shear moduli, G_m, and the lower bound of the effective bulk moduli, K_m, of a matrix containing CB particles and CMC binder were calculated using the inverse rule of mixtures [58]:

$$(1/K_m) = (\phi_{m,cb}/K_{cb}) + (\phi_{m,cmc}/K_{cmc}) \tag{2.1a}$$

$$(1/G_m) = (\phi_{m,cb}/G_{cb}) + (\phi_{m,cmc}/G_{cmc}) \tag{2.1b}$$

with

$$\phi_{m,cb} = \frac{\phi_{cb}}{\phi_{cb} + \phi_{cmc}} \tag{2.2a}$$

$$\phi_{m,cmc} = \frac{\phi_{cmc}}{\phi_{cb} + \phi_{cmc}} \tag{2.2b}$$

where K_{cb} and K_{cmc} were the bulk moduli of the CB and CMC respectively, G_{cb} and G_{cmc} were the shear moduli of the CB and CMC respectively, $\phi_{m,cb}$ and $\phi_{m,cmc}$ were the volume fractions within the CB/CMC matrix of the CB and the CMC respectively, and ϕ_{cb} and ϕ_{cmc} were the volume fractions within the complete composite electrode of the CB and the CMC respectively.

Open cell theory for an isotropic porous solid [59] was adapted to compute the effective bulk modulus of a porous matrix, K_{pm}, with the previously defined CB and CMC matrix as the solid part:

$$K_{pm} = \left(\frac{1}{3\left(1 - 2\nu_{pm}\right)}\right)\left(\frac{9K_mG_m}{3K_m + G_m}\right)\left(\frac{\rho_{pm}}{\rho_m}\right)^2 \tag{2.3}$$

with

$$\rho_m = \phi_{m,cb}\rho_{cb} + \phi_{m,cmc}\rho_{cmc} \tag{2.4a}$$

$$\rho_{pm} = \phi_{pm,cb}\rho_{cb} + \phi_{pm,cmc}\rho_{cmc} \tag{2.4b}$$

and

$$\phi_{pm,cb} = \frac{\phi_{cb}}{\phi_{pm}} \tag{2.5a}$$

$$\phi_{pm,cmc} = \frac{\phi_{cmc}}{\phi_{pm}} \tag{2.5b}$$

$$\phi_{pm} = \phi_{cb} + \phi_{cmc} + \phi_p = 1 - \phi_g \tag{2.5c}$$

where ρ_m was the density the solid portion of the CB/CMC matrix, ρ_{pm} was the density of the porous matrix (CB, CMC, and porosity), $\phi_{pm,cb}$ and $\phi_{pm,cmc}$ were the volume fractions within the CB/CMC porous matrix of CB and CMC respectively, ϕ_p was the porosity within the complete composite electrode, and ϕ_g and ϕ_{pm} were the volume fractions within the complete composite electrode of, respectively, the graphite and porous matrix (i.e. CB, CMC and porosity). The Poisson's ratio of the porous matrix, ν_{pm}, was assumed to be equal to 1/3 [59].

The bulk modulus, K_e, of the complete composite electrode was computed by applying the "S-Combining Rule" [58] for graphite particulates in a porous matrix according to:

$$K_e = \frac{K_{pm}\left(1 + \phi_g \xi_l \chi\right)}{1 - \phi_g \Psi \chi} \tag{2.6}$$

with

$$\chi = \frac{K_g - K_{pm}}{K_g + \xi_l K_{pm}} \tag{2.7a}$$

$$\Psi = 1 + \frac{\phi_g \phi_{pm} \left(1 - \gamma \phi_{pm}\right) \left(K_g - K_{pm}\right) \left(\xi_u - \xi_l\right)}{K_g + \xi_u \left(\phi_g K_g + \phi_{pm} K_{pm}\right)} \tag{2.7b}$$

$$\xi_u = \frac{2\left(1 - 2\nu_g\right) K_g}{\left(1 + \nu_g\right) K_{pm}} \tag{2.7c}$$

$$\xi_l = \frac{2\left(1 - 2\nu_{pm}\right)}{\left(1 + \nu_{pm}\right)} \tag{2.7d}$$

$$\gamma = \frac{2\lambda^* - 1}{\lambda^*} \tag{2.7e}$$

where ν_g was the Poisson's ratio of the G-LICs and K_g was the bulk modulus of randomly oriented particles of G-LICs, calculated from the Young's modulus and Poisson's ratio assuming isotropy and linearly interpolated between discrete phases. The critical volume fraction for random close packing of the particle filler, λ^*, was estimated as 2/3 [58].

2.3.3 Predicted Expansion of the Composite Electrode due to Lithium Intercalation

The linear strain due to lithium intercalation of the complete composite electrode, ϵ_e, was estimated according to:

$$\epsilon_e = \epsilon_{avg} + \left(\frac{\epsilon_{pm} - \epsilon_g}{1/K_{pm} - 1/K_g}\right)\left[\frac{1}{K_e} - \frac{1}{K_{avg}}\right] \tag{2.8}$$

with

$$\epsilon_{avg} = \phi_g \epsilon_g + \phi_{pm} \epsilon_{pm} \tag{2.9a}$$

$$\frac{1}{K_{avg}} = \frac{\phi_g}{K_g} + \frac{\phi_{pm}}{K_{pm}} \tag{2.9b}$$

where ϵ_g was the linear strain of G-LICs due to lithium intercalation (calculated from the volume expansion assuming isotropy (Table 2.1) and linearly interpolated between discrete phases), and where the rule of mixtures and inverse rule of mixtures were used to calculate the volume-fraction averages of the lithium-intercalation strain, ϵ_{avg}, and the bulk modulus, K_{avg}, of the composite electrode. Because the CB/CMC porous matrix does not lithiate, its lithium-intercalation strain, ϵ_{pm}, is zero. Equations (2.8) - (2.9) were adapted from the thermal expansion of a two-part composite where both the composite and its constituents are isotropic [58, 60]. In our model, lithium content is akin to a temperature change. Discussion of the model predictions and comparison of the predictions to experimental results is presented in Sec. 3.2.2.

2.4 Materials and Methods

2.4.1 Materials

Plastic portions of the custom battery cells were fabricated from polychlorotrifluoroethylene (PCTFE, Plastics International), and steel portions of the electrode substrates were fabricated from 316 stainless steel. A Torr-Seal equivalent epoxy was used to adhere electrodes to the substrates in the initial cell design. Armor Crystal o-rings (Valqua America) and a quartz window (99.995% SiO_2, 1.6 mm thick, McMaster-Carr) was used to seal the cell.

The electrolyte consisted of 1M lithium perchlorate ($LiClO_4$, battery grade, dry, 99.99 %, Sigma-Aldrich) dissolved in ethylene carbonate (EC, anhydrous, 99 %, Sigma-Aldrich) and dimethyl carbonate (DMC, anhydrous, >99 %, Sigma-Aldrich) in a 1:3 vol. ratio. Vinylene carbonate (VC, 99 %, Sigma-Aldrich) was added in various weight percents to some electrolyte as an electrolyte additive. Lithium metal (0.75 mm thick, Alfa Aesar) was used as a counter electrode.

Composite graphite electrodes were fabricated from synthetic graphite powder (< 20 µm, Sigma-Aldrich), carbon black (CB, 100 % compressed, 99.9+ % pure, Alfa-Aesar), and sodium carboxymethyl cellulose binder (CMC, average $M_w \sim 700{,}000$, degree of substitution 0.8 - 0.95, Sigma-Aldrich). Composite silicon electrodes were fabricated from either micro-Si (325 mesh, 99 %, Sigma-Aldrich) or nano-Si (100 nm, plasma synthesized, 99 %, MTI), CB (Regal 400R, Cabot) and CMC. Electrodes were fabricated on a substrate of copper foil (9 µm thick, > 99.99 %, MTI).

The synthesis of fluorescent silica nano-particles required the following reagents: 3-aminopropyltriethoxysilane (APS, 99+ %, Gelest), tetraethoxysilane (TEOS, 99.9+%, Gelest), rhodamine B isothiocyanate dye (RITC, mixed isomers, Sigma-Aldrich), ammonium hydroxide (30 wt.%, Fisher), and ethanol (200 proof, Decan labs).

2.4.2 Fluorescent Particle Synthesis

Fluorescent nano-particles were synthesized in house according to [52, 53]. A generalized synthesis procedure is presented in Appendix H, while the specific procedure utilized in this work is presented here. First, 10 mL ethanol, 0.0462 g RITC dye, and 0.0368 g APS were added to the reaction vessel. The vessel was purged with nitrogen, and the contents were mixed with a magnetic stir rod for approximately 24 hours. Next, 170 mL ethanol, 16.67 mL ammonium hydroxide, and 3.3 mL deionized water were added to the reaction vessel and allowed to mix for several minutes. Then, 11.1 mL TEOS was added quickly. The reaction vessel was again purged with nitrogen, and the contents were stirred rapidly for

a few minutes, and then mixed at a slower rate for approximately 24 hours. These steps created the particle cores containing RITC dye. Amounts of reagents were chosen to yield cores of 400 nm in diameter.

After the cores were formed, a protective shell of silica was grown around the cores in four discrete steps. For each step, deionized water was added to the reaction vessel first, and then TEOS was added quickly. The vessel was purged with nitrogen, and the contents were stirred for approximately two hours before the next addition of materials. Equal amounts of water and TEOS were added in the following increments: 1 mL, 10 mL, 17 mL, 17 mL. The total amount of TEOS (45 mL) was chosen such that the final particle diameter would be 700 nm, assuming a core diameter of 400 nm.

Once the particles were fully formed, the contents of the reaction vessel were centrifuged, and the excess reaction liquid was removed. The remaining particles were dispersed in fresh ethanol via sonication. This rinsing procedure was repeated three times, and then the particles were stored in ethanol at approximately -20° C. The final diameter of the particles, as measured from a scanning electron micrograph, was 550 - 620 nm.

In order to generate a speckle pattern for DIC, the particles were sonicated in ethanol immediately before use, and then spincoated at approximately 1000 RPM onto the surface of the electrode prior to battery cell assembly.

2.4.3 Composite Graphite Electrode Fabrication

Graphite electrode slurries were prepared by mixing graphite, carbon black and CMC in water. First, CMC was dissolved in water in a 1:100 wt. ratio. Then, carbon black and graphite were added using one of two protocols. In the first protocol, carbon black was added to the CMC solution, and the carbon black/CMC/water suspension was mixed for several days with a magnetic stir rod in order to fully disperse the carbon black. Then graphite was added and the slurry was mixed with a magnetic stir rod for several more days in order to fully homogenize the slurry. In the second protocol, both graphite and carbon black were

added to the CMC solution at the same time, and the slurry was mixed with a homogenizer (Model 15007ST, ⌀7 mm, sawtooth (fine), stainless steel probe, Omni) at approximately 7,500 RPM for 1 hour. The two different mixing protocols had no noticeable influence on the electrochemical behavior or the strain responses of the electrodes. In both protocols, slurries were made in ca. 5 g quantities, and the weight ratio of solid components ranged from 9:0:1 to 0:9:1 for graphite, carbon black, and CMC respectively.

A substrate of copper foil was cleaned with acetone and ethanol. The electrode slurry was deposited onto the copper foil using a doctor blade to control the slurry thickness and then allowed to dry under ambient conditions. The measured density of the electrodes was ca. 1.0 g cm^{-3}, and the porosity was ca. 50 % by volume, as calculated from the overall electrode density, the density of individual electrode components, and the mass ratio of individual electrode components.

Electrodes on a copper current collector for use in the initial cell were prepared by punching pieces 19 mm in diameter from the electrode sheet. Excluding the mass of the copper current collector, electrodes were approximately 8.9 mg, indicating 7.1 mg of graphite for electrodes with a composition of 8:1:1 wt. ratio of graphite, carbon black, and CMC. The electrode on a current collector was adhered to its substrate by a thin layer of epoxy - either 18 mm or 5 mm in diameter - that was allowed to cure under ambient conditions for 24 hours before the electrode was assembled into the custom battery cell.

In order to prepare electrodes for use in the second cell design, the composite electrode was carefully peeled off of the copper foil, creating a free-standing electrode, 90 - 100 µm thick, with no current collector. The free-standing electrode was cut using a razor blade into pieces approximately 3 x 5 mm or 3 x 7 mm. Electrodes typically massed 1.5 - 2.5 mg total, indicating to 1.2 - 2 mg of graphite for electrodes with a composition of 8:1:1 wt. ratio of graphite, carbon black, and CMC. The electrode was spot welded to its substrate at 120 V through a piece of stainless steel foil.

2.4.4 Custom Cell Assembly

The working electrode (composite graphite electrode or composite silicon electrode) on its substrate was assembled into the custom battery cell, and the cell was transferred to a glovebox with an argon atmosphere with O_2 and H_2O levels both under 10 ppm. A piece of lithium metal (counter electrode) was pressed onto stainless steel pins on its substrate. The cavity of the main body of the cell was filled with approximately 5 mL electrolyte, and the cell was sealed with a quartz window and an o-ring. The sealed cell was then brought into atmospheric conditions for testing. In order to prevent accumulation of gas on the working electrode surface from electrolyte decomposition during the formation of the solid electrolyte interphase (SEI) layer [32], the cell was oriented vertically during cycling.

2.4.5 Electrochemical Cycling

Within approximately 30 minutes of battery cell assembly, the cell was placed in the experimental setup and allowed to rest at open circuit voltage (OCV) for five hours while images were captured of the fluorescent particles on the electrode surface. This five-hour rest period allowed the cell to reach mechanical equilibrium. The reference point for all strain measurements was taken after this rest period, just prior to cycling.

The specific capacity of the battery, Q, is a measure of the total charge passed between the two electrodes during the charge or discharge cycle normalized by the mass of the active material, m, and is defined as:

$$Q = \frac{1}{m} \int_{t_o}^{t_f} I(\tau) d\tau \tag{2.10}$$

where I is the current and t is the time of charge or discharge. Ideally, the capacity is a measure of the number of lithium ions that are transferred to and from the graphite working electrode, but it can also include side reactions such as electrolyte decomposition. All capacities reported were normalized by the mass of the active material in the working electrode, unless otherwise noted.

Galvanostatic Cycling

Galvanostatic cycling tests were performed between 2.00 V and 0.01 V vs $Li^{+/0}$ on an Arbin potentiostat/galvanostat at various C-rates. C-rates reported were calculated using the theoretical capacity of the active material, Q_i, and the mass of the active material in the working electrode, m_i:

$$\text{C-rate} = \frac{Q_i m_i}{I}, \tag{2.11}$$

where I was the current used in the constant current portion of cycling. The theoretical capacity of graphite (Q_g = 372 mA h g^{-1} [61]) was used for graphite composite electrodes, and the theoretical capacity of silicon (Q_{si} = 4200 mA h g^{-1} [62, 63]) was used for silicon composite electrodes.

In this work, discharge of the half cell (i.e. lithium ions moving from the lithium metal counter electrode to the working electrode) is referred to as "lithiation," and charge of the half cell (i.e. lithium ions moving from the working electrode to the lithium metal counter electrode) is referred to as "delithiation." Images of the fluorescent particles were captured every 10 minutes. Therefore, each constant current charge / discharge was followed by a constant current voltage hold of 11 minutes in order to capture an image at the end of each lithiation and delithiation step. Following the constant voltage step, the cell rested for 10 seconds (no applied current or voltage) to allow the potentiostat / galvanostat to switch smoothly to the next step.

Potentiostatic Test

To explore the effect of electrolyte decomposition on electrode deformation, we designed a test in which electrolyte reduction was the dominating electrochemical reaction. Electrodes with a composition of 8:1 wt. ratio of graphite and polymer binder (no carbon black) were held potentiostatically at a voltage of 0.5 V vs $Li^{+/0}$ for a certain amount of time while the

current and strain responses were monitored. The voltage of 0.5 V vs $Li^{+/0}$ was below the threshold for reduction of electrolyte species (ca. 0.8 V vs $Li^{+/0}$ [33]), but above the threshold for lithium intercalation into graphite (ca. 0.3 V vs $Li^{+/0}$ [4]). Electrodes were fabricated without carbon black to avoid any contribution to the capacity from lithium intercalation into carbon black, which occurs at voltages lower than ca. 1.5 V vs $Li^{+/0}$ [4]. Therefore, all capacity gained during this voltage hold was directly associated with irreversible electrolyte reduction.

Cyclic Voltammetry

For the data presented in Chapter 5, cyclic voltammetry (CV) was performed at scan rates of 10 µV s^{-1} (1.00 - 0.01 V vs $Li^{+/0}$), 25 µV s^{-1} (1.00 - 0.01 V vs $Li^{+/0}$), and 100 µV s^{-1} (1.50 - 0.01 V vs $Li^{+/0}$) for three cycles. The first half of the cycle is denoted as the cathodic scan, when the working electrode potential was swept from higher voltages to lower voltages; negative current indicates lithiation of the working electrode. The second half of the scan is denoted as the anodic scan, when the working electrode potential was swept from lower voltages back to higher voltages; positive current indicates delithiation of the working electrode.

For the data presented in Appendix C, linear sweep voltammetry was performed between the open circuit voltage (OCV) of the electrode (ca. 2 - 3 V vs $Li^{+/0}$) and 0.3 V vs $Li^{+/0}$. The electrode potential was swept at 25 µV s^{-1}. Similar to the potentiostatic test, electrodes were fabricated without carbon black (8:1 wt. ratio of graphite and CMC binder) so that electrolyte decomposition was the dominating electrochemical reaction occuring in the voltage range investigated. Before cycling, the cell was allowed to rest for 24 hours. This extended rest period was required to ensure a more stable mechanical equilibrium than the standard five hour rest period, since the strains developed during this test were much smaller than strains developed in standard galvanostatic cycling tests.

2.4.6 Imaging Parameters

To excite the fluorescent nano-particles on the surface of the electrode, a 532 nm, 75 mW laser beam (Crystalaser) was expanded and directed onto the electrode at an angle of ca. 20°, creating an elliptical spot size of approximately 4 x 5 mm. Experiments were carried out under a blackout blanket to prevent ambient light effects and to minimize influence of temperature fluctuations of the ambient lab environment. Images were captured using either Retiga camera (Q-Imaging) or an Aqua camera (Q-Imaging) and a 12X zoom lens (Navitar), for an effective scale of ca. 2.4 µm pixel^{-1}. A 620 nm filter was placed directly in front of the zoom lens to filter reflected laser light so that only emitted fluorescent light was captured in the images. Image exposure of 2 - 5 sec (with the Retiga camera) or 0.2 - 0.5 sec (with the Aqua camera) was used, and images were captured every 5 - 10 minutes. To prevent bleaching of the particles, the laser was shuttered during the majority of the test, and only unshuttered during image capture.

Fig. 2.2c shows an image of the working electrode spot welded to its substrate in the second custom battery cell. The region captured in the images, outlined by the yellow rectangle, was 3 x 2.5 mm. At this length scale, the composite response was considered a homogeneous average of the individual particle responses. Fig. 2.4 shows the experimental configuration of the camera, zoom lens, laser, and custom battery cell during electrochemical cycling as well as a representative speckle pattern created by the fluorescent nano-particles on the electrode surface.

2.4.7 Digital Image Correlation

The Matlab-based DIC code used in this work was adapted from open-source code by Eberl et al. [64], and a complete, working copy is available online [65]. A full description of the code, including an example correlation, is included in Appendix F, and the accuracy and precision of the code is evaluated in Appendix G. In this work, the images were processed through a

low-pass filter of radius 3 pixels (7.2 µm) in order to remove aliasing effects before the images were correlated; the filter was generated using the built-in Matlab function *fspecial* and the images were filtered using the built-in Matlab function *imfilter*. A grid of ca. 90 by 120 control points with horizontal and vertical spacing of 10 pixels (24.4 µm) and a subset size of ca. 21 x 21 pixels (ca. 50 x 50 µm) were used during the image correlation. A smoothing kernel of 11 x 11 control points (260 x 260 µm) was used, and displacements were smoothed three times before strains were calculated.

2.5 Conclusions

A system was developed to quantify the strain in lithium-ion battery electrodes during electrochemical cycling. Two custom battery cells were designed, one that allowed strain measurements of electrodes fabricated on a current collector and one that allowed strain measurements of free-standing, unconstrained electrodes. A speckle pattern for digital image correlation was generated using fluorescent silica nano-particles, and in-house DIC code was used to correlate images captured *in situ* and calculate strains. Finally, a model based on porous composite theory was developed to predict the expansion of unconstrained composite electrodes based on known expansion of the active material particles.

Chapter 3

Deformation of Graphite Electrodes*

In this chapter, the deformation of graphite composite electrodes resulting from electrochemical cycling is discussed. Strain was measured in both electrodes adhered to a current collector and in free-standing, unconstrained electrodes. Two principle deformation mechanisms were identified. Reversible macroscale deformation of the composite electrode was traced to changes in the graphite layer spacing at the atomic scale as different graphite-lithium intercalation compounds were formed. Irreversible deformation was correlated with the formation and growth of the solid-electrolyte interphase (SEI) layer. The expansion of free-standing electrodes agrees well with an analytical model.

3.1 Representative Electrode Response

3.1.1 Electrochemical Response

Figure 3.1 shows the representative electrochemical data for three cycles of a free-standing composite graphite working electrode cycled galvanostatically at C/20 rate in the second custom battery cell (Fig. 2.2). Fig. 3.1a shows the full voltage axis, and Fig. 3.1b expands the voltage axis for clarity. The red circle represents the open circuit voltage (OCV) of the cell before cycling. As lithium ions moved from the lithium metal counter electrode to the graphite working electrode, the voltage decreased and the capacity increased (black lithiation curve). When lithium ions moved in the reverse direction, the voltage increased

*Significant portions of this chapter were published in E. M. C. Jones, M. N. Silberstein, S. R. White, N. R. Sottos. *Exp. Mech.* (2014) 54:971-985

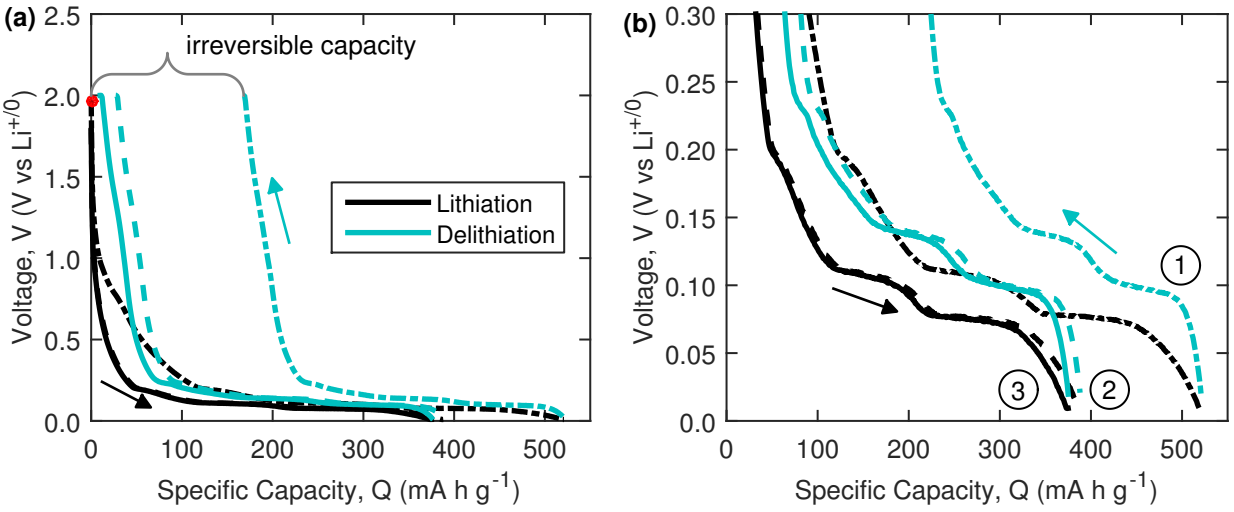

Figure 3.1: Representative electrochemical response of a graphite composite electrode. The electrode had a composition of 8:1:1 wt. ratio of graphite, carbon black and CMC binder and was cycled galvanostatically at C/20 rate for three cycles in the second custom battery cell (Fig. 2.2). The capacity is normalized with respect to the mass of graphite in the working electrode. The red circle represents the open circuit voltage (OCV) at the start of cycling. (a) Full voltage axis and (b) expanded voltage axis.

and the capacity decreased (blue delithiation curve). Electrodes cycled in the initial cell (Fig. 2.1) and electrodes cycled without fluorescent nano-particles in a flooded beaker cell had qualitatively and quantitatively similar electrochemical performance.

The lithiation portion of the first cycle showed an artificially high capacity due to irreversible chemical reactions that occurred during the formation of the solid electrolyte interphase (SEI) layer [32], resulting in 167 mA h g^{-1} of irreversible capacity. The inefficiency of the cell (i.e. the difference between the lithiation capacity and delithiation capacity) indicated continued electrolyte decomposition on cycles two and three, though to a smaller extent than the main decomposition on the first cycle. The irreversible capacity is discussed in more detail in Sec. 3.3. The cell achieved a reversible capacity of approximately 360 mA h g^{-1}, which was close to the theoretical capacity of graphite (372 mA h g^{-1} [61]), indicating that the electrode cycled well in the custom battery cell.

3.1.2 Strain Response of Constrained Electrodes

Figure 3.2 contains line scans of the strain that developed at the end of the first lithiation of the constrained electrode cycled in the initial custom battery cell (Fig. 2.1) using the first attachment configuration (Fig. 2.1c). The line scans were taken along a vertical line (red dashed line) in the center of the region of interest (yellow rectangle), marked in the inset of Fig. 3.2. The horizontal normal strain, E_{xx}, and the shear strain, E_{xy}, were both small over the entire region of interest. The vertical normal strain, E_{yy}, was concentrated in a ring less than 1 mm wide at the edge of the electrode, with negligible strain developed in the center of the electrode. It is hypothesized that the epoxy adhesive layer effectively constrained the majority of the electrode, and that significant strain developed only in the edge of the electrode that is not constrained by the epoxy.

When the constraint was relaxed and the electrode was attached to its substrate using the second attachment configuration (Fig. 2.1d), the electrode curled and uncurled repeatedly during lithiation and delithiation, preventing strain measurements. The curling behavior of

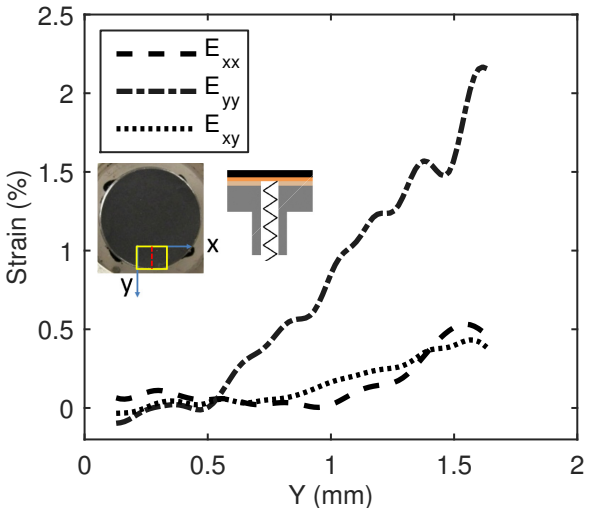

Figure 3.2: Spatial variation of the strain of a constrained graphite composite electrode at the end of the first lithiation. The electrode had a composition of 8:1:1 wt. ratio of graphite, carbon black and CMC binder and was cycled in the initial cell (Fig. 2.1), attached to its substrate via a nearly complete layer of epoxy. The line scans were taken along a vertical line (red dashed line) in the center of the region of interest (yellow rectangle).

the bi-layer electrode / current collector system arose as the graphite electrode expanded and contracted while the copper current collector attempted to retain its size. It was analogous to the curvature change that occurs during a temperature change in a bi-layer system made of materials with different coefficients of thermal expansion, e.g. a bi-metallic thermostat.

3.1.3 Strain Response of Unconstrained Electrodes

During the drying step of the electrode fabrication process (Sec. 2.4.3), the electrode developed a slight concave curvature, which was indicative of the development of residual tensile stress in the electrode [66]. During the five-hour rest step that was performed before every cycling test (Sec. 2.4.5), a negative strain of approximately -0.1 % developed in both of the normal directions, E_{xx} and E_{yy}, while the shear strain, E_{xy}, was zero (Fig. 3.3), indicating that the free-standing electrode underwent a volumetric contraction. We hypothesize that during the five-hour rest period, the polymer binder became more compliant (e.g. due to swelling of the binder in electrolyte or heating of the binder by the laser used during imaging) and contracted to relieve the residual tensile stress. The reference point for all strain

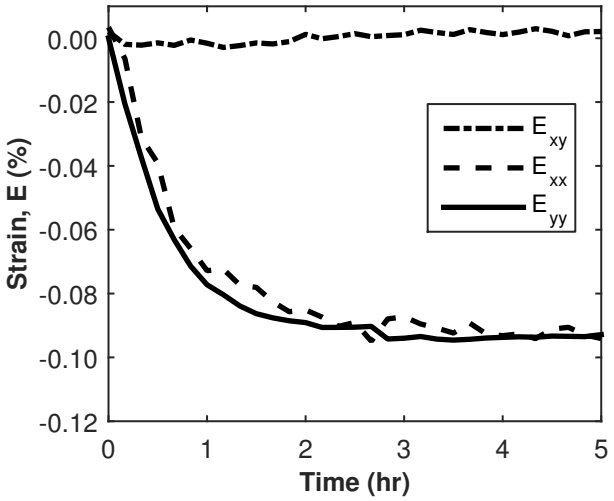

Figure 3.3: Strain evolution of a graphite composite electrode during a five-hour rest period before cycling. The electrode had a composition of 8:1:1 wt. ratio of graphite, carbon black, and CMC binder, and the rest period started less than 30 minutes after the battery cell was assembled.

measurements was taken after this rest period, just prior to cycling. After the electrode reached mechanical equilibrium during the rest period, we believe temperature rise during cycling was negligible because of the small electrode mass (ca. 1.5 - 2.0 mg active material), slow cycling rates (C/5 or slower), large volume of electrolyte that acted as a heat sink (ca. 5 mL) and black-out blanket that minimized influence of temperature fluctuations of the ambient lab environment.

Figure 3.4 contains contour plots and line scans of the strain components of the free-standing graphite electrode at the end of the first lithiation in the second custom battery cell (Fig. 2.2). The line scans were taken along a vertical line (red dashed line) in the center of the region of interest (yellow rectangle), marked in the inset of Fig. 3.4d. The horizontal normal strain, E_{xx}, was spatially uniform, while the vertical normal strain, E_{yy}, was larger towards the unconstrained side of the electrode (right) and smaller towards the side that was spot welded to the substrate (left). The two normal strains were of the same order of magnitude, and the shear strain, E_{xy}, was negligible, as expected for an isotropic volumetric expansion.

The state of strain of the electrode is given by the rotationally invariant equivalent strain:

$$E_{eqv} = \left[\frac{3}{2}\left(E_{ij}E_{ij} - \frac{1}{3}E_{mm}E_{nn}\right)\right]^{1/2} \tag{3.1}$$

where E_{ij} are the components of the two-dimensional finite-strain tensor and repeated indices imply summation. For each image captured during cycling, the equivalent strain was averaged over a vertical line in the middle of the region of interest. The portion of the electrode in the middle of the region of interest was sufficiently far from the constraint of the spot welds to undergo nearly free expansion, yet was close enough to the support of the substrate that it did not undergo significant out-of-plane motion due to electrode bending. Averaging the equivalent strain over a vertical line farthest from the spot weld constraint (right edge of the region of interest) increased the strain by less than 0.1 % strain while

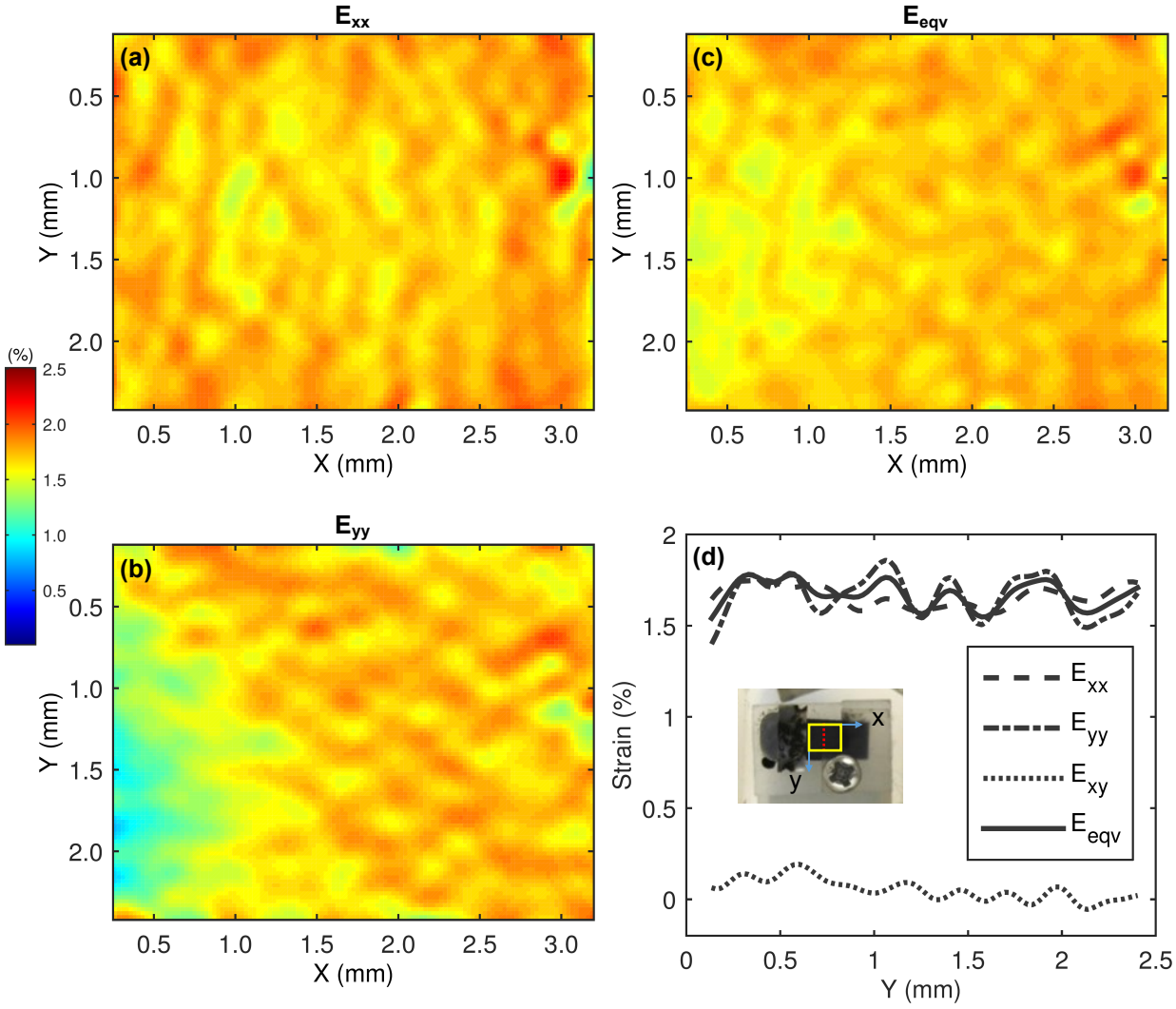

Figure 3.4: Spatial variation of the strain of an unconstrained graphite composite electrode at the end of the first lithiation. The electrode was cycled in the second battery cell (Fig 2.2). The line scans are taken along a vertical line (red dashed line) in the center of the region of interest (yellow rectangle), marked in the inset of (d). This strain data corresponds to the electrochemical data presented in Fig. 3.1.

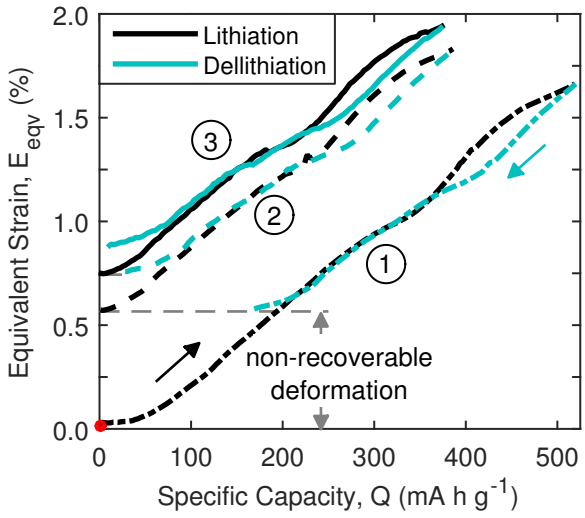

Figure 3.5: Representative strain response of a free-standing graphite composite electrode during galvanostatic cycling. The electrode was cycled in the second custom battery cell (Fig. 2.2). The equivalent strain was averaged along a vertical line in the center of the region of interest (red dashed line in the inset of Fig. 3.4d). The capacity is normalized with respect to the mass of graphite and carbon black in the working electrode. The red circle represents the start of cycling. This strain data corresponds to the electrochemical data presented in Fig. 3.1.

averaging over a vertical line closest to the spot weld constraint (left edge of the region of interest) decreased the strain by less than 0.2 % strain.

The average equivalent strain is plotted in Fig. 3.5 as a function of the working electrode capacity. The start of the test is represented by the red circle, at zero strain and zero capacity. As the electrode was lithiated and the capacity increased (black curves), the strain increased an average of 1.23 % per cycle (averaged over cycles 2-3). When the electrode was subsequently delithiated (blue curves), the strain decreased an average of 1.06 % per cycle (averaged over cycles 2-3). The expansion and contraction of the graphite electrode was not completely reversible. During the first cycle in particular, the electrode expanded during lithiation more than it contracted during delithiation, resulting in 0.56 % strain that was not recovered. The cumulative non-recoverable deformation increased with additional cycles.

From the strain measurements of free-standing electrodes, two deformation mechanisms were identified, as shown schematically in Fig. 3.6. Reversible electrode deformation was traced to changes in the graphite layer spacing as lithium was intercalated and deintercalated while irreversible electrode deformation was correlated with the formation and growth of the solid electrolyte interphase (SEI). These deformation mechanisms are discussed in detail in Sec. 3.2 and Sec. 3.3 respectively.

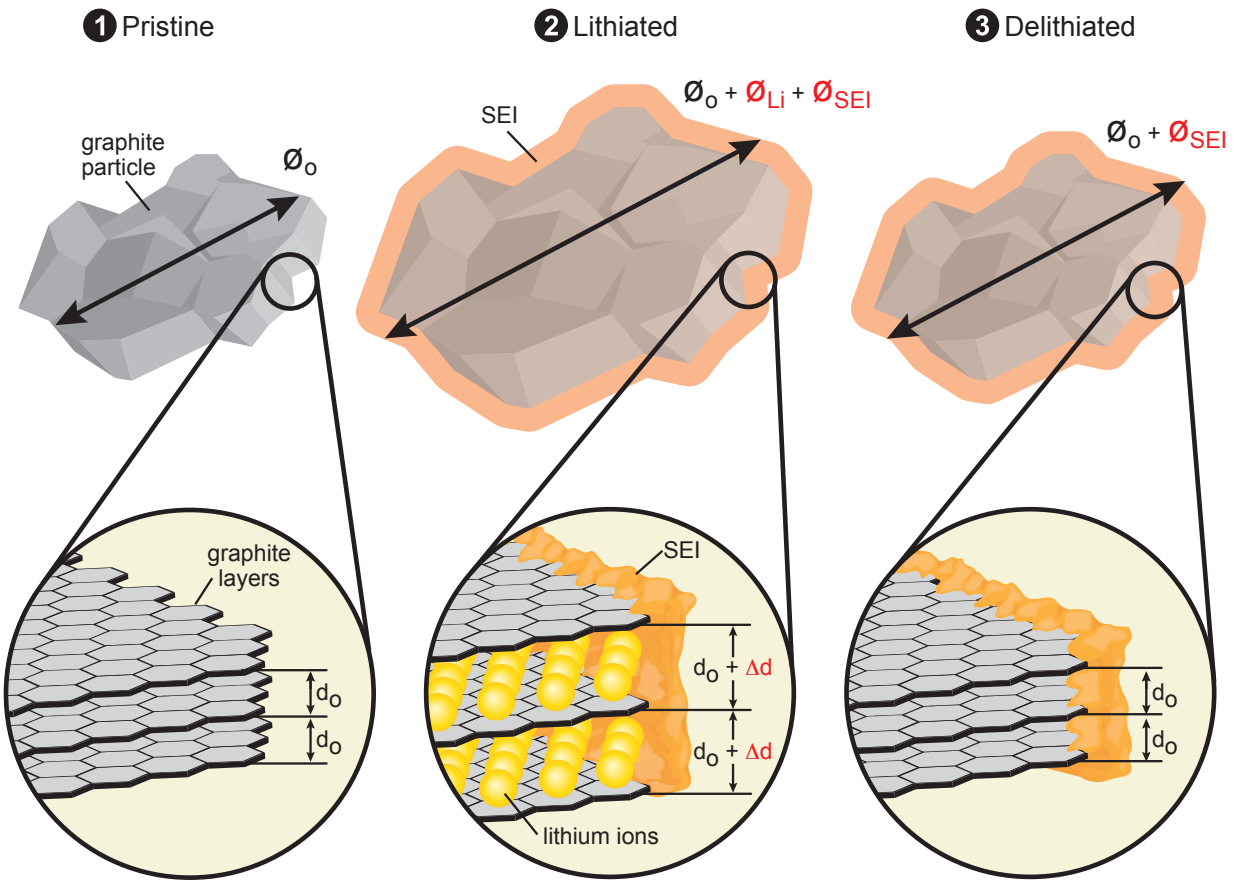

Figure 3.6: Schematic depicting mechanisms of reversible and irreversible deformation of graphite electrodes. (1) A pristine graphite particle has an initial size of ϕ_o determined by the characteristic layer spacing of d_o between graphite layers. (2) Lithium intercalation causes the graphite layer spacing to increase by Δd at the atomic scale, which is translated to the microscale as an overall size increase of the graphite particle by ϕ_{Li}. Deposition of electrolyte reduction products on the surface of the graphite particle during the formation of the SEI causes a further increase in the graphite particle size of ϕ_{SEI}. (3) Upon delithiation, deformation due to lithium intercalation is recovered, but the increase in the particle size due to SEI formation is not recovered.

3.2 Reversible Behavior

3.2.1 Graphite-Lithium Intercalation Compounds

During galvanostatic cycling, transitions between graphite-lithium intercalation compounds (G-LICs) are manifested as voltage plateaus or equivalently as peaks in the derivative of capacity with respect to voltage. Through simultaneous x-ray diffraction measurements of the graphite layer spacing and galvanostatic cycling of composite graphite electrodes, Dahn et al. [4, 5] associated four of the five expected phase transitions between different G-LICs with specific peaks in the capacity derivative. The voltage values where the peaks occurred and the corresponding phase transitions are listed in Table 3.1 for reference.

Following the work of Dahn et al., we present the derivative of capacity with respect to voltage of a graphite composite electrode in Fig. 3.7a. Four peaks were observed in the capacity derivative, labeled A_i, B_i, C_i, and D_i, where the subscript i denotes either the lithiation portion of cycling ($i = L$) or the delithiation portion of cycling ($i = D$). The peaks in the capacity derivative in Fig. 3.7b were associated with specific phase transitions of G-LICs through correlation of the location and relative magnitude of the peaks with those shown by Dahn et al. [4, 5]. The voltages at which the peaks in the capacity derivative occurred, averaged over cycles 2-3, are listed in Table 3.1 with the corresponding phase transitions.

The corresponding derivative of the strain with respect to voltage of a graphite composite electrode is presented in Fig. 3.7b. The voltages at which the peaks of the strain derivative occurred, averaged over cycles 2-3, are listed in Table 3.1. The peaks in the strain derivative correspond remarkably well with the peaks in the capacity derivative, both in terms of location and relative magnitude. This correspondence indicates that the reversible strain that develops at the macroscale in the graphite composite electrode is directly related to the atomic-scale changes in graphite layer spacing associated with different graphite-lithium intercalation compounds.

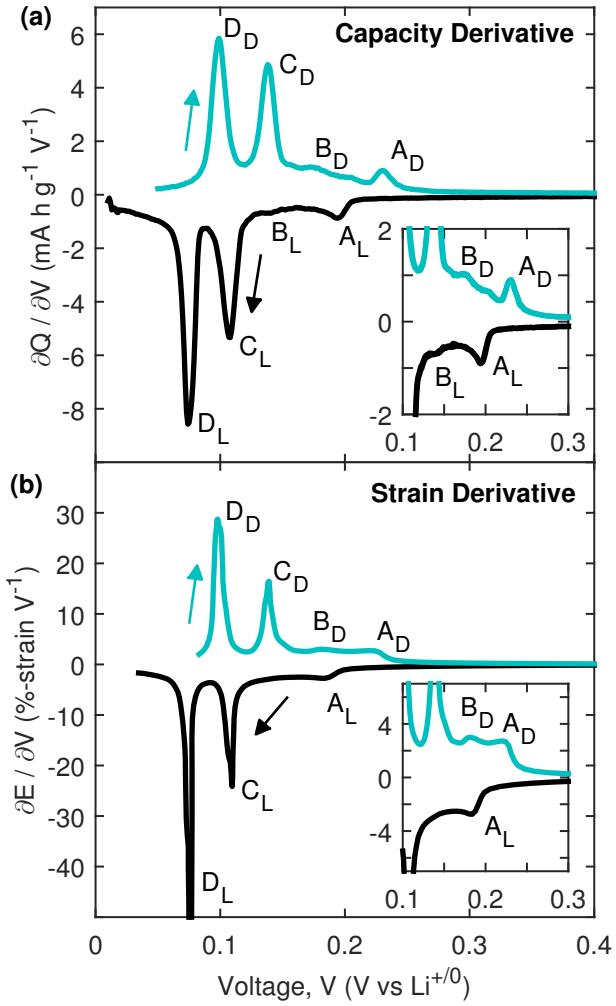

Figure 3.7: Phase transitions between graphite-lithium intercalation compounds (G-LICs) formed during galvanostatic cycling. (a) Derivative of capacity and (b) derivative of strain with respect to voltage for the third cycle. This data is derived from the electrochemical data presented in Fig. 3.1 and the strain data presented in Fig. 3.5. The peaks labeled A_L - D_L and A_D - D_D correspond to the phase transitions between G-LICs during lithiation and delithiation respectively, which are summarized in Table 3.1.

Table 3.1: Voltages associated with specific phase transitions between graphite-lithium intercalation compounds, taken from the peaks in the derivative of capacity and of strain with respect to voltage (Fig. 3.7)

	Peak	Transition	Voltage (V vs $Li^{+/0}$)		
			Capacity Derivative†	Strain Derivative†	Capacity Derivative#
Lithiation	A_L	DI → IV	0.194	0.185	0.195
	B_L	III → DII	0.141	–	0.127
	C_L	DII → II	0.108	0.109	0.107
	D_L	II → I	0.075	0.076	0.060
Delithiation	D_D	I → II	0.098	0.098	0.107
	C_D	II → DII	0.138	0.139	0.141
	B_D	DII → III	0.174	0.175	0.146
	A_D	IV → DI	0.231	0.218	0.231

†This work; #Dahn et al. [4, 5]. Note, Dahn et al. were unable to associate a specific peak in the capacity derivative with the stage IV to stage III transition.

3.2.2 Comparison of Analytical Model to Experimental Results

The predictions of the analytical model described in Sec. 2.3 for the expansion of graphite composite electrodes due to lithium intercalation are presented in Fig. 3.8, along with experimental data for comparison. The model is insensitive to variations in the properties of individual components of the composite electrode. A sensitivity study of the Young's modulus, Poisson's ratio, and density of CMC, CB and G-LICs shows that for a change of +/- 10 % in any property except the Poisson's ratio of the porous matrix or the density of graphite, the maximum composite electrode strain remains at 1.92 %. A change of +/- 10 % in the assumed Poisson's ratio of the porous matrix of 1/3 leads to a maximum composite electrode strain of 1.96 % to 1.87 % (a change of +/- 2 % from the original 1.92 % strain). For a given mass fraction of graphite, increasing the density of graphite by 10 % effectively decreases the volume fraction of graphite, which leads to a decrease in the maximum composite strain to 1.78 % (a change of 7 % from the original 1.92 % strain); the opposite trend holds for a decrease in the density of graphite.

The two experimentally adjustable composite parameters that affect the strain significantly are the density of the electrode (essentially the porosity of the electrode) and the mass ratio of graphite, CB, and CMC. Changing either by +/- 10 % results in a maximum strain in the composite electrode of 2.06 % to 1.76 % (a change of +/- 8 % from the original 1.92 % strain). By tailoring the electrode porosity and loading of graphite, the global strain in the composite electrode (red curve in Fig. 3.8) can be reduced to nearly half of the 3.2 % strain of randomly-oriented graphite particles (green curve in Fig. 3.8).

The experimentally measured strain agrees well with the model predictions, though the model predicts a slightly larger strain. The two most likely sources of error that could account for this discrepancy are the measurement of the mass of graphite in the electrode

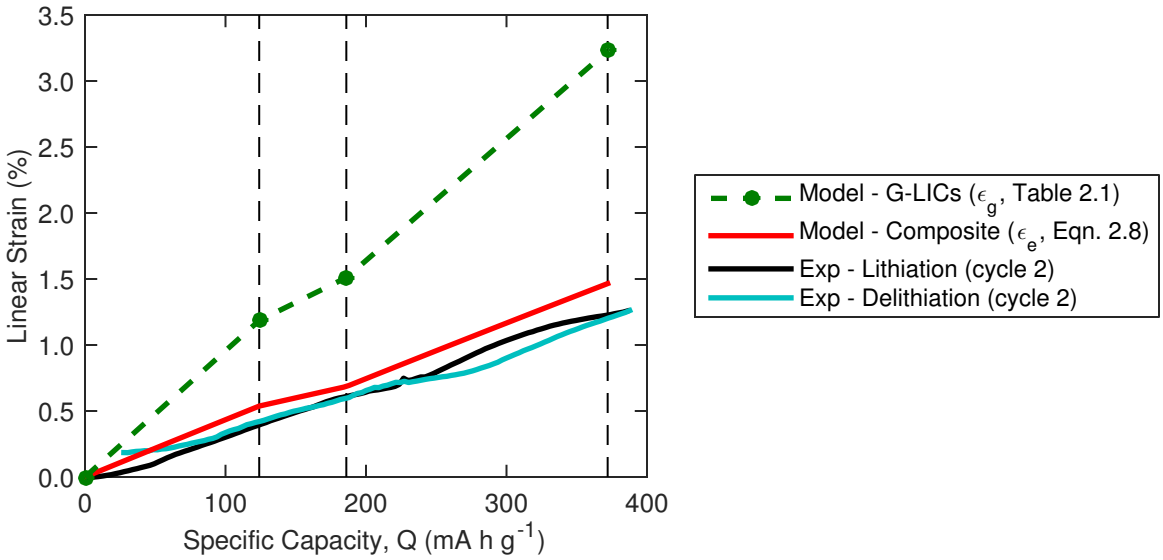

Figure 3.8: Comparison of model predictions with experimental results for the expansion / contraction of graphite composite electrodes. The green curve represents the predicted linear strain of randomly-oriented graphite particles, based on linear interpolation between values of linear strain of each distinct phase of graphite-lithium intercalation compounds (G-LICs) from Table 2.1. The red curve represents the predicted linear strain of an unconstrained composite graphite electrode (Eqn. 2.8). The experimental data, from cycle two of Fig. 3.5, was shifted down on the y-axis by 0.56 %, to account for the non-recoverable deformation developed during the first cycle. The vertical dashed lines represent the three phases of G-LICs used in the model (left to right, stage III LiC_{18}, stage II LiC_{12}, and stage I LiC_6).

and the calculation of the electrode porosity. Because the model assumes elastic, reversible deformation, it does not capture the non-recoverable deformation seen experimentally.

3.3 Irreversible Behavior

Scanning electron micrographs of the edge of a graphite composite electrode before and after galvanostatic cycling are presented in Fig. 3.9. In the images of the cycled electrode, debris is observed to cover the surfaces of the graphite particles and carbon black. This debris composes the solid-electrolyte interphase (SEI), a thin film of electrolyte decomposition products that are deposited on all of the electrically-conductive surfaces of the graphite electrode during the initial portion of cycling.

The formation of the SEI layer is the primary source of irreversible capacity loss associated with graphite electrodes [32]. As shown in Fig. 3.1 and Fig. 3.5, both the irreversible capacity and the non-recoverable deformation of free-standing composite graphite electrodes accumulate primarily during the first cycle of galvanostatic cycling, with smaller increases during later cycles. Additionally, the irreversible capacity and the non-recoverable deformation both increase with increasing carbon black content (see Sec. 4.2) and increasing cycling time (see Sec. 4.3). Thus, the non-recoverable deformation is correlated with the irreversible capacity associated with SEI formation during galvanostatic cycling. Mukhopadhyay and Tokranov et al. [45, 46] similarly correlated irreversible stress development in graphitic carbon electrodes with SEI formation, and Tavassol et al. [47] found that the SEI formed on a model gold electrode also resulted in irreversible stress generation.

To probe the relationship between SEI formation and non-recoverable deformation directly, we subjected graphite composite electrodes to a potentiostatic voltage hold at 0.5 V vs $Li^{+/0}$ (Sec. 2.4.5). In this test, the capacity gained was directly associated with irreversible reduction of electrolyte solvents during the formation and growth of the SEI. Representative current, capacity, and strain responses are presented in Fig. 3.10. A positive strain,

indicating electrode expansion, developed during the voltage hold. These results show that electrolyte decomposition directly caused expansion of composite graphite electrodes.

Motivated by the correlation between irreversible capacity and non-recoverable deformation observed during galvanostatic cycling (Fig. 3.1 and Fig. 3.5), the scanning electron micrographs of the SEI layer on a cycled electrode (Fig. 3.9), and the electrode expansion induced directly by electrolyte reduction (Fig. 3.10), we hypothesize that electrolyte decomposition products deposited onto the surface of the graphite particles (i.e. the SEI layer) cause an overall increase in the size of the graphite particles. This irreversible increase in

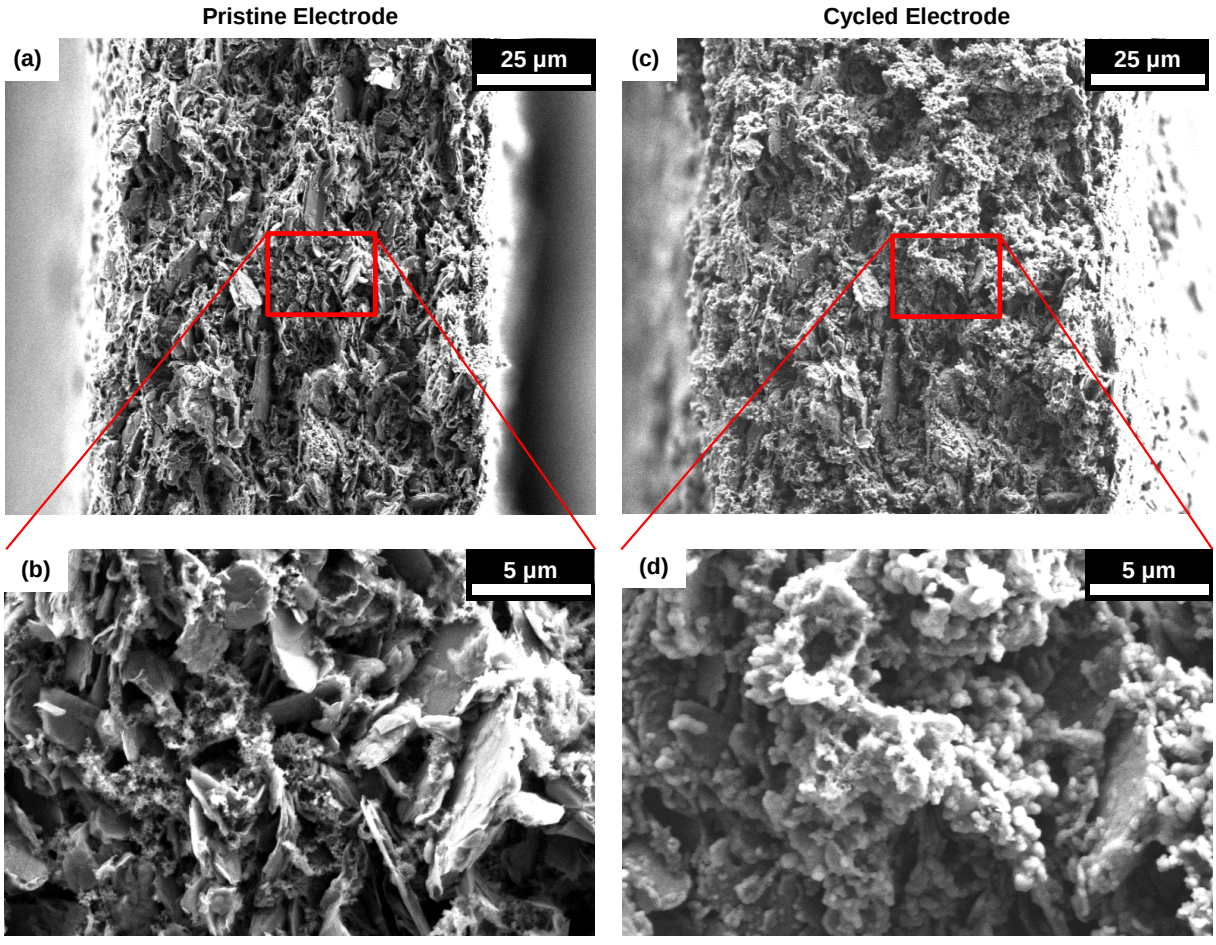

Figure 3.9: Scanning electron micrographs of the edge of a graphite composite electrode. the electrode had a composition of 8:1:1 wt. ratio graphite, carbon black, and CMC binder and was cycled galvanostatically at C/5 rate for five cycles. (a-b) Pristine electrode, before cycling and (c-d) electrode after cycling.

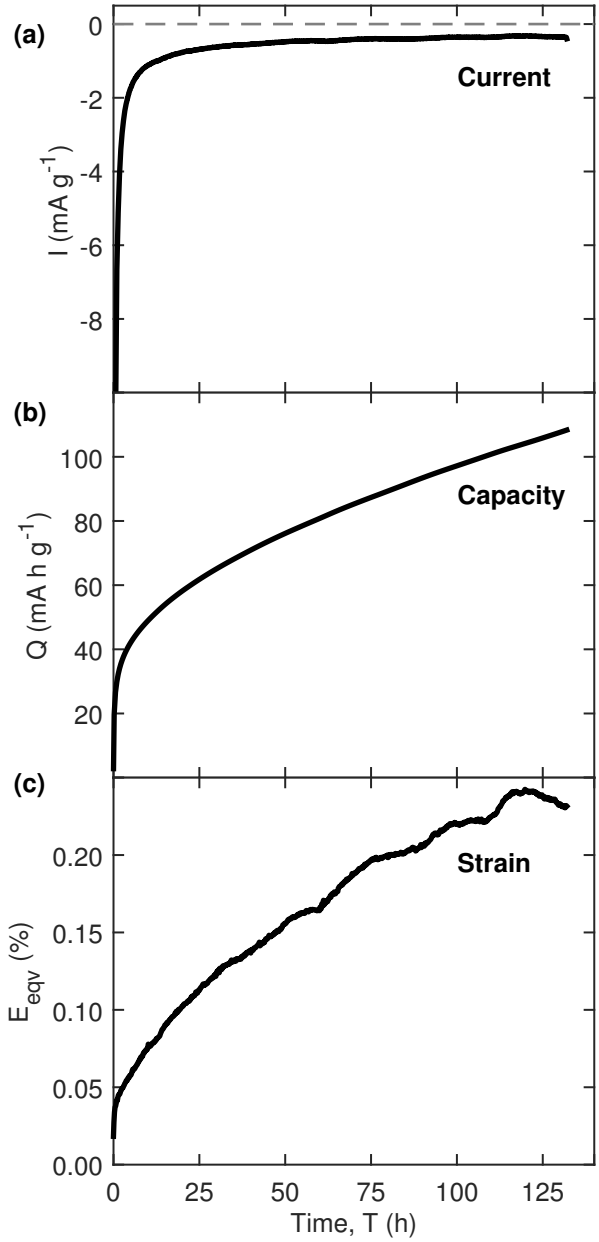

Figure 3.10: Representative electrochemical and mechanical response of a graphite composite electrode during a potentiostatic voltage hold. The electrode had a composition of 8:1 wt. ratio of graphite and CMC binder and was held at 0.5 V vs $Li^{+/0}$ for 132 hours. (a) Current, (b) capacity and (c) strain responses.

particle size leads to non-recoverable macroscopic expansion of the electrode. Two other possible sources of non-recoverable deformation were also investigated - relaxation of residual stress and electrode fracture - but no evidence was found linking these phenomena to non-recoverable deformation (see Sec. A.2 in Appendix A).

3.4 Conclusions

The deformation of graphite composite electrodes induced by electrochemical cycling was measured. Electrodes adhered to a current collector developed minimal strain due to the constraint applied by the underlying substrate. Free-standing electrodes expanded and contracted approximately 1.0 - 1.2 % when lithium was intercalated and removed, which is in good agreement with analytical predictions.

Two principle deformation mechanisms of graphite composite electrodes were identified, as shown schematically in Fig. 3.6. Reversible macroscale electrode deformation was traced to nanoscale changes in graphite layer spacing associated with different graphite-lithium intercalation compounds. Irreversible electrode deformation was correlated with accumulation of electrolyte decomposition products on the surface of graphite and carbon black particles during the formation and growth of the solid-electrolyte interphase (SEI).

Chapter 4

Effect of Electrode Composition, Cycling Rate, and Electrolyte Composition

In this chapter, the influence of several battery parameters on the deformation of graphite composite electrodes is discussed. First, two polymer binders were investigated, a stiffer polymer, carboxymethyl cellulose (CMC) and a softer polymer, poly(vinylidene fluoride) (PVdF). Second, the ratio of active material (graphite) to conductive additive (carbon black) was varied, and the effect of electrode composition was studied. Third, electrodes were cycled at different rates in order to investigate the influence of cycling rate and total cycling time on the strain response of the electrodes. Finally, the influence of electrolyte additives on both the reversible and irreversible behavior of the electrode is discussed.

4.1 Effect of Polymer Binder

4.1.1 Reversible Behavior

Graphite electrodes were fabricated with a composition of 8:1:1 wt. ratio of graphite, carbon black, and either PVdF or CMC binder, and the electrodes were cycled galvanostatically at C/5 rate. The reversible capacity and strain, taken as the average delithiation values for cycles 1-3, are presented in Fig. 4.1. The electrodes with PVdF binder achieved a slightly reduced capacity compared to the electrodes with CMC binder, while both types of electrodes developed the same amount of reversible strain. We define the specific expansion of the composite electrode during galvanostatic cycling, E^s_{GS}, as the reversible electrode deformation induced by a given amount of reversible lithium intercalation / deintercalation:

$$E^s_{GS} = \frac{\Delta E_{rev}}{\Delta Q_{rev}}, \tag{4.1}$$

where ΔE_{rev} is the reversible strain per cycle and ΔQ_{rev} is the reversible capacity per cycle. The specific expansion ranges between 3.6 - 4.5 (average 3.9) percent-strain per A h g^{-1} for CMC-based electrodes (based on 6 tests) and between 4.1 - 4.6 (average 4.4) percent-strain per A h g^{-1} for PVdF-based electrodes (based on 4 tests). On average, electrodes made with CMC binder expanded approximately 14 % less for a given amount of lithium insertion / removal than electrodes made with PVdF binder. This result is consistent with the material properties of the binders themselves: CMC polymer is approximately 20 % less compliant than PVdF polymer (Young's modulus of ca. 1.2 GPa for CMC compared to ca. 1.0 GPa for PVdF [56]). The stiffer CMC binder constrained the electrode more and reduced the macroscopic strain that was developed during electrochemical cycling compared to the more compliant and ductile PVdF binder.

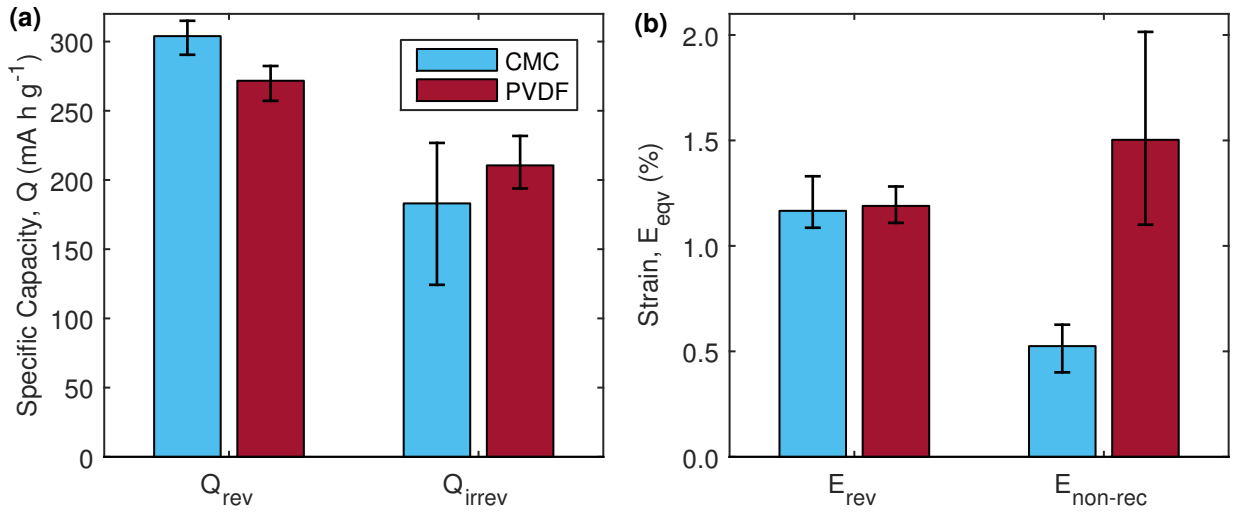

Figure 4.1: Effect of binder on capacity and strain responses for graphite composite electrodes. The electrodes had compositions of 8:1:1 wt. ratio of graphite, carbon black, and polymer binder (either CMC or PVdF) and were cycled galvanostatically at C/5 rate. (a) Reversible capacity (Q_{rev}) averaged over cycles 1-3 and irreversible capacity (Q_{irrev}) accumulated during cycles 1-3. (b) Reversible strain (E_{rev}) averaged over cycles 1-3 and non-recoverable deformation ($E_{non\text{-}rec}$) accumulated during cycles 1-3. Error bars represent minimum and maximum values of the individual tests (6 tests for CMC-based electrodes and 4 tests for PVdF-based electrodes).

4.1.2 Irreversible Behavior

The irreversible capacity and non-recoverable deformation accumulated during cycles 1-3 are also shown in Fig. 4.1. The irreversible capacity of the PVdF-based electrodes was 9 % higher than the irreversible capacity for the CMC-based electrodes, while the non-recoverable deformation was 175 % higher. The irreversible capacity results are consistent with previous work that has repeatedly shown higher irreversible capacity for PVdF-based electrodes compared to electrodes made with water-soluble binders such as CMC [67–70]. The large increase in non-recoverable deformation given a moderate increase in irreversible capacity, however, was not expected.

To investigate the effect of polymer binder on the irreversible behavior of the electrode in more depth, we performed the potentiostatic test (Sec. 2.4.5) on electrodes comprised of 8:1 wt. ratio of graphite and PVdF. In Fig. 4.2, the strain is plotted as a function of capacity developed in a representative electrode during a potentiostatic voltage hold at 0.5 V vs $Li^{+/0}$ over 72.5 hours. For comparison, the strain versus capacity response described in Sec. 3.3 for the electrode comprised of 8:1 wt. ratio of graphite and CMC and held at 0.5 V vs $Li^{+/0}$ for 132 hours is also shown.

The potentiostatic experiment reveals an interesting difference in the irreversible behavior of graphite composite electrodes made with the two different binders. When the SEI initially formed (Region I, corresponding to approximately the first 10 minutes of the voltage hold), the CMC-based electrode developed minimal strain while the PVdF-based electrode developed approximately 0.3 % strain. Previous investigations have shown that the binder influences SEI formation on composite graphite electrodes [67, 69, 71], and our strain analysis during the potentiostatic experiment is consistent with these results. We hypothesize that the large initial development of strain in the PVdF-based electrode at the beginning of the voltage hold was caused by the deposition of electrolyte decomposition products with a large volume (Fig. 4.2c). In contrast, the electrolyte decomposition products on the CMC-

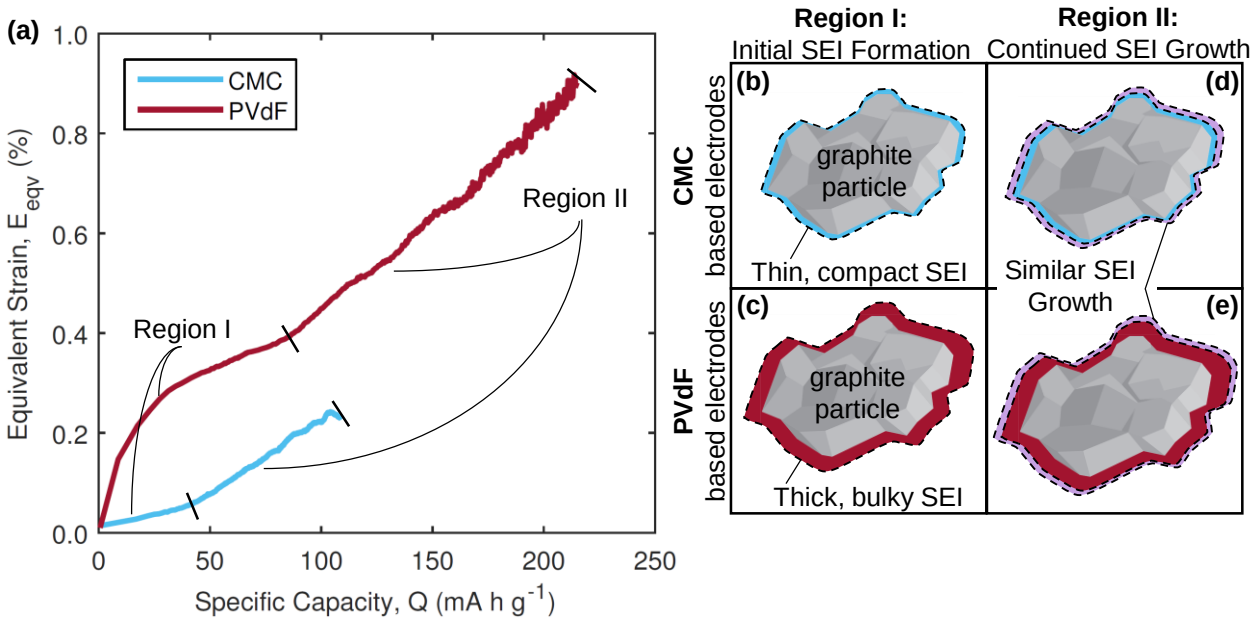

Figure 4.2: Effect of binder on SEI structure. (a) Strain as a function of capacity of graphite composite electrodes during a potentiostatic voltage hold. The electrodes had compositions of 8:1 wt. ratio of graphite and binder, either CMC or PVdF, and were held at 0.5 V vs $Li^{+/0}$. The CMC-based electrode was held for 132 hours (same data as Fig. 3.10) while the PVdF-based electrode was held for 72.5 hours. (b-e) Schematics depicting the structure of the SEI as it initially formed and subsequently grew on electrodes made with CMC or PVdF binders.

based electrode caused little strain to develop and so were likely forming a thin, compact layer (Fig. 4.2b).

During the majority of the potentiostatic test (Region II, corresponding to times greater than approximately 10 minutes), the strain increased linearly with capacity for both the CMC-based electrode and the PVdF-based electrode. The specific expansion of the electrodes during the potentiostatic test, E^s_{PS}, is defined as:

$$E^s_{PS} = \frac{\Delta E_{II}}{\Delta Q_{II}}, \tag{4.2}$$

where ΔE_{II} is the strain developed in the linear region II and ΔQ_{II} is the capacity developed in the linear region II. The specific expansion was approximately 2.9 percent-strain per A h g^{-1} for CMC-based electrodes and 3.9 percent-strain per A h g^{-1} for PVdF-based

electrodes. The reduced expansion of the CMC-based electrodes compared to PVdF-based electrodes in this linear region is similar to the reduced expansion observed during galvanostatic cycling and is likely due to the lower compliance of the CMC binder itself compared to the PVdF binder.

We hypothesize that the transition from Region I to Region II of the strain versus capacity response indicates a change over time in the nature of decomposition products that form on the electrode surface. When the electrolyte initially decomposed, the different binders strongly influenced the reductive reactions and resulting decomposition products. Therefore, the structure of the SEI was different on electrodes fabricated with the two different binders (Fig. 4.2b-c). After an initial SEI was formed over the pristine electrode surface, the binder no longer influenced the electrolyte decomposition, and continued SEI formation proceeded in a similar manner for both types of electrodes (Fig. 4.2d-e). Further characterization is required to confirm this hypothesis.

4.2 Effect of Carbon Black

In addition to the choice of polymer binder, the effect of carbon black content on the strain response of graphite composite electrodes was studied. Composite electrodes were fabricated with 10 wt.% CMC, and the weight ratio of graphite to carbon black was systematically varied from 9:0 (i.e. all graphite, no carbon black) to 0:9 (i.e. all carbon black, no graphite). The electrodes were cycled galvanostatically at various C-rates. The effect of carbon black content on the electrical conductivity of the electrodes is discussed in Appendix B.

Because the carbon black content was significant for some of the electrodes presented in this section, the capacity values reported here were normalized by the combined mass of graphite and carbon black. Additionally, the C-rates reported here were calculated using the theoretical capacity of graphite, $Q_g = 372$ mA h g^{-1} (per gram of graphite) [61], and the combined mass of graphite and carbon black in the electrode, m_{g+cb}:

$$\text{C-rate} = \frac{Q_g m_{g+cb}}{I}, \tag{4.3}$$

where I was the current used in the constant current portion of cycling.

4.2.1 Reversible Behavior

The reversible capacity and strain, taken as the average delithiation values for the first three cycles, are shown in Figs. 4.3(a-b). In general, the reversible capacity decreased with increasing carbon black content / decreasing graphite content at a given cycling rate. This reduction is due to the inherently lower reversible capacity of carbon black (ca. 165 mA h g^{-1} at C/5 rate) compared to graphite (ca. 290 mA h g^{-1} at C/5 rate). The reversible strain followed the capacity results directly: the electrode expanded / contracted more when more lithium was inserted into / removed from the electrode.

4.2.2 Irreversible Behavior

The irreversible capacity and non-recoverable deformation accumulated during cycles 1-3 are shown in Figs. 4.3(c-d). For a given cycling rate, the irreversible capacity increased with increasing carbon black content / decreasing graphite content. This result is consistent with

Table 4.1: Number of tests performed for each composition and cycling rate included in Fig. 4.3 and Fig. 4.4.

	Electrode Composition (wt. ratio of graphite, carbon black, and CMC)			
Cycling Rate	9:0:1	8:1:1	6:3:1	0:9:1
C/1	0	1	0	0
C/2	0	1	0	0
C/3	0	1	0	0
C/5	2	3	1	2
C/10	2	1	1	0
C/20	1	2	0	0

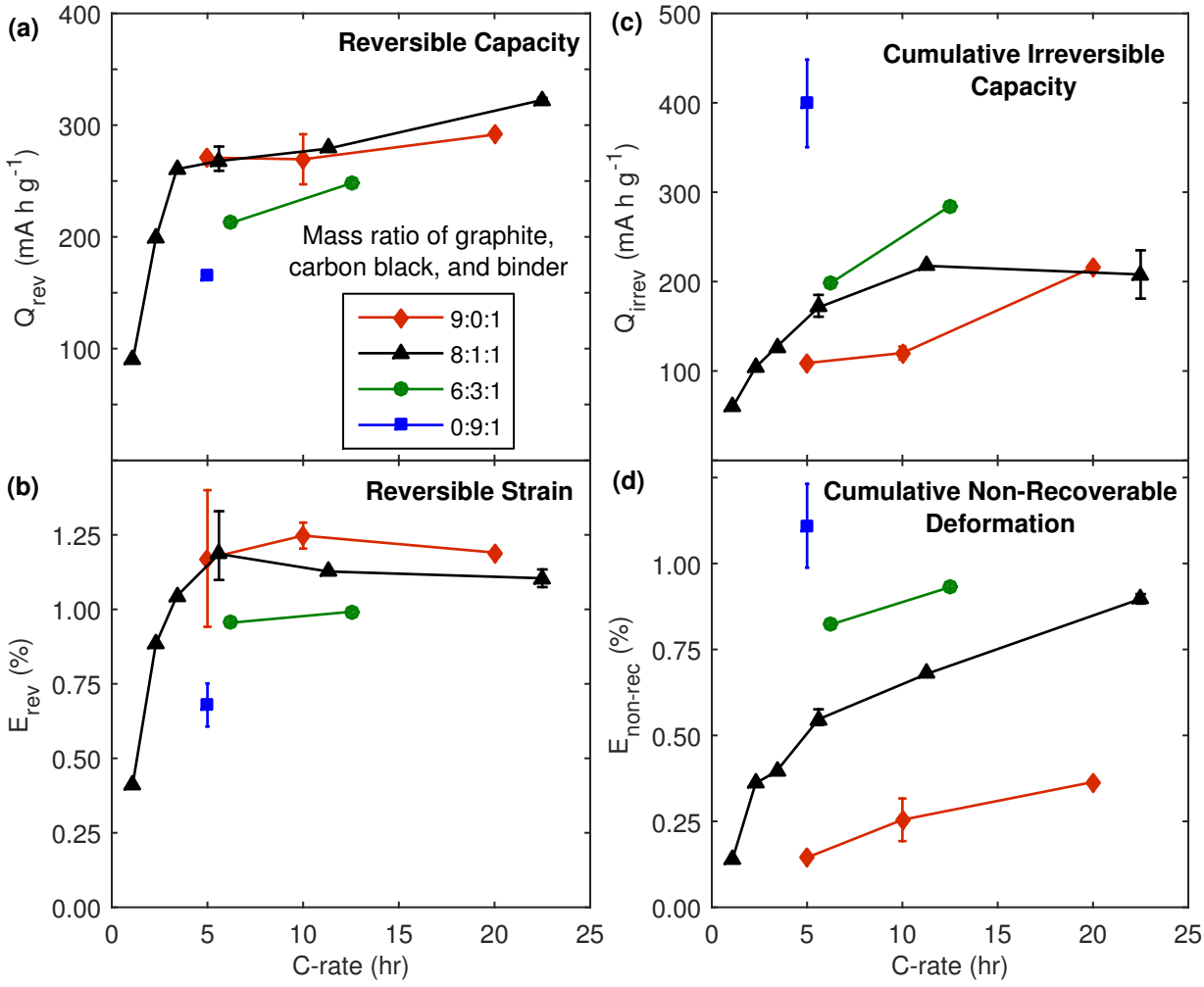

Figure 4.3: Effect of electrode composition and cycling rate on the reversible and irreversible capacity and strain responses of graphite composite electrodes cycled galvanostatically at various C-rates. (a-b) Reversible capacity and strain, averaged over cycles 1-3. (c-d) Irreversible capacity and strain accumulated during cycles 1-3. The legend indicates the electrode composition as a mass ratio of graphite, carbon black, and CMC binder. Error bars represent the minimum and maximum average values arising from variation between electrodes. Table 4.1 summarizes the number of tests performed for each composition and cycling rate.

previous studies that have repeatedly shown that irreversible capacity is proportional to the electrode surface area [32]. Electrodes with higher carbon black content had higher surface area due to the higher intrinsic surface area of carbon black (ca. 60 - 80 m^2 g^{-1}, manufacturer's specification) compared to graphite (ca. 10 m^2 g^{-1} [72]). The non-recoverable deformation followed the same trend as the irreversible capacity, with increasing non-recoverable deformation for increasing carbon black content / decreasing graphite content. The similar trends of the irreversible capacity and non-recoverable deformation with respect to carbon black content support the hypothesis presented in Sec. 3.3 that non-recoverable deformation is caused by accumulation of electrolyte decomposition products on the surface of graphite and carbon black particles.

4.3 Effect of Cycling Rate and Cycling Time

4.3.1 Reversible Behavior

As shown in Figs. 4.3(a-b), electrodes with a composition of 8:1:1 wt. ratio of graphite, carbon black, and CMC cycled at faster rates (C/1 - C/3) achieved a reduced reversible capacity compared to electrodes cycled at slower rates (C/5 - C/20). Reduced capacity at faster cycling rates is a result of limited diffusion rates of lithium ions through the pores of the electrode and within graphite particles [73]. With fewer lithium ions intercalated into the graphite, the reversible strain was correspondingly reduced at faster cycling rates. At slower cycling rates (C/5 - C/20), the reversible capacity and the reversible strain were both nearly constant. The plateau in strain for cycling rates slower than C/5 indicates that cycling rate did not have a large influence on the strain response of graphite composite electrodes at sufficiently slow rates where the electrode was able to fully lithiate and delithiate.

4.3.2 Irreversible Behavior

For a given electrode composition, the cumulative irreversible capacity and the cumulative non-recoverable deformation both appear to increase with decreasing cycling rate (Fig. 4.3c-d). However, Smith et al. observed that irreversible capacity increases continuously, proportional to the square root of time, during galvanostatic cycling regardless of cycling rate [74]. Because of the scaling with the square root of time, they attributed the continuous increase of irreversible capacity to the diffusion of electrolyte components through the SEI layer and subsequent reduction at the graphite particle surface. Similarly, we show in Fig. 4.4a that when the cumulative irreversible capacity was normalized by the square root of the total cycling time, the trend between irreversible capacity and cycling rate was eliminated. In a similar manner, normalizing the cumulative non-recoverable deformation by the square root of time as shown in Fig. 4.4b also eliminated the cycling rate dependence.

The capacity and strain developed during the potentiostatic test (Sec. 3.3 and Fig. 3.10) also scaled linearly with the square root of time after initial transient effects, as shown in Fig. 4.5. The common scaling of the non-recoverable deformation and the irreversible capacity with respect to cycling time that was observed in both galvanostatic cycling and the potentiostatic test further supports the correlation of non-recoverable deformation with irreversible capacity.

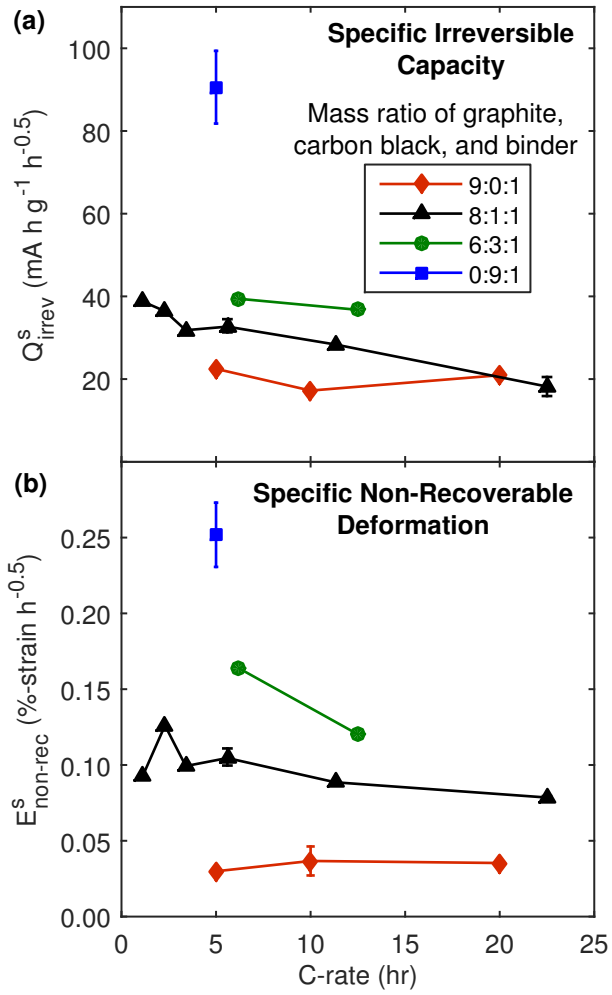

Figure 4.4: Effect of total cycling time on the irreversible behavior of graphite composite electrodes during galvanostatic cycling. (a) Irreversible capacity and (b) non-recoverable strain accumulated during cycles 1-3 and normalized by the square root of total cycling time. The raw data is presented in Figs. 4.3(c-d). The legend indicates the electrode composition as a mass ratio of graphite, carbon black, and CMC binder. Error bars represent the minimum and maximum average values arising from variation between electrodes. Table 4.1 summarizes the number of tests performed for each composition and cycling rate.

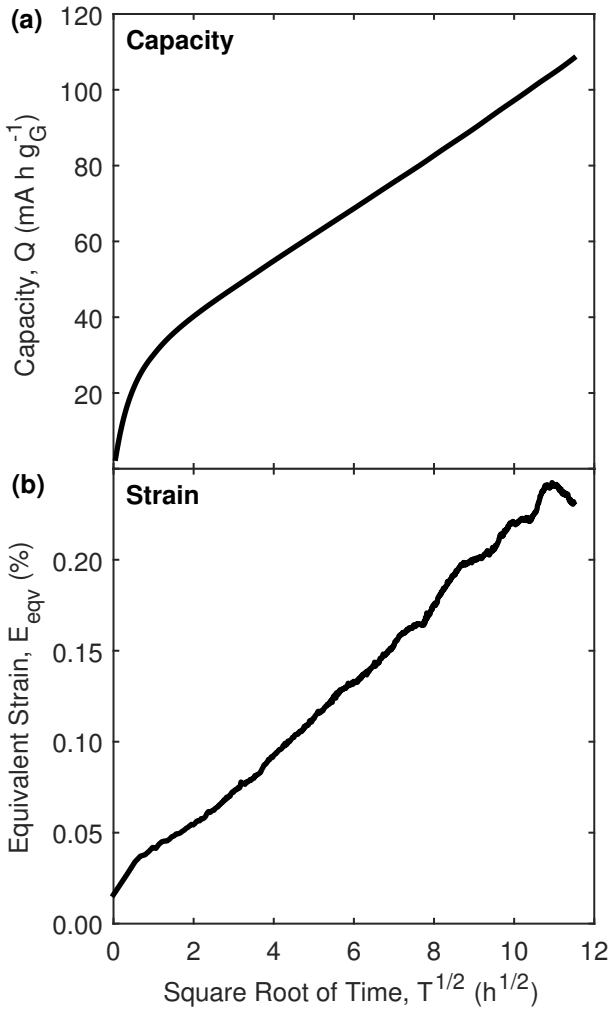

Figure 4.5: Effect of SEI growth on the deformation of a graphite composite electrode. The electrode had a composition of 8:1 wt. ratio of graphite and CMC binder and was held at 0.5 V vs $Li^{+/0}$ for 132 hours. The x-axis is scaled by the square root of time. Unscaled data is presented in Fig. 3.10. (a) Capacity response and (b) strain response.

4.4 Effect of Electrolyte Composition

Graphite composite electrodes (8:1:1 wt. ratio of graphite, carbon black, and CMC binder) were cycled galvanostatically at C/5 rate in different electrolytes. All electrolytes utilized 1 M lithium perchlorate ($LiClO_4$) salt. The volumetric ratio of the main electrolyte solvents, ethylene carbonate (EC) and dimethyl carbonate (DMC), was either 1:3 or 1:1 EC:DMC. Additionally, a common electrolyte additive, vinylene carbonate (VC), was added to the base electrolyte in varying amounts between 0.2 wt.% and 10.0 wt.%. Finally, a ternary electrolyte consisting of equal parts EC, DMC, and VC was utilized.

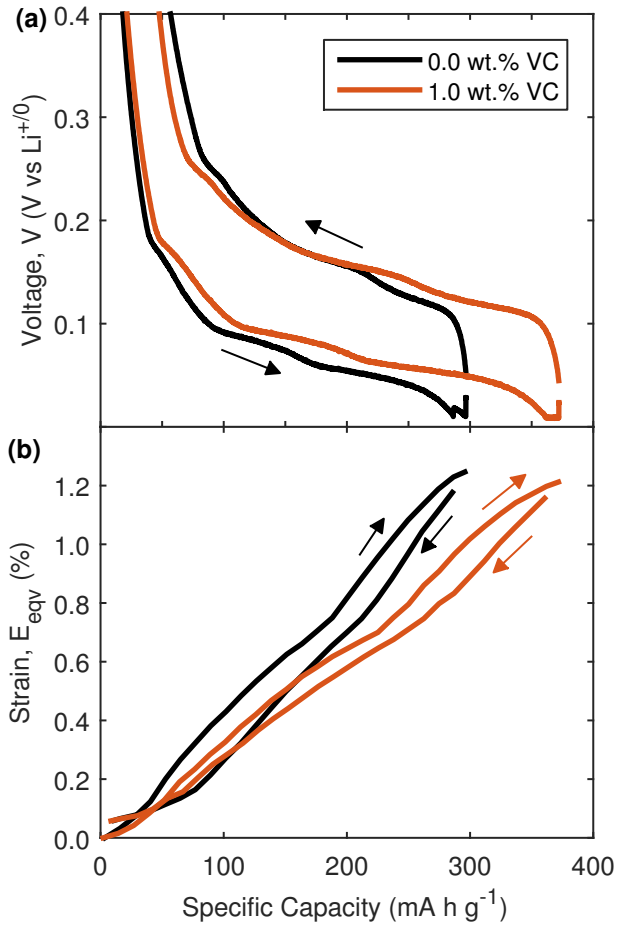

Figure 4.6: Representative electrochemical and mechanical response of graphite composite electrodes cycled galvanostatically in different electrolytes. (a) Voltage response and (b) strain response for the fifth cycle at C/5 rate. The strain was shifted on the y-axis to start at zero for easier comparison.

4.4.1 Reversible Behavior

Fig. 4.6 shows representative voltage and strain responses for the fifth cycle of graphite composite electrodes cycled with either 0.0 wt.% VC or 1.0 wt.% VC. The electrode cycled in electrolyte containing VC achieved higher capacity, though the same amount of strain developed. Additionally, the voltage hysteresis between the lithiation and delithiation portions of cycling was reduced. These differences in the electrochemical and mechanical responses of the electrodes cycled in electrolyte with varying amounts of VC are explored further below.

The reversible capacity, averaged over cycles 1-5, for graphite composite electrodes cycled in different electrolytes is shown in Fig. 4.7a. Increasing the ratio of EC to DMC from 1:3

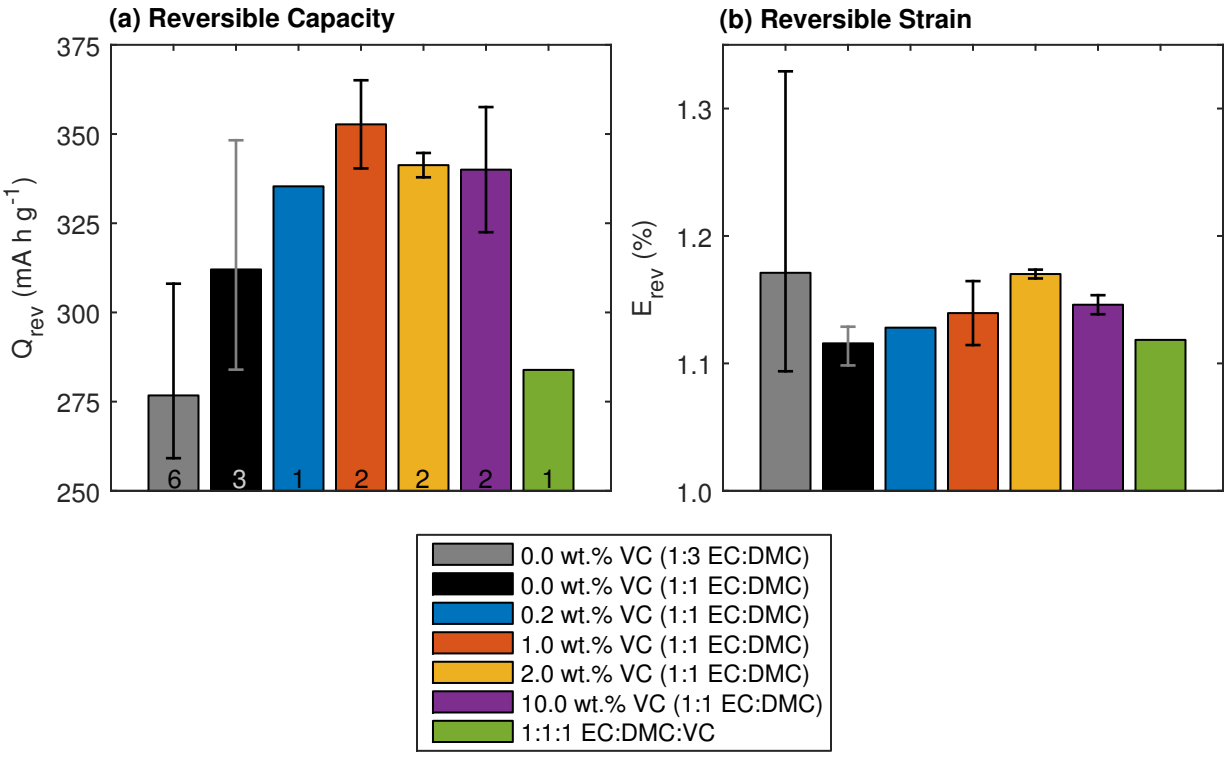

Figure 4.7: Effect of electrolyte composition on the reversible behavior of graphite composite electrodes. The electrodes had compositions of 8:1:1 wt. ratio of graphite, carbon black, and CMC binder and were cycled galvanostatically at C/5 rate for five cycles. (a) Reversible capacity, averaged over cycles 1-5 and (b) reversible strain, averaged over cycles 1-5. Error bars represent the minimum and maximum values of the individual tests, and the number of tests is indicated by the numbers at the base of the bars.

to 1:1 increased the average reversible capacity achieved by the electrodes. The addition of VC caused the capacity to first increase for 0.2 wt.% and 1.0 wt.% VC and then to plateau for 2.0 wt.% and 10.0 wt.% VC. Excess VC in the ternary electrolyte formula reduced the capacity the electrodes achieved. The corresponding reversible strain is presented in Fig. 4.7b. Changing the EC:DMC ratio from 1:3 to 1:1 decreased the reversible strain the electrode experienced. Increasing amounts of VC up to 2.0 wt.% caused the strain to increase slightly, while additional VC (10.0 wt.% and the ternary formula) caused the strain to decrease.

While both the capacity and the strain increased with small concentrations of VC and decreased with larger concentrations of VC, the relative changes in strain were much smaller than the relative changes in capacity. As a result, the specific expansion of the electrode during galvanostatic cycling, E^s_{GS} (Eqn. 4.1), varied with VC concentration, as shown in Fig. 4.8. Essentially, electrodes cycled in electrolyte containing a small amount of VC (ca. 1.0 - 2.0 wt.%) achieved higher capacity while developing the same amount of strain compared to electrodes with no VC or excess VC (ca. 10.0 wt.% or higher).

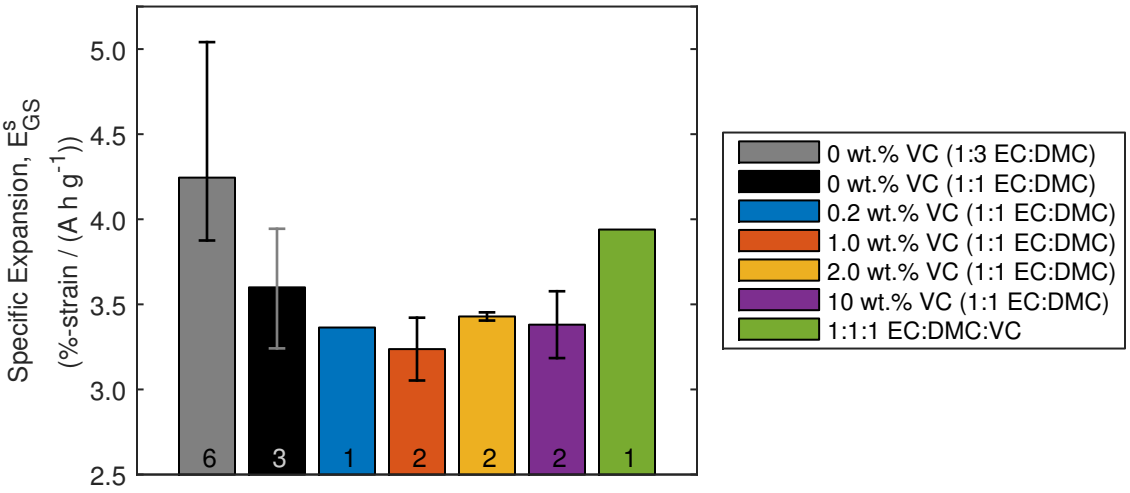

Figure 4.8: Effect of electrolyte composition on the specific expansion of graphite composite electrodes. The electrodes had compositions of 8:1:1 wt. ratio of graphite, carbon black, and CMC binder and were cycled galvanostatically at C/5 rate for five cycles. The mean values are averages over cycles 1-5. Error bars represent the minimum and maximum values of the individual tests, and the number of tests is indicated by the numbers at the base of the bars.

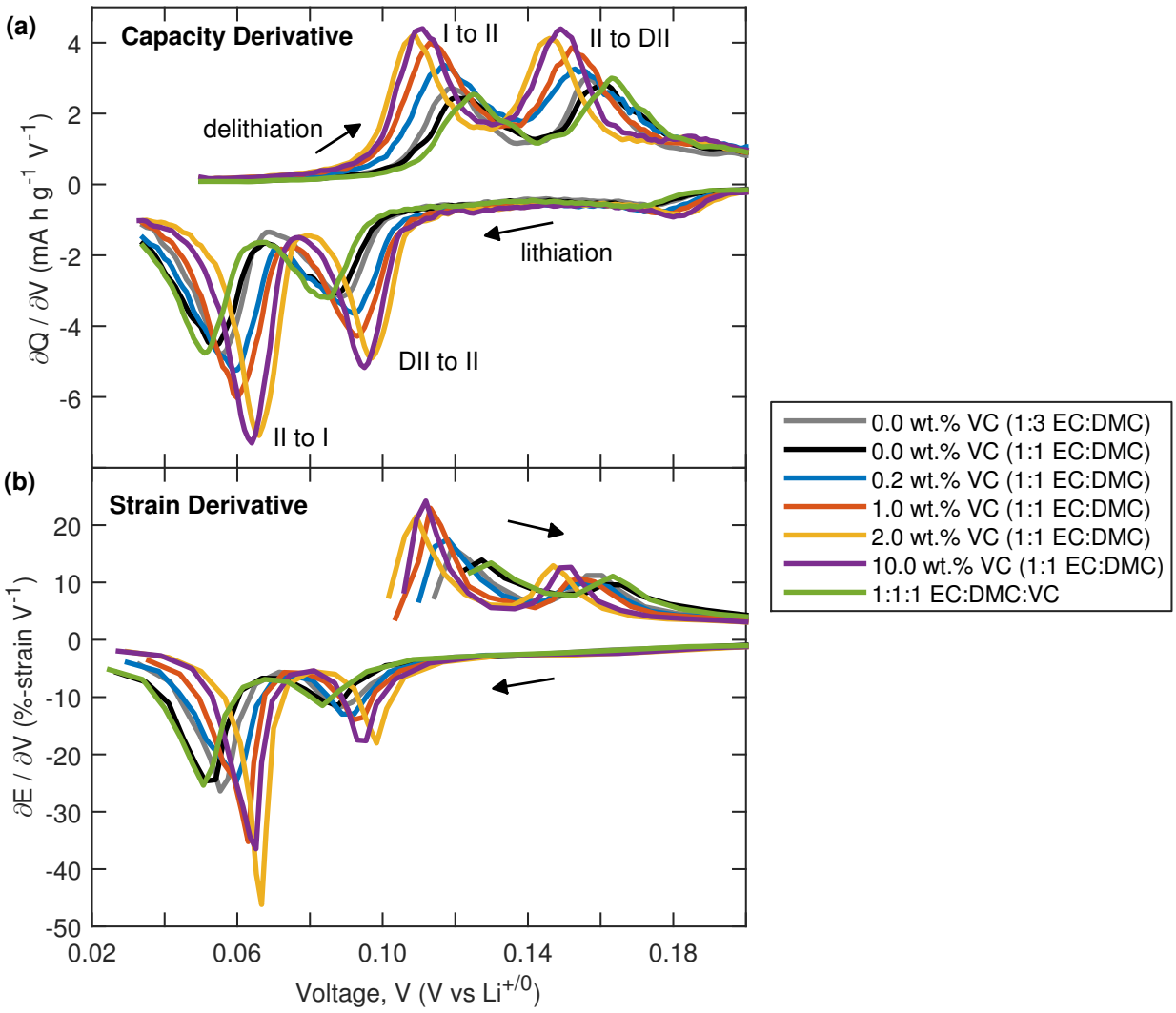

Figure 4.9: Effect of electrolyte composition on the phase transitions between graphite-lithium intercalation compounds (G-LICs) formed during galvanostatic cycling. (a) Derivative of capacity and (b) derivative of strain with respect to voltage for the fifth cycle of representative tests. For clarity, the x-axis has been limited to highlight the peaks in the derivatives corresponding to the dilute stage II to stage II transition and the stage II to stage I transition.

During galvanostatic cycling, a voltage hysteresis exists between the lithiation and delithiation portions of cycling because batteries operate outside of equilibrium conditions. The voltage hysteresis is observed clearly in the derivative of capacity with respect to voltage. It is defined as the difference in the voltage at which a peak in the capacity derivative occurs during lithiation compared to the voltage at which the corresponding peak occurs during delithiation.

Fig. 4.9 presents representative derivatives of capacity with respect to voltage and of strain with respect to voltage for electrodes cycled in different electrolytes. Increasing the VC amount up to 2.0 wt.% reduced the voltage hysteresis (that is, caused the voltages at which the peaks occur to shift to higher values during the lithiation portion of cycling and lower values during the delithiation portion of cycling). Additionally, the peaks became narrower and the peak height increased. Excess VC (10.0 wt.% and higher) increased the voltage hysteresis. These trends were observed in both the capacity derivatives and the strain derivatives.

The voltage hysteresis for the stage II to stage I transition is quantified in Fig. 4.10. There was a slight increase in the hysteresis when the base electrolyte was changed from 1:3 to 1:1 vol. ratio of EC:DMC, though this increase was within the scatter of the data. Increasing the VC concentration up to 10.0 wt.% caused a general decrease in the voltage hysteresis. Increasing the VC concentration further (ternary electrolyte formula) caused the voltage hysteresis to increase higher than the case with no VC.

In general, a moderate amount of VC (ca. 1.0 - 2.0 wt.%) added to the electrolyte increased the reversible capacity the electrode achieved (Fig. 4.7a) and reduced the voltage hysteresis between lithiation and delithiation portions of cycling (Fig. 4.10a). These changes both suggest more facile insertion / removal of lithium ions into / from graphite. Because VC is known to modify the solid-electrolyte interphase (SEI) [41, 75–78], we believe that the facile lithium insertion / removal observed here is caused by enhanced lithium ion transport through the SEI layer, which may be facilitated by a thinner SEI, more porous SEI, and/or differences in the chemical composition of the SEI.

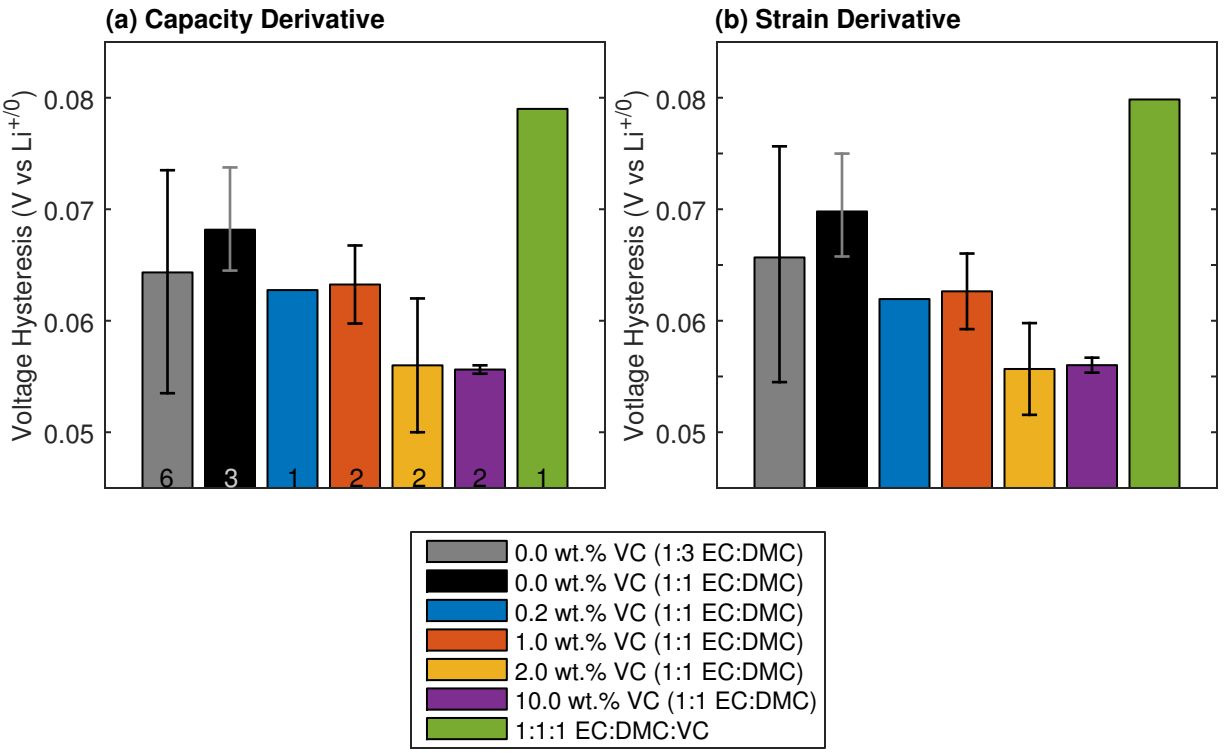

Figure 4.10: Effect of electrolyte composition on the voltage hysteresis between lithiation and delithiation portions of galvanostatic cycling. (a) Voltage hysteresis between the stage II to stage I transition from the capacity data and (b) the same voltage hysteresis from the strain data. The electrodes had compositions of 8:1:1 wt. ratio of graphite, carbon black, and CMC binder and were cycled galvanostatically at C/5 rate for five cycles. The mean values are averages over cycles 1-5. Error bars represent the minimum and maximum values of the individual tests, and the number of tests is indicated by the numbers at the base of the bars.

We hypothesize that the varying specific expansion of graphite electrodes cycled in different electrolytes (Fig. 4.8) can be explained through considerations of lithium-ion transport through the SEI layer. Facile lithiation of electrodes cycled in electrolyte containing a moderate amount of VC (ca. 1.0 - 2.0 wt.%) could have led to graphite particles that were fully and homogeneously lithiated to the stage I graphite-lithium intercalation compound. Concurrent with the complete lithiation, the strain would have reached the maximum value expected for fully lithiated electrodes. In contrast, graphite particles cycled in electrolyte either without VC or with excess VC (ternary electrolyte) could have been inhomogeneously lithiated, such that the edges of the particles developed the fully lithiated stage I graphite-

lithium intercalation compound while the interiors of the particles remained only partially lithiated. If the fully-lithiated shells were sufficiently large, the overall size of the graphite particles could have increased by the same amount as fully-lithiated particles, but with less total lithium content. Thus, the strain measured in electrodes cycled in electrolyte without VC or in excess VC could have been the same as electrodes cycled in electrolyte containing a moderate amount of VC, even though the total capacities were different. Detailed information on the micro- or nanoscale distribution of lithium within graphite particles would be required to confirm this hypothesis.

4.4.2 Irreversible Behavior

The cumulative irreversible capacity and non-recoverable deformation developed in graphite composite electrodes cycled in different electrolytes are shown in Fig. 4.11. The irreversible capacity of electrodes cycled in the base electrolytes that did not contain any VC continued to increase with cycle number, while the irreversible capacity of electrodes cycled in electrolyte containing VC plateaued. In contrast, the non-recoverable deformation for all electrodes continued to increase at approximately the same rate for all types of electrolyte.

The continuous increase of non-recoverable strain given a plateau in the irreversible capacity was initially surprising, since previous work showed a strong one-to-one correlation between these two irreversible electrode parameters (see Sec. 3.3). However, the differences between irreversible capacity and irreversible strain development are explained below in the context of the decomposition mechanisms of EC and VC.

EC decomposes via direct electron transfer from the electrode, forming lithium ethylene dicarbonate (LEdC) as the main decomposition product [41, 76, 79–81] (Fig. 4.12a and Fig. A.1). In previous works [74], cumulative irreversible capacity, which was correlated directly with SEI growth, was found to increase proportionally to the square root of cycling time (see also Sec. 4.3.2). It was proposed that the initial SEI did not fully passivate the electrode, and electrolyte diffused through the SEI and reacted at the electrode surface

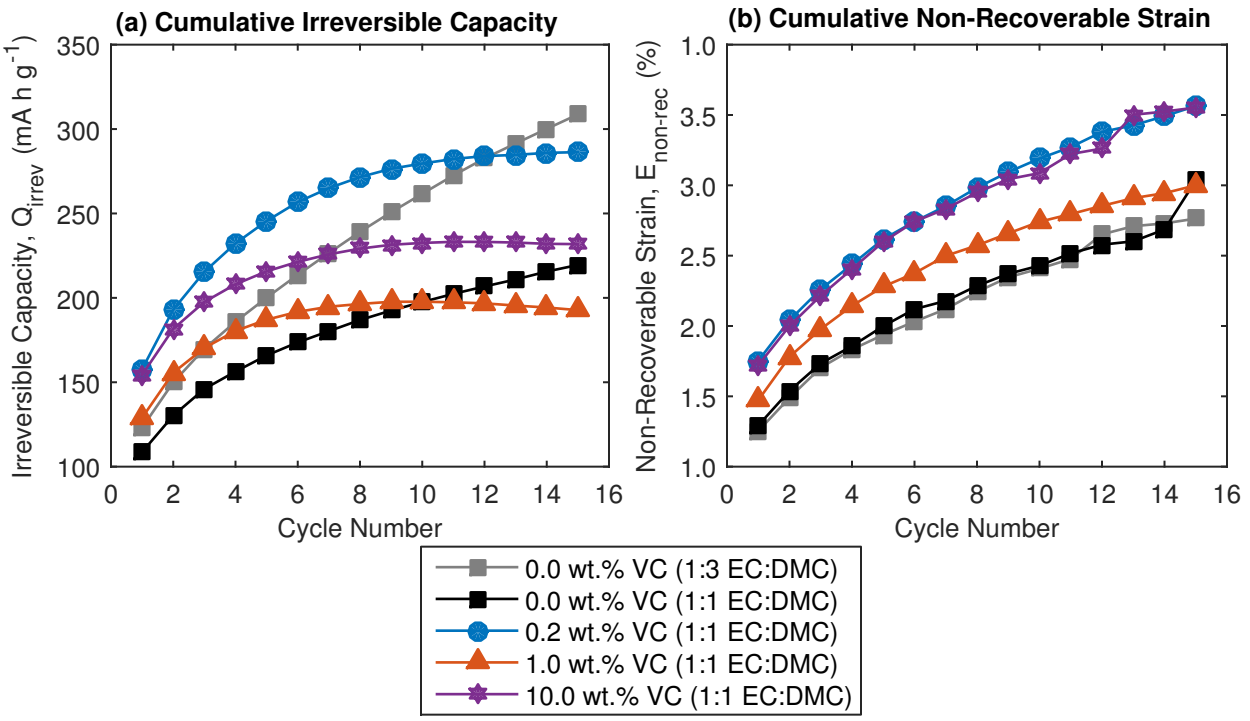

Figure 4.11: Effect of electrolyte composition on irreversible behavior of graphite composite electrodes. The electrodes had compositions of 8:1:1 wt. ratio of graphite, carbon black, and CMC binder and were cycled galvanostatically at C/5 rate for fifteen cycles. Representative curves of (a) the cumulative irreversible capacity and (b) the cumulative non-recoverable strain.

(Fig. 4.12b). Our observations of continuous accumulation of irreversible capacity and irreversible strain are consistent with the idea of continued SEI growth on graphite composite electrodes cycled in the base electrolytes that do not contain VC.

VC decomposes through two general classes of mechanisms. First, VC decomposes via direct electron transfer from the electrode to form decomposition products of lithium vinylene dicarbonate (LVdC) and lithium divinylene dicarbonate (LdVdC) [41, 76, 79, 80] (Fig. A.2). Second, VC radicals are formed via electron transfer from the electrode, and these radicals can then initiate and propagate radical polymerization of in-tact VC molecules [76, 79] (Fig. A.3). We emphasize here that once the radicals are formed, no further electron transfer from the electrode is required to propagate VC polymerization.

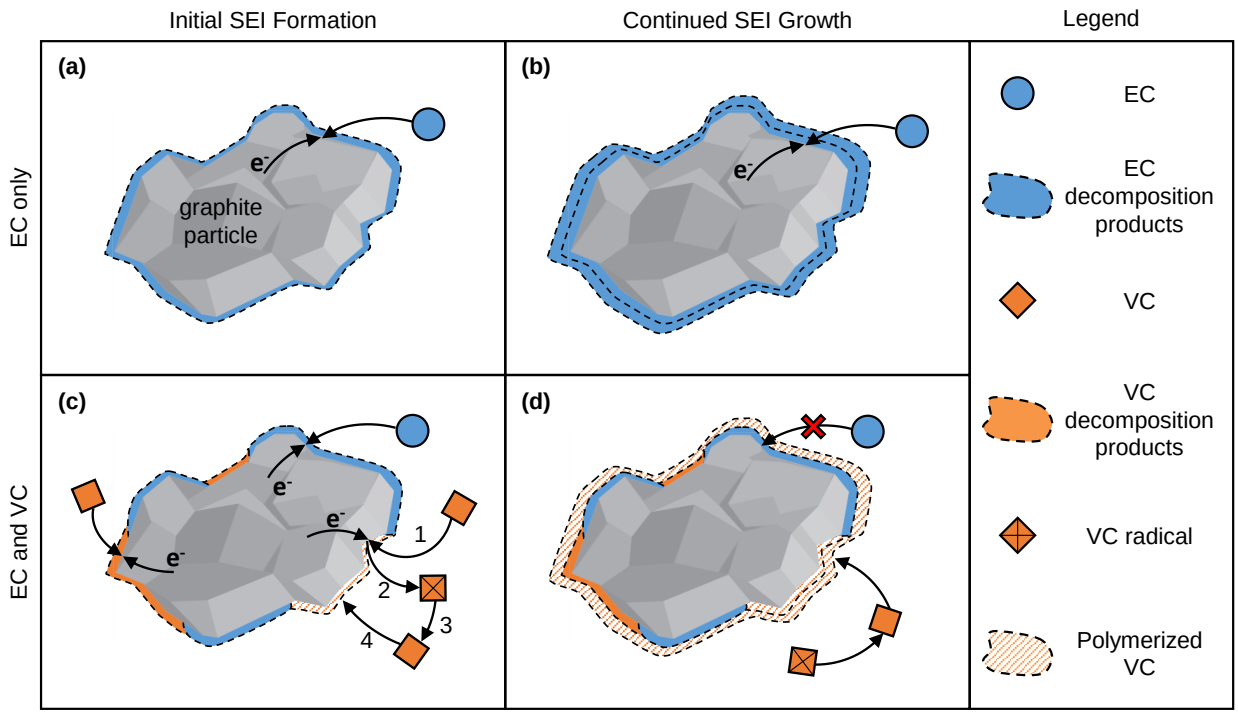

Figure 4.12: Schematics depicting electrolyte decomposition mechanisms and resulting SEI composition on graphite electrodes cycled in different electrolytes. (a) In the base electrolyte, where ethylene carbonate (EC) is the main organic SEI former, EC is reduced via electron transfer from the electrode and lithium ethylene dicarbonate (LEdC) is the main decomposition product. (b) In-tact EC molecules can diffuse through the SEI layer and continue to decompose, consuming electrons from the electrode and growing the SEI. (c) When vinylene carbonate (VC) is added to the electrolyte, both EC and VC are reduced via electron transfer from the electrode, and LEdC, lithium vinylene dicarbonate (LVdC) and lithium divinylene dicarbonate (LdVdC) are the main decomposition products. Additionally, VC radicals are formed through electron transfer from the electrode (steps 1-2), which then attack in-tact VC molecules to form polymerized VC (steps 3-4). (d) Electrolyte cannot diffuse through the well-passivating initial SEI, so no electrons are transferred from the electrode. However, the SEI continues to grow as VC radicals initiate and propagate polymerization of in-tact VC molecules in the electrolyte.

Based on considerations of the two mechanisms of VC decomposition (i.e. formation of LVdC and LdVdC via electron transfer from the electrode and formation of polymerized VC via radical polymerization), we propose the following explanation of the irreversible electrode behavior observed in Fig. 4.11 for electrodes cycled in electrolyte containing VC. We hypothesize that the initial irreversible capacity developed in the first 5 - 10 cycles was caused by the irreversible decomposition of EC and VC as well as the formation of VC radicals (Fig. 4.12c). We believe that the SEI formed during this portion of cycling, which contained VC decomposition products (e.g. LVdC, LdVdC, and polymerized VC), was more passivating than the SEI formed in the base electrolytes that did not contain VC. The irreversible capacity plateaued for cycles 10 - 15 because electrolyte could not diffuse through the more passivating SEI and react. VC radicals in the electrolyte, however, could initiate and propagate radical polymerization of in-tact VC molecules. Thus, the SEI could continue to grow via radical polymerization of VC without a corresponding increase in the cumulative irreversible capacity (Fig. 4.12d). We hypothesize that continued SEI growth via radical polymerization of VC was manifested by continued accumulation of irreversible strain without a corresponding accumulation of irreversible capacity.

In order to probe differences in the initial SEI formation in electrolytes with and without VC, we performed linear sweep voltammetry and potentiostatic voltage hold tests on graphite composite electrodes. A discussion of these results are presented in Appendix C. Due to the complex and intertwined mechanisms of EC and VC reduction (see Appendix A), however, the results of these tests were inconclusive. We propose that electrochemical quartz crystal microbalance experiments could be used to directly measure residual mass on an electrode associated with SEI formation and growth [82]. Such measurements would provide an independent metric for SEI growth, which could be correlated with non-recoverable deformation.

4.5 Conclusions

A more complete understanding of the interplay between electrode mechanics and electrochemical behavior is critical for the amelioration of current electrode materials and the development of new high-capacity electrodes for lithium-ion batteries. In this chapter, we investigated the effect of several battery parameters - polymer binder, carbon black content, cycling rate, and electrolyte composition - on the strain response of graphite composite electrodes.

Electrodes made with a stiffer polymer binder (i.e. CMC) developed less reversible strain for a given capacity than electrodes made with a more compliant binder (i.e. PVdF). Carbon black content and cycling rate were found to be secondary influences on the reversible strain response of graphite composite electrodes: increasing carbon content and faster cycling rates reduced the capacity the electrodes were able to achieve, and the reversible strain followed the capacity results directly. Irreversible capacity and non-recoverable deformation developed during galvanostatic cycling scaled together with respect to carbon black content and cycling rate / cycling time, indicating a strong correlation between these two irreversible quantities. The addition of a moderate amount of vinylene carbonate (ca. 1.0 - 2.0 wt.%) to the electrolyte allowed electrodes to achieve a higher capacity without increased strain compared to electrodes cycled in standard electrolyte. Additionally, we hypothesize that the SEI formed with VC passivated the electrode surface so that irreversible capacity plateaued, but that radical polymerization of VC caused continued SEI growth during extended galvanostatic cycling.

Chapter 5

Electrochemical Stiffness Variations of Graphite Electrodes*

To date, stress and strain development in lithium-ion battery electrodes during electrochemical cycling have only been studied individually. Unknown are the relative contributions of stress and strain to battery performance / degradation and how stress and strain scale with respect to electrochemical cycling parameters. In this chapter, we combine *in situ* stress and strain measurements of graphite composite electrodes during electrochemical cycling to calculate an electrochemical stiffness of the electrodes. In contrast to the elastic stiffness constants (e.g. Youngs modulus), the electrochemical stiffness reported here is a measure of the potential or capacity dependence of the stress and strain responses of the electrodes. We show that tracking changes in the electrochemical stiffness provides new insights into the effects of individual phase changes on the mechanical responses of electrodes. This novel approach offers a new analytical tool for interrogating advanced battery materials, enabling the design and assessment of high power and high rate battery materials.

5.1 Electrochemical Stiffness

We define the electrochemical stiffness, k, as the ratio of an incremental change in stress, $\partial(\Delta\sigma)$, induced by insertion of lithium into a constrained electrode compared to the corresponding incremental change in strain, $\partial(E)$, induced by the same lithium insertion into an unconstrained electrode:

*Significant portions of this chapter were submitted as H. Tavassol[#], E. M. C. Jones[#], N. R. Sottos, A. A. Gewirth. *Nat. Mater.* (2015), [#]Equal contribution authors. The studies presented in this chapter were done in close collaboration with Dr. Hadi Tavassol during his graduate studies under Professor Andrew Gewirth in the Department of Chemistry at the University of Illinois at Urbana-Champaign.

$$k_i = \left. \frac{\partial (-\sigma)}{\partial E} \right|_i , \tag{5.1}$$

where i is either the electrode potential, V, or the electrode capacity, Q. The methodology used to link independent but coordinated stress and strain measurements and to compute the electrochemical stiffness of lithium-ion battery electrodes is illustrated in Fig. 5.1. In cyclic voltammetry (CV), where electrode potential is the independent variable, the potential-dependent stiffness, k_V, is calculated. In galvanostatic cycling (GS), where electrode ca-

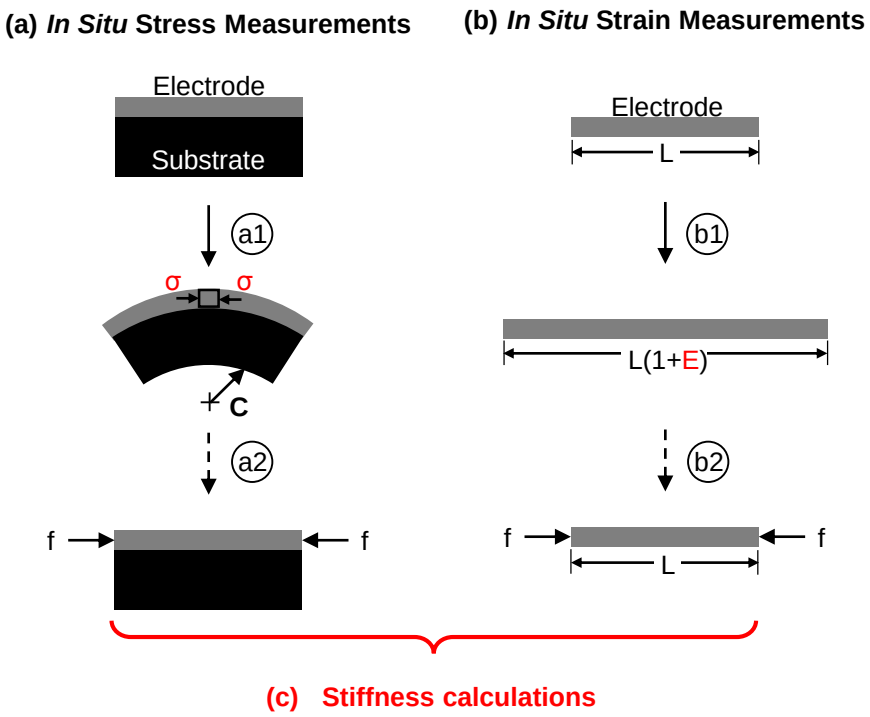

Figure 5.1: Methodology utilized for electrochemical stiffness calculations. (a) Schematic of *in situ* stress measurements. An electrode with an unknown stress state is attached to a substrate. During lithiation, the substrate constrains the free expansion of the electrode, so a change in stress, σ, develops in the electrode, resulting in a change in curvature, C, of the substrate (step a1). An imaginary, external force, f, then compresses the electrode to remove the curvature (step a2). (b) Schematic of *in situ* strain measurements. An unconstrained electrode with characteristic size L undergoes free expansion during lithiation, generating a strain of E (step b1). The same imaginary, external force, f, then compresses the electrode to its original size (step b2). (c) The electrodes at the end of the steps a2 and b2 have the same size and stress state, and are viewed as the same electrode for the purposes of stiffness calculations.

pacity is the independent variable, the capacity-dependent stiffness, k_Q, is calculated. The negative sign in the numerator is included to rectify the negative (compressive) stress with the positive (expansive) strain developed in the electrode during lithiation. The stress and strain found here are both dependent variables of electrode potential and capacity. Therefore, the reported electrochemical stiffness values provide a measure of the relative effects of stress compared to strain at a particular point during electrochemical cycling, which is different from the traditional definition of stiffness as a material property such as Young's modulus.

5.2 Stress and Strain Development

In situ stress and strain measurements of graphite composite electrodes were performed in coordinated experiments using the methodologies shown in Fig. 5.1. Detailed information on the experimental procedures are found in Appendix D. The third cycle of cyclic voltammetry and the corresponding stress and strain measurements of graphite composite electrodes are shown in Fig. 5.2. The compressive stress of ca. -9.5 MPa and expansive strain of ca. 0.41 % at the start of the cycle (1.0 V) are due to the non-recoverable stress and strain generated during the first two cycles. The irreversible electrode responses are primarily attributed to the irreversible electrochemical reactions that occur during the formation of the solid electrolyte interphase (SEI) [10, 17, 32, 47, 82, 83]. During the cathodic sweep, where the working electrode potential is linearly decreased with time, lithium ions are driven into the working electrode. Between 1 V and 0.3 V, the current is primarily due to lithiation of disordered carbon black and early lithiation of graphite [5] as well as continued SEI formation [32, 84, 85]. In this voltage region, a small compressive stress develops in the constrained electrode, and the unconstrained electrode expands slightly. At more negative potentials (ca. 0.3 V 0.01 V vs $Li^{+/0}$), the voltammetry shows features corresponding to the phase transitions between distinct graphite-lithium intercalation compounds (G-LICs)

[85, 86]. The formation of intercalation compounds in this lower voltage region results in a rapid increase and changes in the rate of stress and strain development. During the anodic sweep, where the working electrode potential is linearly increased with time, lithium ions

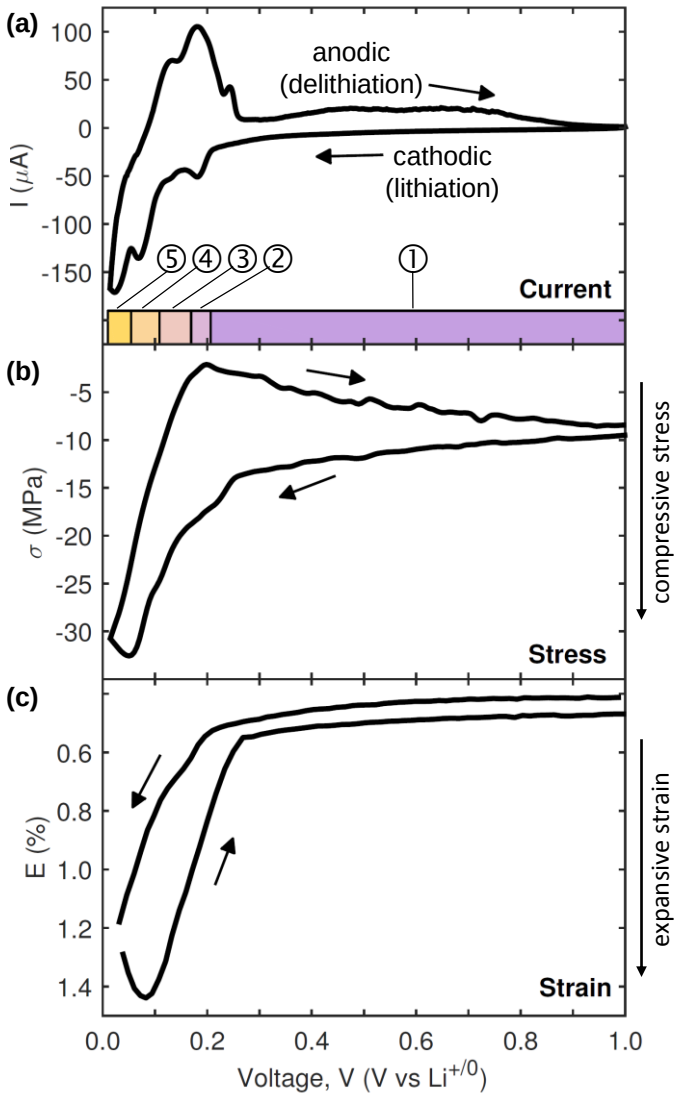

Figure 5.2: Potential-dependent electrode response during cyclic voltammetry (CV). (a) Third cycle CV at 25 μV s^{-1} (from stress experiment) with corresponding (b) stress and (c) strain measurements of a graphite anode. The colored regions in (a) correspond to phase transitions between graphite-lithium intercalation compounds (G-LICs) during the cathodic sweep: (1) = formation of dilute stage I, (2) = dilute stage I to stage IV, (3) = stage IV to stage III to dilute stage II, (4) = dilute stage II to stage II, and (5) = stage II to stage I.

are removed from the working electrode. As a result, the compressive stress is relieved and the electrode contracts. The electrode response during the anodic sweep is further discussed in Sec. D.5 in Appendix D.

5.3 Potential Dependence of the Mechanical Response

The independent stress and strain values from the third cycle of CV are coordinated at each potential and plotted in Fig. 5.3a. Changes in the slope result from differences in the development of stress and strain as different intercalation compounds form during lithiation and delithiation of the graphite electrode. The potential-dependent stiffness, k_V, calculated as the slope of the stress vs. strain curve (Eqn. 5.1), is reported in Fig. 5.3b. At the beginning of the cathodic sweep, the electrode exhibits an initially stiff response. This stiff response is caused by the immediate development of stress as the first few lithium ions are intercalated into the graphite with minimal corresponding strain development. As the formation of the dilute stage I graphite-lithium intercalation compound progresses (through ca. 0.3 V), strain develops at a faster rate once enough ions are inserted to cause an appreciable increase in graphite layer spacing. This later strain increase causes a corresponding decrease in the stiffness of the electrode.

As potential is swept to more negative values, a sharp oscillation in the stiffness occurs at ca. 0.24 V, just prior to the transition between the disordered dilute stage I compound and the first ordered stage IV compound. At more negative potentials, two additional oscillations in the stiffness are observed at ca. 0.13 V and ca. 0.08 V as high-lithium content, ordered intercalation compounds are formed. Surprisingly, the increase in stiffness just prior to the dilute stage I to stage IV transitions (ca. 0.24 V) is the most intense oscillation that occurs during lithiation of graphitic anodes. This observation is consistent with *in situ* XRD analyses, which show that formation of low-lithium content, dilute phases causes a

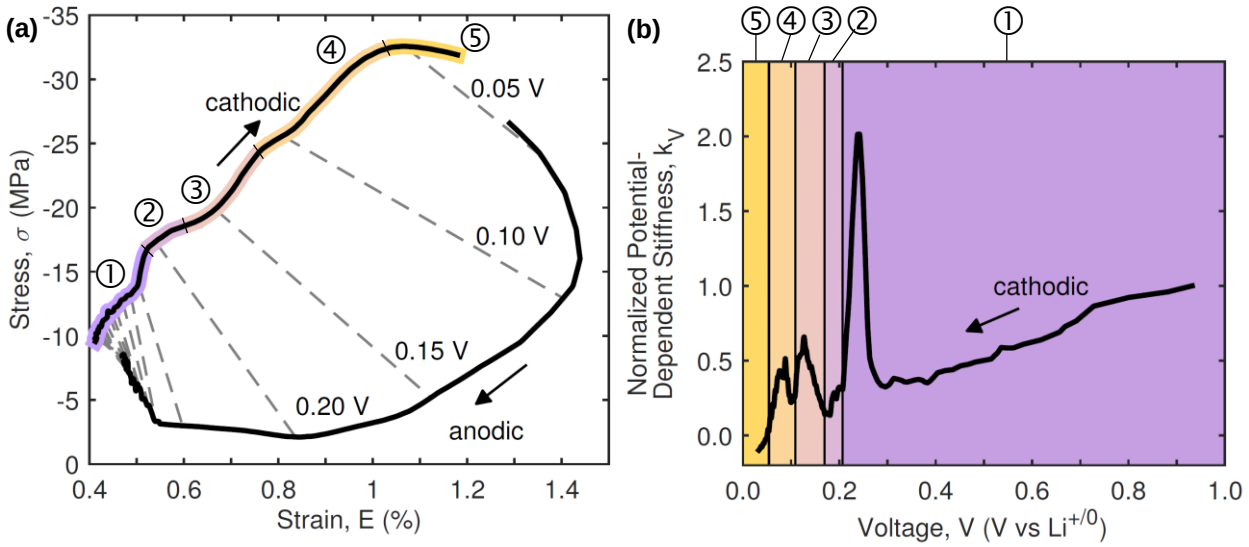

Figure 5.3: Coordination of stress and strain measurements and calculation of the electrochemical stiffness. (a) The stress and strain response from the third cycle of cyclic voltammetry at 25 μV s^{-1} (Fig. 5.2), coordinated at each potential value. The dashed lines represent contours of constant potential in increments of 0.05 V. (b) Potential dependent stiffness variations of the electrode during the cathodic sweep. The y-axis is normalized with respect to the stiffness value at the beginning of the cycle. Absolute values of the stiffness are presented in Table D.2. The colored regions in the voltammetry correspond to phase transitions between graphite-lithium intercalation compounds (G-LICs) during the cathodic sweep: (1) = formation of dilute stage I, (2) = dilute stage I to stage IV, (3) = stage IV to stage III to dilute stage II, (4) = dilute stage II to stage II, and (5) = stage II to stage I.

more significant change in the rate of the increase in the graphite layer spacing compared to formation of high-lithium content phases [5, 9].

The asynchronous rate of stress and strain development with respect to potential (Fig. 5.4) leads to potential-dependent variations in stiffness. Interestingly, the evolution of the strain derivative (Fig. 5.4c) follows the current closely (Fig. 5.4a). In contrast, significant jumps in the stress derivative (Fig. 5.4b) precede any significant changes in strain for each of the phase transitions observed. For example, the increase in stiffness at 0.24 V shown in Fig. 5.3b is traced to a sharp increase in the rate of stress development with no corresponding increase in the rate of strain development. That is, stress develops before the active materials expands significantly.

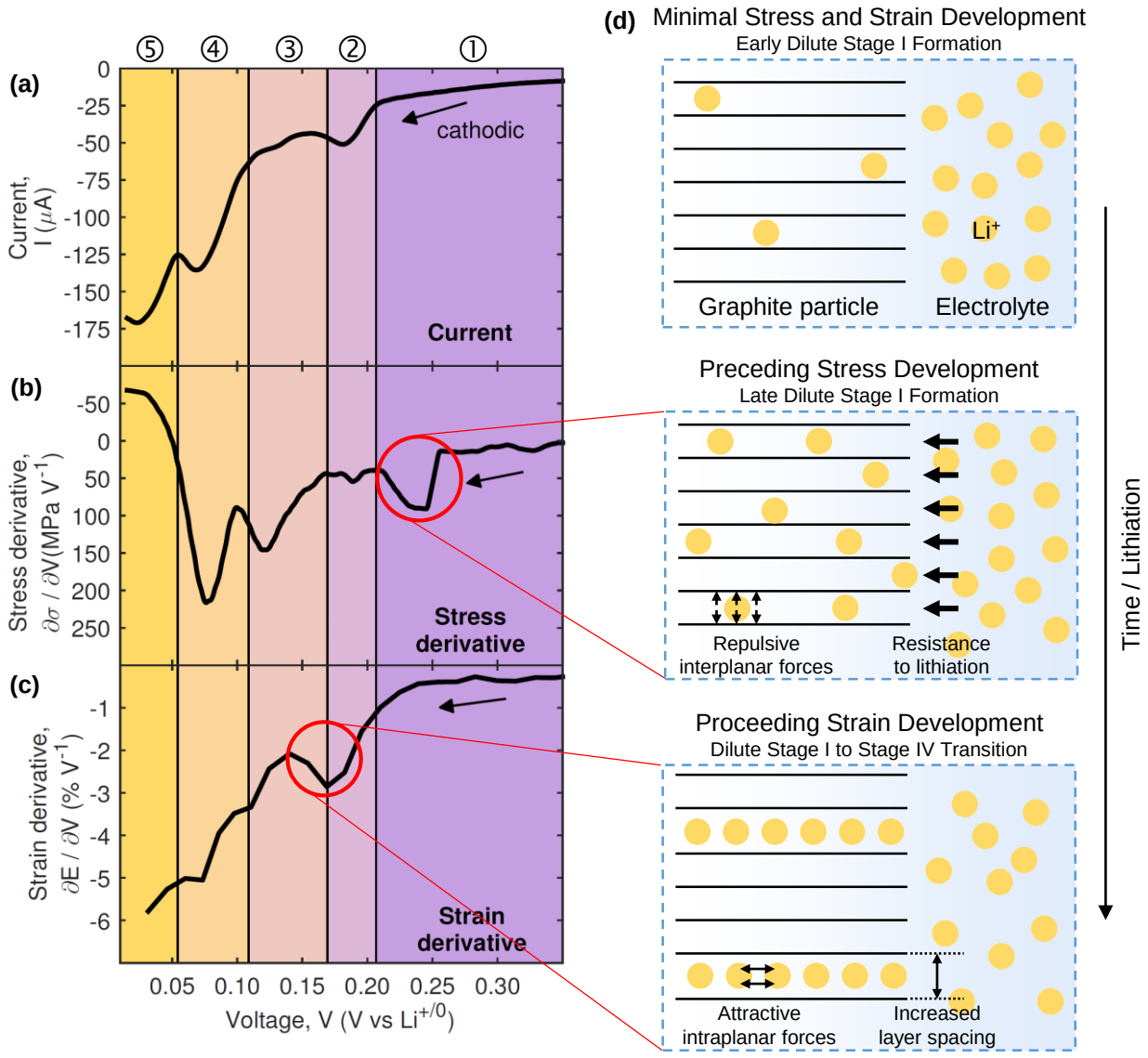

Figure 5.4: Asynchronous development of stress and strain. (a) Current response during third cycle of cyclic voltammetry at 25 μV s^{-1} (repeated from Fig. 5.2a) with corresponding rate of (b) stress accumulation and (c) strain accumulation during the cathodic sweep. The colored regions in the voltammetry correspond to phase transitions between graphite-lithium intercalation compounds (G-LICs) during the cathodic sweep: (1) = formation of dilute stage I, (2) = dilute stage I to stage IV, (3) = stage IV to stage III to dilute stage II, (4) = dilute stage II to stage II, and (5) = stage II to stage I. (d) Schematic representation of leading stress developing at the end of the formation of dilute stage I and lagging strain developing concurrent with the dilute stage I to stage IV transition.

The mechanical response of the electrode reported here contrasts the conventional understanding of stress development in lithium-ion battery electrodes, which asserts that stress results from the expansion of the active material while the electrode is constrained, either globally by a substrate (i.e. current collector) or locally by particle-particle interactions in a composite electrode [29]. Rather, our observation of the development of stress with minimal concurrent electrode expansion indicates some resistance to the insertion of the lithium that must be overcome, the consequences of which are explored below. This asynchronous development of stress and strain is the first indication that different mechanisms govern stress and strain evolution in graphite electrodes.

Fig. 5.4d presents a schematic illustration of the proposed driving forces of stress and strain development that cause the stiffness increase at 0.24 V prior to the dilute stage I to stage IV transition. We hypothesize that the increase of stress prior to the transition is a manifestation of an increase in repulsive forces building between graphitic layers as more lithium is intercalated into the dilute stage I phase [5, 6, 87]. Once the repulsive forces reach a critical level, the stage IV phase is energetically preferable, and the transition is initiated. Concurrent with the dilute stage I to stage IV transition, the strain increases, leading to the decrease in the stiffness of the electrode. Similar considerations attend the other phase transitions.

5.4 Capacity Dependence of the Mechanical Response

During cyclic voltammetry, the instantaneous rate of lithiation is potential-dependent and therefore changes throughout one cycle. Therefore, we also evaluated the capacity-dependent mechanical response developed during galvanostatic cycling, where the rate of lithiation and delithiation is constant through the entire cycle. The fifth cycle of galvanostatic cycling of the graphite anode at C/5 rate is shown in Fig. 5.5a, with the corresponding stress developed in a constrained electrode (Fig. 5.5b), and strain developed in an unconstrained electrode

(Fig. 5.5c). The independent stress and strain values are coordinated at each capacity value and plotted in Fig. 5.5d. The capacity-dependent stiffness, k_Q, calculated as the slope of the stress vs strain curve (Eqn. 5.1), is reported in Fig. 5.5e.

In the initial stages of lithiation, up to ca. 40 mA h g^{-1} (corresponding to voltages above ca. 0.2 V), the capacity is attributed to lithiation of carbon black and early lithiation of graphite. Similar to the high-voltage region (ca. 0.3 1.0 V) probed during cyclic voltammetry, these early lithiation events result in an immediate stress development with minimal corresponding strain development. The lagging strain gives rise to an initially stiff response followed by a decrease in the stiffness at the beginning of the cycle (Fig. 5.5e). This behavior is again attributed to stress generated during the initiation of lithiation followed by electrode expansion as a significant number of lithium ions are intercalated. As the capacity is further increased, distinct voltage plateaus corresponding to the transitions between different stages of intercalation compounds are observed [4, 5, 9]. The rate of stress and strain accumulation varies, leading to oscillations in the capacity-dependent stiffness, with peaks at ca. 150 mA h g^{-1} and at ca. 250 mA h g^{-1}.

Though the oscillations of the capacity-dependent stiffness observed during galvanostatic cycling are similar to the oscillations of the potential-dependent stiffness observed during cyclic voltammetry, the peaks of the oscillations occur within different phase transitions. No modulation is observed during galvanostatic cycling in the capacity-dependent stiffness prior to the dilute stage I to stage IV transition or within the stage IV to stage III to dilute stage II transition region. We believe that the faster rate of lithiation used during galvanostatic cycling (compared to the effective lithiation rate during cyclic voltammetry at 25 µV s^{-1} in the corresponding regions) did not allow sufficient time for the these stages to fully develop. Hence, the transitions between these stages were blurred, and no stiffness oscillations were observed. On the other hand, a peak is observed within the stage II to stage I transition during galvanostatic cycling, while a corresponding peak is not observed during cyclic voltammetry. We believe that here, the faster effective lithiation rate during cyclic voltammetry

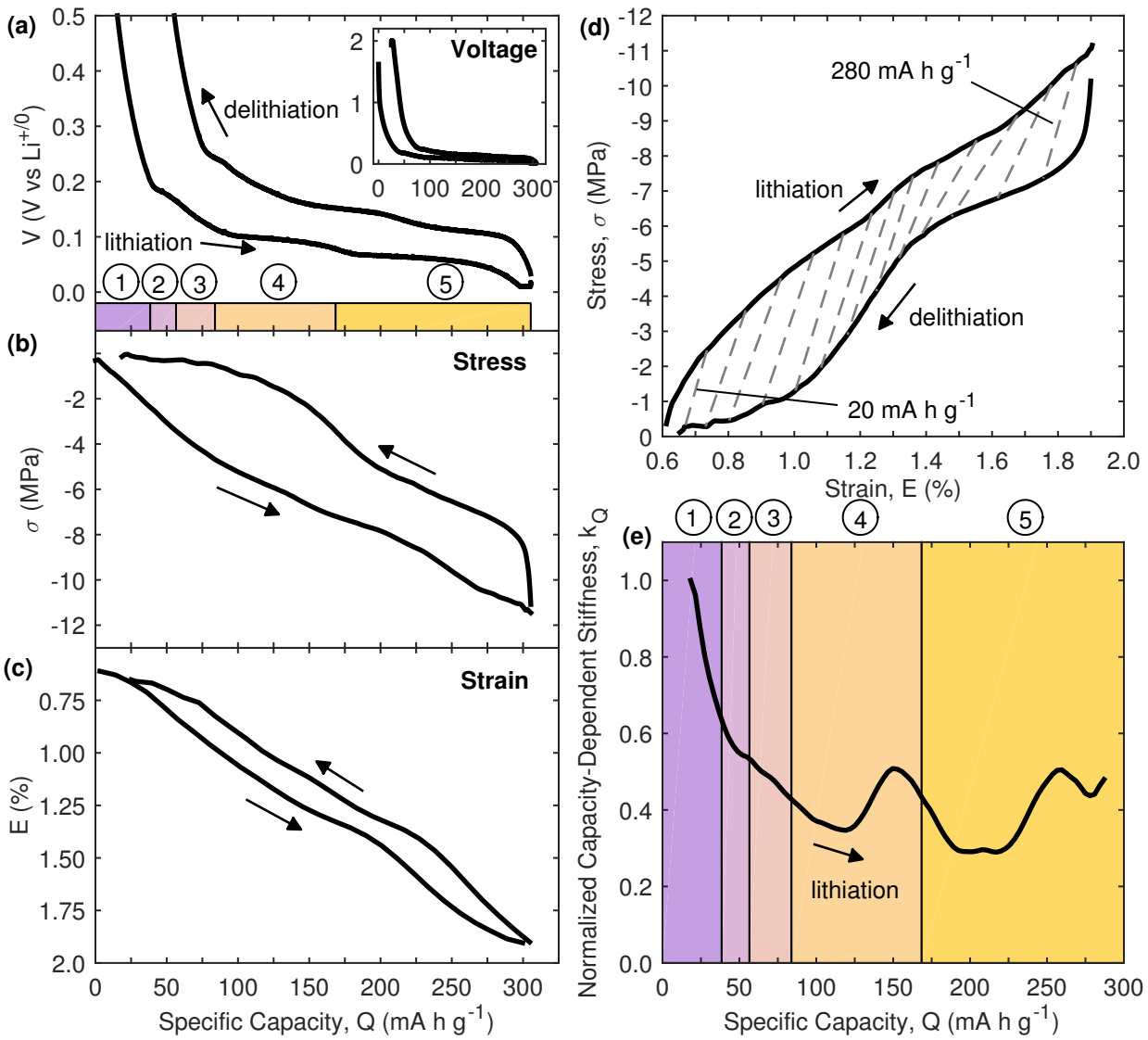

Figure 5.5: Capacity-dependent electrode response during galvanostatic (GS) cycling. (a) Fifth cycle of galvanostatic cycling at C/5 rate (from strain experiment) with corresponding (b) stress and (c) strain measurements of a graphite anode. (d) The stress and strain response coordinated at each capacity value. The dashed lines represent contours of constant capacity in increments of 20 mA h g^{-1}. (e) Capacity-dependent stiffness variations of the electrode during the lithiation portion of the cycle. The y-axis is normalized with respect to the stiffness value at the beginning of the cycle. Absolute values of the stiffness are presented in Table D.2. In (a,e), the colored regions correspond to phase transitions between graphite-lithium intercalation compounds (G-LICs) during the cathodic sweep: (1) = formation of dilute stage I, (2) = dilute stage I to stage IV, (3) = stage IV to stage III to dilute stage II, (4) = dilute stage II to stage II, and (5) = stage II to stage I.

in this region did not allow for full development of the stage II or stage I compounds. In both galvanostatic cycling and cyclic voltammetry, a peak in the electrochemically-induced stiffness is observed during the dilute stage II to stage II transition, where the effective rates of lithiation are similar between the two tests.

These results indicate that stiffness variations caused by transitions between different graphite-lithium intercalation compounds can be masked when the cycling rate is too fast and multiple phases of intercalation compounds co-exist. To control the time allowed for different phase transitions, cyclic voltammetry is a more suitable tool for probing the effects of low-lithium content intercalation compounds, and galvanostatic cycling is more appropriate for probing the effects of high-lithium content compounds.

5.5 Rate Dependence of the Mechanical Response

Intrigued by the asynchronous, potential-dependent stress and strain development in the graphite electrode, we explored the effect of cycling rate on the stress and strain responses. Fig. 5.6 reports the current, capacity, stress-thickness, and strain responses of graphite composite electrodes during CV at scan rates of 10 $\mu V\ s^{-1}$, 25 $\mu V\ s^{-1}$, and 100 $\mu V\ s^{-1}$. Here, stress-thickness, the product of the stress in the electrode and the thickness of the electrode, is used instead of stress, since the active thickness of the electrode is unknown for the different scan rates. As expected, slower scan rate voltammetries exhibit more defined features corresponding to the lithium intercalation events, lower current magnitudes arising from slower lithiation rates (Fig. 5.6a, and higher specific capacities, i.e. higher total lithium content (Fig. 5.6c) [88, 89]. Interestingly, the magnitude of the stress (Fig. 5.6b) correlates with the rate of lithiation, with both stress and current magnitudes decreasing with decreasing potential scan rate. In contrast, the strain development (Fig. 5.6d) correlates with the total lithium content, with both strain and capacity magnitudes increasing with decreasing scan rate. Thus, stress scales with current while strain scales with capacity, emphasizing that different mechanisms control these two mechanical responses.

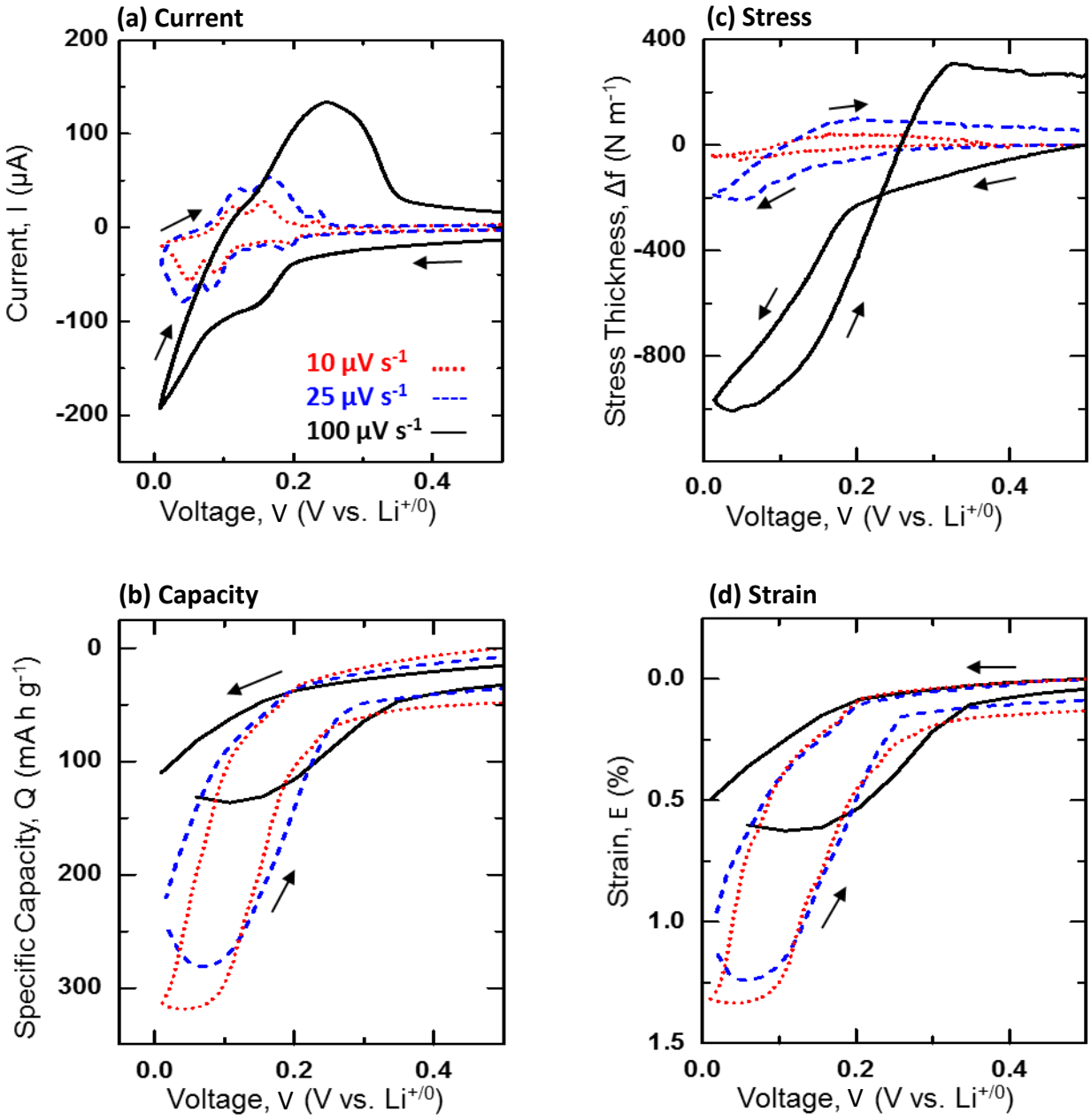

Figure 5.6: Effect of the potential scan rate on the development of stress and strain in graphite electrodes. (a) Current, (b) specific capacity, (c) stress-thickness and (d) strain responses of graphite electrodes during the third cycle of cyclic voltammetry at 100 μV s^{-1}, 25 μV s^{-1}, and 10 μV s^{-1}. For better comparison, stress and strain values of different scan rates are shifted to start from zero. The magnitude of stress scales with current (i.e. rate of lithium exchange) while the magnitude of strain scales with the specific capacity of the electrode (i.e. total lithium content).

When the cycling rate is slow and the rate of lithiation is slow (i.e. the current magnitude is small), there is less resistance to the insertion of lithium ions into the electrode, and the stress is correspondingly small. In contrast, at a faster cycling rate, the graphite electrode cannot as easily accommodate the high lithiation rate. The increased resistance to lithium insertion results in a higher stress response. This is in part due to the slow diffusion of lithium [88, 90] into the graphite microstructures.

The strain response follows the opposite trend with cycling rate. During slow cycling, the slow rate of lithiation allows for more complete lithiation of the electrode, and the electrode achieves a higher specific capacity. The strain response follows the capacity response directly, and a larger strain is developed at a slower cycling rate. At a faster cycling rate, however, lithium ions do not have sufficient time to diffuse through the graphite electrode, and the capacity is correspondingly reduced. With fewer lithium ions inserted into the electrode, the strain response is also reduced.

Together, the potential-dependence, the capacity-dependence, and the rate-dependence of the mechanical responses of graphite composite electrodes paint a picture of fundamentally different mechanisms that drive stress and strain development induced by lithium-ion exchange from electrodes. Significant development of stress occurs with a relatively small amount of lithium insertion, indicating the difficulty to initiate the insertion of lithium ions into the electrode or to initiate a phase transition between two graphite-lithium intercalation compounds. In this sense, the stress response corresponds to the resistance to lithium-ion insertion rather than the actual amount of lithium ions inserted. On the other hand, significant strain develops only when a sufficient amount of lithium ions have been inserted into the electrode. Thus, the strain response measured how many lithium ions have already been inserted into the electrode. In principle, such mechanistic differences could also apply to any insertion-based electrochemical process, depending on the inherent rate capabilities of the material.

5.6 Conclusions

We have developed a new method to interrogate the mechanical response of battery electrodes. Combining coordinated, *in situ* measurements of stress and strain in battery electrodes enables us to calculate the electrochemical stiffness of lithium-ion battery electrodes. The electrochemical stiffness response reveals that intrinsically different mechanisms dictate stress and strain development in graphite electrodes. Stress is governed by resistance against lithium insertion into the electrode while strain is governed by the amount of lithium inserted into the electrode. This stiffness response provides fundamental insight into rate behavior possible from this and other battery materials. Resistance to lithium insertion, manifested as a stiff electrode response, indicates a rate-limited material. To increase the rate capability of battery electrodes, lithium insertion needs to be more facile, so that the stress and the strain develop more synchronously and electrochemical stiffness is lowered. This technique is application to any insertion-based material, the response from which will exhibit potential- and rate-dependent stiffnesses. Thus, the electrochemical stiffness response can be used to design and screen materials for battery electrodes for high-rate and power applications.

Chapter 6

Deformation of Silicon Electrodes

One approach for increasing the energy density of lithium-ion batteries is the development of high-capacity electrode materials such as silicon. Compared with graphite, the most common anode material in current commercial batteries, the specific capacity of silicon is more than ten times larger (ca. 4200 mA h g^{-1} for silicon [62, 63] compared to 372 mA h g^{-1} for graphite [61]). During the alloying process with lithium, however, high-capacity electrodes undergo enormous volume expansion, leading to large stresses and electrode fracture. In this chapter, we describe the fabrication of free-standing silicon particle composite electrodes and four different methods of attaching the free-standing electrodes to the substrate in the custom battery cell. We compare the strain developed in high-capacity silicon composite electrodes during lithiation to the strain developed in standard graphite composite electrodes. The effects of the ratio of electrode components (active material, conductive additive, and polymer binder) and size of the active material particles on the strain response of silicon composite electrodes are presented. Additionally, the mechanical behavior of silicon composite electrodes fabricated with a novel polymer binder system is discussed in Appendix E.

6.1 Electrode Fabrication

Composite silicon electrodes comprised of silicon powder, carbon black (CB), and carboxymethyl cellulose (CMC) were fabricated using a similar procedure as that described in Sec. 2.4.3, where silicon powder replaced graphite powder as the active material. Two

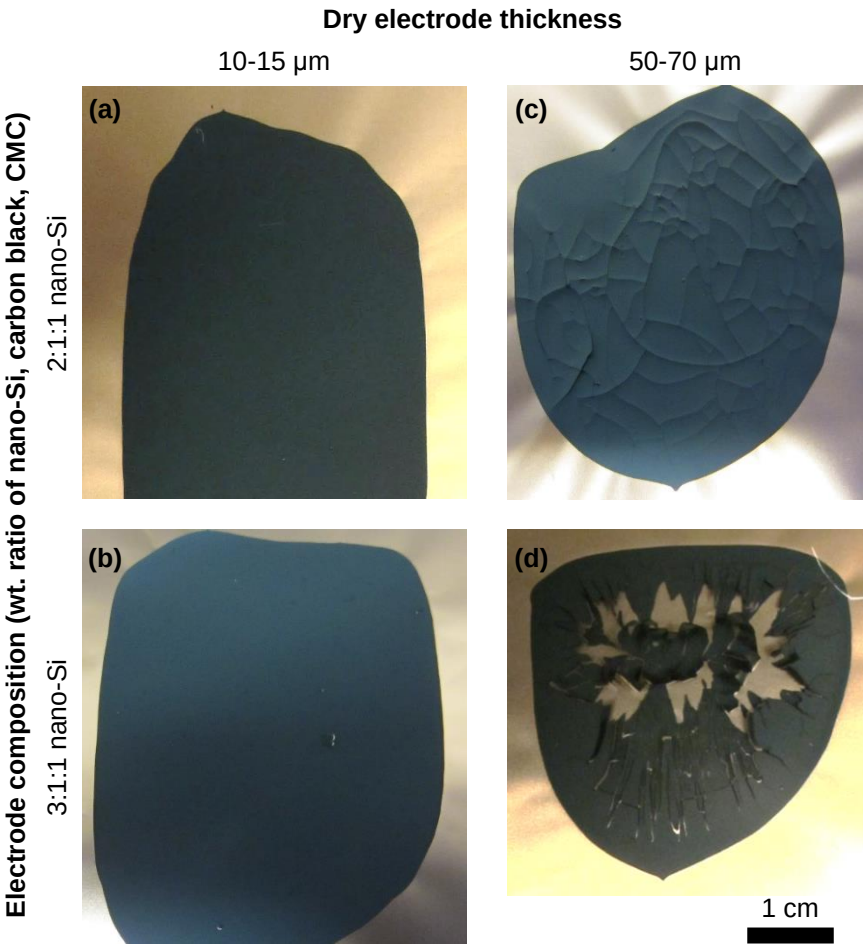

Figure 6.1: Representative images of dried nano-Si electrodes on copper foil substrates. Electrodes had a composition of either (a,c) 2:1:1 wt. ratio or (b,d) 3:1:1 wt. ratio of nano-Si, carbon black, and CMC binder. Wet electrode slurries were deposited at either (a,b) 380 µm or (c,d) 1270 µm doctor blade heights, resulting in dried electrode thicknesses of (a,b) ca. 10 - 15 µm or (c,d) ca. 50 - 70 µm. The thinner electrodes dried without cracking but could not be peeled off the copper foil while thicker electrodes fractured during the drying process.

types of silicon powders were used, one with micro-sized particles (ca. 44 µm), denoted as "micro-Si," and one with nano-sized particles (ca. 100 nm), denoted as "nano-Si." Electrode slurries were prepared by first predissolving CMC in water in a 1:50 wt. ratio and then adding silicon and carbon black. The slurries were homogenized using a plastic probe tip (⌀7 mm, serrated edge, Omni) at approximately 7500 RPM for 1 hour. After homogenizing, the slurries were deposited onto copper foil using a doctor blade to control the slurry

thickness, and the electrodes were allowed to dry under ambient conditions. The electrodes were then peeled from the copper foil, spin-coated with fluorescent silica nano-particles, and cut into ca. 3 x 7 mm pieces to create free-standing electrodes for strain measurements.

In order to evaluate the effect of electrode composition on the electrochemically-induced strain response of the electrodes, we targeted a range of electrode compositions of x:1:1 wt. ratio of silicon, carbon black, and CMC, where $1 \leq x \leq 8$. Micro-Si electrodes were successfully fabricated with 8:1:1, 3:1:1, and 1:1:1 wt. ratios of micro-Si, carbon black, and CMC. However, nano-Si electrodes with high silicon contents ($2 \leq x \leq 8$) suffered from severe cracking during the electrode drying process, as shown in Fig. 6.1c-d. The drying-induced fracture was reduced with thinner electrodes (ca. 10 - 15 µm compared to ca. 50 - 70 µm), but the thinner electrodes could not be removed from the copper foil substrate (Fig. 6.1a-b). Several different drying conditions were investigated, including flash drying the electrodes in an oven at 60 deg. C for 1 hour, retarded drying by partially covering the electrodes to slow water evaporation, and addition of ethanol to the slurry, but none of these different conditions reduced electrode fracture. Therefore, electrochemical and strain measurements were made only on nano-Si electrodes with 1:1:1 composition and micro-Si electrodes with 8:1:1 composition (to compare with standard graphite graphite electrodes) and 1:1:1 composition (to compare with nano-Si electrodes). Figure 6.2 shows representative scanning electron micrographs of the these electrodes.

6.2 Electrode Attachment to Custom Battery Cell

Four methods of attaching free-standing composite silicon electrodes to a substrate in the custom battery cell to create electrical and mechanical connections were investigated. These methods are illustrated schematically in Fig. 6.3.

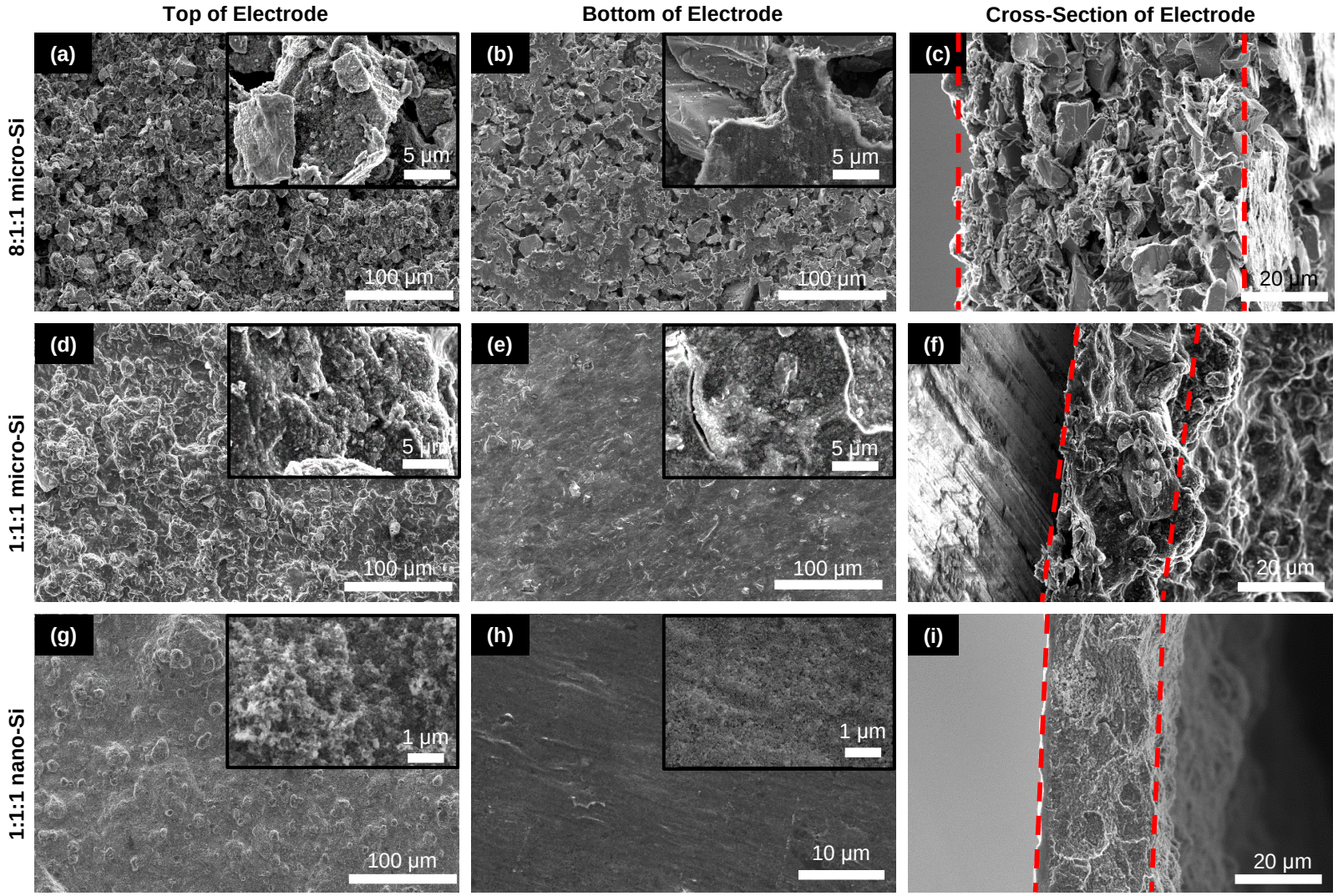

Figure 6.2: Representative scanning electron micrographs of silicon composite electrodes. The column denoted "top" refers to the side of the electrode exposed to air during the drying process, while the column denoted "bottom" refers to the side of the electrode that was on the copper foil substrate during the drying process. The red dashed lines mark the cross-section of the electrodes, with either empty space or the SEM substrate on the left and the electrode surface on the right.

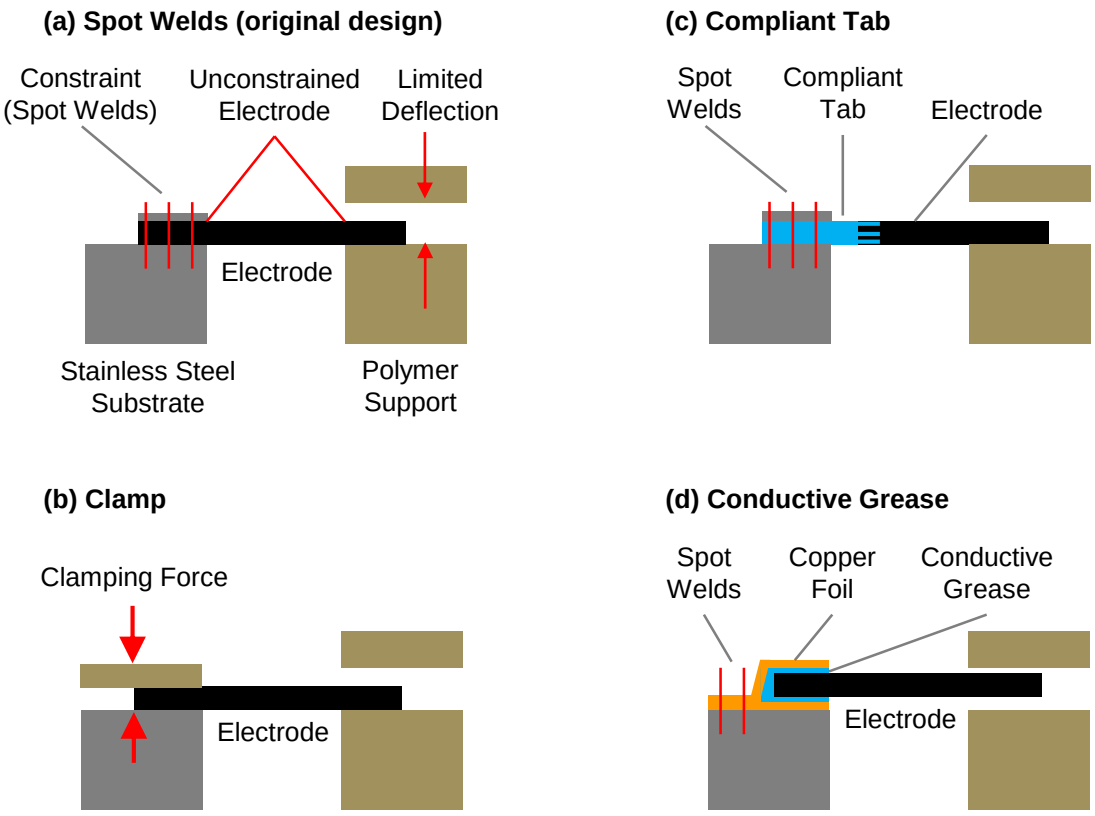

Figure 6.3: Four methods of mechanically and electrically connecting silicon composite electrodes to the substrate. (a) The electrode was spot welded between a piece of stainless steel foil and the stainless substrate, as was done with graphite composite electrodes (Sec. 2.1.2). (b) The electrode was clamped gently with a spring force. (c) The electrode was solvent welded to a compliant tab, and the tab was spot welded to the substrate. (d) The electrode was sandwiched between two layers of copper foil with electrically-conductive grease, and the copper foil was spot welded to the substrate.

6.2.1 Spot Weld Attachment

First, the spot weld based attachment developed previously for graphite composite electrodes (Sec. 2.1.2) was employed (Fig. 6.3a). During the initial lithiation of micro-Si electrodes (8:1:1 wt. ratio of micro-Si, carbon black, and CMC), the electrodes expanded as expected in the unconstrained portion of the electrode but fractured near the spot welds before the electrode was fully lithiated. We hypothesized that the fracture was caused by large stresses developed in the electrode due to constraint by the spot welds of the free expansion of the electrodes. These fractures electrically isolated the electrode and prevented further electrochemical cycling.

6.2.2 Clamp Attachment

In order to reduce the constraint applied to the electrode where it was attached to the substrate, we replaced the spot weld design with a clamp (Fig. 6.3b). The clamp was comprised of a plastic rectangular bar with rounded edges that was pressed onto the electrode from above by two springs, sandwiching the electrode between the top clamp bar and the substrate. The goal of the clamp design was to press the electrode with minimal force, creating a reliable electrical connection but allowing the electrode to slide freely in plane between the top clamp bar and the substrate, thereby reducing constraint on the electrode at the attachment point. Five micro-Si electrodes with 8:1:1 composition were lithiated galvanostatically at C/100 rate using the clamp design. Of these tests, two did not have a reliable electrical connection, presumably because the clamping force was too small, and were therefore not able to be electrochemically cycled. The other three tests fractured at the clamp during the initial lithiation in a similar manner as electrodes attached via spot welds, presumably because the clamping force, and thus the constraint and resulting lithiation-induced stresses, were too large.

In order to investigate the electrode response during delithiation, we cycled micro-Si electrodes galvanostatically at C/100 rate using truncated cycles. In the first five cycles, the lithiation portion of cycling was limited to two hours, corresponding to 84 mA h g^{-1} or $1/50^{th}$ of the theoretical capacity, and in cycles 6-10, the lithiation protion of cycling was limited to five hours, corresponding to 210 mA h g^{-1} or $1/20^{th}$ of the theoretical capacity. The results from this truncated galvanostatic cycling are presented in Fig. 6.4. During the first five cycles, the electrode lithiated and delithiated as expected. When the lithiation time was increased from two hours to five hours, however, the electrode achieved the expected lithiation capacity only on cycles 6 and 7. The electrode then fractured near the clamp and lost electrical connection, resulting in reduced capacity on cycle 8 and nearly zero capacity on cycles 9-10. In summary, constraint of the electrode near the attachment to the substrate

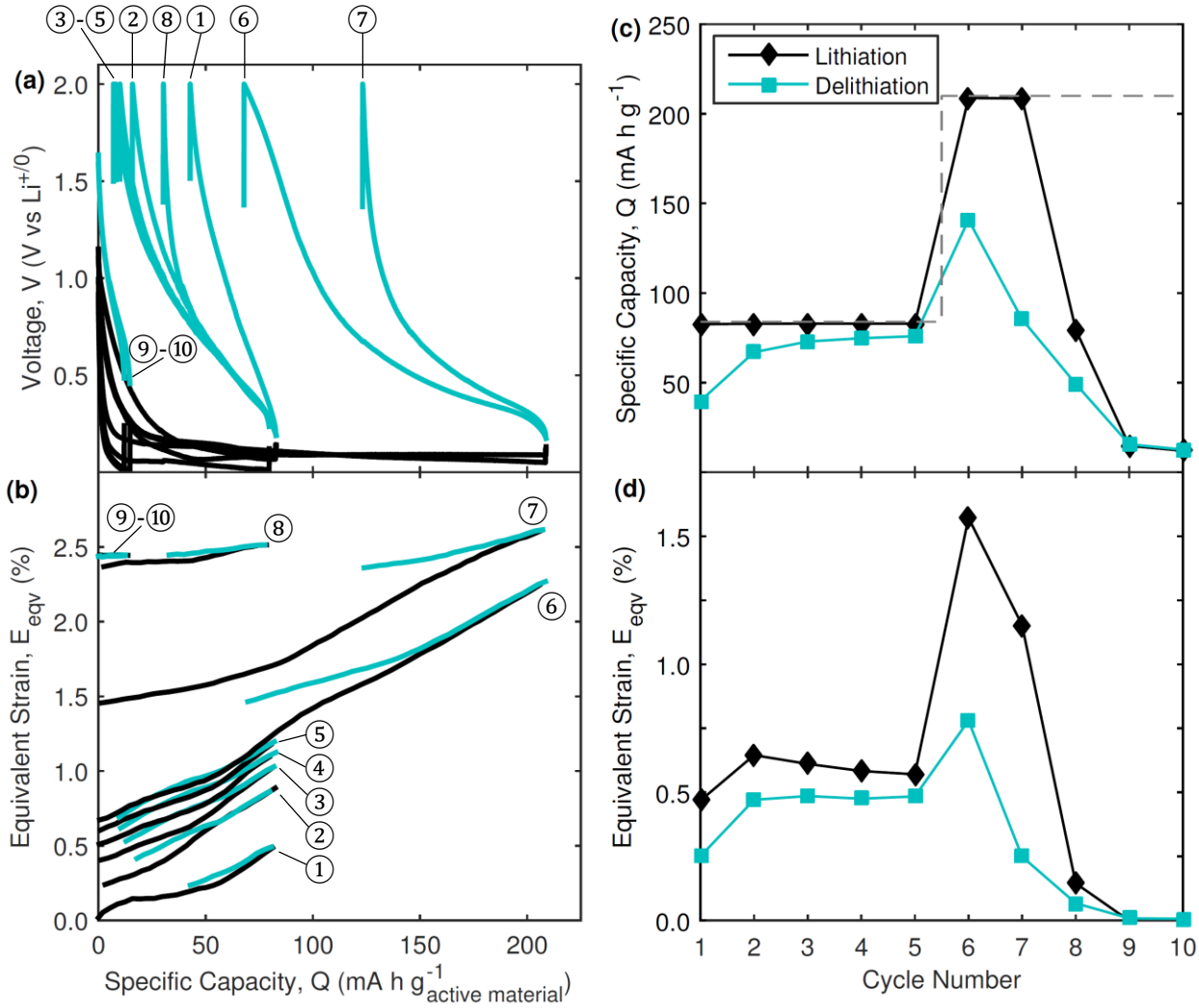

Figure 6.4: Electrochemical and strain response of a silicon composite electrode during truncated galvanostatic cycling at C/100 rate. The electrode had a composition of 8:1:1 wt. ratio micro-Si, carbon black, CMC and was attached to the substrate with a clamp attachment (Fig. 6.3b). Lithiation during cycles 1-5 was limited to 2 hours (84 mA h g^{-1}), and lithiation for cycles 6-10 was limited to 5 hours (210 mA h g^{-1}). (a) Voltage response, (b) strain response, (c) capacity as a function of cycle number (dotted gray line represents theoretically specified capacity) and (d) strain as a function of cycle number. Circled numbers in (a-b) represent the cycle number.

caused electrode fracture under both monotonically increasing electrode expansion during continuous lithiation as well as under cyclic fatigue during truncated galvanostatic cycling. We believe that the clamping attachment configuration could be optimized (e.g. by careful selection of spring constants and length) to provide a reliable electrical connection with minimal constraint, but this optimization was not completed as part of this work.

6.2.3 Compliant Tab Attachment

The third electrode attachment that we investigated was solvent welding the composite silicon electrode to a compliant tab (Fig. 6.3c). Because the silicon composite electrode did not fracture in the free-standing portion away from the attachment point to the substrate when the spot weld or clamp attachment was utilized, CMC binder was chosen as the base material for the tab. Carbon black (CB) was added to the CMC in a 2:1 wt. ratio to make the tab electrically conductive. Samples were fabricated by making a CB/CMC slurry in water, depositing a drop of slurry onto copper foil, and inserting one end of a free-standing micro-Si electrode into the slurry. The water in the slurry locally dissolved the CMC in the

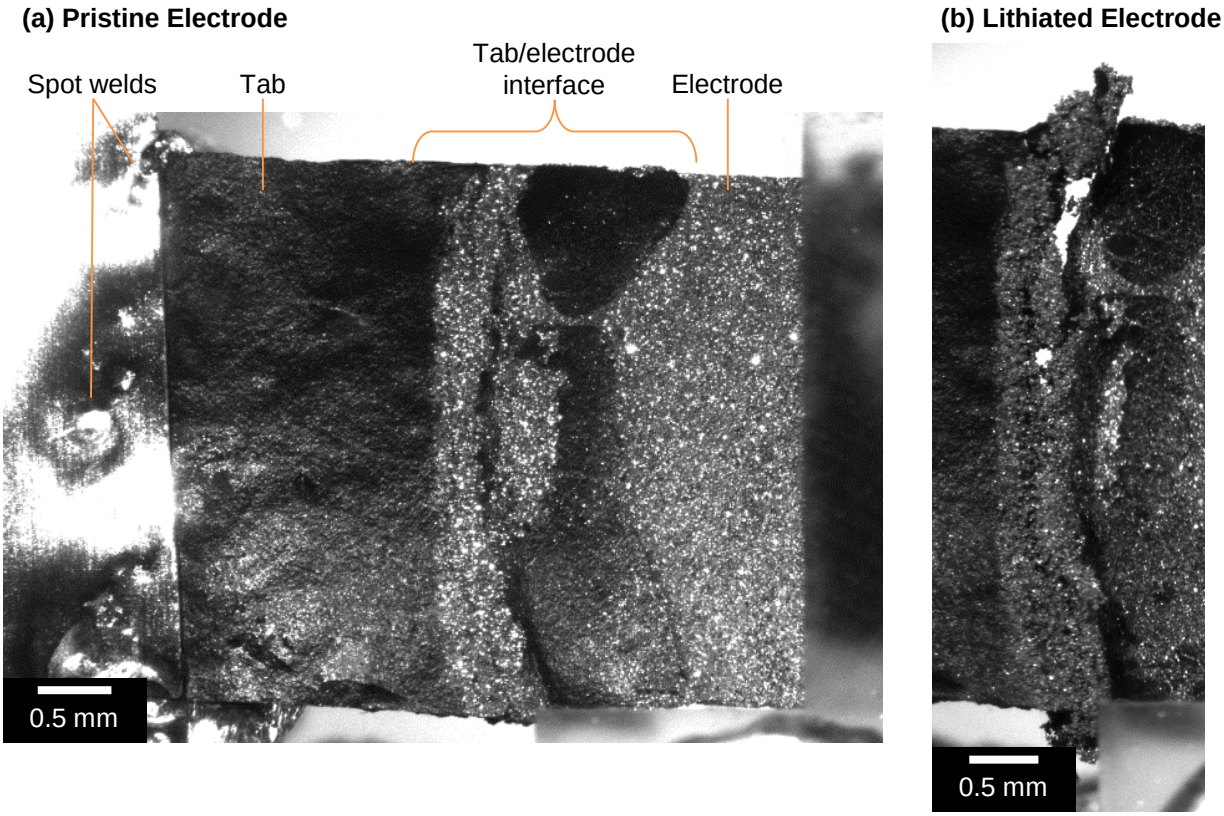

Figure 6.5: Fracture between a micro-Si composite electrode and a compliant tab during galvanostatic cycling at C/100 rate. The electrode had a composition of 8:1:1 wt. ratio of micro-Si, carbon black, and CMC, and the tab had a composition of 2:1 wt. ratio of carbon black and CMC. Optical images of (a) the pristine electrode and (b) the same electrode at the point of fracture after being partially lithiated.

electrode and solvent-welded the electrode to the CB/CMC tab. After the electrode and tab were dry, the sample was peeled off of the copper foil. The tab was then spot welded to the substrate in the custom battery cell.

An optical image of a pristine micro-Si electrode and CB/CMC tab in the custom battery cell is presented in Fig. 6.5a. During galvanostatic cycling, the electrodes fractured at the interface of the electrode and the compliant tab during the initial lithiation, as shown in Fig. 6.5b. Similar to electrodes attached via spot welds or a clamp, these fractures prevented further electrochemical cycling.

6.2.4 Grease Attachment

The final attachment option that we investigated was the use of electrically-conductive grease (Fig. 6.3d). Three types of grease were utilized: (1) a mixture of high vacuum grease (Dow Corning) and carbon black in a 10:3 wt. ratio, (2) a mixture of high vacuum grease and nickel metal flake (Ni-101, Micron Metals) in a 2:3 wt. ratio, and (3) a commercially available conductive grease based on a perfluoropolyether polymer and a copper additive (Krytox GPL246, DuPont). To attach the electrodes to the substrate, the electrode was sandwiched between two layers of grease and two layers of copper foil. The edge of the copper foil away from the electrode was then spot welded to the substrate in the custom battery cell. In order to evaluate the electrical connection itself without complications arising from the large expansion of silicon composite electrodes, we utilized graphite composite electrodes (8:1:1 wt. ratio of graphite, carbon black, and CMC) for some of the trials.

Four of the five electrodes attached using the conductive grease were unable to be electrochemically lithiated. We hypothesize that the resistance through the grease and through the grease/electrode and grease/copper foil interfaces was too high to allow electrochemical cycling, even at rates as slow as C/100. One of the five trials exhibited somewhat promising cycling behavior, as shown in Fig. 6.6, when using the vacuum grease / Ni flake mixture. In

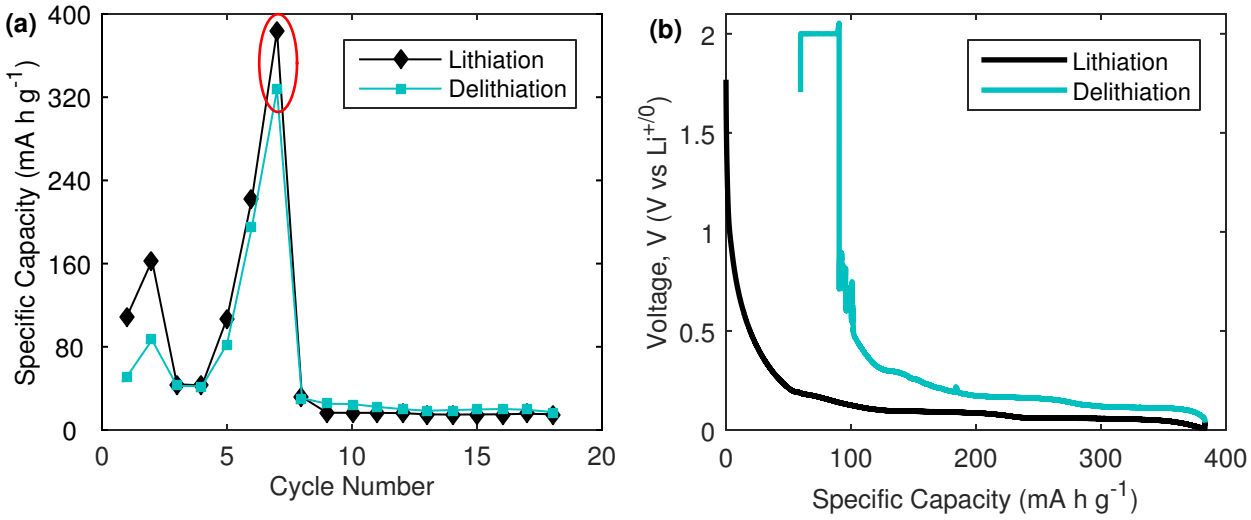

Figure 6.6: Electrochemical performance of a composite graphite electrode attached to the substrate with electrically-conductive grease (Fig. 6.3d). The electrode had a composition of 8:1:1 wt. ratio of graphite, carbon black, CMC, and the grease had a composition of 2:3 wt. ratio of grease and Ni flake. (a) Capacity as a function of cycle number. Erratic capacity retention indicates an unreliable electrical connection. (b) Voltage as a function of capacity for the same electrode for cycle 7. Distinct voltage plateaus are observed, indicating normal lithiation and delithiation of the electrode during this cycle.

the seventh cycle of this trail, the composite graphite electrode achieved nearly theoretical capacity and exhibited the distinct voltage plateaus characteristic of the lithiation / delithiation of graphite. However, the large variations in capacity as a function of cycle number was indicative of a generally unreliable and changing electrical connection.

In an attempt to increase the electrical conductance through the grease, we increased the contact area of the substrate/grease/electrode interfaces by putting a thin layer of grease along the entire back-side of the electrode (opposed to placing the grease only under one end of the electrode). However, electrodes were still not able to by cycled using this variation in the attachment configuration.

6.2.5 Summary of Attachments

The reliability of the electrical connection of the different electrode attachments is summarized in Table 6.1. The spot welds and the tab attachments both provided a reliable electrical connection for the initial lithiation of the electrodes. All electrodes lithiated with

Table 6.1: Number of silicon composite electrodes (8:1:1 wt. micro-silicon, carbon black, and CMC) tested in each attachment configuration (Fig. 6.3).

	Number of samples tested	Number of samples with significant first cycle lithiation capacity[#]
Weld	3	3
Clamp	5	3
Tab	2	2
Grease*	5	0

*Two samples were tested with silicon composite electrodes, and three samples were tested with graphite composite electrodes. All samples had 80 wt.% active material.

[#]Significant capacity was taken as capacity greater than 500 mA h g^{-1} for silicon composite electrodes or greater than 200 mA h g^{-1} for graphite composite electrodes.

these attachments exhibited a smooth initial lithiation profile and achieved a significant capacity during the initial lithiation. In contrast, the clamp and the grease attachments both provided unreliable electrical connections. Only three of five electrodes attached with the clamp and none of the electrodes attached with the grease exhibited smooth initial lithiation profiles or significant capacities during the initial lithiation.

Of the electrodes that exhibited smooth initial lithiation profiles and significant first cycle lithiation capacities, Fig. 6.7 summarizes the capacity results of the first and second cycles. The electrodes achieved between ca. 700 - 1000 mA h g^{-1} capacity during the first lithiation and less than ca. 170 mA h g^{-1} during the first delithiation. Later cycles produced essentially no capacity. The limited first lithiation capacity (compared to the theoretical value of 4200 mA h g^{-1}) and the negligible capacity retention were due to fracture of the electrode near the attachment point. Because no attachment design was found that allowed the silicon electrode to be fully lithiated, the spot weld attachment used previously with graphite composite electrodes was utilized for strain measurements of silicon composite electrodes (see Sec. 6.3).

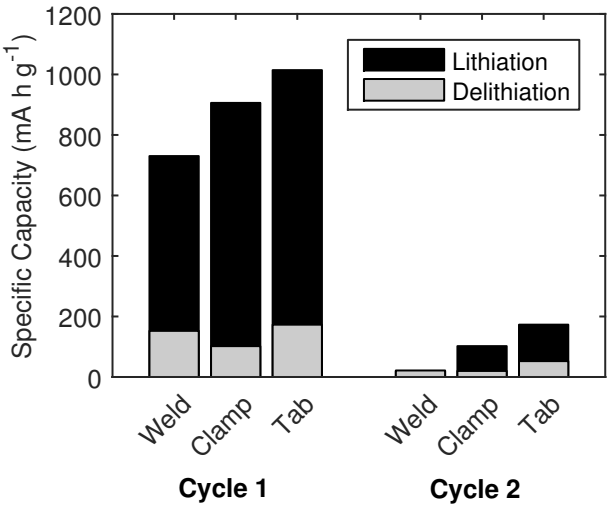

Figure 6.7: First and second cycle capacities for silicon composite electrodes cycled using different attachment configurations (Fig. 6.3). The electrodes all had compositions of 8:1:1 wt. micro-Si, carbon black, and CMC.

6.3 Strain Response of Silicon Composite Electrodes

6.3.1 Electrochemical Response

The electrochemical behavior of silicon composite electrodes during the initial galvanostatic lithiation is shown in Fig. 6.8. Two independent tests are shown for 8:1:1 micro-Si electrodes and 1:1:1 nano-Si electrodes, and one test is shown for 1:1:1 micro-Si electrodes. For comparison, the electrochemical response of an 8:1:1 graphite electrode is also included (repeated from Fig. 3.1). The 8:1:1 and 1:1:1 micro-Si electrodes achieved ca. 850 mA h g^{-1} and 2600 mA h g^{-1} capacity, respectively, during lithiation (normalized by the mass of silicon), with negligible reversible capacity during delithiation. The 1:1:1 nano-Si electrodes achieved the highest capacity during lithiation (ca. 3500 mA h g^{-1}) but they attained only ca. 600 - 750 mA h g^{-1} reversible capacity. The poor cycling of the silicon electrodes (i.e. low lithiation capacity compared to the 4200 mA h g^{-1} expected theoretically and minimal reversible capacity) was caused by fracture of the silicon electrodes where they were cantilevered from the substrate during cycling (see Sec. 6.2).

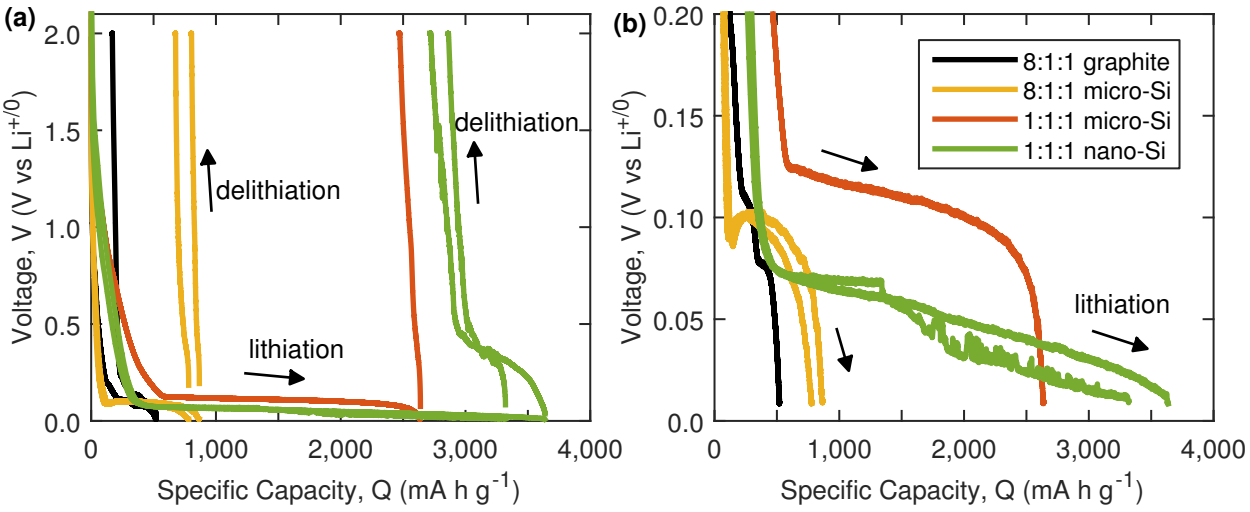

Figure 6.8: Electrochemical response of different types of electrodes during the initial galvanostatic lithiation. Silicon electrodes were lithiated at C/100 rate and graphite electrodes were lithiated at C/20 rate. The curve labels represent the weight ratio of active material (either graphite, micro-Si, or nano-Si), carbon black, and CMC binder. Two tests are shown for 8:1:1 micro-Si and 1:1:1 nano-Si electrodes, while one test is shown for 8:1:1 graphite and 1:1:1 micro-Si electrodes. The capacity is normalized with respect to the mass of active material in the working electrode. (a) Full voltage axis, showing both lithiation and delithiation during the first cycle and (b) expanded voltage axis, showing only the initial lithiation during the first cycle.

6.3.2 Spatial Variation of Strain

Fig. 6.9a presents a representative contour plot of the horizontal normal strain, E_{xx}, for a silicon composite electrode (8:1:1 wt. ratio of micro-Si, carbon black, and CMC binder) at the end of the initial lithiation. The 8:1:1 micro-Si electrode developed a strong strain gradient, with the highest strain at the end of the electrode closest to the connection to the substrate (left side) and the lowest strain farthest from the substrate (right side). The vertical normal strain, E_{yy}, had a similar strain gradient. Line scans of E_{xx} along a horizontal line in the center of the region of interest (marked by the black dashed line in Fig. 6.9a) are presented in Fig. 6.9b. Four line scans are shown, at even intervals during the initial lithiation. When the electrode was lithiated to 1/4 of the final capacity (Q = 193 mA h g^{-1}), E_{xx} was fairly uniform across the width of the region of interest. As the electrode was lithiated further, the strain gradient increased. Representative line scans of E_{xx} for a 1:1:1

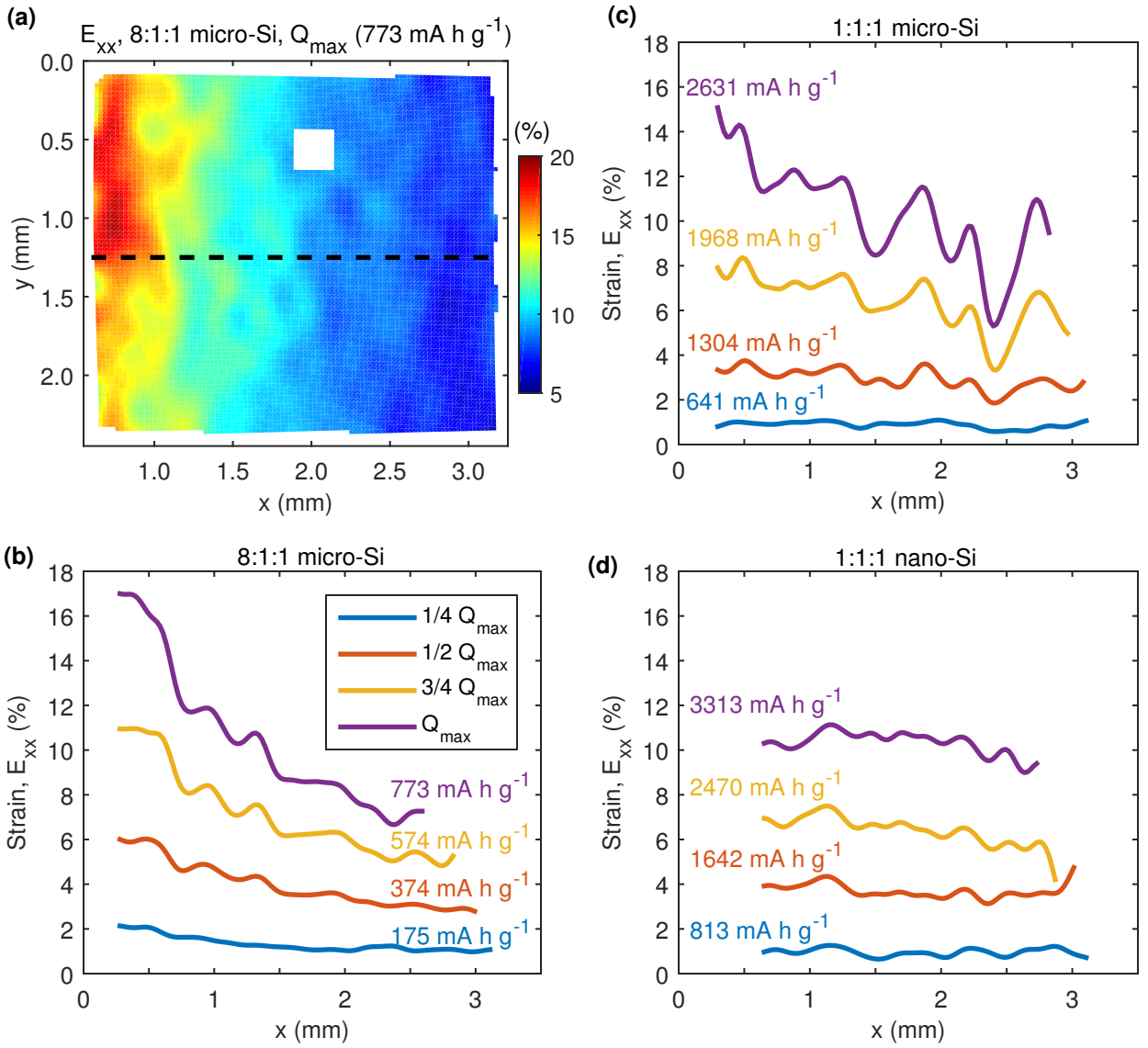

Figure 6.9: Spatial variation of the strain of silicon composite electrodes. (a) Contour of E_{xx} for an 8:1:1 micro-Si electrode at the end of the initial lithiation. A poorly correlated region of the images is masked by a white rectangle. (b-d) Horizontal line scans of E_{xx} along the line $y = 1.25$ mm, marked by the black dashed line in (a), at four different evenly-spaced points during the initial lithiation. (b) 8:1:1 micro-Si, (c) 1:1:1 micro-Si, and (d) 1:1:1 nano-Si.

micro-Si electrode and for a 1:1:1 nano-Si electrode are presented in Fig. 6.9c-d respectively. The 1:1:1 micro-Si electrode showed a similar strain gradient as the 8:1:1 micro-Si electrode, but with more local oscillations of a period of approximately 0.5 mm. The 1:1:1 nano-Si electrode showed the most homogenous strain field, with only a slight gradient across the width of the region of interest.

The spatial strain variation of the micro-Si electrodes was qualitatively different from that in graphite electrodes (Fig. 3.4), where the horizontal normal strain was uniform and the vertical normal strain was reduced, instead of enhanced, near the connection to the substrate. In graphite electrodes, the reduction of E_{yy} near the connection was attributed to constraint applied to the electrode by the spot welds. In contrast, the spatial variation in the strain field for the micro-Si electrodes is attributed to the high electrical resistance across the length of the cantilevered portion of the electrode (ca. 50 kΩ for 8:1:1 micro-Si electrodes and ca. 15 kΩ for 1:1:1 micro-Si electrodes compared to ca. 30 Ω for 8:1:1 graphite electrodes, as measured with a multimeter with probes approximately 5 mm apart). The high electrical resistance likely induces a gradient in the capacity of the electrode, with the highest specific capacity occurring closest to the electrical connection. It is hypothesized that the strain gradient results from the probable capacity gradient. With a resistance of ca. 9 kΩ, the 1:1:1 nano-Si electrodes were less resistive than both of the micro-Si electrodes, though they were still significantly more resistive than the graphite electrodes. Electrical resistance is therefore likely only one factor contributing to the spatial variation of the strain fields, but a full investigation of the spatial variation of the strain fields was not completed.

6.3.3 Average Strain Response

The equivalent strain, averaged over the entire region of interest for each image, of the silicon composite electrodes is presented in Fig. 6.10a. The strain response of an 8:1:1 graphite electrode (repeated from Fig. 3.5) is included for comparison. The 8:1:1 micro-Si electrodes exhibited a higher strain than the 8:1:1 graphite electrode at a given capacity. These results indicate that the macroscale expansion of the electrodes depends on the type of active material, and not just the amount of lithium inserted into the active material. The 1:1:1 micro-Si electrode exhibited lower strain than the 8:1:1 micro-Si electrodes at a given specific capacity. Since there was less total silicon in the 1:1:1 micro-Si electrode, though, less total lithium was inserted into this electrode compared to the 8:1:1 micro-Si electrodes,

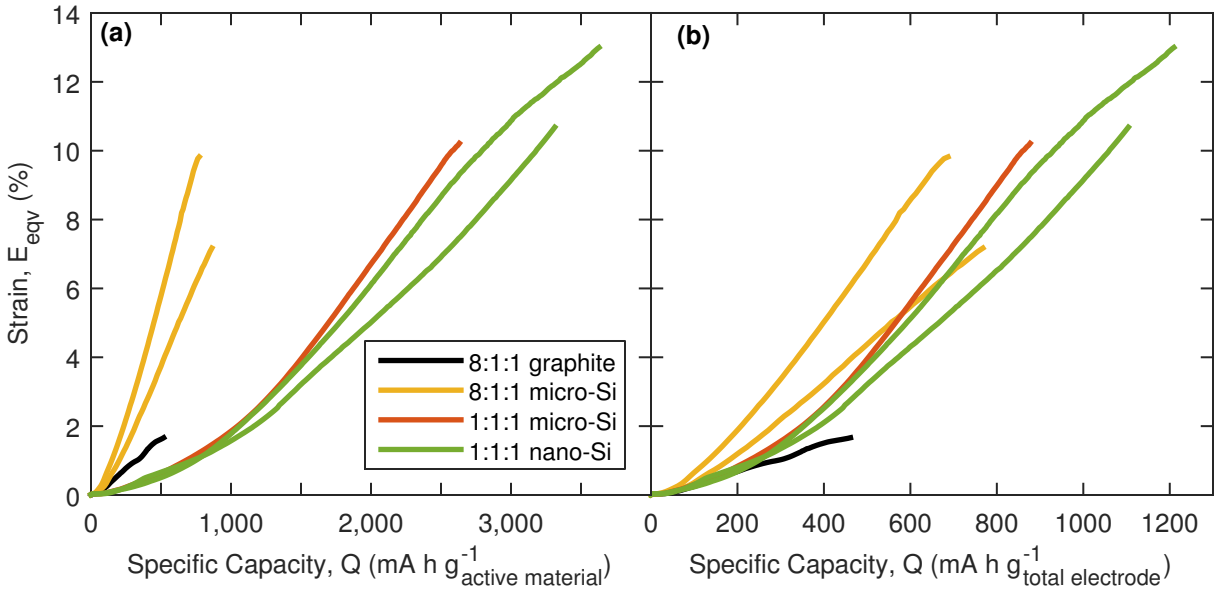

Figure 6.10: Strain responses of different types of electrodes during the initial galvanostatic lithiation. The equivalent strain was averaged over the entire region of interest for each image. In (a), the capacity is normalized by the mass of the active material (either graphite or silicon). In (c), the capacity is normalized by the total electrode mass. This strain data corresponds to the electrochemical data presented in Fig. 6.8.

and hence the strain of the 1:1:1 micro-Si electrode was correspondingly reduced. The 1:1:1 micro-Si electrode and the 1:1:1 nano-Si electrodes exhibited similar strain responses, indicating that the size of the active material particles did not influence the macroscale electrode expansion.

The strain responses are plotted in Fig. 6.10b as a function of the capacity normalized by the total electrode mass, including mass of the active material, carbon black, and polymer binder. By normalizing by the total electrode mass instead of the mass of the active material, the reduced total silicon content of the 1:1:1 micro-Si and 1:1:1 nano-Si electrodes was taken into account. The discrepancies between the maximum lithiation capacity of the 8:1:1 micro-Si electrodes and the 1:1:1 micro-Si and the 1:1:1 nano-Si electrodes were therefore reduced. Interestingly, when the capacity was normalized by the total electrode mass, the strain responses nearly collapsed onto one line for all types of electrodes. This result suggests that the total lithium quantity inserted into the electrode dominates the macroscale electrode

expansion, and that type of active material, ratio of electrode components, and size of active material particles are all secondary factors.

6.4 Conclusions

Silicon composite electrodes were fabricated with both micron-sized silicon powder and nano-sized silicon powder. Fracture of the nano-Si electrodes during the drying process prevented fabrication of free-standing nano-Si electrodes with high nano-Si content ($x > 1$ in x:1:1 wt. ratio of nano-Si, carbon black, and polymer binder). Constraint of the electrode at the attachment point to the substrate in the custom battery cell resulted in fracture of the electrode when the electrode expanded during lithiation. This fracture caused the electrode to loose electrical connection to the substrate, which subsequently limited the first cycle lithiation capacity and the capacity retention of the electrode during galvanostatic cycling. To overcome the limitations regarding fabrication and electrochemical cycling of free-standing silicon composite electrodes, we propose measuring out-of-plane deformation of thin electrodes adhered to a substrate as a possible direction for future work.

The in-plane expansion of free-standing electrodes induced by lithium insertion during the first cycle was measured using digital image correlation. The electrochemically-induced strain of the composite electrodes was dominated by the total amount of lithium inserted into the electrode. Both the type of active material (either graphite or silicon) and the ratio of electrode components (active material, conductive additive, and polymer binder) were found to be secondary influences on the strain response of the electrodes. The size of the active material particles had insignificant influence on the strain response.

Chapter 7

Summary and Directions for Future Work

Lithium-ion batteries offer the highest volumetric and gravimetric energy densities of all commercial battery technology to date [1], rendering them appealing for a wide variety of applications, from portable electronics to electric vehicles. The demand for lighter, smaller, and longer-lasting batteries continues to drive research towards both improving lithium-ion battery technology and to developing new battery chemistries.

One facet of this research has centered on new high-capacity anode materials, such as silicon. High-capacity electrodes have the potential to extend operation time between battery charges (compared to conventional batteries of the same size) and/or to reduce the size and weight of batteries (compared to conventional batteries with the same operation time). The main road block preventing the commercialization of these materials is the large volumetric expansion that occurs when the electrodes are lithiated and subsequent fracture of the electrodes. This mechanical aspect of battery degradation opened the door for members of the mechanics community to contribute to lithium-ion battery research. Since then, mechanicians and material scientists in collaboration with electrochemists have explored many aspects of combined electro-chemo-mechanical phenomena that contribute to battery performance and degradation. A snap shot of past investigations related to the electrochemically-induced mechanical response of anodes is presented in Ch. 1.

The work presented in this dissertation progresses from fundamental studies of the electrochemically-induced volumetric expansion of idealized model electrodes (e.g. thin films or individual nano-particles) by investigating the mechanical response of particulate composite electrodes. An experimental protocol was developed to measure the free expansion

of composite electrodes during electrochemical cycling (Ch. 2). First, graphite composite electrodes were studied, and fundamental insight regarding reversible and non-recoverable electrode deformation was gained (Ch. 3). Next, the effect of varying the electrode composition, electrolyte composition, and cycling rate was investigated in order to establish basic trends for how the strain response varies with respect to these basic battery parameters (Ch. 4). With Dr. Hadi Tavassol, *in situ* stress and strain measurements of graphite electrodes were combined in order to calculate the electrochemical stiffness, and changes in the electrochemical stiffness as a function of electrode potential and electrode capacity shed new light onto the mechanisms governing stress and strain development in battery electrodes (Ch. 5). Finally, the mechanical behavior of high-capacity silicon composite electrodes was also examined (Ch. 6).

A clear and defined *END* to a research trajectory does not exist. While some conclusions are drawn, the results always spark more questions and a desire to understand phenomena and mechanisms more thoroughly. Several remaining open areas and suggested trajectories for future work building off this dissertation are described below.

Non-recoverable deformation and the solid-electrolyte interphase: What is the exact mechanism by which the formation of the SEI causes non-recoverable electrode deformation (Sec. 3.3)? How does the binder of composite electrodes influence the non-recoverable electrode deformation (Sec. 4.1)? Are different electrolyte decomposition products catalyzed by different binders? Finally, how does vinylene carbonate modify the reaction pathway of electrolyte decomposition and how does it modify the final SEI structure (Sec. 4.4)?

To understand the relationship between non-recoverable deformation and SEI formation, we need to complement the *in situ* strain measurements performed so far with techniques that probe the composition, structure, and growth of the SEI directly. For instance, an electrochemical quartz crystal microbalance can measure residual mass associated with the SEI on an electrode *in situ* during electrochemical cycling. X-ray photon spectroscopy (XPS) could be utilized to characterize the chemical composition of the SEI layer, and in combina-

tion with ion-beam etching, could be used to determine the SEI thickness postmortem.

Electrochemical stiffness: What are the mechanisms that cause stress to develop in graphite electrodes before significant lithiation of the electrode (Ch. 5)? The mechanisms of strain generation at the nanoscale have been established with x-ray diffraction measurements, but are there small-scale experiments (microscale or nanoscale) that can provide complementary information about the mechanisms of stress generation in the electrodes? Also, how does electrochemical stiffness evolve in different electrode materials? It would be interesting to apply the technique developed in this work to other battery materials.

Silicon composite electrodes: There are a several questions that follow immediately from the results presented in this thesis on silicon composite electrodes. Regarding electrode fabrication, what physical phenomena govern residual stresses and subsequent fracture of electrodes during the drying process (Sec. 6.1)? How can sufficiently thick (i.e. thick enough to be free-standing) nano-Si composite electrodes with a high nano-Si content be fabricated? Regarding custom battery cell design, can an electrode attachment be engineered that applies minimal constraint to the electrode while at the same time provides a reliable electrical connection (Sec. 6.2)? Or is there a more suitable technique for the measurement of strains in high-capacity composite electrodes, such as measuring the out-of-plane expansion of electrodes adhered to a substrate?

Taking a step back, though, the main question regarding high-capacity electrodes is this: Can high-capacity anodes be commercialized, and what fundamental research is required to achieve commercialization? Stress and fracture resulting from the volumetric expansion of silicon can be mitigated to an extent through clever design of the electrode architecture (e.g. nanosize particles, one-dimensional nano-tubes or nano-pillars, composites with multiple active materials, etc.), but stable passivation of the electrode remains a huge challenge [91]. Moving forward, mechanicians can have a large impact on lithium-ion battery technology by focusing on the mechanical behavior and failure of the solid-electrolyte interphase (SEI) on high-capacity materials. Targeted studies on the fracture properties of the SEI formed

in situ during battery operation as well as design of artificial passivation layers that can retain their passivating properties when the underlying electrode material undergoes large volumetric expansion are critical.

The big picture: A final, overarching question that remains is how to productively and practically employ the results presented in this thesis to the design of more robust, longer-lasting lithium-ion battery anodes. While the information presented here is interesting from a basic science point of view, the driving force for this work has always been to push lithium-ion battery technology to the next generation. Though this work does not, in itself, quite fulfill the goal of directly impacting commercial lithium-ion battery technology, it sets the stage for some exciting follow-up research. I hope that others will be able to use these results as a springboard for cutting-edge research that will revolutionize battery technology with cascading effects in the innumerable areas where batteries are, and will be, utilized.

Appendices

Appendix A

Supplementary Information on the Solid-Electrolyte Interphase

A.1 Electrolyte Solvent Decomposition Mechanisms

Decomposition products from ethylene carbonate (EC) and vinylene carbonate (VC) electrolyte solvents form the basis of the organic portion of the solid-electrolyte interphase (SEI). In this Appendix, a summary of the main decomposition products from these solvents as well as proposed reaction mechanisms are presented.

Lithium ethylene dicarbonate (LEDC) is the main component in the SEI derived from EC [41, 76]. Two possible mechanisms have been proposed to form LEDC, one involving a one-electron reduction of EC and a second route involving a two-electron reduction of EC, as shown in Fig. A.1.

Lithium vinylene dicarbonate (LVDC) and lithium divinylene dicarbonate (LDVDC) have both been identified as SEI components derived from electrolyte containing VC additive [41, 76]. Fig. A.2 shows proposed mechanisms by which VC is reduced and then combined to form LVDC and LDVDC. Polymerized VC has also been identified as a main SEI component [76]. Fig. A.3 depicts two possible radical polymerization mechanisms to form two different types of polymerized VC. The formation of polymer B was found to be more favorable from thermodynamic considerations [79], but polymer A was found in the SEI experimentally [76].

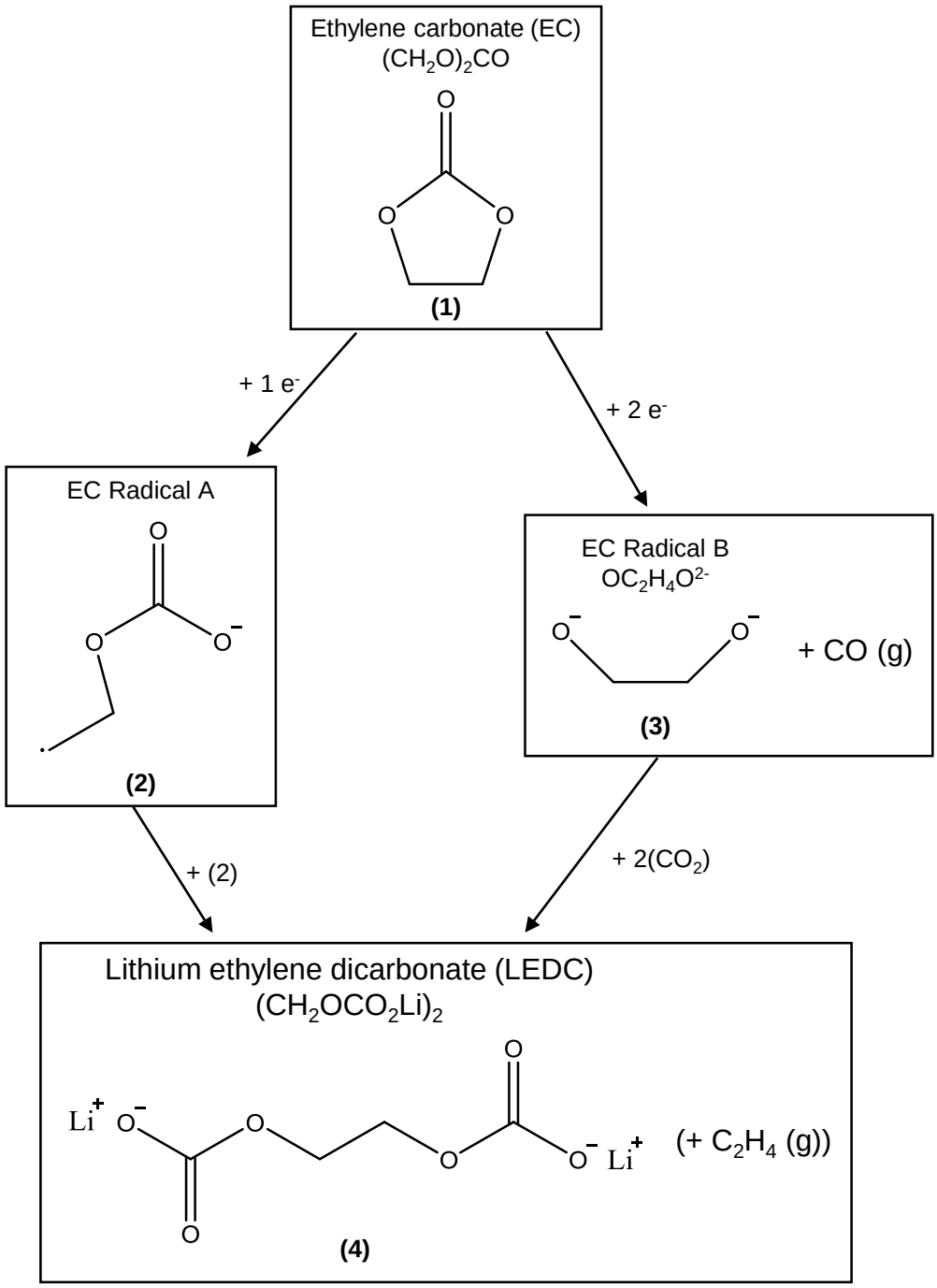

Figure A.1: Proposed decomposition mechanisms of ethylene carbonate (EC). EC can be reduced via one electron to form EC radical A, which can subsequently react with a second EC radical A to form lithium ethylene dicarbonate (LEDC) [79, 80]. Alternatively, EC can be reduced via two electrons to form EC radical B, which can subsequently react with other electrolyte decomposition products (e.g. CO_2 among others) to form LEDC [81].

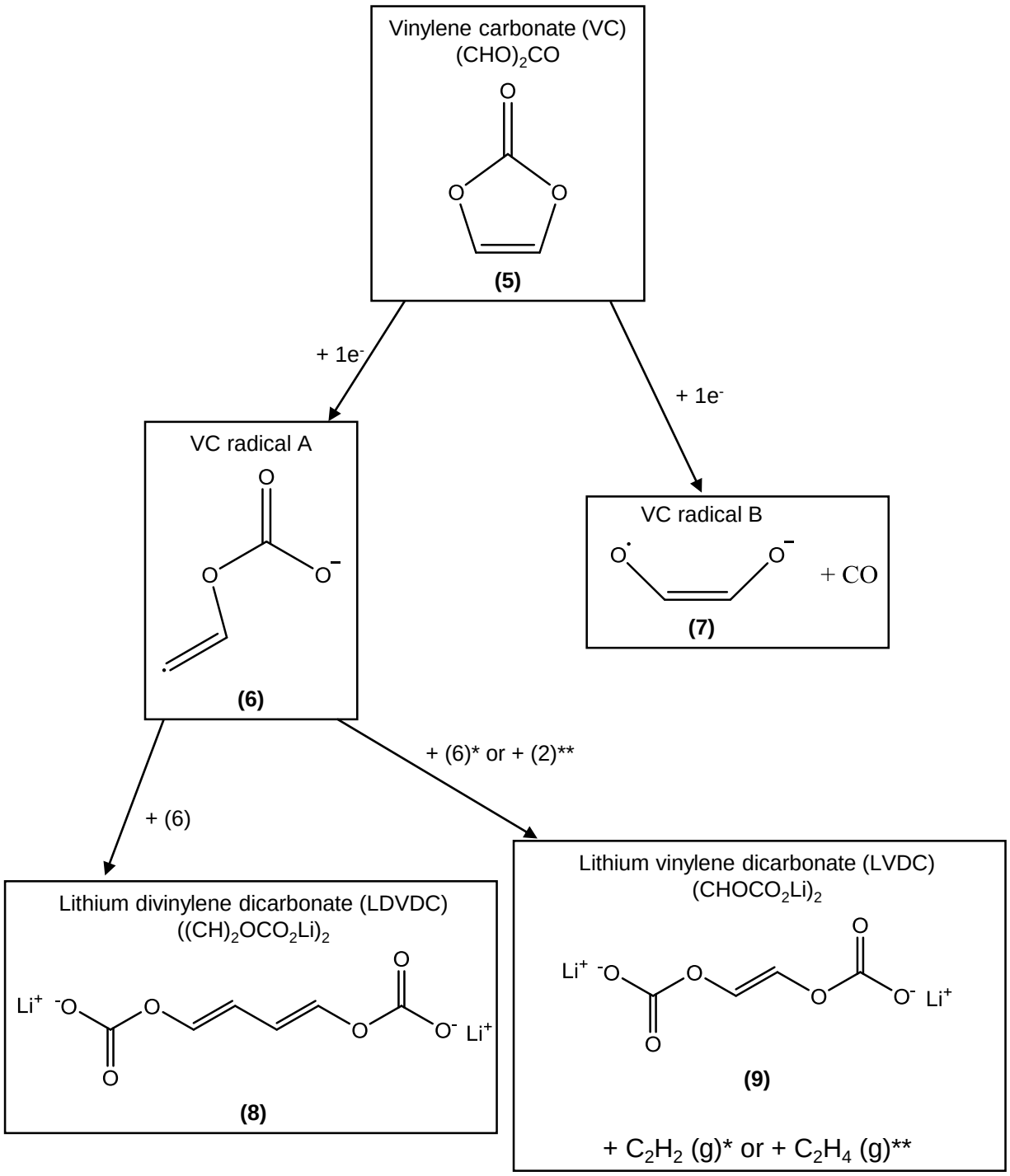

Figure A.2: Proposed decomposition mechanisms of vinylene carbonate (VC). VC can be reduced via one electron to form VC radical A, which can subsequently react with a second VC radical A to form lithium divinylene dicarbonate (LDVDC) or to form lithium vinylene dicarbonate (LVDC) and C_2H_2 gas. Also, VC radical A can react with EC radical A to form LVDC and C_2H_4 gas [79]. VC radical B is proposed as a more likely radical to be formed by a one-electron reduction, but the authors did not propose any subsequent termination reactions [80].

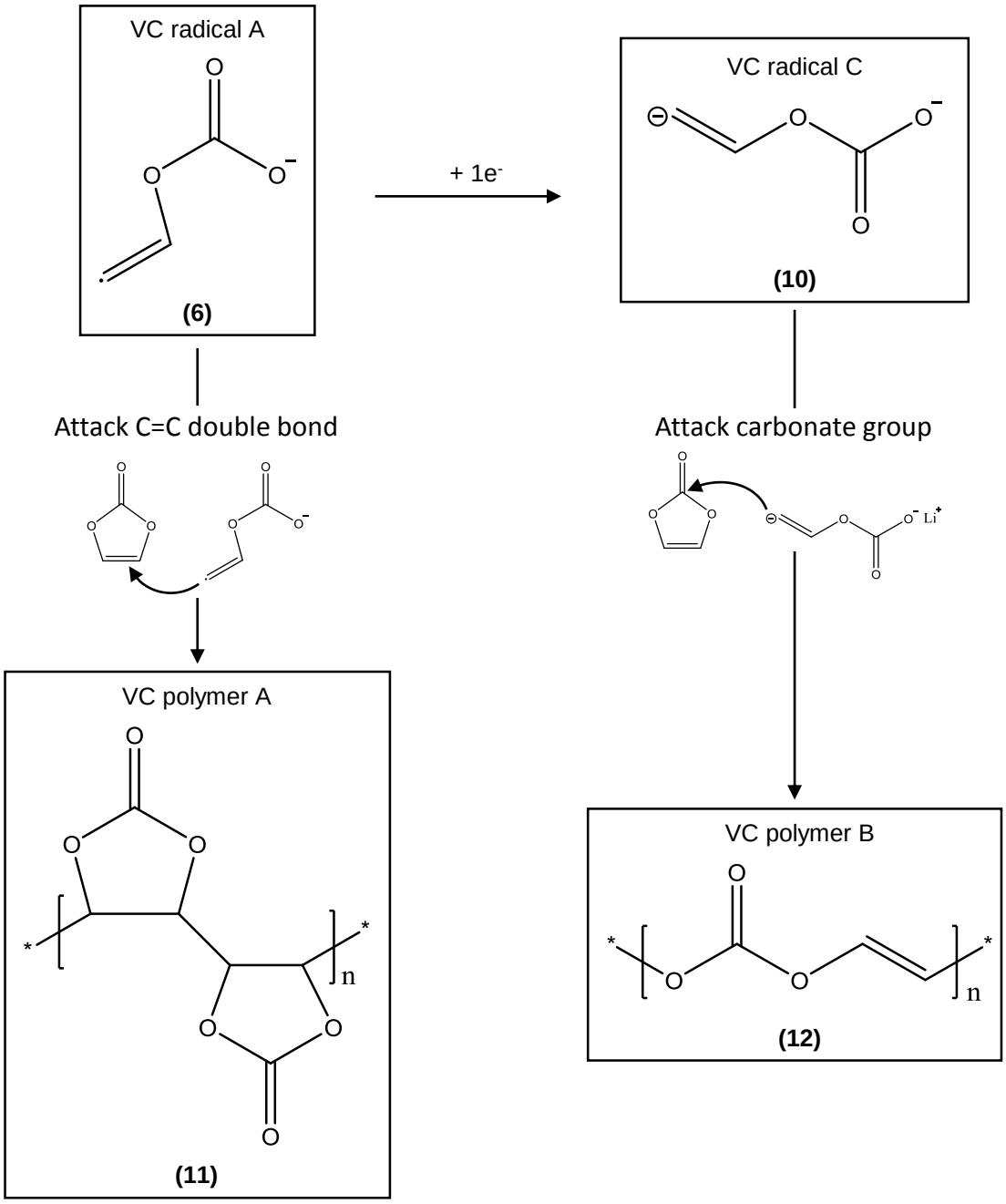

Figure A.3: Proposed polymerization mechanisms of vinylene carbonate (VC). VC radical A can attack the C=C double bond in in-tact VC molecules, initiating a radical poylmerization to form VC polymer A. Alternatively, VC radical A can be further reduced to VC radical C, which can then attack the carbonate group of in-tact VC molecules to form VC polymer B [79].

A.2 Non-Recoverable Deformation of Electrodes

We hypothesized that there were three possible sources of non-recoverable deformation of composite graphite electrodes: (1) relaxation of residual stress from electrode fabrication, (2) debonding of polymer binder from graphite or carbon black particles and/or the breaking up of carbon black agglomerates, and (3) accumulation of irreversible electrolyte decomposition products on graphite and carbon black particles. The latter is discussed in detail in Sec. 3.3, with supporting information presented in Sec. A.2.1 and Sec. A.2.2. Because of the direct relationship between irreversible capacity and non-recoverable deformation, we concluded that the irreversible capacity is the primary factor concerning non-recoverable deformation. However, to form a more complete picture, the first two hypotheses were also investigated.

A.2.1 Predicted Expansion of Composite Electrodes due to Growth of the SEI

The model developed in Sec. 2.3 was adapted to predict the expansion of composite graphite electrodes due to the formation and growth of the solid-electrolyte interphase (SEI). The effective expansion of graphite particles due to deposition of electrolyte decomposition products on the surface of the particles was modeled analogously to a thermal expansion of the particles. The thermal analogy was not as strong in this case as it was for the expansion of graphite due to lithium intercalation since here the expansion of the particles was due to formation of a surface film rather than expansion of the bulk particles; however, we believe it provided a reasonable estimate for the expected composite electrode expansion. Several assumptions were made to allow the problem to be analytically solvable:

- The SEI forms on graphite particles only. (The formation of SEI on carbon black was ignored.)
- The SEI forms a conformal layer of uniform thickness on the graphite particles.
- The SEI is homogeneous and isotropic.

Experimental results have shown that the SEI layer typically ranges from 10 - 100 nm in thickness [32, 34]. With the simplifying assumption of spherical graphite particles of 10 µm in diameter, the expected volumetric expansion of graphite particles due to a 100 nm thick SEI layer was 6.1 %. The corresponding linear strain of graphite-SEI core-shell particles, ϵ_p, was calculated from the volumetric expansion assuming isotropy to be 2.0 %.

Nano-indendation experiments have estimated the Young's modulus of the SEI layer to be in the range of ca. 10 MPa to 10 GPa [92–98], and the Poisson's ratio of the SEI has been assumed to be 0.5 for rubber elasticity [93, 98]. Here, composite electrode expansion was predicted for ranges of the Young's modulus (10 MPa to 10 GPa) and the Poisson's ratio (0.4 - 0.5) for the SEI layer. The corresponding ranges for the bulk modulus, K_{sei}, and shear modulus, G_{sei}, of the SEI were calculated according to standard relationships of elastic constants for isotropic materials.

The lower bound of the effective shear moduli, G_p, and the lower bound of the effective bulk moduli, K_p, of graphite-SEI core-shell particles were calculated using the inverse rule of mixtures:

$$(1/K_p) = (\phi_{p,g}/K_g) + (\phi_{p,sei}/K_{sei}) \tag{A.1a}$$
$$(1/G_p) = (\phi_{p,g}/G_g) + (\phi_{p,sei}/G_{sei}) \tag{A.1b}$$

where K_g and G_g are the bulk and shear moduli of unlithiated graphite (Table 2.1), and $\phi_{p,g}$ and $\phi_{p,sei}$ are the volume fractions of graphite and SEI, respectively, within the graphite-SEI core-shell particles. The values of $\phi_{p,g}$ and $\phi_{p,sei}$, and therefore the values of K_p and G_p, evolve as the SEI grows on the particles. The effective Poisson's ratio for the graphite-SEI core-shell particles, ν_p, was calculated from the effective bulk and shear moduli according to the standard relationship for isotropic materials.

The bulk modulus of the composite electrode, K_{e*}, was computed by applying the "S-Combining Rule" [58] for graphite-SEI core-shell particles in a porous matrix according to Eqn. 2.6 and Eqn. 2.7, where the bulk modulus and Poisson's ratio of graphite, K_g and ν_g, were replaced with the effective bulk modulus and Poisson's ratio of graphite-SEI core-shell particles, K_p and ν_p.

The linear strain developed in the composite electrode due to growth of the SEI layer, ϵ_{e*}, was then estimated according to Eqn. 2.8 and Eqn. 2.9, where the bulk modulus of graphite, K_g, was replaced with the effective bulk modulus of graphite-SEI core-shell particles, K_p. Additionally, the linear strain of graphite particles due to lithium intercalation, ϵ_g, was replaced by the linear strain of graphite-SEI core-shell particles due to SEI growth, ϵ_p. Discussion of the model predictions and comparison of the predictions to experimental results is presented in Sec. A.2.2.

A.2.2 Comparison of Analytical Model to Experimental Results

The predictions of the model adapted in Sec. A.2.1 for the expansion of composite graphite electrodes due to formation and growth of the SEI layer on graphite particles are presented in Fig. A.4. Ranges for the predicted composite electrode expansion are shown for ranges of the Young's modulus and Poisson's ratio of the SEI layer. In general, volumetric expansions of graphite-SEI core-shell particles of up to 6.1 %, corresponding to SEI thicknesses of up to ca. 100 µm, are predicted to cause ca. 0.93 - 1.18 % strain in composite graphite electrodes.

As shown in Fig. 3.1 and Fig. 3.5, a total of 157 mA h g^{-1} of irreversible capacity and 0.88 % non-recoverable deformation was developed in a graphite composite electrode during three cycles (129 hours) of galvanostatic cycling. During a potentiostatic voltage hold of 132 hours, reduction of electrolyte solvents caused 108 mA h g^{-1} of capacity and 0.25 % strain to develop in a graphite composite electrode (Fig. 3.10). According to our model, 0.25 - 0.90 % composite electrode strain corresponds to ca. 1.3 - 5.8 % volumetric expansion of graphite-SEI core-shell particles, or equivalently to an SEI with thickness of ca. 20 - 95 nm. These estimated SEI thicknesses are within the expected range of 10 - 100 nm

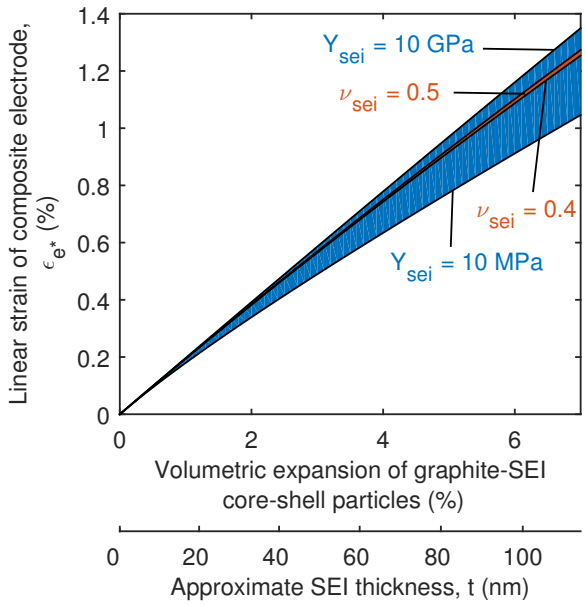

Figure A.4: Model predictions for the expansion of graphite composite electrodes due to SEI formation and growth. The blue region shows the predictions for a range of Young's moduli of the SEI, 10 MPa $< Y_{sei} <$ 10 GPa (Poisson's ratio of $\nu_{sei} = 0.45$). The red region shows the predictions for a range of Poisson's ratio of the SEI, $0.4 < \nu_{sei} < 0.5$ (Young's modulus of $Y_{sei} = 100$ MPa). An estimation for the SEI thickness, t, corresponding to the volumetric expansion of the graphite-SEI core-shell particles is calculated assuming spherical graphite particles of 10 µm diameter and a conformal, uniform SEI layer.

[32, 34]. Therefore, this model supports the hypothesis that formation and growth of the SEI layer causes non-recoverable composite electrode deformation.

The lower capacity and strain developed during the potentiostatic test compared to the galvanostatic test are attributed to two primary differences between the two types of electrochemical tests. First, while the primary electrolyte decomposition reactions occur starting at ca. 0.8 V vs $Li^{+/0}$, electrolyte components continue to react at voltages down to 0 V vs $Li^{+/0}$ [33]. Therefore, the decomposition products formed on the graphite electrode during the potentiostatic test at 0.5 V vs $Li^{+/0}$ are not identical to those formed during galvanostatic cycling over the voltage window of 2 V - 0.01 V vs Li $^{+/0}$. Additionally, the graphite electrode cycled galvanostatically contained 10 wt. % carbon black, while the electrode used in the potentiostatic test contained no carbon black. Since electrolyte decomposition scales with surface area of the electrode [32], larger irreversible capacity is expected to develop in electrodes containing carbon black.

In addition to the formation of the SEI layer, a second possible mechanism of electrolyte decomposition is the co-intercalation and subsequent reduction of electrolyte solvent molecules between graphite layers, which would cause an irreversible increase in graphite layer spacing. An astute choice of electrolyte components (i.e. the exclusion of propylene carbonate and the inclusion of ethylene carbonate) greatly reduces solvent co-intercalation [99]. With the electrolyte used in this work (1M $LiClO_4$ in 1:3 vol. ratio of ethylene carbon-

ate and dimethyl carbonate), solvent co-intercalation should have been minimal, and SEI formation should have been the dominate form of electrolyte decomposition.

A.2.3 Other Possible Sources of Non-Recoverable Deformation

In addition to formation and growth of the SEI, two other possible sources of non-recoverable deformation were hypothesized: relaxation of residual stress and electrode fracture. Investigations of these hypotheses are briefly described here, but no evidence was found linking these phenomena to non-recoverable electrode deformation.

The non-recoverable deformation observed during galvanostatic cycling was a residual *positive* strain, in contrast to the *negative* strain developed during the five-hour rest period (Fig. 3.3). For a positive residual strain to be caused by the relief of residual stress, the residual stress would have to have been compressive. However, the curvature of the electrode after solvent evaporation clearly indicates a residual tensile stress, which is typical for films formed from solvent evaporation techniques. Therefore, relief of residual stress was not the cause of the non-recoverable deformation that developed during galvanostatic cycling.

To investigate the possibility of electrode fracture, we imaged an electrode (8:1:1 wt. ratio of graphite, carbon black, and carboxymethyl cellulose (CMC)) in a scanning electron microscope before and after galvanostatic cycling at C/5 for 5 cycles. Representative images of the electrode edge are shown in Fig. 3.9. None of the images taken of the cycled electrode surface or edge showed any visual evidence of fracture.

Appendix B

Effect of Carbon Black on Electrode Conductivity

Conductive additives, such as carbon black, are typically incorporated in composite lithium-ion battery electrodes in order to increase the electrical conductivity and rate capability of the electrodes [100, 101]. While the focus of the main article was to investigate the effect of carbon black on the electrochemically-induced deformation of composite graphite electrodes, we discuss in this section the concurrent effects of carbon black on electrical conductivity.

B.1 Electrical Conductivity Measurements

Electrode conductivity tests were performed on a Pro4 four-point probe from Lucas Labs, with a probe tip spacing of 1.02 mm. Free-standing composite graphite electrodes were fabricated as described in Sec. 2.4.3. The mass ratio of graphite to carbon black was varied between 9:0 (all graphite, no carbon black) to 0:9 (all carbon black, no graphite), while the binder content was kept constant at 10 wt. % carboxymethyl cellulose (CMC). Free-standing electrodes were cut into approximately 15 x 20 mm pieces. Some electrodes with higher carbon black contents fractured during drying, and in these cases, electrode pieces small as 6 x 7 mm were used for conductivity tests. Electrode thicknesses varied from 37 µm to 125 µm for the different compositions.

Resistivity measurements were calculated according to Eqn. (B.1), where ρ_s is the sheet resistivity, I is the applied current, V is the measured voltage, and f is a multiplier based on the geometry of the sample.

$$\rho_s = \frac{V}{I} f \tag{B.1}$$

Exact expressions for the geometry factor f can be found for infinitesimally thin samples of finite in-plane dimensions or for samples of finite thickness and infinite in-plane dimensions [102–104]. However, compensating for both finite thickness and finite in-plane dimensions at the same time requires a more complicated mathematical treatment. Here, the finite thickness is treated first, and then the finite in-plane sample dimensions are taken into account.

For a sample with infinite in-plane dimensions and finite thickness, the geometry factor f is a function of the ratio of the probe tip spacing, s, and the sample thickness, w, and is tabulated in Ref. [104]. For $\frac{w}{s} = 0.4$, $f\left(\frac{w}{s}\right) = 0.9995$, and $f\left(\frac{w}{s}\right)$ approaches 1 as $\frac{w}{s}$ approaches zero. For the electrodes tested in this work, the maximum ratio of probe spacing to sample thickness was $\frac{w}{s} = 0.123$. For $\frac{w}{s} < 0.123$, the correction factor is unity ($f(\frac{w}{s} \leq 0.123)$=1).

Therefore, the samples were considered to be have infinitesimal thickness compared to the probe spacing, and no correction was performed for finite thickness.

For a rectangular sample of infinitesimal thickness and finite in-plane dimensions, the geometry factor f is defined according to Eqn. (B.2) [104],

$$f\left(\frac{a}{d},\frac{d}{s}\right) = \pi\left\{\frac{\pi}{d/s} + \ln\left[1-\exp\left(\frac{-4\pi}{d/s}\right)\right] - \ln\left[1-\exp\left(\frac{-2\pi}{d/s}\right)\right] + \sum_{m=1}^{\infty} a_m\right\}^{-1} \tag{B.2a}$$

$$a_m = \frac{1}{m}\exp\left[\frac{-2\pi(a/d-2)m}{(d/s)}\right]\frac{\left[1-\exp\left(\frac{-6\pi m}{d/s}\right)\right]\left[1-\exp\left(\frac{-2\pi m}{d/s}\right)\right]}{\left[1+\exp\left(-2\pi m a/d\right)\right]} \tag{B.2b}$$

where a and d are the two in-plane dimensions and s is the probe tip spacing. In this work, correcting for finite in-plane dimensions reduced the uncorrected sheet resistivity calculations by an average of 3.8 %, with a maximum reduction of 13.2 % for the smallest sample.

The electrode conductivity, σ, is calculated from the corrected sheet resistivity, ρ_s, and the sample thickness, w, according to Eqn. (B.3),

$$\sigma = \frac{1}{w\rho_s} \tag{B.3}$$

B.2 Conductivity Results

Fig. B.1 shows the variation of electrode conductivity as a function of graphite and carbon black content. Electrodes containing only graphite and binder (no carbon black) had a conductivity of approximately 1 S cm^{-1} (point I). As the mass fraction of carbon black is increased, the conductivity of the electrode at first increases (region II), reaches a maximum conductivity of approximately 18 S cm^{-1} at 30 wt % carbon black (point III), and then gradually decreases and plateaus to approximately 8 S cm^{-1} (region IV). These values are of the same order of magnitude as those measured by Striebel et al. [105].

The conductivity of a composite graphite electrode is governed by both the intrinsic conductivities of the constituents as well as the microstructure of the composite [106]. The intrinsic conductivity of natural graphite crystals is approximately 28,000 S cm^{-1} parallel to the basal planes and in the range of 150-230 S cm^{-1} perpendicular to the basal planes [107]. While there are no reported values for the intrinsic conductivity of a single particle of carbon black, several studies have investigated the conductivity of conductive powders as a function of compression pressure, or equivalently, of density or volume fraction of the compressed powder. Values from these studies suggest that compacted graphite powder has a bulk conductivity of approximately 20 S cm^{-1} [108, 109] while carbon black has a bulk conductivity of 0.06 S cm^{-1} [108] to 5 S cm^{-1} [109]. These values lead to the conclusion that carbon black has a lower bulk conductivity than graphite.

The influence of microstructure is highlighted in Fig. B.2. In an electrode with no carbon black, the conductivity is limited by the contact area of the graphite particles, indicated by red lines in Fig. B.2(a). As carbon black is added, it fills in the interstitial regions between the graphite particles, increasing the contact area and therefore also increasing the composite

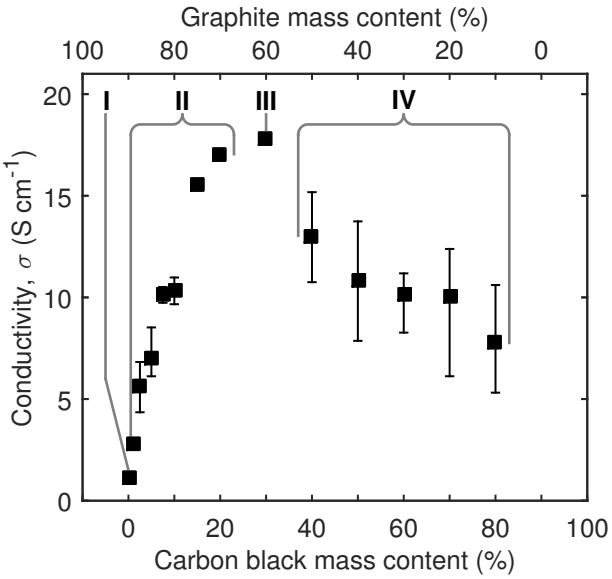

Figure B.1: Conductivity of graphite composite electrodes as a function of graphite to carbon black ratio. All electrodes contained 10 wt. % CMC binder.

electrode conductivity (Fig. B.2(b)). A maximum conductivity is reached when a complete percolation network is formed (Fig. B.2(c)). With the addition of more carbon black, there is a phase inversion and the electrode microstructure is that of a matrix of carbon black with isolated graphite particles (Fig. B.2(d)), and the lower intrinsic conductivity of carbon black dominates the composite electrode conductivity.

B.3 Effect of Electrode Conductivity on Electrochemical Response

The effect of carbon black content on electrochemical and mechanical behavior of graphite composite electrodes is depicted in Fig. B.3. Electrode composition is denoted as X:Y:Z, the mass ratio of graphite (G), carbon black (CB), and carboxymethyl cellulose (CMC). The voltage plateaus, which indicate phase transitions in graphite-lithium intercalation compounds (G-LICs) during lithiation and delithiation, are not as apparent in the 9:0:1 electrode (graphite and CMC, no carbon black) cycled at C/5 (Fig. B.3(a)) as they are in the 8:1:1 electrode (Fig. B.3(c)) and the 6:3:1 electrode (Fig. B.3(d)) . It is believed that the decreased electrical conductivity of the 9:0:1 electrode (1 S cm^{-1}) compared to the 8:1:1 and 6:3:1 electrodes (10 S cm^{-1} and 18 S cm^{-1} respectively) limited the rate performance of the 9:0:1 electrode. Indeed, when a 9:0:1 electrode was cycled more slowly at C/20 rate, the characteristic voltage plateaus were recovered (Fig. B.3(b)). The 0:9:1 electrode (carbon black and CMC, no graphite) shows the smooth voltage profile characteristic of lithium intercalation into carbon black (Fig. B.3(e)), where the disordered structure of carbon black suppresses stage formation.

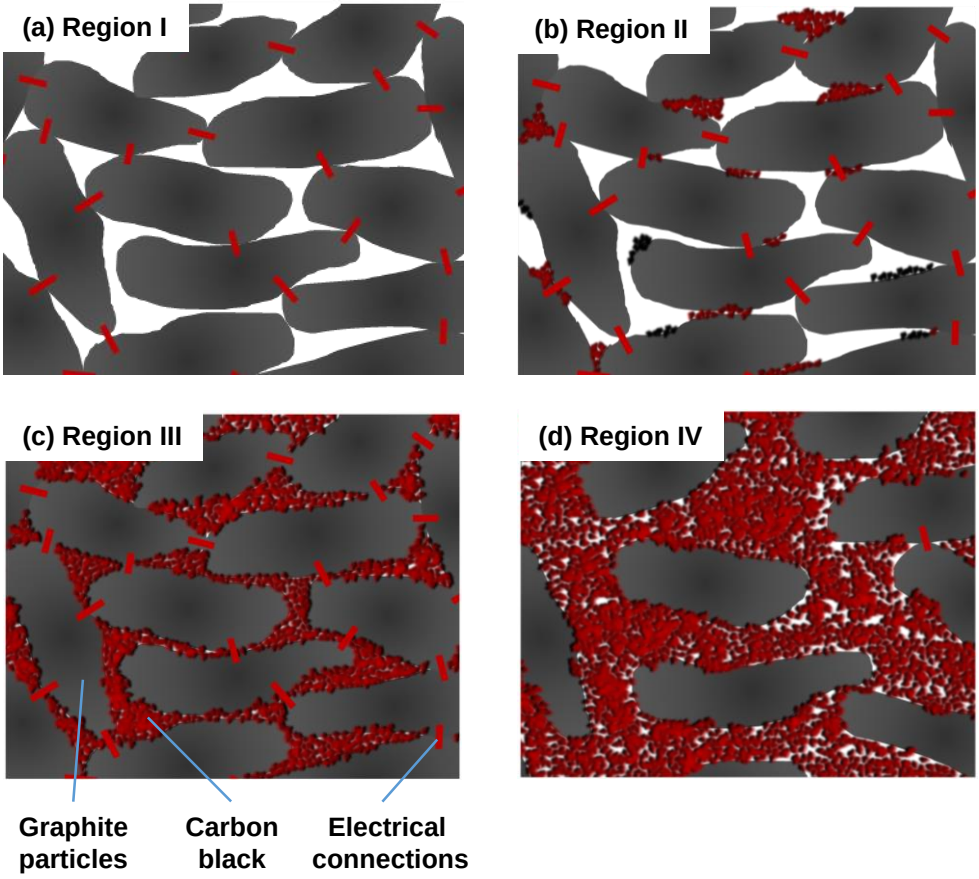

Figure B.2: Schematic of electrode microstructure with varying ratios of graphite to carbon black. (a) No carbon black. Contact area of conductive network is limited to graphite particle contact, represented by red lines. (b) Contact area is increased with addition of carbon black. (c) Contact area is maximized. (d) Electrode structure is inverted to contain graphite particles within a carbon black matrix. Conductivity is limited by lower intrinsic conductivity of carbon black. Region I - Region IV refer to the conductivity regimes in Fig. B.1.

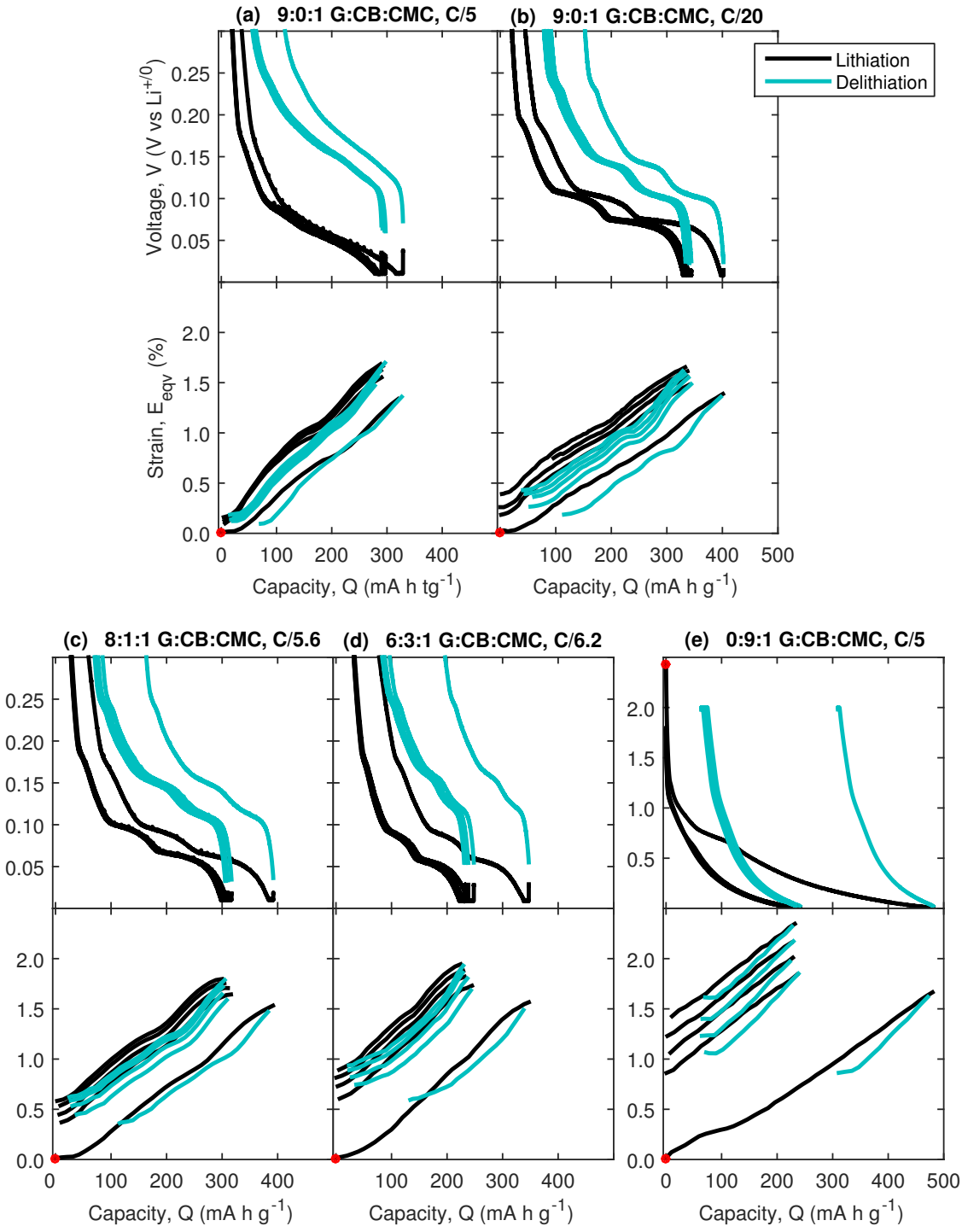

Figure B.3: Electrochemical and strain response of graphite composite electrodes of varying composition cycled galvanostatically at various rates. The titles denote the composition as the mass ratio of graphite (G), carbon black (CB), and carboxymethyl cellulose (CMC) binder, as well as the cycling rate, normalized by the combined mass of graphite and carbon black.

Appendix C

Supplementary Information on Vinylene Carbonate Study

In order to investigate the different irreversible behaviors of graphite electrodes, we performed linear sweep voltammetry on graphite electrodes comprised of 8:1 wt. ratio graphite and CMC binder. Since the electrodes contained no carbon black, the dominating electrochemical reactions at voltages greater than approximately 0.3 V vs $Li^{+/0}$ should have been the reduction of electrolyte solvents. Prior to sweeping the electrode potential, the electrodes were allowed to rest for 24 hours to ensure they were at mechanical equilibrium. During this rest period, the strain varied by less than 0.01 %. Therefore, any strain measured during the voltage sweep that was less than +/- 0.005 % was within the noise and was not significant. The current, capacity, and strain responses of the electrodes during the voltage sweep are presented in Fig. C.1.

The expected reduction potential of VC is ca. 1.0 - 1.2 V vs $Li^{+/0}$, which is above the expected reduction potential of EC (ca. 0.8 V vs $Li^{+/0}$) [75, 77, 78]. While a clear peak was observed in the current response in Fig. C.1a at 0.8 V indicating EC reduction, there was no peak near 1.0 V corresponding to VC reduction, even in the ternary electrolyte that contained VC as a primary solvent. It is unclear at this time why the peak corresponding to VC reduction was not present.

The strain measurements during the linear sweep voltammetry did not follow a clear trend with respect to VC concentration. Both electrodes tested in 2.0 wt.% VC contracted slightly at higher voltages (above ca. 0.8 - 0.9 V), though only one of these contractions was outside of the noise window. Additionally, the strain responses from both tests both crossed the upper noise boundary at ca. 0.6 - 0.7 V. In contrast, electrodes cycled in electrolyte containing 10.0 wt.% VC or in the ternary electrolyte formula showed no contraction, and they crossed the upper noise boundary at a higher voltage of ca. 1.0 - 1.3 V. However, one of the control tests cycled in electrolyte without VC behaved similarly to the electrodes cycled in electrolyte containing 2.0 wt.% VC while the other control test behaved similarly to the electrodes cycled in higher concentrations of VC. Thus, the differences observed appear to result from experimental variation and cannot be attributed to different VC concentrations in the electrolyte.

In a second set of tests, we held the potential of the electrodes constant at 0.9 V for 48.5 hours and then at 0.5 V for an additional 48.5 hours. The current, capacity, and strain responses are shown in Fig. C.2. Because VC should reduce below 1.0 - 1.2 V but EC should not reduce until below 0.8 V, we expected a larger current to develop in the electrodes held in electrolyte containing VC during the 0.9 V step compared to electrodes held in electrolyte without VC. Additionally, we expected a larger strain response, indicating the deposition of VC decomposition products on the electrode surface. However, the current, capacity, and strain responses of the two electrodes during both voltage hold steps was nearly identical.

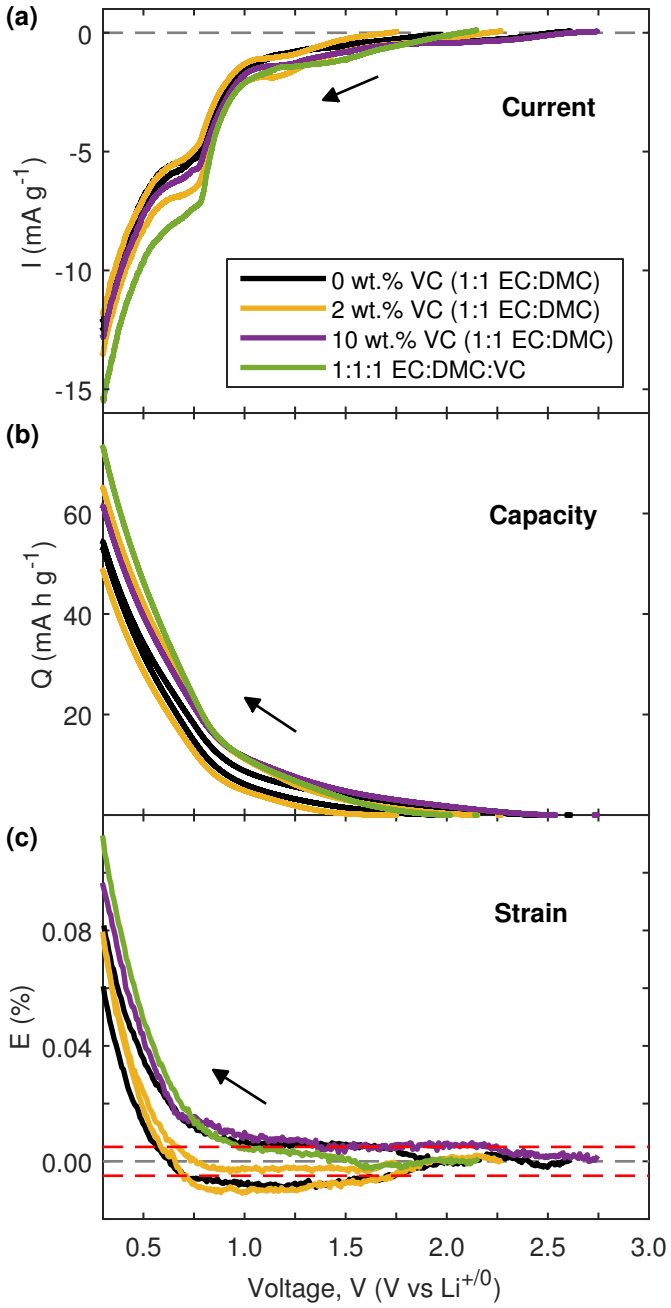

Figure C.1: Strain induced in graphite composite electrodes by electrolyte decomposition during linear sweep voltammetry in different compositions of electrolyte. The electrodes had compositions of 8:1 wt. ratio of graphite and CMC binder. The working electrode voltage was swept linearly from the open circuit voltage to 0.3 V vs $Li^{+/}$ at 25 µV s^{-1}. Two tests are shown for the 0 wt.% VC electrolyte and the 2 wt.% VC electrolyte, while one test is shown for the 10 wt.% VC electrolyte and the ternary electrolyte. (a) Current, (b) capacity, (c) strain. In (c), the red dashed lines at +/- 0.005 % strain mark the noise thresholds. Any strains within this region are not significant.

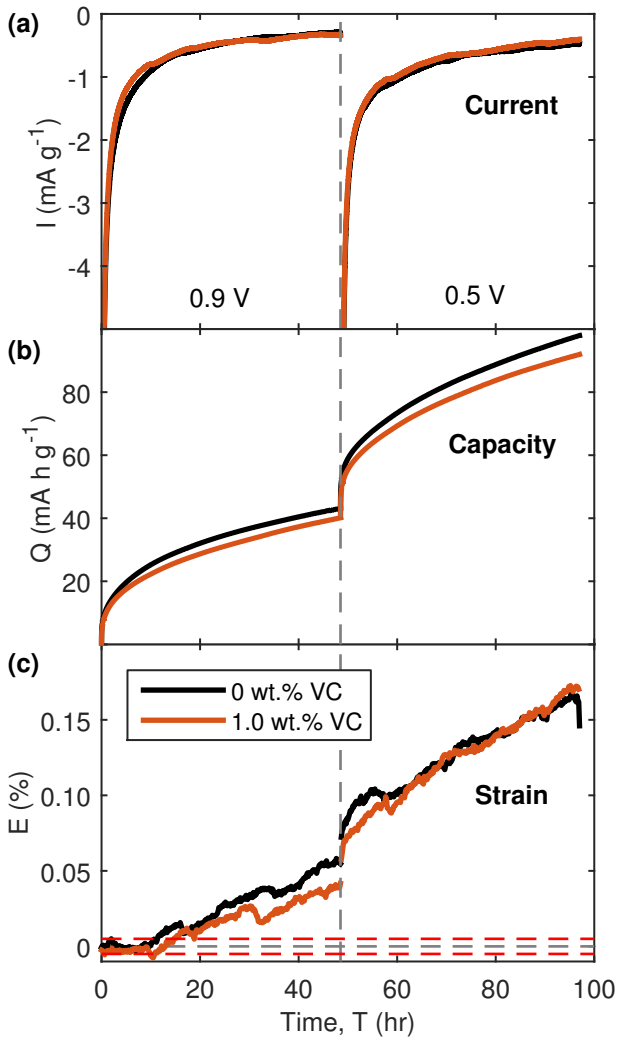

Figure C.2: Electrochemical and mechanical response of graphite composite electrodes during a two-stage potentiostatic voltage hold. The electrodes had compositions of 8:1 wt. ratio of graphite and CMC binder and were held at 0.9 V vs $Li^{+/0}$ for 48.5 hours and then held at 0.5 V vs $Li^{+/0}$ for an additional 48.5 hours. (a) Current, (b) capacity, (c) strain. In (c), the red dashed lines at +/- 0.005 % strain mark the noise thresholds. Any strains within this region are not significant.

Theoretical studies have shown that decomposition mechanisms of EC and VC are complicated and highly intertwined [79–81] (see Appendix A). Thus, we believe that our initial expectation that VC would reduce first below ca. 1.0 V followed sequentially by EC reduction below ca. 0.8 V was too simplistic. Therefore, the experiments described here are insufficient to distinguish differences in the initial SEI layer formed in electrolytes with and without VC. However, differences in the SEI layers formed in different electrolytes are observed during the relatively long-term galvanostatic cycling results presented in Sec. 4.4.2.

Appendix D

Supplementary Information for Electrochemical Stiffness Study*

*Significant portions of this chapter will be submitted as H. Tavassol#, E. M. C. Jones#, N. R. Sottos, A. A. Gewirth. *Nature Mater.* (2015), #Equal contribution authors. The studies presented in this chapter were done in close collaboration with Dr. Hadi Tavassol during his graduate studies under Professor Andrew Gewirth in the Department of Chemistry at the University of Illinois at Urbana-Champaign.

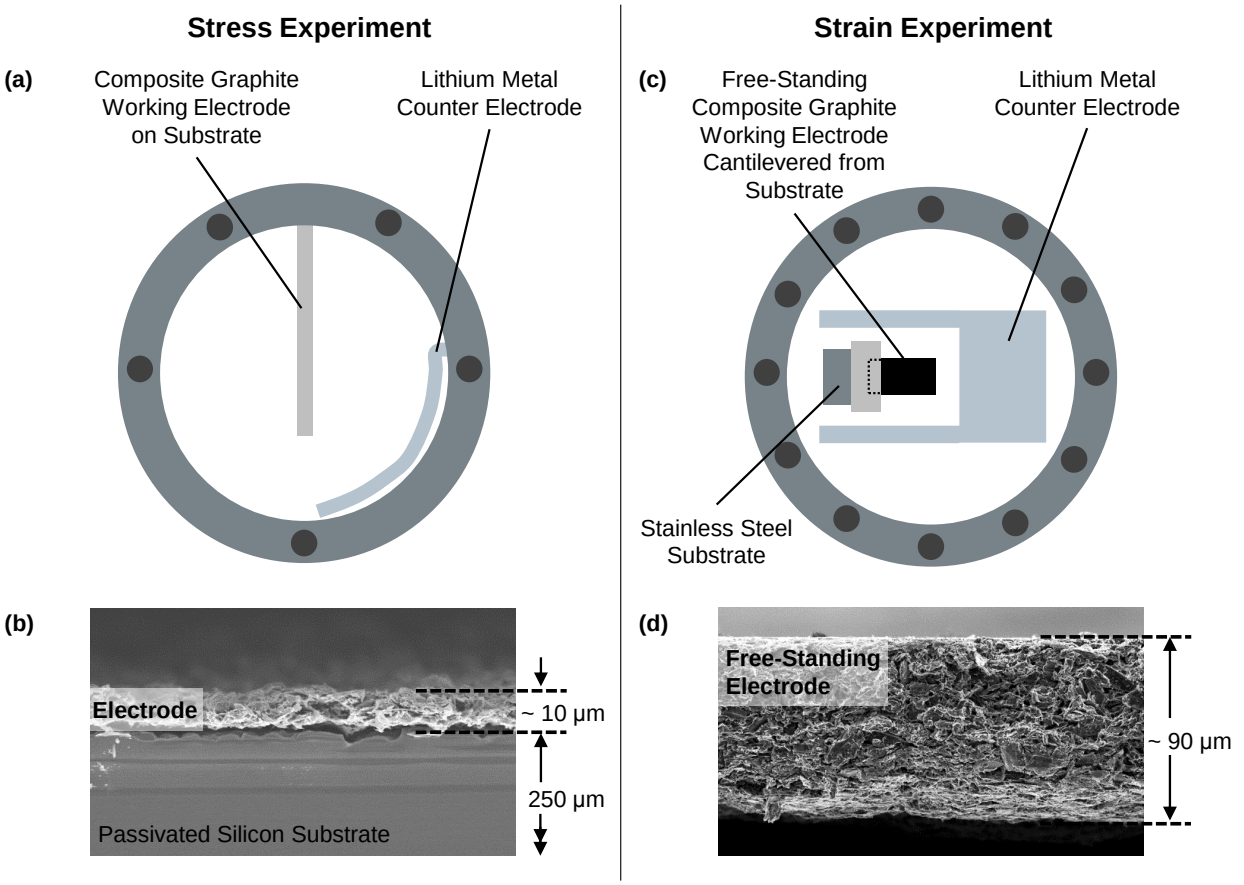

Figure D.1: Custom battery cells for *in situ* stress and strain measurements. (a) Front view of custom battery cell and (b) scanning electron micrograph of the graphite composite electrode on a silicon wafer substrate used in the stress experiment. (c) Front view of custom battery cell and (d) scanning electron micrograph of the free-standing composite graphite electrode used in the strain experiment.

D.1 Electrode Fabrication

Electrode slurry comprised of graphite, carbon black, and carboxymethyl cellulose (CMC) binder in water was prepared as described previously (Sec. 2.4.3). Electrode slurries were prepared with either a 1:100 wt. or a 1:200 wt. ratio of CMC in water for electrodes for strain measurements and stress measurements, respectively. The final electrode composition was 80 wt. % graphite, 10 wt. % carbon black, and 10 wt. % CMC.

Electrodes for stress measurements were fabricated on the unpolished side of a silicon wafer (University Wafers, (100) orientation, 250 µm thick), which had previously been cleaned with acetone. The silicon wafer had a 200 nm thick thermally-grown oxide layer which electrically isolated the wafer. The graphite layer was approximately 10 µm thick (Fig. D.1(b)), and the wafer was cut into 5 x 25 mm rectangular pieces. Typical graphite loading was approximately 2 mg. Cutting the wafer into cantilever beams exposed unpassivated silicon at the edges of the cantilever. The effect of exposed, unpassivated silicon at the edges of the cantilever is discussed in Sec. D.5.

Electrodes for strain measurements were fabricated as described previously (Sec. 2.4.3), creating a free-standing electrode 90-100 µm thick (Fig. D.1(d)). The electrode was cut into 3 x 7 mm rectangular pieces. Typical graphite loading was 1.2-2.0 mg.

D.2 Electrochemical Cycling

Composite graphite working electrodes were cycled against a lithium metal counter electrode in a carbonate-based electrolyte (1M $LiClO_4$ in a 1:3 vol. ratio mixture of ethylene carbonate and dimethyl carbonate). Stress and strain measurements were performed in independent custom battery cells, as shown schematically in Fig. D.1(a,c). The custom battery cells were assembled and sealed in an argon atmosphere prior to measurements.

Cyclic voltammetry (CV) was performed between 1 V and 0.01 V vs $Li^{+/0}$ at scan rates of 100 µV s^{-1}, 25 µV s^{-1} and 10 µV s^{-1} for three cycles. As each cycle took 22.2 hours to complete, bleaching of the fluorescent particles utilized during the strain measurements prevented longer cycling. Galvanostatic measurements (GS) were performed at C/5 rate, between 2 V and 0.01 V vs $Li^{+/0}$, for five cycles. Electrochemistry utilized an Arbin potentiostat / galvanostat for the strain measurements, and a CHI 760D instrument for stress measurements.

D.3 Stress and Strain Measurements

The stress-thickness (f) developed in the constrained electrode during electrochemical cycling was calculated from cantilever curvature changes using an optical setup [47]. Stress values, σ, were calculated by normalizing the stress-thickness values by the thickness of the graphite electrode layer ($t_e = 10$ µm) as $\sigma = \frac{f}{t_e}$. All stress-thickness values and stress values reported are changes in the values relative to the initial stress state of the pristine, as fabricated electrode, which was unknown. The strain developed in the unconstrained electrode, E, during electrochemical cycling was measured by using digital image correlation

(DIC), as described in Sec. 2.4.7. At the macroscopic length scale (ca. 2-4 mm), the composite electrode response was considered a homogeneous, isotropic average of the individual, anisotropic particle responses. The macroscopic stress state of the constrained electrode was therefore bi-axial compression or tension, and the average stress along the long axis of the cantilever is reported. The unconstrained electrode underwent free expansion and contraction isotropically, and the average strain along a line perpendicular to the long axis of the electrode is reported.

D.4 Synchronization of Stress and Strain Data

D.4.1 Cyclic Voltammetry

A comparison between the current response in the stress experiment and the current response in the strain experiment during cyclic voltammetry at 25 µV s^{-1} is presented in Fig. D.2. A

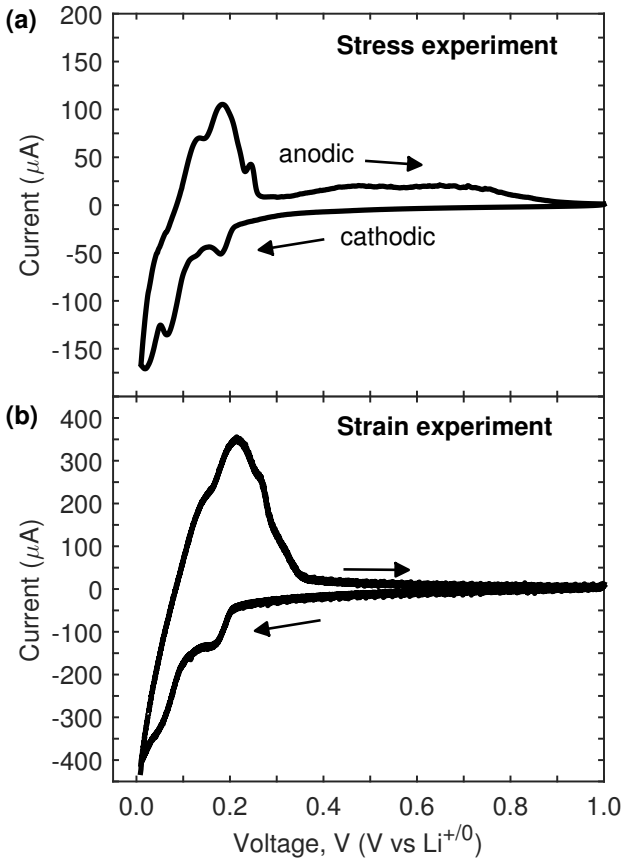

Figure D.2: Comparison of electrochemical behavior during cyclic voltammetry (CV). Current response of a graphite composite electrode cycled in the custom battery cell used for (a) the stress experiments and for (b) the strain experiments, during the third cycle of cyclic voltammetry at 25 µV s^{-1}.

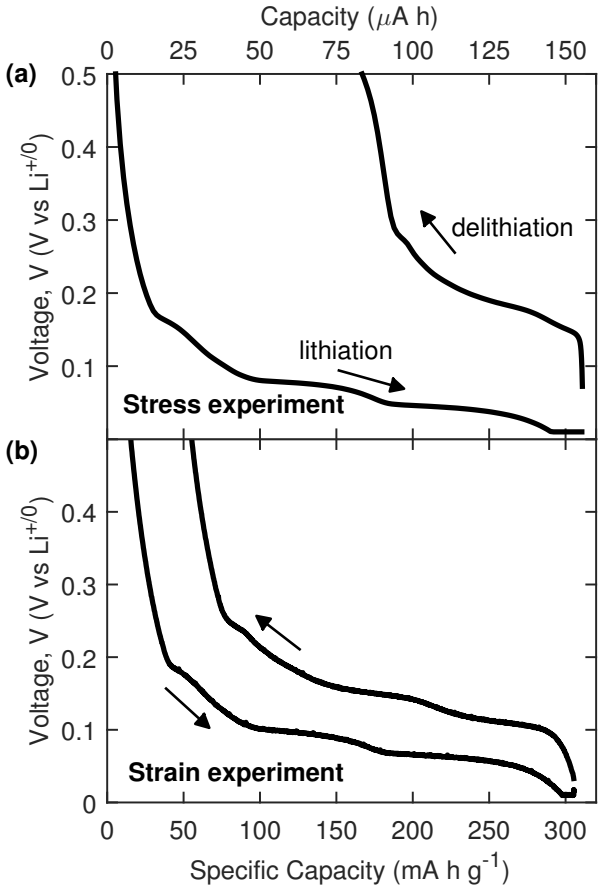

Figure D.3: Comparison of electrochemical behavior during galvanostatic (GS) cycling. Voltage response of a graphite composite electrode cycled in custom battery cells used for the (a) stress experiment and for the (b) strain experiment, during the fifth cycle of galvanostatic cycling at C/5 rate.

larger voltage hysteresis between the cathodic and anodic sweeps in conjunction with less distinct peaks in the current response from the strain experiment are possibly indicative of greater heterogeneity and/or geometric differences in the electrode used for the strain experiment compared to that used for the stress experiment. To account for differences in the electrochemical responses, the solution resistance of both cells was estimated using electrochemical impedance spectroscopy (EIS). A copper foil working electrode was used in place of the graphite composite electrode to isolate the solution resistance from electrical resistance of the graphite electrode. EIS was performed on a Biologic potentiostat between 675 kHz and 0.5 Hz frequencies. The solution resistance, taken as the real part of the measured impedance when the imaginary part of the impedance was zero, was determined to be 26 Ohm for the stress experiment cell and 57 Ohm for the strain experiment cell. The corrected voltage, V, was then calculated according to $V = V_{org} - I\Omega$, where I is the measured current during CV, Ω is the solution resistance measured in EIS, and V_{org} is the original, uncorrected voltage. The stress and strain data from the two independent experiments were then correlated using the corrected voltage.

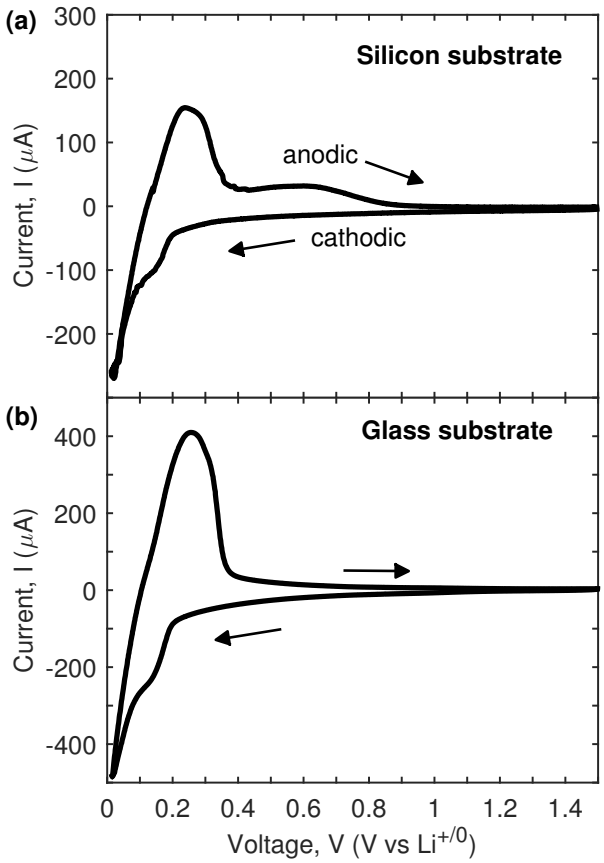

Figure D.4: Effect of substrate material on electrochemical measurements. Current response during cyclic voltammetry at 100 µV s^{-1} of a graphite composite electrode on a (a) silicon substrate or on a (b) glass substrate, cycled in the custom battery cell used for the stress measurements.

D.4.2 Galvanostatic Cycling

A comparison of the voltage responses as a function of capacity from the galvanostatic stress experiment and the strain experiment is presented in Fig. D.3. The electrochemical response during lithiation is remarkably similar between the two independent experiments, as exemplified by the distinct voltage plateaus. The high voltage observed during delithiation in the stress experiment is similar to the anodic current developed during CV at ca. 0.30.9 V, and is attributed to side reactions occurring at the exposed silicon wafer edge. An accurate measure of the mass of the electrode in the stress experiment could not be obtained; therefore, to synchronize the two experiments, we assumed the electrodes in each experiment achieved the same specific capacity at the end of the lithiation portion of the cycle, and scaled the capacity from the stress experiment accordingly. Stress and strain experiments were then correlated through the corresponding capacity values.

D.5 Anodic Sweep of Cyclic Voltammetry

The third cycle CV and the corresponding stress and strain measurements of a graphite composite electrode at a scan rate of 25 μV s^{-1} are shown in Fig. 5.2. The cathodic sweep is discussed in Sec. 5.3. The features observed during the anodic sweep between 0.01 V and 0.3 V correspond to phase transitions between graphite-lithium intercalation compounds (G-LICs) as lithium is removed from the graphite electrode. The small anodic current present in the higher voltage region (0.3 V0.9 V) is indicative of side-reactions that occurred at the exposed silicon substrate edge of the cantilever (Sec. D.1). These side reactions were not present when the graphite electrode was cycled on a glass substrate, as shown in Fig. D.4.

During the anodic sweep, the compressive stress developed during the cathodic sweep is first relieved, reaches a local maximum at ca. 0.2 V, and then slowly decays to the original value at the start of the cycle. The overshoot of the stress relaxation at 0.2 V is hypothesized to result from non-uniform delithiation of the graphite film across the film thickness as its magnitude is scan rate dependent (Fig. 5.6(b)). Expansive strain continues to develop until ca. 0.05 V during the anodic sweep while the current remains negative and the graphite is still being lithiated. At higher potentials, contraction is observed as delithiation of the graphite anode occurs. The rate of contraction decreases substantially at ca. 0.24 V, following the de-intercalation of the main G-LICs. Because the stress overshoot at ca. 0.2 V dominates the stress response of the electrode during the anodic sweep, we focus our discussion in Ch. 4 on the cathodic portion of the cyclic voltammetry.

D.6 Identification of G-LICs

Similar to Sec. 3.2, voltage values at which transitions occur between different graphite-lithium intercalation compounds (G-LICs) are identified by comparing features in the electrochemistry data in this work with the results from Dahn et al. [4, 5]. These values are tabulated in Table D.1 and are represented graphically by colored regions in the figures.

Table D.1: Voltage values associated with specific phase transitions between graphite-lithium intercalation compounds (G-LICs) during the cathodic / lithiation portion of the cycle.

Transition	**Voltage (V vs $Li^{+/0}$)**		
	Galvanostatic Cycling[#] (C/80, C/800)	Cyclic Voltammetry[†] (25 μV s^{-1})	Galvanostatic Cycling[†] (C/5)
DI → IV	0.20	0.18	0.18
III → DII	0.13	*	*
DII → II	0.11	0.07	0.10
II → I	0.06	0.02	0.06

[#]Dahn et al. [4, 5]; [†]This work.

[*]No features were able to be identified for the III → DII transition in this work.

D.7 Absolute Magnitude of Electrode Stiffness

Fig. D.5(a) presents the normalized potential-dependent stiffness of graphite electrodes during the third cycle of cyclic voltammetry (CV) at 25 μV s^{-1}. Results are shown for two independent data sets. Similarly, Fig. D.5(b) presents two independent data sets for the normalized capacity-dependent stiffness of graphite electrodes during the fifth cycle of galvanostatic cycling (GS) at C/5 rate. The absolute magnitudes of the stiffness at the beginning of the cycles are tabulated in Table D.2. Though the absolute magnitude of the stiffness varied between different tests, the potential-dependent and capacity-dependent trends of the stiffness were repeatable.

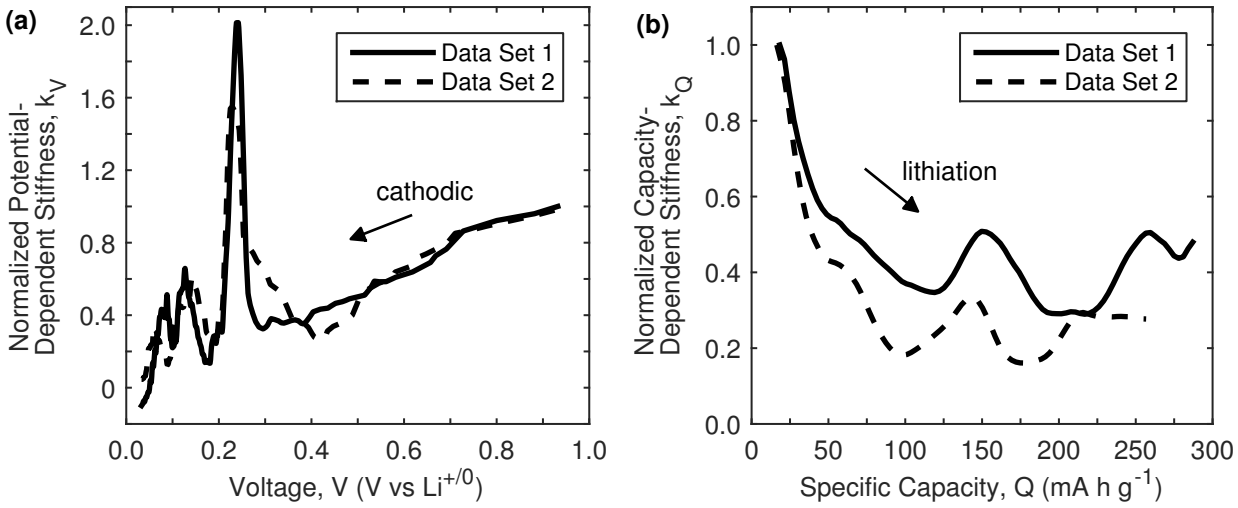

Figure D.5: Comparison of electrochemical stiffness variations of multiple experiments. (a) Two independent data sets of the normalized potential-dependent stiffness of graphite electrodes during the third cycle of cyclic voltammetry at 25 μV s^{-1}. (b) Two independent data sets of the capacity-dependent stiffness of graphite electrodes during the fifth cycle of galvanostatic cycling at C/5 rate.

Table D.2: Electrochemical stiffness values at the beginning of the third cycle of CV and fifth cycle of GS cycling.

	Potential-Dependent Stiffness, k_V (GPa)
Data Set 1 (Fig. 5.3(b))	9.4
Data Set 2	2.6
	Capacity-Dependent Stiffness, k_Q (GPa)
Data Set 1 (Fig. 5.5(e))	1.8
Data Set 2	2.6

Appendix E

Mechanical Behavior of Silicon Electrodes with Dynamic Bonding*

One source of mechanical degradation of particulate-composite electrodes is debonding between particles of active material and polymer binder, which can result in electrical isolation of active material particles and decreased capacity [110]. Possible solutions include increasing the strength of the polymer / particle bond, increasing the compliance of the polymer (to allow for large extension of the polymer), and designing a reversible polymer / particle bond that can be broken and reformed as the particles of active material expand and contract [56, 110–112].

Through a collaboration with Dr. Sen Kang, the effect of tailored polymer binders on the strain response of silicon composite electrodes was investigated. Kang previously developed an electrode system based on reversible ionic bonding between functionalized silicon nanoparticles and poly(acrylic acid) (PAA) binder (Fig. E.1). This system showed increased capacity retention compared to control electrodes fabricated without functionalized silicon that did not have reversible bonding capabilities [113]. Kang hypothesized that as the silicon particles expanded, contracted, and underwent rigid body motion during cycling, the ionic bonds were broken and reformed at new sites. This reversible bonding was hypothesized to allow for large deformation of the electrode on the macroscale without electrically isolating silicon particles.

To test this hypothesis, we cycled the functionalized nano-Si / PAA electrodes galvanostatically in the custom battery cell and concurrently imaged the electrodes. Fig. E.2 shows the electrochemical data from two tests, at C/100 and C/20 rates, and select images of the electrodes at different points during the cycling. During the initial lithiation, the electrodes at first curled and then subsequently developed cracks. In one of the electrodes (Fig. E.2a), the cracks reached a steady size and did not grow with continued cycling. Despite the apparent plateau in visible damage, this electrode had negligible capacity retention for cycles 5-9. In the other electrode (Fig. E.2b), a crack propagated through the entire width of the electrode during the second lithiation, causing a large portion of the electrode to become completely unattached from the battery circuit. Despite this significant mechanical failure, the electrode maintained 150 - 200 mA h g^{-1} capacity, based on the mass of the complete electrode, or approximately 600 mA h g^{-1} capacity, based on the estimated remaining mass after the fracture, during cycles 5-10.

The fracture of the functionalized nano-Si / PAA electrodes conflicts with our original hypothesis that reversible, ionic bonding allowed for larger deformation while still maintaining

*The study presented in this Appendix was performed in collaboration with Dr. Sen Kang during her graduate studies under Professor Nancy Sottos in the Department of Material Science and Engineering at the University of Illinois at Urbana-Champaign.

mechanical integrity. Instead, we observed macroscale fracture in the unconstrained portion (i.e. away from the spot welds) of the functionalized nano-Si / PAA electrodes. These results suggest that another mechanism other than improved mechanical integrity though reversible bonding governs the improved capacity retention that Kang measured with the functionalized nano-Si / PAA electrodes. However, such a mechanism has not been identified at this time.

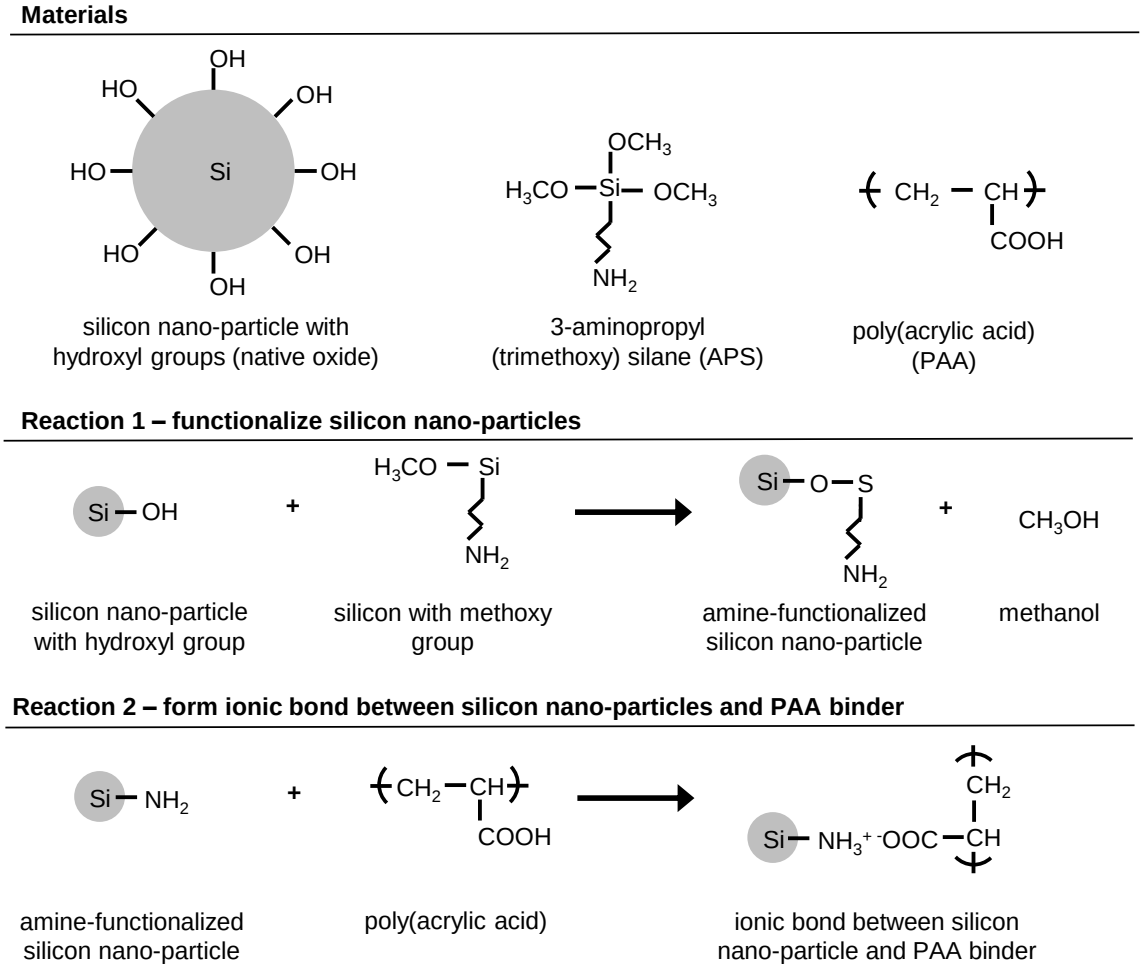

Figure E.1: Proposed scheme to create a network of reversible ionic bonds between silicon nano-particles and poly(acrylic acid) polymer binder. Reaction 1: Silicon nano-particles are functionalized with an amine group by reacting the hydroxyl group from the native oxide of the silicon with the methoxyl group from 3-aminopropyl(trimethoxy)silane (APS). Reaction 2: During the fabrication of an electrode with amine-functionalized silicon nano-particles and poly(acrylic acid) (PAA), a hydrogen is donated from the PAA side chain to the amine group, giving the silicon particles a positive charge and the PAA binder a negative charge. Thus, the positively-charged silicon particles will bond ionically to the negatively-charged binder.

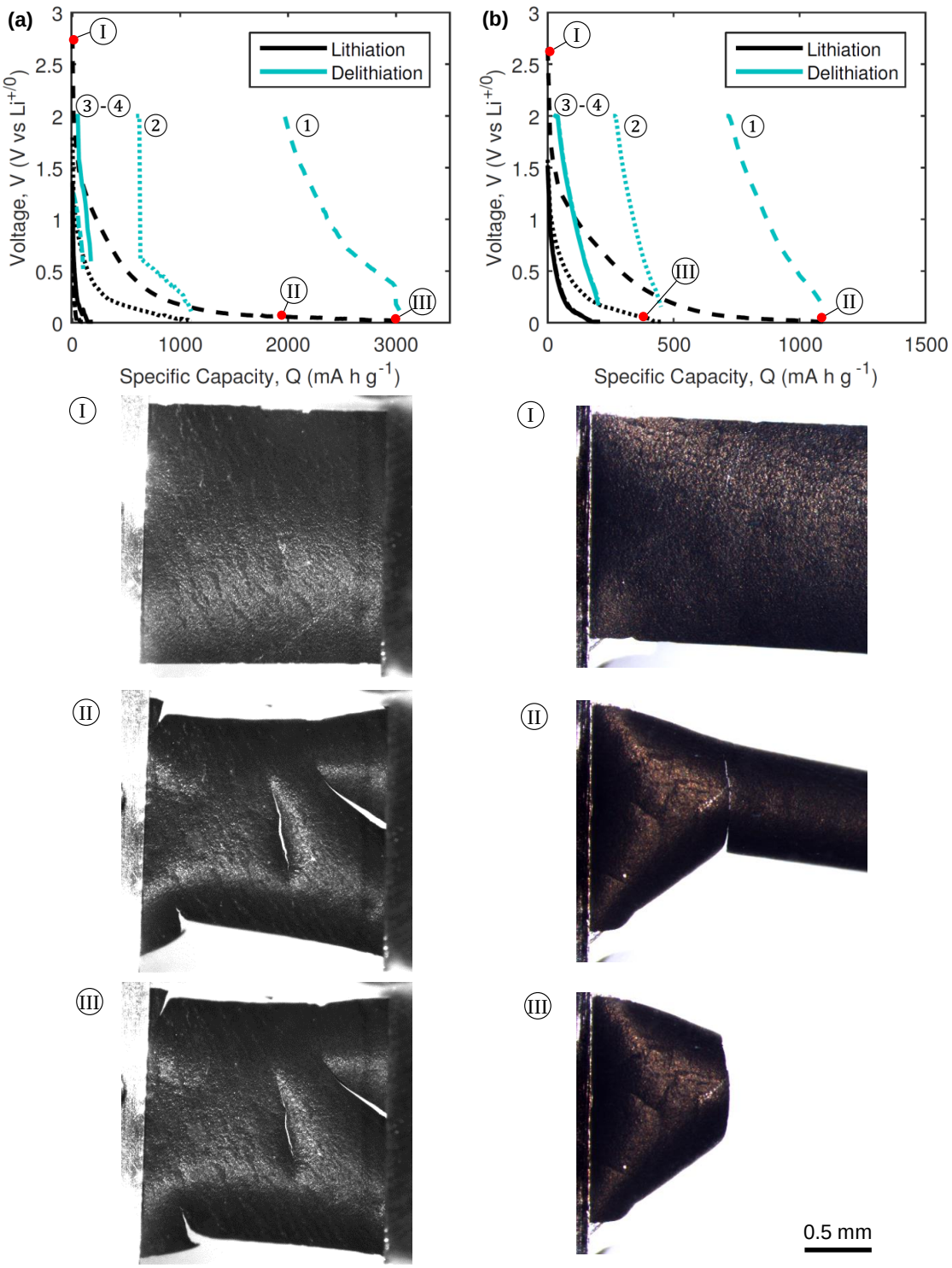

Figure E.2: Electrochemical and mechanical responses of functionalized nano-Si electrodes. The electrodes had compositions of 1:1:1 wt. ratio of functionalized nano-Si, carbon black, and PAA binder and were cycled galvanostatically for 9 cycles (only cycles (1)-(4) are shown for clarity). (a) C/100 rate and (b) C/20 rate. Circled numbers indicate the cycle number. Roman numerals indicate the location of the select images.

Appendix F

Documentation for Matlab-Based Digital Image Correlation Code

F.1 Introduction

This chapter describes a Matlab-based code that performs digital image correlation (DIC). This DIC code is based on code written by Christoph Eberl *et al.* at the John Hopkins University. The original code and documentation can be found on Matlab's File Exchange: http://www.mathworks.com/matlabcentral/fileexchange/12413. The current code has been heavily modified by the current author, Elizabeth Jones. The current code can be found on Matlab's File Exchange: http://www.mathworks.com/matlabcentral/fileexchange/43073-improved-digital-image-correlation--dic-. The author requests that users of this code notify the author of any modifications, improvements, or adaptations they make to this code, so that such modifications can be addressed and possibly incorporated in future versions of this code.

This chapter assumes that the reader has a basic knowledge of Matlab and of the digital image correlation process. The purpose of this chapter is to describe the code so that the reader can use the code to obtain displacements and strains from their own experiments and modify the code as necessary.

The accuracy and precision of the code was evaluated using the test images from the DIC Challenge (https://www.sem.org/dic-challenge/), conducted under the auspices of the Society of Experimental Mechanics (SEM). A complete evaluation of the code is provided in Appendix G.

F.2 Updates

F.2.1 Version 4

Version 4 fixes an error concerning plotting contour plots of displacements and strains over a background image. In previous versions of the code, if the user set the "Image skip" parameter in the *image_setup_GUI* to something other than "1", and then visualized the correlated data as a contour plot over background images, the image in the background did not correspond to the data. For instance, if there were 5 images total and the "Image skip" was set to "2", then images 1, 3, and 5 would be correlated; however, the contour plots would be plotted over images 1, 2, and 3. This issue has been rectified, so that now, the correlated data is plotted over the correct background images.

Version 4 also fixes an error that occurred when plotting a strain contour plot over the deformed grid.

An improvement was made concerning the correlation of reduced images. Previously, control points in the reduced grid that did not correlate resulted in no initial guess for nearby control points in the full grid during the correlation of the full images. Now, the displacements from the reduced correlation and interpolated / extrapolated over any points that did not correlate, so that all control points in the full grid will have an initial guess. This change requires that the user have the function *scatteredInterpolant*, which may not be available for earlier releases of Matlab (ca. before R2014b). If a large region of the reduced grid control points did not correlate (e.g. because the displacements were too large in one region of the image), the user may consider running the correlation of reduced images a second time, using the input from the first reduced correlation as initial guesses for the second reduced correlation, before correlating the full images. Concurrent with this change, *visualize_data_GUI* has been updated to allow the user to see either the raw or the interpolated reduced displacements.

F.2.2 Version 3

Version 2 of this code contained an error involving smoothing the displacements after deleting some grid points using the *delete_data_GUI*. Specifically, the following error would arise if two or more complete rows of grid points were deleted from the bottom of the region of interest:

Error using smooth_moving_average_V2>smooth_moving_average_loop (line 187)
Index exceeds matrix dimensions.

This error was related to a typographical error in the function *pad_disp_setup*. In Version 2, line 66 erroneously read:

Btemp = find(ind_col == B);

In version 3, this line was corrected to read:

Btemp = find(ind_row == B);

F.2.3 Version 2

Version 2 of this code contains the following updates:

Matlab Version and OS

Version 2 of the code has been tested and is compatible with Matlab versions R2012b and R2014b running on a PC with 64-bit Windows 7 Professional.

Correlation of the Images

- To more accurately reflect the algorithm used in the code and to be consistent with other DIC codes, the subset size was adjusted to accept only odd values . Previously, the code accepted only even values of the subset, but the actual subset cropped from the image around each control point was one pixel larger than the subset size entered in the *correlate_images_GUI*. That is, if a subset size of 20 was entered in the GUI, the code actually cropped a subset of pixels around the control point that was 21 x 21 pixels. Now, the cropped subset is exactly the size requested in the GUI.

- Fixed a bug concerning correlating images using the preceding image as a reference image and using initial guesses from the correlation results of reduced images. Previously, initial guesses generated by the correlation of reduced images were calculated with respect to the first image only. Now, they are calculated with respect to the correct reference image, either the first image or the preceding image, depending on the correlation mode of the full images.

- Added the option to control the threshold of the correlation coefficients for both reduced and full correlations.

- Added the option to control the search zone for both the reduced and full correlations.

- The values of the correlation coefficients are saved as the variable *corr_coeff_reduced* for the correlation of the reduced images or *corr_coeff_full* for the correlation of the full images. These variables are saved in the .mat files *disp_reduced_data* and *valid_data* respectively.

Computation of the Data

Version 1 of the code contained an error in the algorithm used to smooth the displacements before calculating the strains. In certain cases, when displacements were large enough that the control points near the edges of the images moved out of the field of view of the images, the smoothing algorithm did not properly pad the displacements near the edges of the region of interest (ROI). This resulted in inaccurate strain calculations near the edge of the ROI. Version 2 of the code implements a new built-in interpolation/extrapolation function, *scatteredInterpolant*, to properly pad the displacements even in cases of large displacements. Note that the new smoothing algorithm requires a longer computation time; therefore, parallel computing is recommended for large image sets.

The function *scatteredInterpolant* is not available in older versions of Matlab. For people using older version of Matlab, the smoothing algorithm used in Version 1 of this code is utilized. As long as displacements are small enough that the control points do not leave the field of view, the two smoothing algorithms should give similar results.

The use of *scatteredInterpolant* also provides more accurate strain calculations near the borders of regions of deleted data (i.e. near the edges of a crack or a hole).

Finally, the user now has more control over how the smoothing algorithm handles regions of uncorrelated data. An additional control has been added to the *compute_data_GUI* that

allows the user to choose the maximum size of a group of contiguous uncorrelated points that the code will smooth over. If there is a group of neighboring uncorrelated points larger than this maximum, the code will not extrapolate data over that region.

Visualization of the Data

- Added the option to visualize either the raw displacements or the smoothed displacements from the same data set.
- Added the option to visualize the correlation coefficients so that the user can evaluate the confidence in the correlation results.
- Added the option to spatially average the data over a rectangular region that is a certain fraction of the region of interest (ROI) and is centered at the image center.
- Fixed a bug concerning plotting a contour plot of the reduced image correlation over a background image. Previously, the x- and y-coordinates used for the patch contour plot were in terms of the full-size image scale but the image itself was scaled by the "reduction" factor used for the reduced correlation. Now, the images and the results from the reduced correlation are scaled back to the scale of the full-sized images.

F.3 Configuration

F.3.1 Version and OS

Version 1 of the code was written in Matlab version R2012b, on a PC running 64-bit Windows 7 Professional, and was tested on both a PC and a Mac running Matlab version R2011a. Version 2 of the code was tested with Matlab version R2012b and R2014b, both on a PC running 64-bit Windows 7 Professional. Versions 3 and 4 of the code were tested with Matlab version R2014b on a PC running 64-bit Windows 7 Professional.

F.3.2 Toolboxes

Three Matlab Toolboxes are required or suggested:

1. *Image Processing Toolbox* is used extensively throughout this code and is therefore required.
2. *Parallel Computing Toolbox* is required if the user wishes to process multiple images concurrently, which greatly reduces processing time. However, the user may choose to process the images in serial, thereby avoiding the need for the Parallel Computing Toolbox.
3. *Statistics Toolbox* is used in the smoothing algorithm (*compute_data_GUI* $\rightarrow$ *smooth_disp* $\rightarrow$ *smooth_moving_average* $\rightarrow$ *normal_distribution* $\rightarrow$ *normcdf*).

F.3.3 Additional Code from FileExchange

The code makes use of two sets of code downloaded from Matlab Central File Exchange. For simplicity, these codes are contained in the Matlab DIC files in this FileExchange. **There is no need to download these files separately.**

1. *Parfor Progress Bar:* This progress bar allows the user to monitor the progress the code is making while executing "parfor" loops during parallel computing. For compatibility with Matlab version R2014b, versions 2 and later of this DIC code contains V0.2.8 of the parfor progress bar code. http://www.mathworks.com/matlabcentral/fileexchange/35609

2. *Freeze Colors:* This code is used in *visualize_data_GUI* when plotting semi-transparent DIC data over background images. http://www.mathworks.com/matlabcentral/fileexchange/7943-freezecolors-unfreezecolors

F.3.4 Configuration Steps

There is minimal configuration required to set up this DIC code:

1. Place the DIC Matlab files in one folder, and add the folder to the Matlab search path, directly below the default folder. This needs to be done only once, when you first install the code.

   - In Matlab R2012b and R2014b, go to the "Home tab". In the "Environment" box, click on "Set Path". Click on "Add Folder...", and navigate to the folder containing the DIC Matlab files. Move this folder directly below the default folder (usually "...\Documents\MATLAB").
   - In earlier versions of Matlab, "Set Path" is under "File".

2. Change the Image Processing Toolbox preferences to display axes on images when using "imshow." This needs to be done only once, when you first install the code. The preference will be remembered.

   - In Matlab 2012b and 2014b, type "iptprefs" in the command window. Check the box for "IMSHOW Display - Axes visible."
   - Alternatively, type *iptsetpref('ImshowAxesVisible','on')* in the Command Window.

3. If the images to be correlated are too large to be displayed at 100 % magnification on the computer screen, the warning "Warning: Image is too big to fit on screen; displaying at 67 %." may be displayed. This warning does not affect the correlation results. To turn off the warning, type "warning('off','images:initSize:adjustingMag')" in the Command Window of Matlab. Matlab should remember the setting for the future.

4. Check to see if the message catalog "menu.xml" exists in the following location (or equivalent location): C:\ Program Files\ MATLAB\ R2012b\ resources\ MATLAB\ en\ uistring\ menu.xml. If the folder "uistring" does not exist, create a folder called "uistring" within the "en" folder. Then place the "menu.xml" file, included in the DIC files in this FileExchange, into the "uistring" folder. If the folder "uistring" exists and contains the "menu.xml" file, then you do not need to do anything.

5. Some Mac users may encounter an error, similar to the one found below, when running the code in parallel mode:

   >> matlabpool open

   Error using matlabpool (line 134)

   Java exception occurred:

   java.lang.NullPointerException

   at java.util.logging.Logger.demandLogger(Logger.java:286)

   at java.util.logging.Logger.getLogger(Logger.java:321)

   If you experience this issue, please see the bug report 919688 on the MathWorks website: http://www.mathworks.com/support/bugreports/919688. Alternatively, you can run the code in serial mode.

F.4 Code Structure

F.4.1 Main Graphical User Interfaces

There are four main components to this code, each with its own graphical user interface (GUI). To run these GUIs, simply type the name of the GUI in the Matlab command window and press enter. No input arguments are needed. A more detailed description of the different GUIs is presented in Section F.6.

1. *image_setup_GUI*: Prepares images for correlation
2. *correlate_images_GUI*: Performs the image correlation and outputs raw displacements
3. *compute_data_GUI*: Smooths and interpolates displacements and calculates strains using finite element shape functions
4. *visualize_data_GUI*: Displays displacements and strains in a variety of formats

Additionally, there are two supplementary GUIs that can be useful under certain circumstances, but are not required:

1. *delete_data_GUI*: Allows the user to delete data that did not correlate well
2. *movie_GUI*: Combines contour plots of correlated data from all images into a time lapsed movie

F.4.2 File Format

There are two main types of files generated by this code, "setup" files and "data" files. The "setup" files are named "XX_setup", and contain information about the correlation, such as the subset size used, the grid spacing, the number of images correlated, etc. These are used by the code, but are also available for your reference. To view the information contained in a "setup" file, simply load the data into Matlab by typing "load XX_setup" in the Command Window and then view the data by typing "XX_setup" in the Command Window. For example, to see the number of images correlated, type the commands as shown in Fig. F.1.

The main data generated by the code is stored in ".mat" files saved in the working directory. To manipulate the data directly, first load the data into Matlab by typing "load XX" in the Command Window, where "XX" is the file name. Note that several variables appear in the workspace when a single file is loaded. Each variable can be manipulated individually.

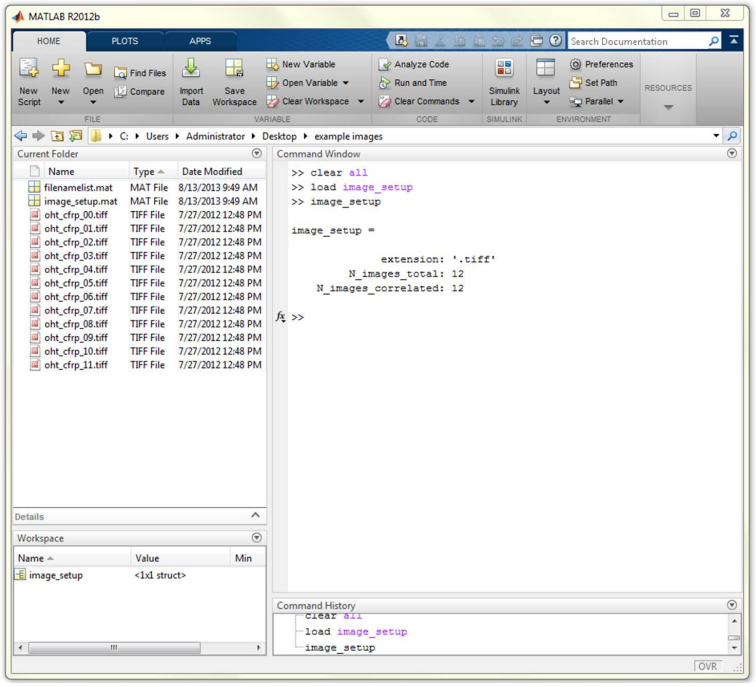

Figure F.1: Example of loading a setup file, in this case *image_setup*, to see the parameters used for a correlation.

F.4.3 Steps of a Typical Correlation

The steps involved to run a typical correlation are found below. An example correlation using the provided images is found in Section F.5.

1. Set up the images to be correlated.
   (a) Place all images to be processed in one folder.
   (b) Set the working directory in Matlab to the folder containing the images.
   (c) Run *image_setup_GUI* to prepare the images.
2. Determine if displacements are large enough to require an initial guess.
   (a) Run *correlate_images_GUI*, and correlate full-sized images only using a sparse grid (step size of about 50-75 pixels for images about 1000x1000 pixels). Using a sparse grid reduces computation time.
   (b) Run *visualize_data_GUI* and look at the contour plot of the image that you anticipate to have the largest displacements.
   (c) If the entire region of interest correlated well (there are no large areas of missing data where there are large displacements), then displacements are small enough that no initial guess is required, and the reduced-size images do not need to be correlated. Proceed to step 4.
   (d) If the images did not correlate well in regions where displacements are large, then you need to generate initial guesses for the displacements by correlating reduced-size images. Proceed to step 3.
3. If necessary, generate initial guesses for displacements by correlating reduced-size images.
   (a) Run *correlate_images_GUI*, and correlate reduced-size images only. Use approximately 100-200 grid points.
   (b) Run *visualize_data_GUI* and evaluate the results.
   (c) If the correlation of the reduced images did not capture the large displacements, adjust one or more of three parameters until satisfactory results are obtained:
      i. Change the subset size.
      ii. Change the image reduction factor.
      iii. Iterate the correlation of the reduced images, using the results from the previous correlation of reduced images as initial guesses for the current correlation of reduced images.
      iv. Increase the search zone. This method should be used as a last resort. See Sec. F.6.2 for more information.

4. Determine the optimal subset size for the correlation of the full-sized images*.
   (a) Run *correlate_images_GUI*, and correlate full-sized images only, using results from the correlation of the reduced-size images as initial guesses as necessary, and using a sparse grid (step size of about 50-75 pixels for images about 1000x1000 pixels).
   (b) Run *visualize_data_GUI* and evaluate the results.
   (c) If there are very few points that did not correlate, then run *correlate_images_GUI* again, using a smaller subset size.
   (d) Repeat this process until the subset size is too small to provide a good correlation. Note the smallest subset size that provided a good correlation, and use this in the final correlation.
5. Run final correlation.
   (a) Run *correlate_images_GUI*.
   (b) Correlate full-size images only.
   (c) Use results from the correlation of reduced-size images if necessary.
   (d) Use the optimal subset size found in the previous step.
   (e) Create a new, dense grid (step size of approximately 5-10 pixels for images about 1000x1000 pixels).
6. Delete regions of poorly-correlated data. (Optional)
   (a) Run *visualize_data_GUI*.
   (b) Determine if there are regions where data did not correlate well.
   (c) Run *delete_data_GUI*.
   (d) Select a single image to preview, and choose regions of data to delete. Data will be deleted for all the images.
7. Smooth displacements and calculate strains.
   (a) Run *compute_data_GUI*.
   (b) If desired, enter the scale of your images (must be determined separately).
   (c) Choose a smoothing kernel size and the number of smoothing passes.
   (d) Choose finite element used in the interpolation of displacements and subsequent strain calculations. The author recommends always using cubic elements.
   (e) Compute the deformed grid if desired.

*A fundamental assumption of this DIC code is that each subset undergoes only rigid translation in two directions; that is, that there is no deformation (or rigid rotation) within a single subset. For this reason, it is desirable to make the subset as small as possible. However, one must have a sufficiently large subset in order to have enough information within the subset to have a good correlation. The optimal subset size is a balance between these two competing requirements.

(f) Run *visualize_data_GUI* to view the smoothed displacements and strains. Line scans of displacements and of strains are particularly useful to judge the effectiveness of the smoothing.

(g) Re-run *compute_data_GUI*, adjusting the smoothing parameters as necessary until smoothed displacements and strains are satisfactory.

8. Visualize results.

   (a) Run *visualize_data_GUI*.

   (b) Save plots as desired.

   (c) Run *movie_GUI*. Make a time-lapsed movie of the contour plot if desired.

F.5 Example Correlation

An example correlation is provided here that follows the steps outlined in Sec. F.4.3. The images used in the example correlation are from the DIC Challenge, conducted under the auspices of the Society of Experimental Mechanics (SEM), image set 12. More information on the DIC Challenge can be found at `www.sem.org/dic-challenge/` and in Appendix G.

F.5.1 Image Setup

Set up the images to be correlated.

1. Place all the example images into one folder. In this example, the folder is called "example images" and is located on the Desktop.

2. Set the working directory in Matlab to the folder containing the images.

3. (Fig. F.2) Run *image_setup_GUI* by typing "image_setup_GUI" into the Command Window and pressing Enter.

4. (Fig. F.3) Choose the appropriate file extension for the images. For this example, choose ".tiff". Set "Image skip" to 1 in order to correlate all the images in the folder.

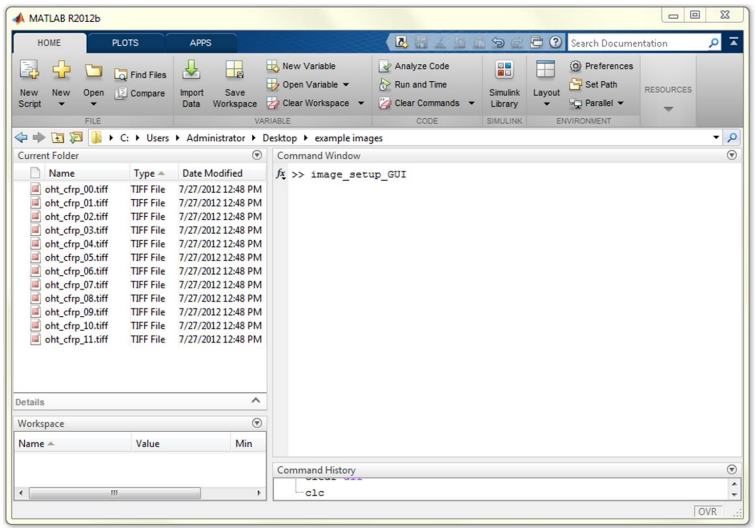

Figure F.2: The working directory is set to the folder containing the example images. Run *image_setup_GUI* by typing "image_setup_GUI" into the Command Window and pressing Enter.

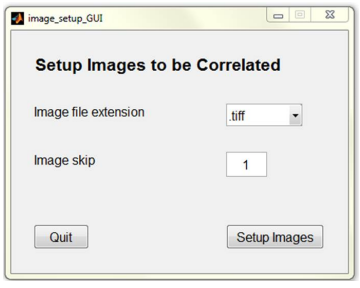

Figure F.3: Options available for preparing the images.

F.5.2 Large Displacements

Determine if displacements are large enough to require initial guesses.

1. Correlate the full images using a sparse grid.

   (a) (Fig. F.4) Run *correlate_images_GUI* by typing "correlate_images_GUI" into the Command Window and pressing Enter.

   (b) (Fig. F.5) Choose to run in parallel or serial. This example uses parallel computing. If you choose to run in serial, choose "First Image" as the reference image. Correlate full images only, and define a new full grid. Use a subset of 21 pixels.

   (c) (Fig. F.6) If you choose to use parallel computing, the matlabpool must initialize. This happens only once every time you open Matlab.

   (d) (Fig. F.7) When prompted, select the reference image (first image) to open. When the image opens in Matlab, click on the top left corner and the bottom right corner to define the region of interest. Choose a step size of 50 pixels. When prompted, choose to "Keep this grid." The images will automatically be correlated, and the data from the correlation will be saved in the working directory.

2. Visualize the results to determine if the images correlated well.

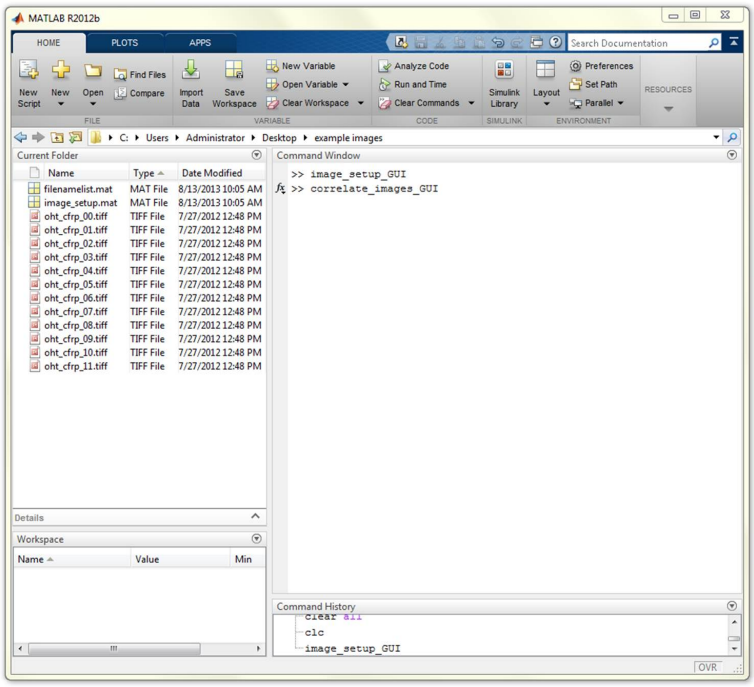

Figure F.4: Run *correlate_images_GUI* by typing "correlate_images_GUI" into the Command Window and pressing Enter.

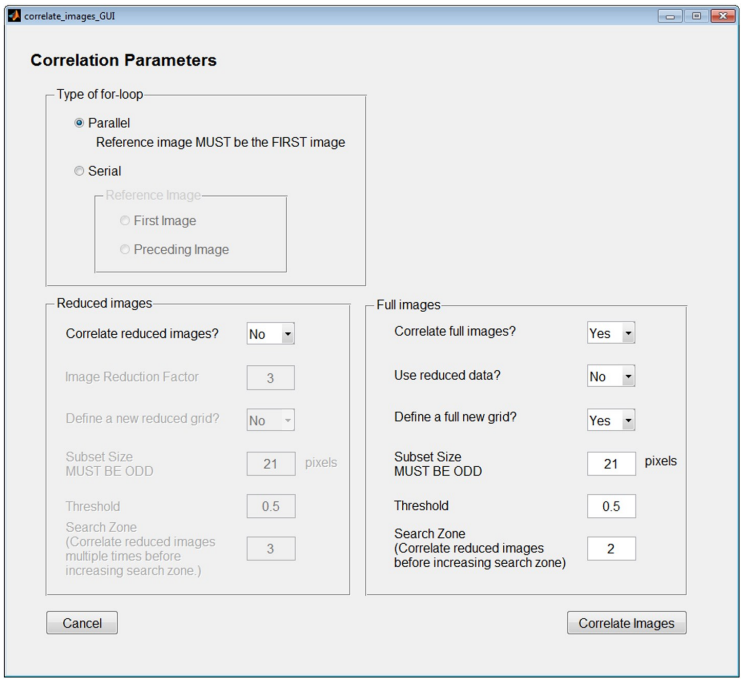

Figure F.5: Correlation parameters for the correlation of full-sized images, used to determine if initial guesses are required to capture large displacements. If running in serial mode, choose the first image as the reference image.

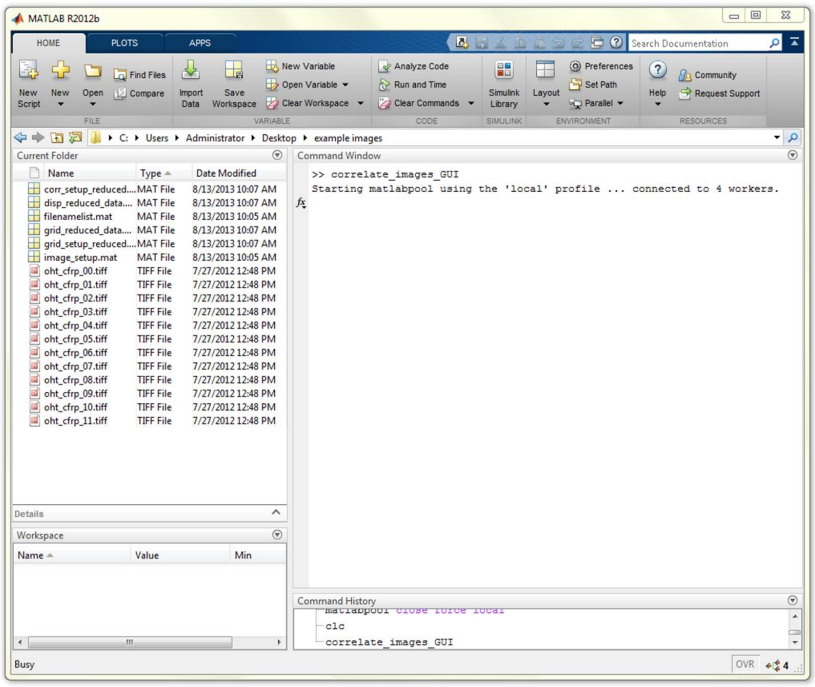

Figure F.6: The first time parallel computing is used after Matlab is opened, the matlabpool must initialize.

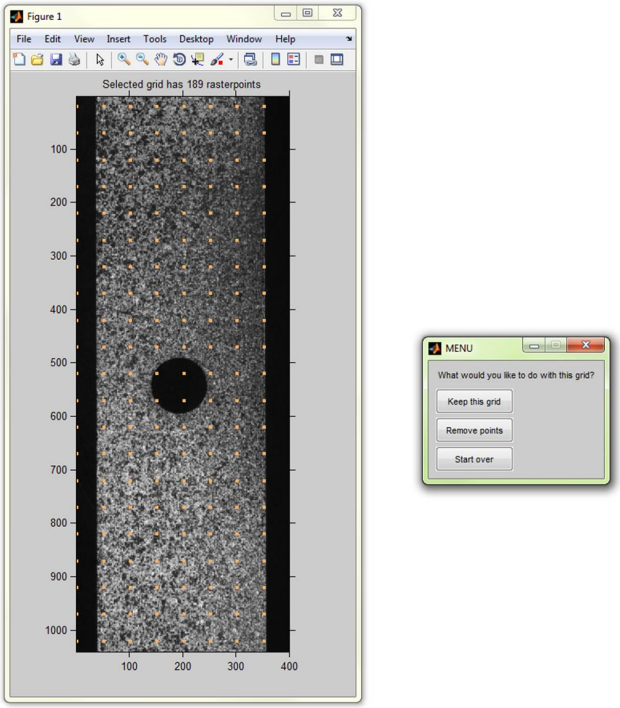

Figure F.7: Sparse grid (step size of 50 pixels), defined on a full-size image.

(a) (Fig. F.8) Run *visualize_data_GUI* by typing "visualize_data_GUI" in the Command Window and pressing Enter.

(b) (Fig. F.9) Visualize the full data (data from the correlation of full-sized images). Click on "Filled Contour Plot". To view data from all of the images, leave "Image Skip" set to 1.

(c) (Fig. F.10) Choose to view the vertical displacements (V), and use the same scale for all of the images. Ignore the "Plot over images?" box in order to plot the contours without a background image. Click on "View Contour Plot."

(d) (Fig. F.11) The first image is a self-correlation, and should have nearly zero displacements. Images 2 though 8 correlated over the entire region of interest, while images 9 through 12 did not correlate near the top of the region of interest, where the displacements are large. Therefore, initial guesses for the displacements are required.

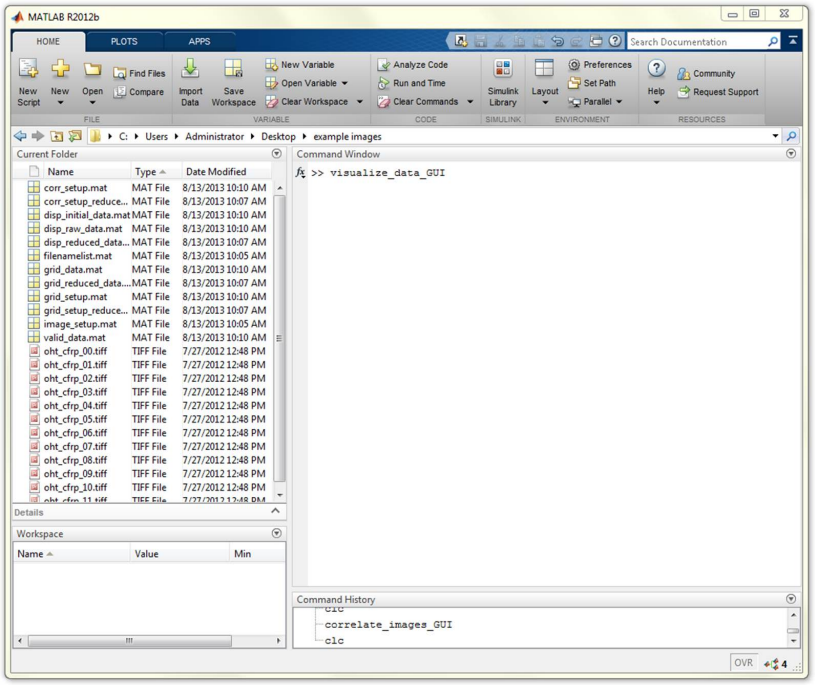

Figure F.8: Run *visualize_data_GUI* by typing "visualize_data_GUI" into the Command Window and pressing Enter.

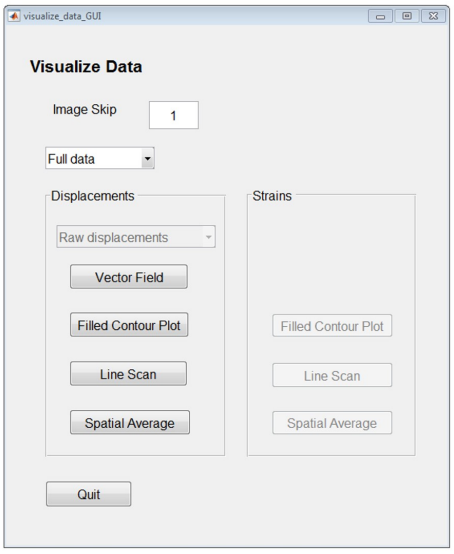

Figure F.9: Options available for visualizing the results of the correlation of the full-size images. For this example, choose "Filled Contour Plot."

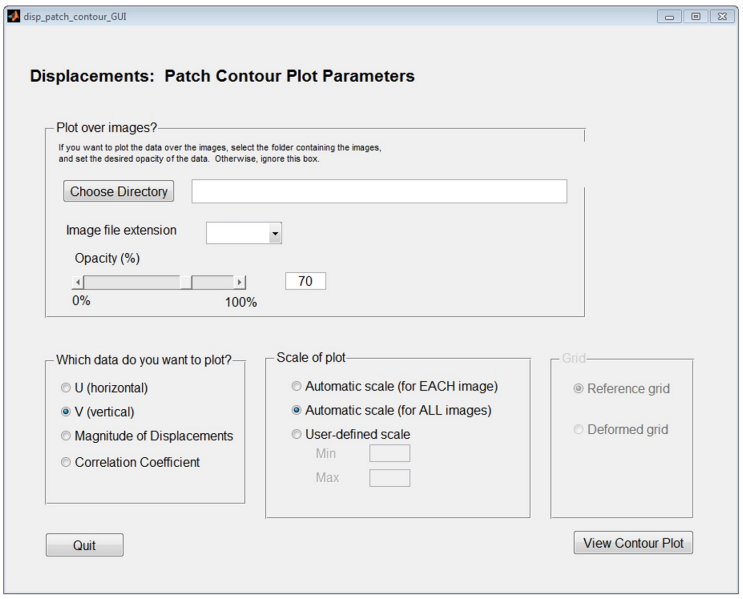

Figure F.10: Options available for visualizing contour plots of displacements. For this example, choose the vertical displacements, V, and use the same scale for all images.

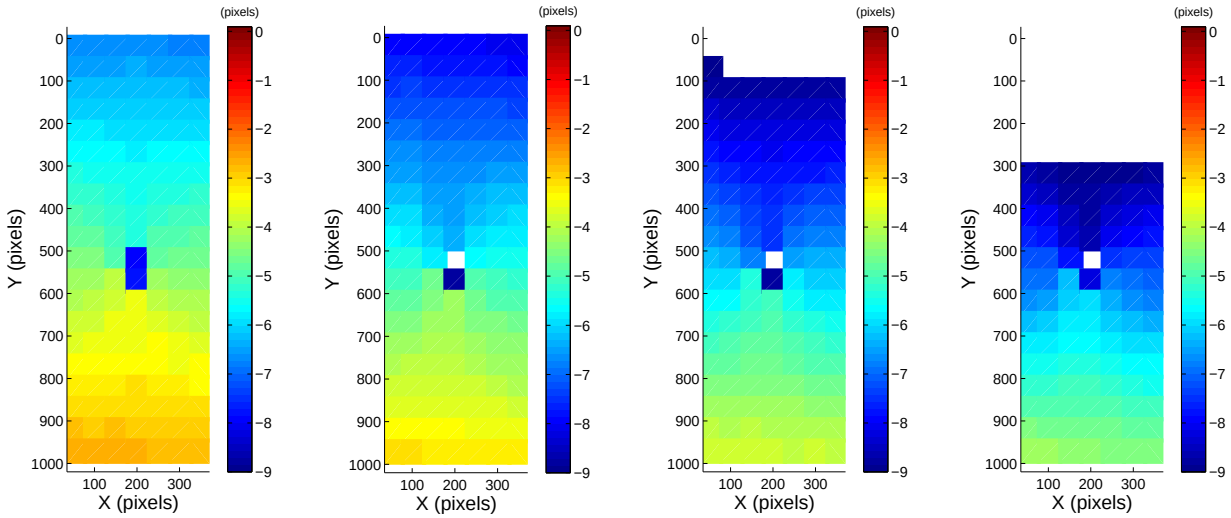

(a) Image 7 **(b)** Image 8 **(c)** Image 9 **(d)** Image 10

Figure F.11: Contour plots of the vertical displacements, V, for images 7-10 for the first correlation on a sparse grid of the full-size images without using initial guesses. Images 2-8 correlated well, but images 9-12 have large regions of data missing near the top of the region of interest, where there are large displacements.

F.5.3 Generate Initial Guesses (Correlate Reduced Images)

Generate initial guesses for displacements by correlating reduced-size images.

1. Correlate the reduced-size images.
   (a) Run *correlate_images_GUI*.
   (b) (Fig. F.12) Correlate the reduced-size images only. Set the correlation parameters as shown in Fig. F.12.
   (c) (Fig. F.13) When prompted, select the reference image (first image) to open. Note that the image is now shown in the reduced size. Click on the top left and bottom right corners of the image to define the region of interest. Choose a step size of 20 pixels. Keep this grid. The reduced-size images will automatically be correlated.

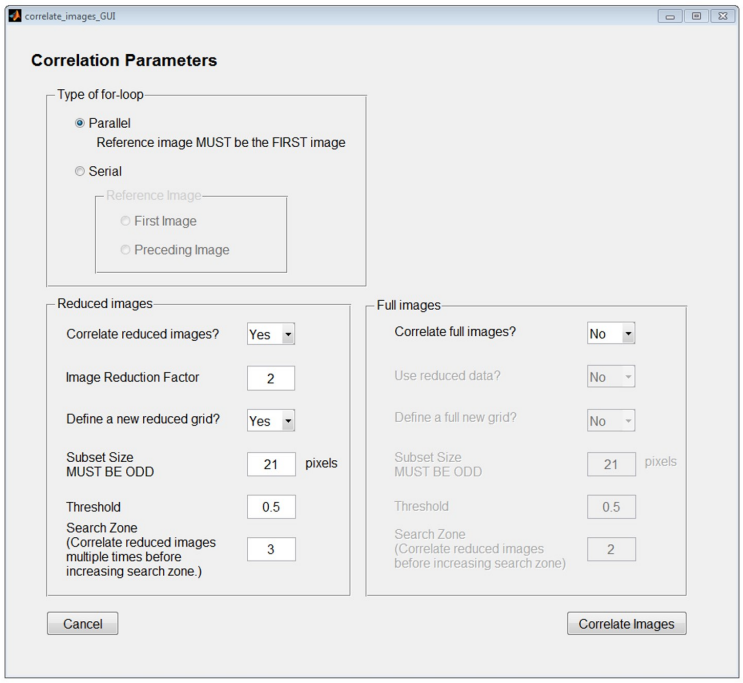

Figure F.12: Correlation parameters for the correlation of reduced-size images, used to generate initial guesses for the correlation of full-sized images.

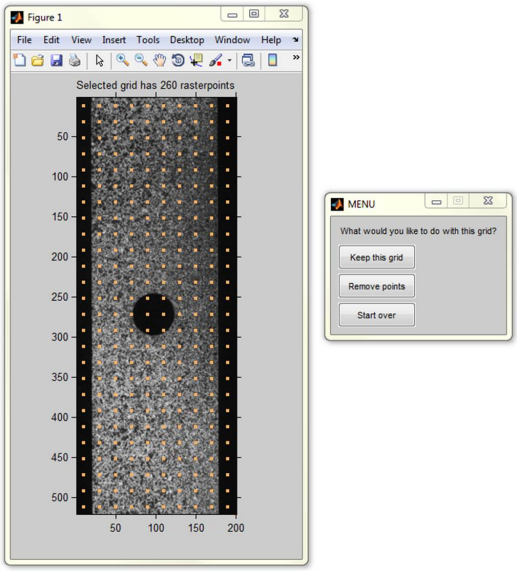

Figure F.13: Grid used for the correlation of the reduced-size images. The step size was 20 pixels.

2. Visualize the results of the correlation of the reduced-size images to determine if the images correlated well.

   (a) Run *visualize_data_GUI*.

   (b) (Fig. F.14) Visualize the reduced data (data from the correlation of the reduced-size images). Click on "Filled Contour Plot." To view data from all of the images, leave "Image Skip" set to 1.

   (c) Choose to view the vertical displacements (V), and use the same scale for all of the images. Click on "View Contour Plot."

   (d) (Fig. F.16a) The large displacements for all images were captured effectively by the reduced-size images. These results will provide initial guesses for the final correlation of the full-sized images. There is no need to re-correlate the reduced-size images; future correlations of the full-sized images will use the data from this correlation, which is saved in the working directory, as initial guesses.

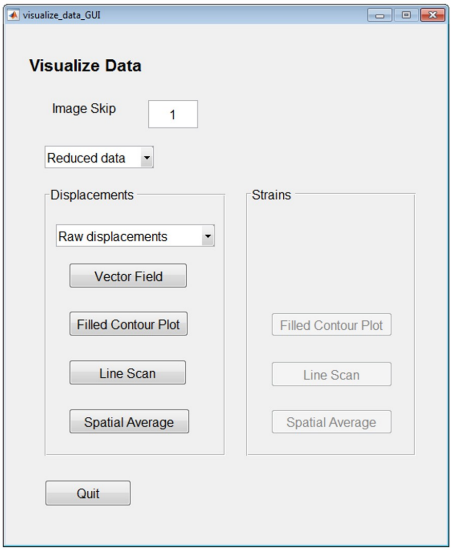

Figure F.14: Options available for visualizing the results of the correlation of the reduced-size images. For this example, choose "Filled Contour Plot."

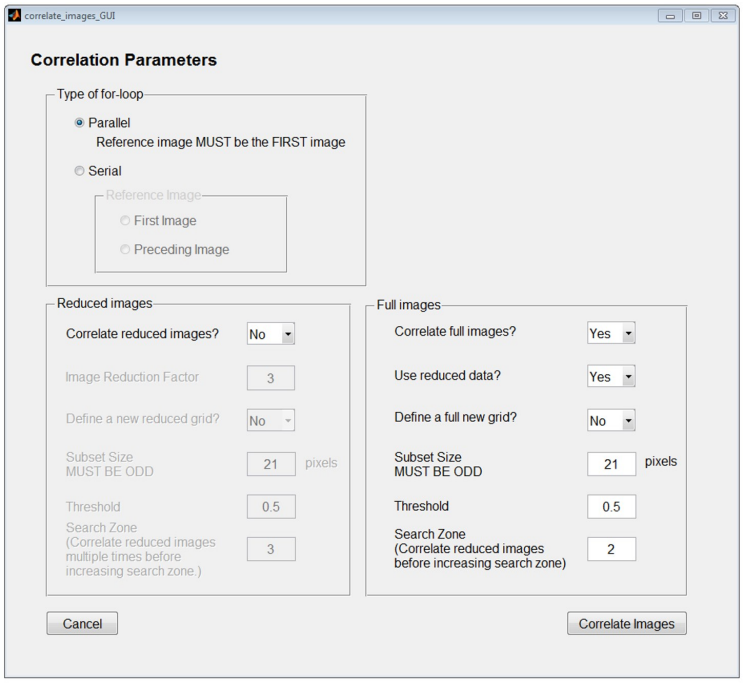

Figure F.15: Correlation parameters for the correlation of full-size images, using the results of the correlation of the reduced-size images as initial guesses.

3. Correlate the full-sized images using the results from the correlation of the reduced-size images as initial guesses.

   (a) Run *correlate_images_GUI*.

   (b) (Fig. F.15) Correlate the full-sized images only. Use the results of the correlation of the reduced-size images from the previous step as initial guesses. Use the same sparse grid that was defined in Sec. F.5.2.

   (c) Run *visualize_data_GUI*, go to "Full data", and look at the contour plot of the vertical displacements.

   (d) (Fig. F.16b) Verify that all regions of large displacements are captured using the initial guesses. Note that the very top row of data may be missing in images 11 and/or 12. This is due to the top portion of the sample moving out of the field of view of the camera. It is NOT a result of the displacements being too large.

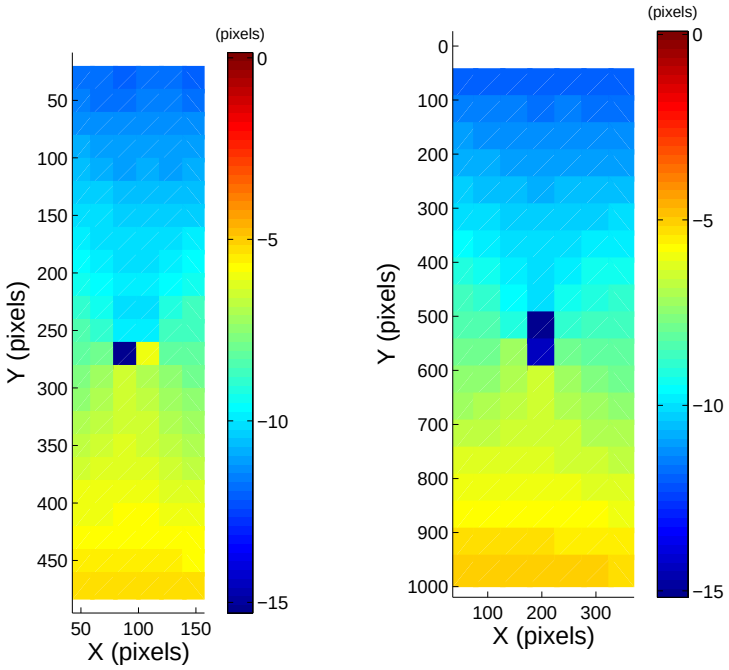

(a) Reduced correlation

(b) Full correlation, with initial guesses

Figure F.16: Contour plot of the vertical displacements, V, for the last image (image 12) for (a) the reduced-size images and (b) the full-size images using initial guesses. All large displacements are captured well.

F.5.4 Optimal Subset Size

Determine the optimal subset size for the correlation of the full-sized images.

1. Correlate the full images, using initial guesses if necessary, using a smaller subset size.

   (a) (Fig. F.17) When using a subset size of 21 pixels in the previous step, all the subsets correlated well, suggesting that a smaller subset may be sufficient. Run *correlate_images_GUI*. Correlate full images only, using the reduced data, using the same sparse grid that was previously defined, but use a smaller subset of 11 pixels.

   (b) Run *visualize_data_GUI*, go to "Full data", and look at the contour plot of the vertical displacements.

   (c) (Fig. F.18) All of the data points correlated well, indicating that a smaller subset could be used.

   (d) (Fig. F.18) Repeat the previous steps, using a subset size of 7 pixels, and then repeat the steps using a subset size of 5 pixels. The correlations for subset sizes of 21, 11, and 7 are all nearly equivalent. The correlation for subset size of 5, however, is missing several data points, indicating that the subset size of 5 contains insufficient data to provide robust correlation results. Therefore, the optimal subset size is 7 for this particular set of images.

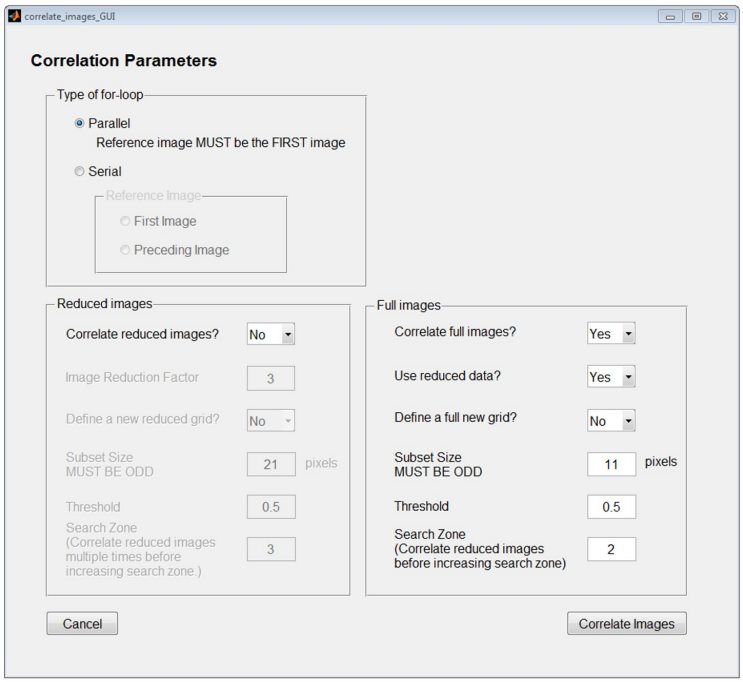

Figure F.17: Correlation parameters for the correlation of full-size images, using a smaller subset size.

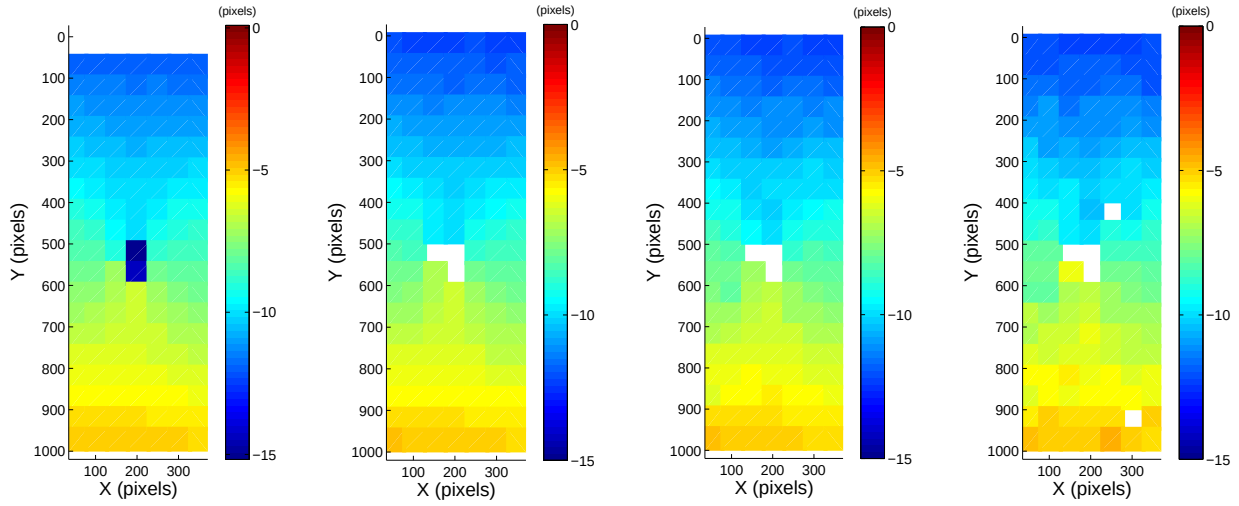

(a) Subset 21 **(b)** Subset 11 **(c)** Subset 7 **(d)** Subset 5

Figure F.18: Contour plots for the vertical displacements for the last image (image 12) for four different correlations with varying subset sizes. Correlations with subsets larger than 7 pixels correlated well, while the correlation with a subset size of 5 pixels did not correlation well. Therefore, the optimal subset size for this set of example images is 7 pixels.

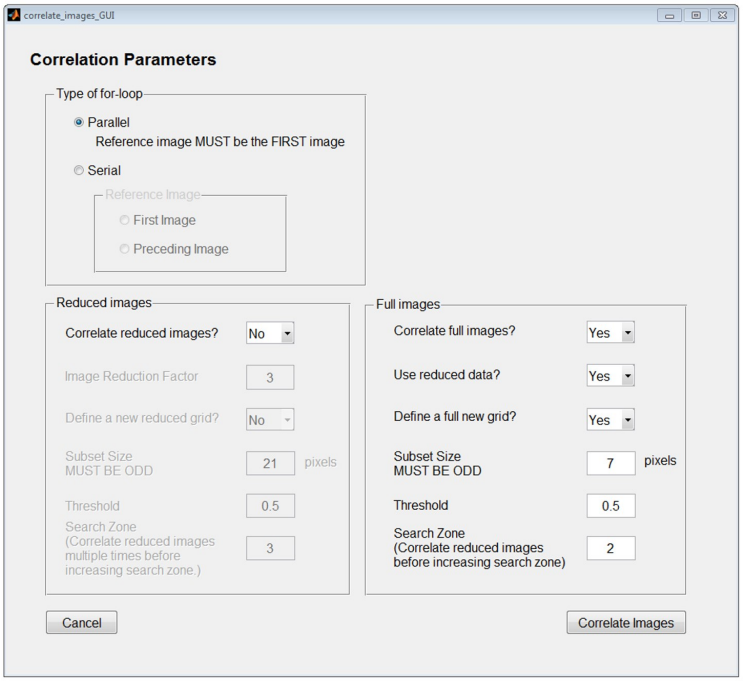

Figure F.19: Correlation parameters for the correlation of full-size images, where a new grid will be defined.

F.5.5 Final Correlation

Run the final correlation, using a dense grid.

1. Correlate the full images, defining a new, dense grid.
   (a) (Fig. F.19) Run *correlate_images_GUI*. Choose the parameters as shown in Fig. F.19.
   (b) (Fig. F.20) When prompted, define a new grid with a step size of 5 pixels.

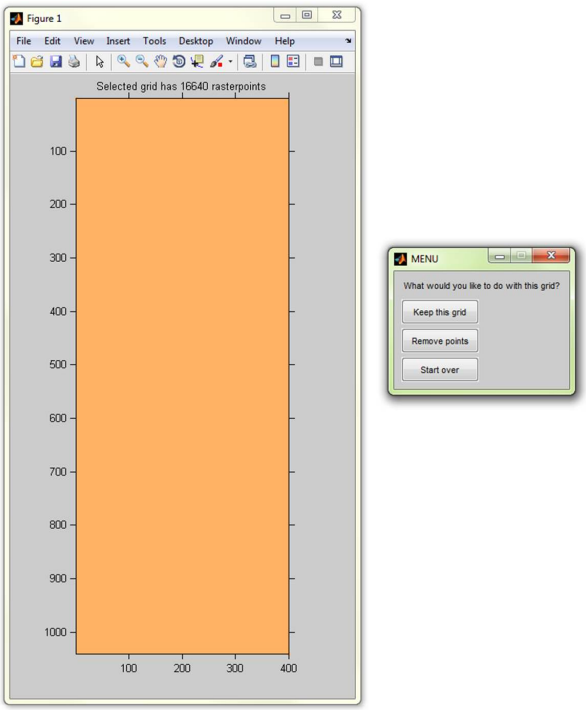

Figure F.20: Dense grid (step size of 5 pixels) used for the final correlation of full-size images. Note that the grid is so dense, it appears as a solid rectangle.

2. Visualize the results of the correlation with a dense grid.

   (a) (Fig. F.21) Run *visualize_data_GUI*, and look at the contour plots of the vertical displacements.

   (b) Notice that for the most part, the grid points that were not over the test specimen (i.e. at the left and right edges of the image and in the hole in the specimen center), did not correlate. However, there are some false correlations in these regions. These false correlations can affect the strain results if they remain in the data. Therefore, they should be deleted before smoothing displacements and calculating strains.

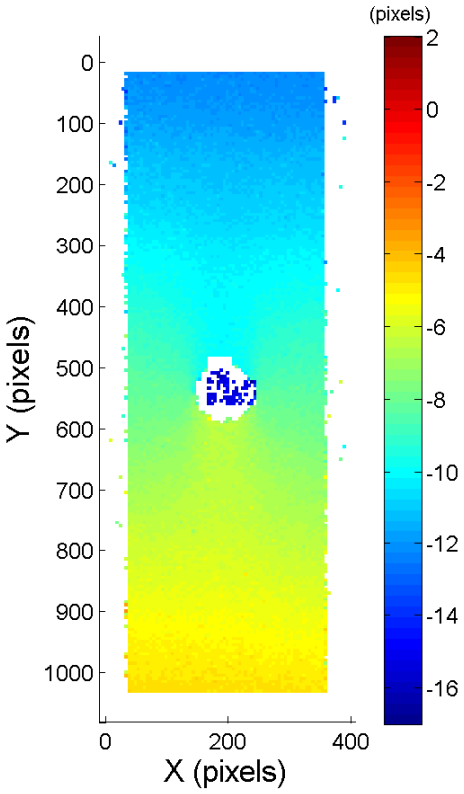

Figure F.21: Contour plot of the vertical displacements, V, for the last image (image 12) after the final correlation of the full-size images using a dense grid.

F.5.6 Delete Poorly Correlated Data

Delete regions of poorly-correlated data.

1. Save a copy of the original data in a separate folder. This saves you from needing to re-do the correlation if you accidentally deletes too much data.

2. Delete poorly-correlated data.

   (a) Run *delete_data_GUI* by typing "delete_data_GUI" into the Command Window and pressing Enter.

   (b) (Fig. F.22) Choose image 1 to preview. Choose "Grid Points" as the data representation. When prompted, select the reference image (first image) to open. This will plot the original grid over image 1.

   (c) (Fig. F.23a) Click on the top left and bottom right corners of the region you wish to delete. If necessary, choose "Yes" when prompted with "Would you like to select more points to delete?" and select more regions until all the grid points that are not over the specimen have been selected and temporarily deleted.

   (d) Note: Once you select data, you cannot deselect it. However, data is not deleted until you click on "Delete Data." Therefore, if you accidentally selected data you don't want to delete, simply close the figure without clicking on "Delete Data." You can then, click on "Grid Points" again, and select more data.

   (e) When you've selected all the desired data to delete, click on "Delete Data" to permanently delete the data.

   (f) When you're finished using the *delete_data_GUI*, click on "Done / Quit."

3. Visualize correlation results with poorly-correlated data deleted.

   (a) Run *visualize_data_GUI* and look at the contour plots of the vertical displacements.

   (b) (Fig. F.23b) There is no longer any falsely-correlated data at the edges of the image and in the center hole of the specimen.

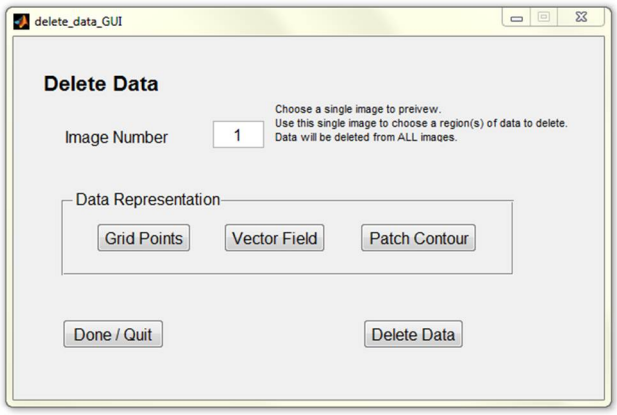

Figure F.22: Options available to delete data. For this example, click on "Grid Points" and leave the image preview number set to 1.

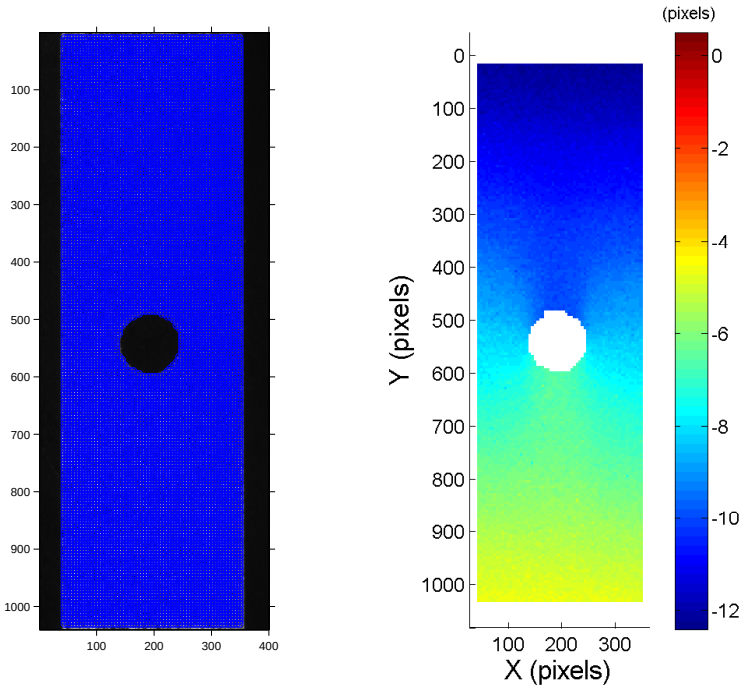

(a) New grid

(b) V, with new grid

Figure F.23: (a) New grid, after all the grid points that were not over the specimen (i.e. left and right sides of the image and the hole in the center of the specimen) have been deleted. (b) Contour plot of the vertical displacements for the last image (image 12) after extraneous grid points have been deleted.

F.5.7 Smooth Displacements and Calculate Strains

1. Smooth displacements to reduce noise and calculate strains.
   (a) Run *compute_data_GUI*.
   (b) (Fig. F.24) For this example, leave the scale at 1 µm/pixel.
   (c) Use the default smoothing kernel of 15 and smooth the displacements 3 times. Leave the number of contiguous non-correlated points to smooth over at 15.
   (d) Calculate strains using the 16-node, bi-cubic finite element interpolation scheme.
   (e) Compute the deformed grid.
2. Visualize smoothed data and strains.
   (a) Run *visualize_data_GUI*.
   (b) Look at both the contour plots and line scans of the smoothed displacements and strains to determine if the smoothing parameters produced satisfactory results.
   (c) If necessary, re-run *compute_data_GUI* and adjust smoothing parameters[†].

[†]In order to determine the best smoothing parameters to use, run *compute_data_GUI* several times, using different kernel sizes and different numbers of smoothing passes. The correct amount of smoothing is subjective, and is a compromise between low noise in the strains and high spatial resolution of the strains.

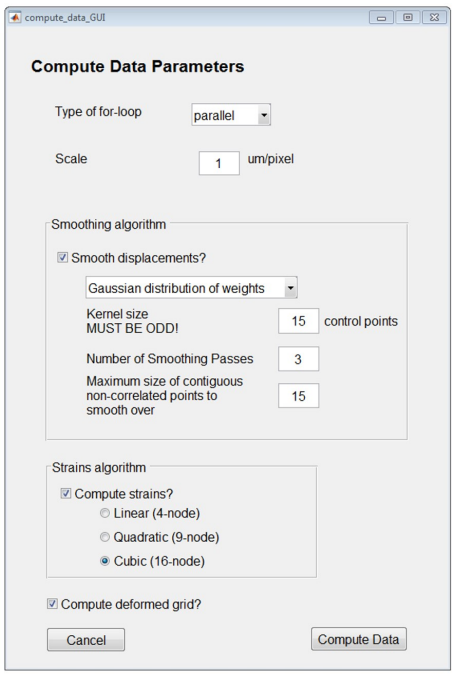

Figure F.24: Options available for smoothing displacements and calculating strains.

F.5.8 Visualize Data

Visualize the data and save any desired plots.

1. Run *visualize_data_GUI*.
2. (Fig. F.25) View the vertical displacements (V) and the vertical normal strains (E_{yy}) as contour plots and compare to Fig. F.26.
3. The analytical solution for a hole in an infinite plate undergoing uniaxial tension shows that there should be a stress and strain concentration of three times the nominal stress and strain at the edge of the two edges of the hole perpendicular to the loading. In this example, the nominal strain, away from the hole, is approximately 0.6% strain, while the strain at the horizontal edges of the hole is approximately 1.6% strain. This is close to the expected strain concentration of a hole in an infinite plate.

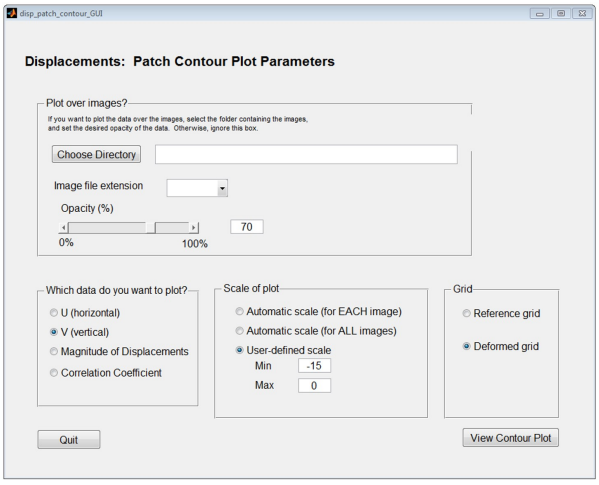

(a) Contour Parameters for V

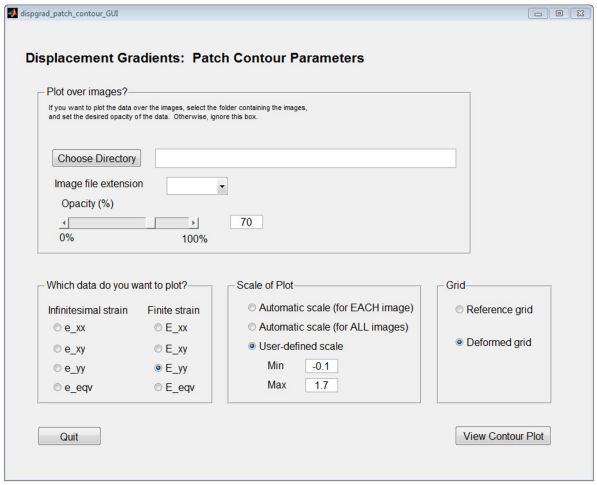

(b) Contour Parameters for E_{yy}

Figure F.25: Settings used to generate contour plots of the vertical displacements, V (a) and vertical normal strains, E_{yy} (b) shown in Fig. F.26.

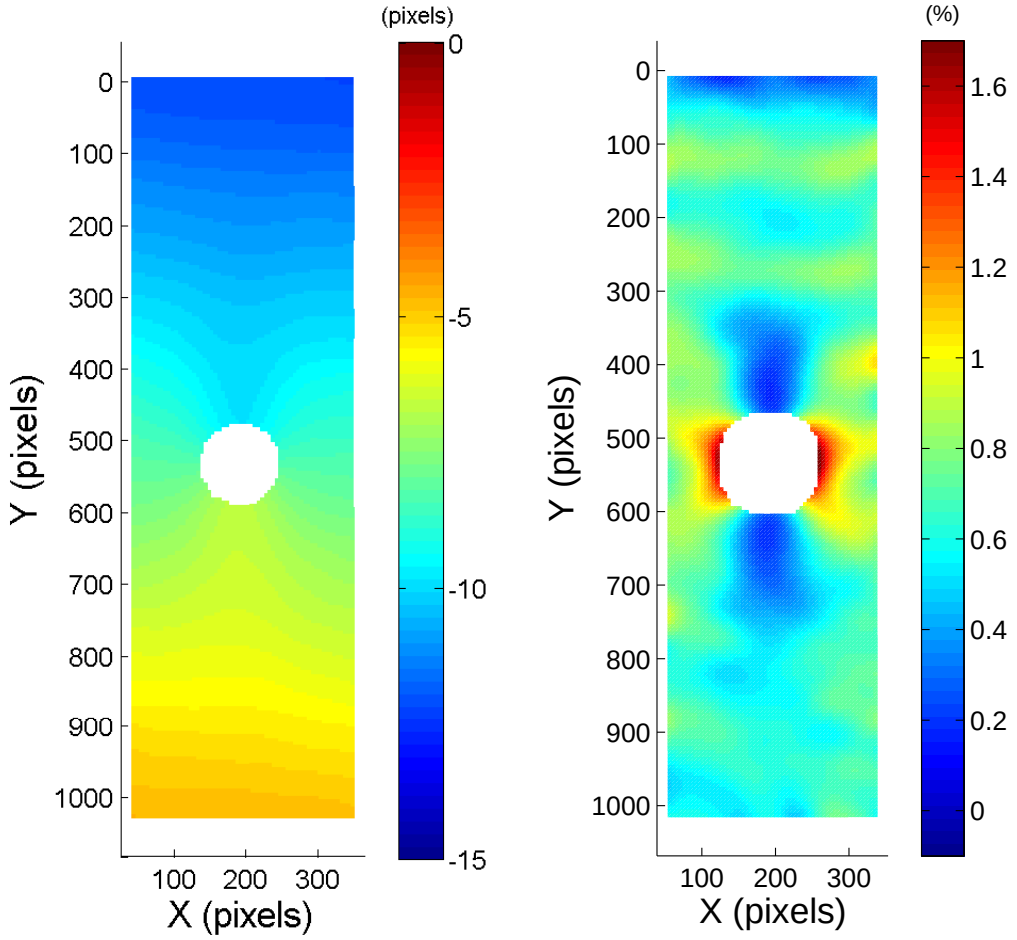

(a) Vertical displacement, V **(b)** Vertical normal strain, E_{yy}

Figure F.26: Contour plots of vertical displacements, V (a), and vertical normal strians, E_{yy} (b) for image 12. These are the final results.

F.6 Detailed Explanation of Main GUIs

F.6.1 Image Setup

Table F.1: Image Setup parameters

GUI name:	*image_setup_GUI*
Input arguments:	Images to be analyzed
Output arguments:	*filenamelist.mat*
	image_setup.mat
Parameters:	– File extension of images (e.g. .tiff, .tif, .jpg)
	– Image skip

The purpose of this GUI is to prepare a list of the images the user wishes to correlate at once, saved as a Matlab variable *filenamelist.mat* in the current working directory. All images contained in this list will have as a reference image either a) the alphabetically first image in the folder or b) the preceeding image in the folder. (See Sec. F.6.2 for more information concerning reference images.) If one wishes to correlate some images against one reference image, and other images against a different reference image, one must separate these two groups of images into two different folders, with the corresponding reference image as the first image in the folder, and run this code two times, once for each set of images.

The current working directory must contain all the images one wishes to correlate at once. The images must all have the same file extension, and they can be either black and white or color. They should be named such that their alphabetic order follows a logical sequence. The image names need not be the same length. Examples of acceptable naming conventions are found in Table F.2.

Table F.2: Examples of acceptable image name conventions

1.tif	Pic1.jpg	347900.734375.tiff
2.tif	Pic5.jpg	348802.156250.tiff
3.tif	Pic10.jpg	349703.171875.tiff

Though the image names need not have the same number of characters, the variable *filenamelist.mat* is a matrix, with each row corresponding to an image, and each column corresponding to a character in the image name. Therefore, to keep the matrix dimensions consistent, the *image_setup_GUI* finds the image with the longest name, and adds the appropriate number of zeros to the beginning of all image names that are shorter than the longest image name. This GUI will rename all the images in the folder. If you do not wish to have the images renamed, keep a copy of the original images in a different folder.

Though the original images can be in color, the correlation code requires black and white images. Therefore, the *image_setup_GUI* automatically converts all images in the folder to black and white if they are not already in this format. If you have color images and do not

want to have the images converted to black and white, keep a copy of the original images in a different folder.

The parameter "Image Skip" allows the user to correlate only some of the images in the folder. If "Image Skip" is set to 3, for example, then images 1, 4, 7, etc... will be correlated. This is useful paricularly for the first couple of correlations, when the user wants to see the effect of various correlation parameters on the results, and does not need to see (or want to wait on) the results of every image.

The output of this GUI is the Matlab variable *filenamelist.mat*. Any method can be used to generate this variable. This GUI simply provides an automatized method that should work for most image naming conventions. The output *image_setup.mat* saves the parameters chosen when the *image_setup_GUI* was run.

F.6.2 Correlate Images

The purpose of this GUI is to define all the parameters for the correlation process. One must first have run *image_setup_GUI*, or have generated the variables *filenamelist.mat* and *image_setup.mat* in the appropriate format through some other means.

Serial/Parallel Computing and Reference Image

This code has the option of running in serial (each image is correlated sequentially, one at a time) or in parallel (multiple images are correlated independently at the same time on separate processor cores). Running the code in parallel is much faster than running it in serial for a large number of images. For only a few images, serial computing may be faster due to the overhead computation time associated with parallel computing. Serial computing is recommended if the user is editing the code as the code is easier to debug in serial mode.

The default reference image is the first image in the current working directory, which should also be the first image in the variable *filenamelist.mat*. However, this code allows for the option of using the preceding image as a reference image, which could be useful when dealing with large deformations and/or speckle patterns that become distorted during the specimen deformation process. If one uses this option, the cumulative displacements are calculated and reported with respect to the first image. Note that there is cumulative error associated with using the preceding image as a reference image. Therefore, the author recommends using the first image as a reference image when possible. See Sec. F.6.2 for the recommended technique for correlating images with large displacements.

Because the par-for loop requires each loop iteration to be independent, when using parallel computation, the reference image MUST be the same for all the images to be correlated. To use the preceding image as the reference image, one must choose the serial computing option.

Grid Generator

A grid of control points at which one wishes to compute displacements must be defined. Though this grid can be generated by the user via any method he wishes, the function

Table F.3: Correlate Images parameters

GUI name:	*correlate_images_GUI*
Input arguments:	Images to be analyzed *image_setup.mat* *filenamelist.mat*
Output arguments:	*corr_setup.mat* *corr_setup_reduced.mat* *disp_initial_data.mat* *disp_raw_data.mat* *disp_reduced_data.mat* *grid_data.mat* *grid_reduced_data.mat* *grid_setup.mat* *grid_setup_reduced.mat* *valid_data.mat*
Parameters:	– Parallel or serial computation – Reference image (for serial computation only) – Correlation of reduced images (for large displacements) • Image Reduction Factor • Grid of control points • Subset Size • Threshold • Search Zone – Correlation of full-sized images • Use of data from reduced images • Grid of control points • Subset Size • Threshold • Search Zone

grid_generator_GUI_compatible_3.m, included within the *correlate_images_GUI*, provides a semi-automated method for generating the grid.

If a grid has not already been defined (either by the user, or via previous iteration of *correlate_images_GUI*), then *correlate_images_GUI* will prompt the user to define a grid using the default *grid_generator_GUI_compatible_3.m*. If a grid does already exist, then the user has the option of using the existing grid or defining a new grid. If the user defines a new grid, then the new grid will overwrite the old grid.

When the grid generator function *grid_generator_GUI_compatible_3.m* runs, the user is first prompted to open the reference / first image. Then the user must choose the region of interest (ROI) by selecting two points that form the diagonal corners of a rectangle. The user is then prompted to select a grid spacing. This value will define the number of pixels in between adjacent control points, both in the vertical and horizontal direction. The grid is then plotted over the image, and the user is given the option of accepting the grid as is, removing points, or starting over. If the user wishes to remove some grid points, he must select the diagonal corners of a rectangle surrounding the points he wishes to remove. He may choose to do this as many times as desired to remove points from different regions. If the user chooses to start over, the original grid is erased and the user must select a new ROI and a new grid spacing. When the user is satisfied with the grid, he must choose "Accept the grid." The code then proceeds directly to correlating the images.

Note that the original grid generator function, written by C. Eberl, contains many options for generating grids, for example circular grids with radial or circumferential points. The current author eliminated all options except for the rectangular grid option because the other original options are not compatible with the strain measurement code in *compute_data_GUI* (see Sec. F.6.3).

Large Displacements and Reduced Images

The code has a maximum allowable vertical and horizontal displacement that it can find for any given control point, determined by the subset size and the search zone through Eqn. F.1:

$$u_{max} = \frac{SS}{2}(SZ - 1) - 1 \tag{F.1}$$

where u_{max} is the maximum allowable vertical or horizontal displacement, SS is the subset size, and SZ is the search zone. The search zone is the area about the subset in which the code searches during the correlation. By default, $SZ = 2$. See Section F.6.2 for more information on how the search zone is used during the correlation.

If the actual displacement at a control point is larger than the maximum allowed displacement, then the code will not correlate at that control point, and no displacement data will be returned. In order to obtain displacement data when the test specimen underwent large displacements, the user has two options: increase the search zone size or provide initial guesses for the displacements. Increasing the search zone size has two significant drawbacks. First, it drastically increases the computation time required for a correlation. Second, it requires a larger border between the outermost control points and the image edges. The recommended method for capturing large displacements is to provide initial guesses for the

displacements, which is described in the remainder of this section. In some extreme cases, however, the user will need to both provide initial guesses and increase the search zone. For this reason, Version 2 of the code allows the user to control the search zone value.

In order to provide initial guesses of the displacements in an automatic fashion, the user can correlate the reduced-size images. The code for correlating reduced images essentially shrinks the images by the amount chosen in "Image Reduction Factor," which serves to effectively reduce the size of displacements (in terms of pixels). The code then correlates the reduced images, and uses the results of the reduced correlation as initial guesses for the correlation of the full-size images.

The "Image Reduction Factor" should be set between 2 and 4. Reducing the images to less than 1/4 of their original size leads to poor correlation results. If a reduction of 4 is not sufficient to capture the large displacements, one can run the reduced image correlation iteratively. By selecting "Yes - use previous iteration" from the "Correlate reduced images?" drop down box, the code will use the results from the previous reduced correlation as initial guesses in the current reduced correlation.

It is recommended that the user obtain satisfactory reduced correlation results before running the full correlation, otherwise the adage "garbage in, garbage out" applies to the full correlation. To use the data from the reduced correlation as initial guesses in the full correlation, the user must select "Yes" under the "Use reduced data?" drop down box in the *correlate_images_GUI*.

Correlation of the images

The heart of the correlation process is in the *cpcorr_mod.m* function, a slightly modified version of the standard function in the Image Processing Toolbox, *cpcorr.m*, written by Matlab. For each control point, the code takes a subset of pixels around the control point in the deformed image, and a larger subset (generally twice as big) around the corresponding control point in the reference image, as shown in Fig. F.27. The size of the reference subset with respect to the deformed subset is controlled by the search zone. Increasing the search zone will increase the maximum allowable displacement, but at the cost of a larger border around the region of interest in which control points cannot be correlated and increased computation time.

The code computes the normalized cross-correlation coefficient, C, [114] for a range of theoretical displacements, (u', v'), in 1 pixel increments by convolving the subset from the deformed image with the larger subset from the reference image according to:

$$C\left(u',v'\right)=\frac{\sum_{x',y'}\left[\left(r\left(x',y'\right)-\bar{r}_{u',v'}\right)\left(d\left(x'-u',y'-v'\right)-\bar{d}\right)\right]}{\left\{\sum_{x',y'}\left[\left(r\left(x',y'\right)-\bar{r}_{u',v'}\right)^2\right]\sum_{x',y'}\left[\left(d\left(x'-u',y'-v'\right)-\bar{d}\right)^2\right]\right\}^{1/2}} \tag{F.2}$$

where r is the intensity of the pixels in the reference subset, d is the intensity of the pixels in the deformed subset, and (x', y') are local subset coordinate axes whose origin is at the control point at the subset center. If the value of the computed correlation coefficient at a given control point is less than the value set for the threshold (typically 0.5), the correlation

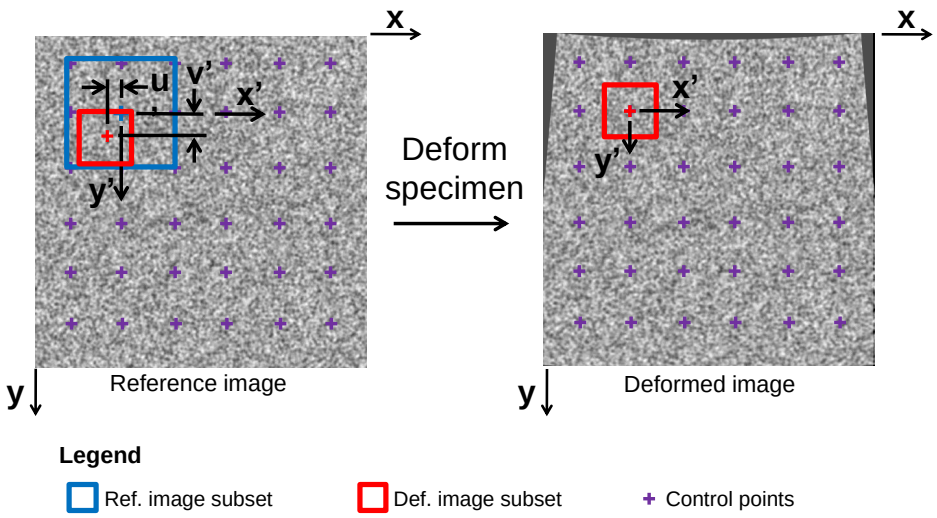

Figure F.27: Schematic of digital image correlation methodology. A grid of control points (purple crosses) is defined over the region of interest. The normalized cross-correlation coefficient (Eqn. F.2) is computed by convolving a subset in the deformed image (red box) with the corresponding larger subset in the reference image (blue box). The actual displacement (u,v) is the displacement that maximized the correlation coefficient.

is determined to be poor and no data is returned for that control point. By decreasing the threshold value, the user can allow more grid points to be correlated, but at the expense of having less certainty in the validity of the correlations.

In order to calculate displacements to within 1/100 of a pixel, the nine discrete correlation coefficients surrounding the absolute maximum coefficient are interpolated using a second order polynomial in u' and v'. The actual displacement (u, v) for a control point is the theoretical displacement (u', v') corresponding to the maximum interpolated correlation coefficient. The output of the code is discrete displacement values for each control point for each image.

F.6.3 Compute Data

This GUI performs four main functions: it scales the displacement data from pixels to microns, smooths the displacement data, computes strains from the displacement data, and computes the deformed grids. These four functions are independent, but due to noise inherent in DIC displacements, it is strongly recommended that the user smooths the displacements before calculating strains and the deformed grid. The user can run this GUI multiple times in order to fine-tune the smoothing parameters before calculating strains. (The code uses the raw displacement data each time it runs.)

Scaling the displacements

The displacements from the *correlate_images_GUI* have pixels for units as default. In order to scale the data appropriately, the user must enter the pre-determined scale. The GUI, as

Table F.4: Compute Data parameters

GUI name:	*compute_data_GUI*
Input arguments:	All output from previous GUIs
Output arguments:	*disp_smooth_data.mat*
	DU_data.mat
	FEM_setup.mat
	disp_raw_data.mat
	grid_scale_data.mat
	smooth_setup.mat
	grid_deformed_data.mat
Parameters:	– Parallel or serial computation
	– Scale (um/pixel)
	– Smoothing parameters
	• Even or Gaussian distribution of weights
	• Kernel size
	• Number of smoothing passes
	• Maximum size of uncorrelated points to smooth over
	– Strain computation parameters
	• Type of finite element used for interpolation of displacements
	– Computation of deformed grids

set up, requires the physical units to be microns. However it is straight forward to edit the GUI and associated code in order to use a different unit that is appropriate to the user's length scale. If the user leaves the scale at 1 um/pixel, then all the displacement data is reported in pixels in the *visualize_data_GUI*.

Smoothing of displacements

Displacements are smoothed prior to calculating strains to provide robustness against the noise inherent to DIC. In order to reduce edge effects, the borders of the region of interest are first padded by reflecting displacement values at the edge of the region of interest across the border such that the first derivative is continuous. Versions 2 and later of the code does this by using the built-in function *scatteredInterpolant*.

The user can select the kernel size of control points used in the smoothing process, as well as the weighting function. If "Even distribution of weights" is selected, then all the control points in the smoothing kernel are given equal weighting during the averaging. If "Gaussian distribution of weights" is selected, the displacements at control points within the kernel are weighted with a Gaussian distribution centered at the central control point and then averaged. The displacement at the central control point is replaced by the weighted average. To obtain smoother results, this process can repeated, by increasing the "Number of Smoothing Passes," whereby the averaged displacements from the previous smoothing iteration are used as inputs in the next smoothing iteration.

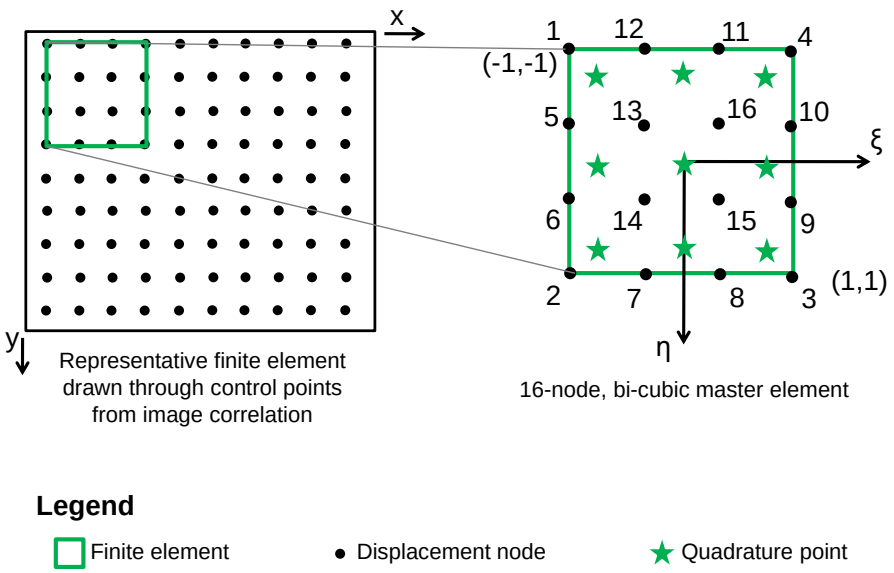

Figure F.28: Schematic of finite element methodology used in strain calculations. Given displacements at a grid of control points (black circles), a 16-node finite element (green box) is drawn through the control points. This element is mapped to a master element, with local coordinates ξ and η, and the displacements are interpolated over the master element using bi-cubic finite element shape functions. The derivatives of the interpolated displacements are calculated at the nine Legendre-Gauss points of the element (green stars), and then mapped back to the original element.

When an uncorrelated point is encountered, the code will extrapolate the displacements from neighboring control points to provide a displacement value for the uncorrelated point. For small numbers of contiguous uncorrelated points, this extrapolation process is reasonable; however, for large regions of uncorrelated points, the user may wish to not have the code extrapolate data over the region. The user can choose the maximum size of contiguous uncorrelated points for which the code will extrapolate the displacement data.

Strain Calculations

Strains are calculated by interpolating displacements using finite element shape functions.

A 16-node finite element is drawn such that the nodes of the finite element correspond to the control points from the image correlation. This element is then mapped to a master element, as shown in Fig. F.28, through:

$$(x, y) = f^i(\xi, \eta) = \underline{\hat{N}}(\xi, \eta)\underline{X}^i \tag{F.3}$$

where (x, y) are the image coordinates, (ξ, η) are the local coordinates of the master element, and f^i is the mapping function, defined by the matrix multiplication of the finite element shape functions defined on the master element, $\underline{\hat{N}}$, and the image coordinates of the nodes for element i, $\underline{X}^i$. The sixteen bi-cubic finite element shape functions, $\hat{N}_j$, are defined according

to:

$$\hat{N}_j(\xi,\eta) = \left(a\xi^3 + b\xi^2 + c\xi + d\right)\left(e\eta^3 + f\eta^2 + g\eta + h\right) \tag{F.4a}$$

$$\hat{N}_j(\xi,\eta) = \begin{cases} 1 & \text{at node } j \\ 0 & \text{at all other nodes} \end{cases} \tag{F.4b}$$

where $a, b, ..., h$ are constants. Displacements are interpolated over the master element and mapped back to the original element through:

$$\underline{U}^I(x,y)|_{(x,y)=f^i(\xi,\eta)} = \underline{\hat{N}}(\xi,\eta)\underline{U}^i_{EL} \tag{F.5}$$

where $\underline{U}^I(x,y)$ are the interpolated displacements as a function of image coordinates (x,y) and $\underline{U}^i_{EL}$ is a matrix containing displacements in x and y directions of the element nodes for element i. The first partial derivatives, $\underline{\nabla U}(x,y)$, of the interpolated displacements are calculated through:

$$\underline{\nabla U}(x,y)|_{(x,y)=f^i(\xi,\eta)} = \underline{\nabla \hat{N}}(\xi,\eta)\left[\underline{J}^i(\xi,\eta)\right]^{-1}\underline{U}^i_{EL} \tag{F.6}$$

where $\underline{J}^i$ is the Jacobian of the mapping function for element i, defined according to:

$$\underline{J}^i(\xi,\eta) = \left[f^i(\xi,\eta)\right]' = \underline{\nabla \hat{N}}(\xi,\eta)\underline{X}^i \tag{F.7}$$

The interpolation scheme is most accurate at the nine Legendre-Gauss points of the master element [115, 116], defined by combinations of $(\xi,\eta) = \{-\sqrt{3/5}, 0, \sqrt{3/5}\}$. The displacement derivatives are therefore calculated at these discrete points for all possible elements that can be drawn through the control points. Overlapping Gauss points from neighboring elements are then averaged, giving discrete displacement gradient values on a grid slightly smaller than the grid of control points. Components of the small-strain tensor, ϵ_{ij}, and the Green-Lagrangian finite strain tensor, E_{ij}, are then calculated:

$$\epsilon_{ij} = \frac{1}{2}\left(\frac{\partial U_i}{\partial X_j} + \frac{\partial U_j}{\partial X_i}\right) \tag{F.8a}$$

$$E_{ij} = \frac{1}{2}\left(\frac{\partial U_i}{\partial X_j} + \frac{\partial U_j}{\partial X_i} + \frac{\partial U_k}{\partial X_i}\frac{\partial U_k}{\partial X_j}\right) \tag{F.8b}$$

A rotationally-invariant equivalent strain is included in the code, in order define a state of strain that is independent of the orientation of the test specimen with respect to the image. This definition is based on the Von Mises equivalent stress, and is defined as:

$$
\begin{aligned}
E_{eqv} &= \left[\frac{3}{2}\left(E_{ij}E_{ij} - \frac{1}{3}E_{mm}E_{mm}\right)\right]^{1/2} \\
&= \left[\frac{3}{2}\left(E_{11}^2 + E_{12}^2 + E_{21}^2 + E_{22}^2 - \frac{1}{3}\left(E_{11}+E_{22}\right)\left(E_{11}+E_{22}\right)\right)\right]^{1/2} \\
&= \left[E_{11}^2 + E_{22}^2 - E_{11}E_{22} + \frac{3}{2}\left(E_{12}^2 + E_{21}^2\right)\right]^{1/2}
\end{aligned} \tag{F.9}
$$

Note that this definition of equivalent strain is invariant to rotations, shown in Eqns. F.10 & F.11, where Q_{ri} is a rotation matrix, and prime notation denotes tensor components in the rotated coordinate system. Note that $E'_{kk} = E_{kk}$ because the trace of tensors is rotation invariant.

$$
E'_{rs} = Q_{ri}Q_{sj}E_{ij} \tag{F.10}
$$

$$
\begin{aligned}
E'_{eqv} &= \left[\frac{3}{2}\left(E'_{rs}E'_{rs} - \frac{1}{3}E'_{mm}E'_{kk}\right)\right]^{1/2} \\
&= \left[\frac{3}{2}\left(Q_{ri}Q_{sj}E_{ij}Q_{ro}Q_{sp}E_{op} - \frac{1}{3}E_{mm}E_{kk}\right)\right]^{1/2} \\
&= \left[\frac{3}{2}\left(\delta_{io}\delta_{jp}E_{ij}E_{op} - \frac{1}{3}E_{mm}E_{kk}\right)\right]^{1/2} \\
&= \left[\frac{3}{2}\left(E_{ij}E_{ij} - \frac{1}{3}E_{mm}E_{kk}\right)\right]^{1/2} \\
&= E_{eqv}
\end{aligned} \tag{F.11}
$$

Computation of the Deformed Grid

The user can choose to compute the deformed grids for both displacements and strains. For displacements, this function simply adjusts the reference grid control points based on the smoothed displacements (or raw displacements, if displacements are not smoothed) for each image correlated. For the strains, the function first interpolates the displacement field to obtain displacement values for at the control points in the strain reference grid. (Recall that the strain results are presented on a slightly different grid than the displacements.) Then, the strain reference grid control points are shifted by the interpolated displacement values.

If the user computes the deformed grids, then the user has the option of plotting the data in *visualize_data_GUI* over either the reference grid or the deformed grid. Note that the deformed grid is only calculated for correlation of the full images; it is not calculated for correlation results of reduced images.

F.6.4 Visualize Data

Table F.5: Visualize Data parameters

GUI name:	*compute_data_GUI*
Input arguments:	Images to be analyzed All output from previous GUIs
Output arguments:	Graphs and Plots of data
Parameters:	– Reduced vs Full Correlation Results – Raw or Smoothed Displacements – Type of plot: • Vector field (displacements only) • Contour plot • Line scan • Spatial average

There are four default methods of visualizing the displacement and strain data: as a vector field (displacements only), a filled contour plot, a line scan, or a spatial average. The first three options plot the data for one image at a time. To advance through the data from all of the correlated images, the user clicks on the figure. At any point, the user can save a Matlab figure and then continue to advance. If the user wishes to generate other types of plots, he could easily incorporate them into the *visualize_data_GUI*. The author requests that if a user expands the visualization options, he notifies the author so that the additional capabilities can be incorporated into a future version of the code.

Vector Field

This function uses Matlab's *quiver.m* to generate a vector field of displacements. The user can adjust the scale of the arrows used in the plot via the "Quiver Scale" parameter. Matlab scales the arrows by first scaling them such that they fit within the grid, and then stretching them by a factor of "Quiver Scale". See http://www.mathworks.com/help/matlab/ref/quiver.html for more information.

As DIC data is often very dense (i.e. control points every 5-10 pixels), the user may choose to reduce the number of arrows plotted through the "Quiver Skip" parameter. If the "Quiver Skip" is set to 10, then every 10th quiver will be plotted.

Filled Contour Plot

This function uses Matlab's *patch.m* function to generate a filled contour plot of displacements and strains. The function generates a square patch around each control point and adjusts the color of the patch based on the value of the data at that control point. By plotting all of the patches together, a filled contour plot is generated. When plotting a contour plot over the deformed grid, which is no longer regularly spaced, the patches are no longer

contiguous and may either over lap and/or have a gap between them. This behavior is a known deficiency of the code, and the author welcomes any suggestions for improvement.

Of note is the absence of a line contour plot using Matlab's *contour.m* function. The *contour.m* requires an evenly-spaced, rectangular grid over which to plot the data. The grid from the image correlation, however, is often not strictly rectangular because e.g. the region of interest may not be rectangular, there may be a hole in the specimen, regions of data that did not correlate well may be deleted, etc. Additionally, the *contour.m* function would not allow the user to plot a contour plot over the deformed grid. Using the *contour.m* function with a non-rectangular or unevenly-spaced grid would require interpolating data over an evenly-spaced, rectangular grid, which could lead to errors from the interpolation. For these reasons, the author decided to have contour plots generated through the *patch.m* function.

The user can choose to plot the contour by itself, or can plot the contour semi-transparently over the corresponding image in the background. To plot a simple contour plot without the images, simply leave the "Choose Directory" box blank or enter a zero in the box. To plot over a background image, select the folder containing the images, and select how opaque the data should be. The folder containing the images does not necessarily need to be the same folder that contains the correlated data, but it should contain the exact same images that were used in the correlation. Note, in order to see x- and y-coordinate tick marks when plotting a contour plot over a background image, you must set the tick mark preference by using the command *iptsetpref('ImshowAxesVisible','on')*. You only need to type this command in the command window one time, and the preference will be set permanently.

The user can also choose the scale desired for the contour plot color bar. The option "Automatic scale (for EACH image)" automatically calculates the minimum and maximum of the appropriate data for each image. This option will allow the color bar to be scaled for EACH image. The second option, "Automatic scale (for ALL images)"calculates the minimum and maximum of the appropriate data for all images. This option will keep the color bar constant for all images. As the third option, the user can specify the scale to uses; this option keeps the color bar constant for all images.

Line Scan

This function plots data along a line scan in the region of interest. The user can select either a vertical or a horizontal line at any location within the region of interest (ROI). For example, if the "Fraction of ROI" is set to 0.1, and the "Direction of line scan" is vertical, the line scan will be along a vertical line close to the left side of the ROI. If "Fraction of ROI" is 0.9 and "Direction of line scan" is horizontal, the line scan will be along a horizontal line near the bottom of the ROI.

Spatial Average

This function plots an average of the data over either the entire region of interest (ROI), over a certain line, or over a rectangular region that is a fraction of the ROI and is centered with the image center. The user can choose to plot the averaged data against either image number or time on the x-axis.

F.6.5 Delete Poorly Correlated Data

It is not uncommon in DIC to have portions of the region of interest that do not correlate well because, e.g. the test specimen rotated and the image went out of focus or the speckle pattern was poor. In these instances, it can be advantageous to delete the poorly correlated data and have a smaller region of interest with good data.

In principle, the user could either (a) delete the raw displacement data first, and then smooth the data and compute strains, or (b) smooth all of the data and compute strains and then delete the poorly correlated regions. Both methods have their advantages and their drawbacks. A disadvantage of (b) is that the strains near the poorly-correlated region are affected by the poorly correlated displacements. Also, the smoothing function interpolates data at control points that did not correlate at all, making it more difficult to determine the poorly-correlated region accurately. In contrast, method (a) allows the user to delete poorly correlated data before strains are calculated, so that the poor displacement data does not affect the strains. However, a disadvantage of (a) is that edge effects are introduced during the smoothing process along edges of deleted data.

It is the author's opinion that method (a) is preferred, and therefore the *delete_data_GUI* must be used with only raw displacement data; smoothed data and strains must be computed after the desired raw data is deleted. The author is currently working on reducing edge effects during the smoothing process, and would gladly accept suggestions from users.

F.6.6 Create Movies

The *movie_GUI* creates time-lapsed movies of the contour data for either displacements or strains. The user can control the frame rate and whether or not to plot the plain contour plot or plot over a background image.

To create the movie, the user firsts previews a representative figure (determined by the *Preview Image Number*, and here, the user can adjust the figure parameters (e.g. title). When creating the movie, it is important that the user not cover the Matlab figure with the mouse or other windows. Otherwise, the windows covering the figure will be captured in the movie.

The function currently is set to make MPEG-4 movies. However, the user can modify these options in line 45 of *patch_contour_movie*. See http:/www.mathworks.com/help/matlab/ref/videowriterclass.html for more information.

At this time, the author has only written code for making movies of contour plots, but the user may wish to make movies of the changing vector field, changing line scan, etc. The author requests that if a user expands the movie options, he notifies the author so that the additional capabilities can be included in future versions of this code.

F.7 Performance of Code

The accuracy and precision of this DIC code is of extreme importance to all users. The author is currently participating in the DIC Challenge, a round-robin style competition conducted under the auspices of the Society of Experimental Mechanics (SEM) with the

purpose of providing a set of standard images and evaluation criteria for all university and professional DIC codes and software. See http://www.sem.org/dic-challenge/ for more information. A complete evaluation of this DIC code using the DIC Challenge image sets is provided in Appendix G.

F.7.1 Known Deficiencies

There are two main areas of this code that the author currently recognizes as needing further improvement. First, during the smoothing of displacements, edge effects can be significant. To reduce edge effects, the code first pads displacements around the border of the ROI before smoothing them, but this does not eliminate the edge effects. Additionally, when control points are deleted, either before correlation using the *grid_generator_GUI_compatible_3.m* function, or after correlation using the *delete_data.m* function, the displacements are not padded on edges where data was deleted. Therefore, edge effects are even more pronounced on these edges. The author welcomes any suggestions for improved smoothing algorithms that have smaller edge effects.

Second, based on results of the DIC Challenge evaluation, the author found that this code does not capture large rotations well. At this time, the author does not have plans to improve the ability of the code to capture rigid rotations. If any user wishes to work on improving this aspect of the code, the author would be happy to discuss possible solutions.

F.8 Concluding Remarks

The author is pleased to present this free, open-source DIC software to the general Matlab community. The code is constantly evolving as improvements are made, but the set of Matlab files included in this version represent a fairly complete, working DIC code.

Part of the appeal of this code, compared to commercial "black box" codes, is the ease of modification. As you use this code, please notify the author of any modification you make - either improvements or adaptations for a specific situation - so that such modifications can be addressed in future versions.

Appendix G

Accuracy and Precision of Matlab-Based DIC Code

G.1 Introduction

The DIC Challenge, conducted under the auspices of the Society of Experimental Mechanics (SEM), is a round-robin style competition to compare and contrast different DIC algorithms, both commercial software and University-based DIC codes [117]. The DIC Challenge board provides a set of standard images that DIC code developers can use to evaluate the performance and accuracy of their code. As stated on the DIC Challenge website, "The use of a common image data set removes the experimental errors associated with multiple hardware setups created by a typical, specimen-based, round-robin style test." As of May 2015, the DIC Challenge is on-going, and final results are not yet available. However, we have evaluated our DIC code, described in Appendix F and available on the Matlab File Exchange website (File Exchange ID #43073) [65], using the standard image set provided by the DIC Challenge board, the results of which are presented here.

The complete image sets associated with the DIC Challenge are available from the DIC Challenge website. In total, 13 image sets covering different aspects of the performance of the code were evaluated: rigid translation (image sets 1-7), rigid rotation (image sets 8-9), large strain (image set 10), constant strain and strain discontinuity (image set 11b), sinusoidal variation of the strain (image set 14) and overlapping strain peaks (image set 15). The deformations depicted in image sets 1-11, 14, and 15 were generated with different computer algorithms. We assume that the errors resulting from the image transformations are negligible compared to the errors resulting from the correlation process. No analytic solution was provided for image set 10; therefore, only a qualitative evaluation of this image set is performed. Image set 12 is an experimental image set with no known solution; a discussion of the performance of the code for this image set is provided in the main documentation for the code, "Matlab based DIC code documentation." Image set 14 is another experimental image set with no known solution; it was not evaluated.

The follow parameters are used for all the analyses presented in this document unless otherwise noted: step size of 5 pixels, threshold value of 0.5 for the minimum correlation coefficient, search zone of 2, Gaussian distribution of the weighting factors during the smoothing of displacements, displacement interpolation over 16 node, bi-cubic finite elements for strain calculations, and finite strain values (i.e. E_{xx}) rather than infinitesimal strain values (i.e. e_{xx}). Throughout this document, the smoothing parameters are listed as [smoothing kernel size, number of smoothing passes], e.g. [11,3]. The smoothing parameters refer to the smoothing of the displacements prior to calculating strains. No post-processing of the strains

is performed.

For simplicity and clarity, only one displacement (horizontal, U, or vertical, V) and one normal strain (horizontal, E_{xx}, or vertical, E_{yy}) are shown for the rigid body translations (image sets 1-5) and rigid body rotations (image sets 8-9). The other displacement and strain components follow similar trends for accuracy and precision with regard to smoothing parameters, subset size, threshold value, etc.

Strains calculated from unsmoothed displacements are extremely noisy and cannot be used. Therefore, only strains calculated from smoothed displacements are presented in the evaluations.

A concise summary and a complete summary of the results are found in Sec. G.2. Detailed results for each image set are found in the following sections.

G.2 Results Summary

Table G.1 provides a concise summary of the results of the evaluation of this DIC code using the images provided by the DIC Challenge. The noise threshold provides an approximate baseline for the noise or error associated with the code. Table G.2 provides a summary of the results of each image set. Full explanations of the results for each image set are found in the following sections.

Table G.1: Concise Summary of Correlation Results

Deformation		Samples	Noise Threshold* Displacement (pixels)	Noise Threshold* Strain (% strain)	Comments	
Rigid Translation	Good speckle pattern	1, 3, 5, 6, 7	0.03	0.06	Quality of speckle pattern greatly influences noise threshold	
	Poor speckle pattern	2, 4	0.07-0.17	0.20-0.63		
Rigid Rotation		8, 9	0.03	0.07	1 deg. applied rotation	
			0.25	0.45	5 deg. applied rotation	
Large Strain		10	--	--	Analytic solution unknown	
Constant Strain		11	0.04	0.06	0.2 % applied strain	Error is approximately 30 % of constant strain value
			0.04	0.12	0.4 % applied strain	
Strain Discontinuity		11	46	--	0.2 % applied strain	Width of strain discontinuity
			61	--	0.4 % applied strain	
Sinusoidal Strain Modulations		14	0.03	0.10	$1.8*10^{-3}$ $pixels^{-1}$ average applied strain frequency	
			0.06	0.36	8.8*10-3 pixels-1 average applied strain frequency	
Overlapping Strain Peaks		15	--	1.3	Ratio of peak spacing to peak width of 1.2	Error is approximately 24 % of maximum strain value (5.4 % strain)
				2.6	Ratio of peak spacing to peak width of 0.2	Error is approximately 30 % of maximum strain value (8.8 % strain)

* The noise threshold is taken as 3*(standard deviation) of the error.

Table G.2: Complete Summary of Correlation Results (part 1)

Sample No.	Deformation	Speckle Pattern
1	Rigid translation; 0.05 pixel increments up to 1.00 pixel	Good speckle pattern; varying contrast
2	Rigid translation; 0.05 pixel increments up to 1.00 pixel	Poor speckle pattern; low contrast
3	Rigid translation; 0.1 pixel increments up to 1.00 pixel	Good speckle pattern
4	Rigid translation; 0.1 pixel increments up to 1.00 pixel	Poor speckle pattern; low contrast
5	Rigid translation; 0.1 pixel increments up to 1.00 pixel	Good speckle pattern; varying contrast
6	Rigid translation; 0.1 pixel increments up to 1.00 pixel	Isolated dot speckle pattern
7	Rigid translation; 0.1 pixel increments up to 1.00 pixel	Good speckle pattern (but with less contrast than other speckle patterns)
8	Rigid rotation; 1 deg increments up to 9 deg	Good speckle pattern
9	Rigid rotation; 1 deg increments up to 9 deg	Good speckle pattern
10	Large strain in the vertical normal direction	Good speckle pattern
11	Constant positive strain on left half of image, constant negative strain on right half of image, strain discontinuity in center of image	Good speckle pattern
14	Sinusoidal variation in strain with increasing frequency and amplitude	Good speckle pattern; varying contrast across individual images
15	Modulating strain with increasing distance between strain peaks	Good speckle pattern

Table G.2: Complete Summary of Correlation Results (part 2)

Displacement (pixels)		Strain (% strain)			
Error	**Std. Dev.**	**Error**	**Std. Dev.**	**Comments**	
0.007	0.004	0.017	0.014	Subset 20, Smooth 11,3; Averaged over all images	
0.050	0.039	0.187	0.146	Subset 30, Smooth 11,3, Thresh 0.5; Averaged over all images	
0.005	0.004	0.015	0.013	Subset 20, Smooth 11,3; Averaged over all images	
0.023	0.014	0.058	0.045	Subset 30, Smooth 11,3, Thresh 0.5; Averaged over all images	
0.011	0.004	0.015	0.013	Subset 20, Smooth 11,3; Averaged over all images	
0.009	0.004	0.014	0.012	Subset 20+A9:I9, Smooth 11,3; Averaged over all images	
0.012	0.005	0.015	0.013	Subset 20, Smooth 11,3; Averaged over all images	
0.018	0.005	0.020	0.015	1 deg applied rotation	
0.034	0.010	0.037	0.028	2 deg applied rotation	Subset 20, Smooth 11,3; Averaged over center of image
0.050	0.016	0.057	0.045	3 deg applied rotation	
0.088	0.057	0.121	0.119	5 deg applied rotation	
0.017	0.005	0.019	0.014	1 deg applied rotation	
0.033	0.012	0.036	0.029	2 deg applied rotation	Subset 20, Smooth 11,3; Averaged over center of image
0.043	0.019	0.054	0.050	3 deg applied rotation	
0.073	0.052	0.096	0.110	5 deg applied rotation	
--	--	--	--	Analytic solution unknown.	
0.017	0.007	0.019	0.014	0.195 % applied strain	Subset 20, Smooth 11,3; Averaged over left and right portions of image, where strain is constant
0.014	0.007	0.039	0.026	0.391 % applied strain	
40.1*	2.1*	--	--	0.195 % applied strain	Subset 20, Smooth 11,3; *Width of the sharp strain discontinuity
54.4*	2.2*	--	--	0.391 % applied strain	
0.008	0.006	0.029	0.022	$1.8*10^{-3}$ pixels^{-1} average applied strain frequency	Subset 20, Smooth 11,3; Averaged over the right portion of the image, for X>1478
0.012	0.008	0.043	0.030	$5.3*10^{-3}$ pixels^{-1} average applied strain frequency	
0.023	0.013	0.130	0.075	$8.8*10^{-3}$ pixels^{-1} average applied strain frequency	
--	--	0.534	0.686	Ratio peak spacing to peak width = 0.24	Subset 20, Smooth 11,1; Averaged over the portion of the image where the applied strain is non-zero
--	--	0.315	0.562	Ratio peak spacing to peak width = 0.95	
--	--	0.202	0.378	Ratio peak spacing to peak width >1.19	

Sample 1 (TexGen Shift in X, Y with varying contrast)

Deformation: Rigid translation in both X and Y directions, with a step size of 0.05 pixels.

Images: 512 x 512 pixels. Varying contrast of images, but all images have a relatively good speckle pattern.

Results:

Using a threshold value of 0.5, all of the grid points correlated for all of the images (Fig. G.2). The error in the displacements has a local minimum at 0.5 pixels of applied displacement (Fig. G.3). The cause of this local minimum is unknown; it could be related to either the DIC code or to the image manipulation algorithm. The error in the raw correlated displacement values, averaged over the entire field of view for all images (except the self-correlation of the reference image), is approximately 0.05 +/- 0.04 pixels for a subset of 10 and 0.02 + 0.01 pixels for a subset of 20 (Fig. G.5).

In theory, the raw displacements could be infinitely smoothed and a nearly-exact solution recovered since the deformation is rigid translation. However, in practice, if the data is smoothed too much, information on spatial variation will be lost. The smoothing parameters chosen in this section are similar to those chosen in the varying strain samples described in Samples 11, 14, and 15, and so are considered to be reasonable. Using a kernel size of 11 and smoothing 3 times provides the most reduction in error. A kernel size of 7 with 3 smoothing passes and a kernel size of 11 with 1 smoothing pass provide nearly identical reductions in error.

The average error in the strain values computed from the raw displacements is 1.5-2.0 % strain for a subset of 20 and 0.5-0.6 % strain for a subset of 10. These results emphasize the need for some smoothing of the raw displacements before computation of strains. The reduction of error in the calculated strains follows the same trend as the error in displacements with regard to the different smoothing parameters.

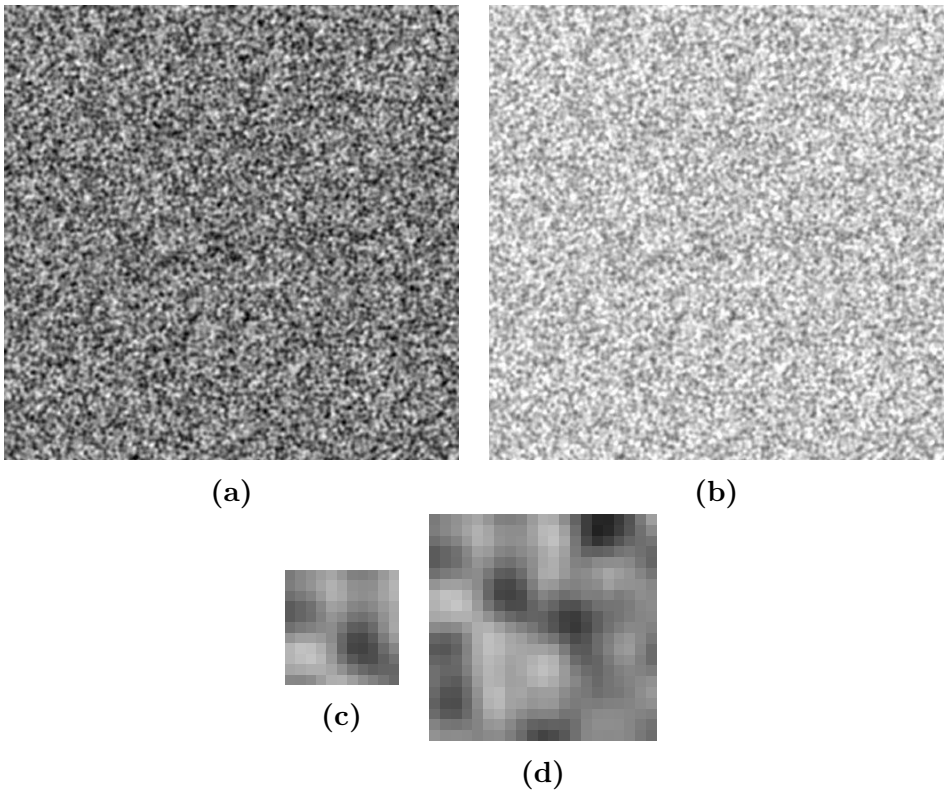

Figure G.1: (a) Reference image and (b) final image. The contrast of the images decreases moving from the reference to the final image. (c-d) Representative subsets for subset size 10 and 20 respectively.

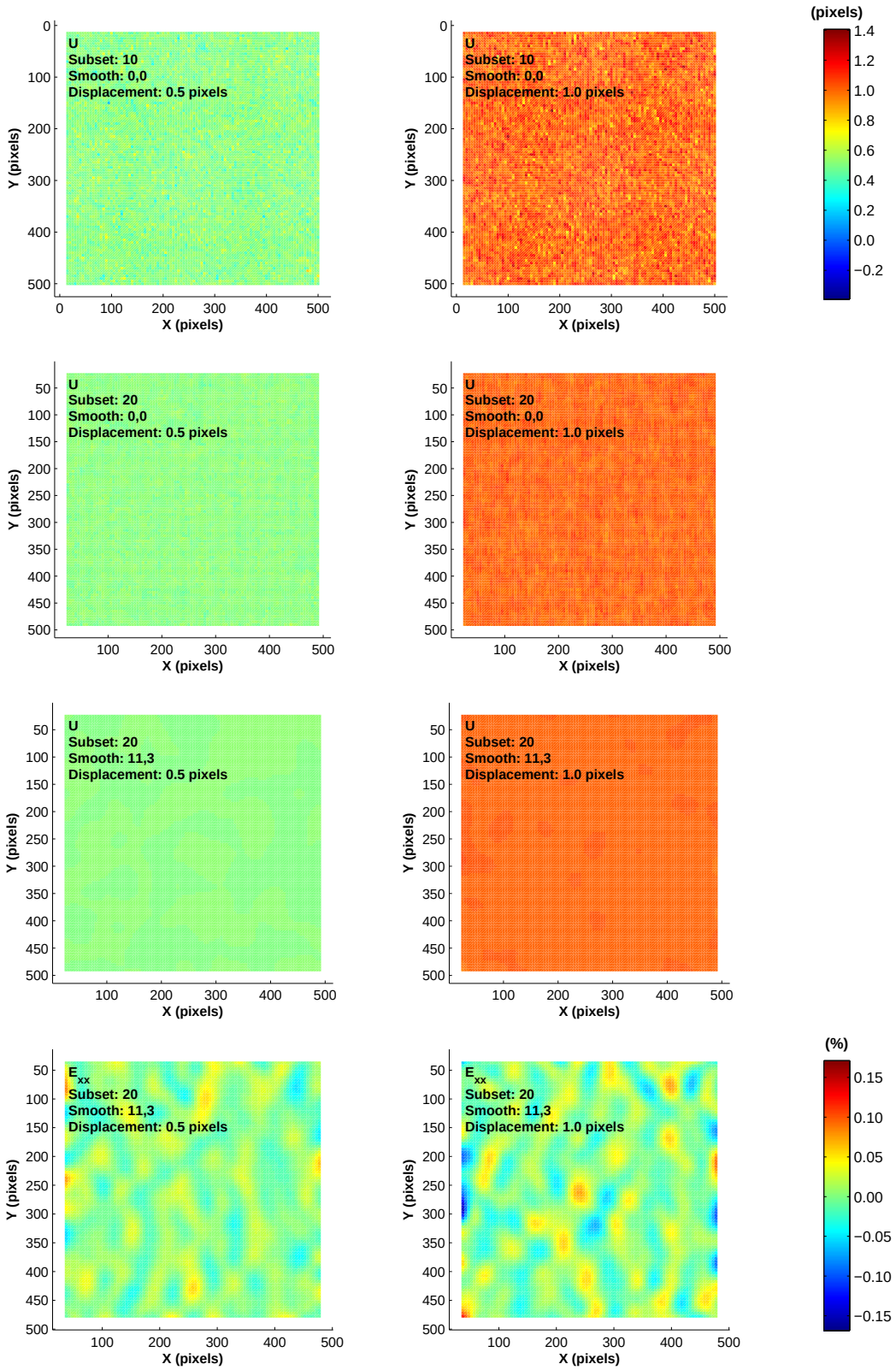

Figure G.2: Select contour plots of the horizontal displacement, U, and the horizontal normal strain, E_{xx}.

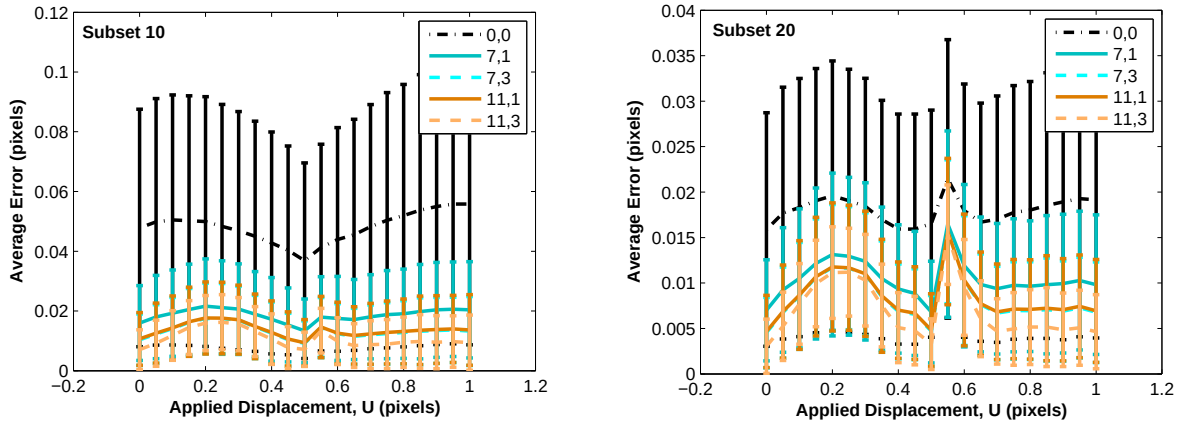

Figure G.3: Error, averaged over the entire image, of the horizontal displacement, U, as a function of the applied horizontal displacement. The legend indicates different smoothing parameters as [smooth kernel size, number of smoothing passes]. The error bars represent one standard deviation.

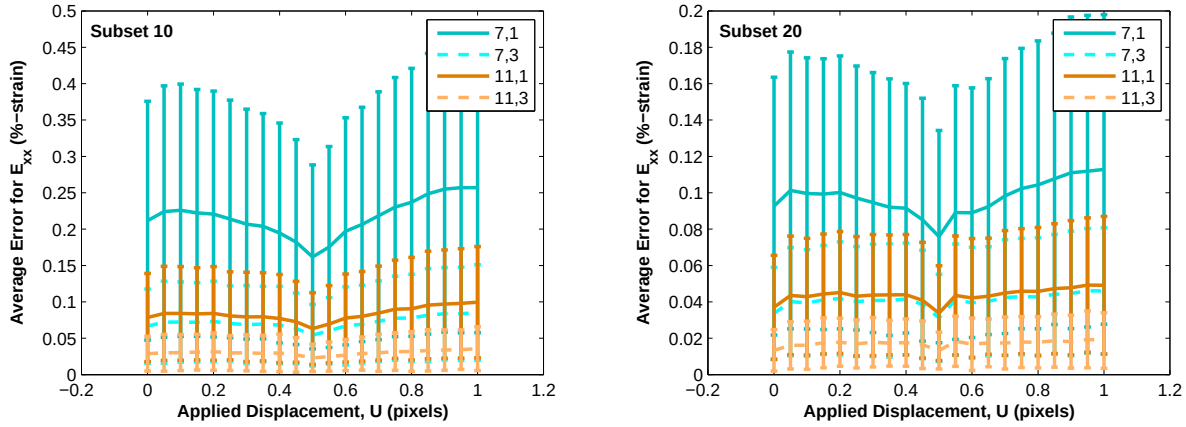

Figure G.4: Error, averaged over the entire image, of the horizontal normal strain, E_{xx}, as a function of the applied horizontal displacement. The legend indicates different smoothing parameters as [smooth kernel size, number of smoothing passes]. The error bars represent one standard deviation.

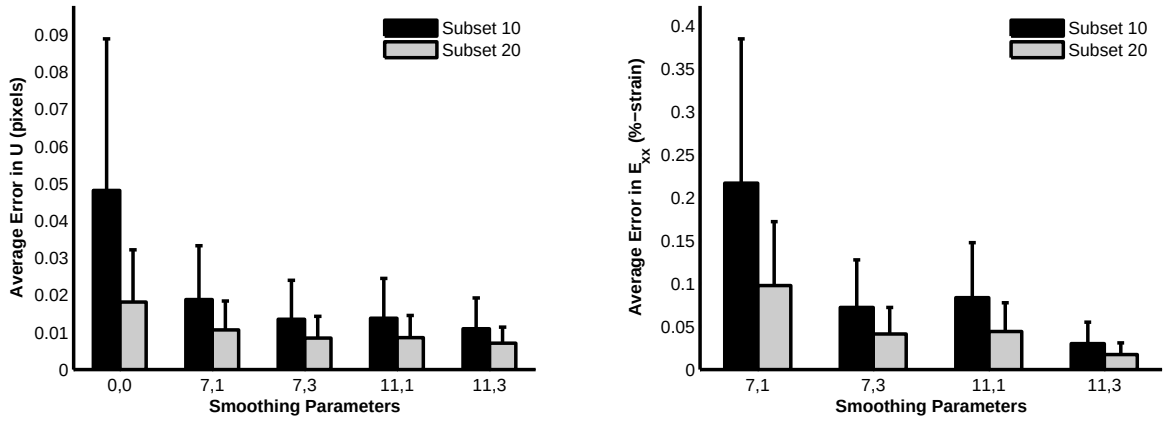

Figure G.5: Error, averaged over all the images except for the self-correlation of the reference image, of the horizontal displacement, U, and the horizontal normal strain, E_{xx}, as a function of subset size and smoothing parameters. The smoothing parameters labeled on the x-axis are [smooth kernel size, number of smoothing passes]. The error bars represent one standard deviation.

Sample 2 (TexGen Shift in X, Y with low contrast)

Deformation: Rigid translation in both X and Y directions, with a step size of 0.05 pixels.

Images: 512 x 512 pixels. Poor quality speckle pattern; low contrast.

Results:

Compared to Sample 1, the speckle pattern in Sample 2 has low contrast and more blank space between identifiable features. Therefore, larger subset sizes (20 and 30) are evaluated in this section compared to the previous section.

Using a threshold of 0.50, on average 8 % of grid points did not correlate for a subset of 20, and an average of 2 % of grid points did not correlate for a subset of 30. For a subset of 30, less than 4 grid points (0.05 % of grid points) did not correlate when the threshold was reduced to 0.35, and all points correlated when the threshold was further reduced to 0.25 (Fig. G.7). The errors in the raw displacements, smoothed displacements and strains are equivalent for all thresholds, given a subset of 30 (Fig G.10). No improvement is observed by reducing the threshold to have more correlated points.

As a result of the poorer speckle pattern, the errors in the displacements are larger for Sample 2 compared to Sample 1. The same trends with regards to smoothing are observed in Sample 2 as in Sample 1. Given this speckle pattern, the parameters with the least error in the strain (subset 30, smooth 11,3, any threshold) still resulted in fairly large strain errors of approximately 0.2 %. Therefore, caution must be used when using this DIC code to correlate images with a poor speckle pattern.

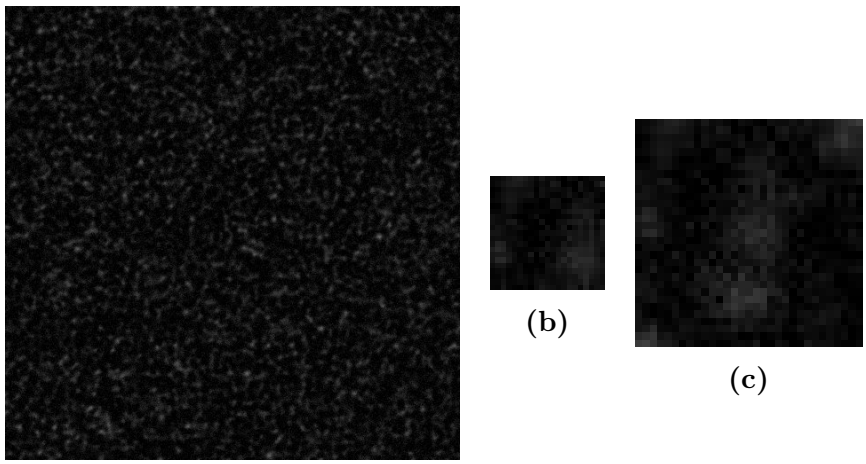

Figure G.6: (a) Reference image. (b-c) Representative subsets for subset size 20 and 30 respectively.

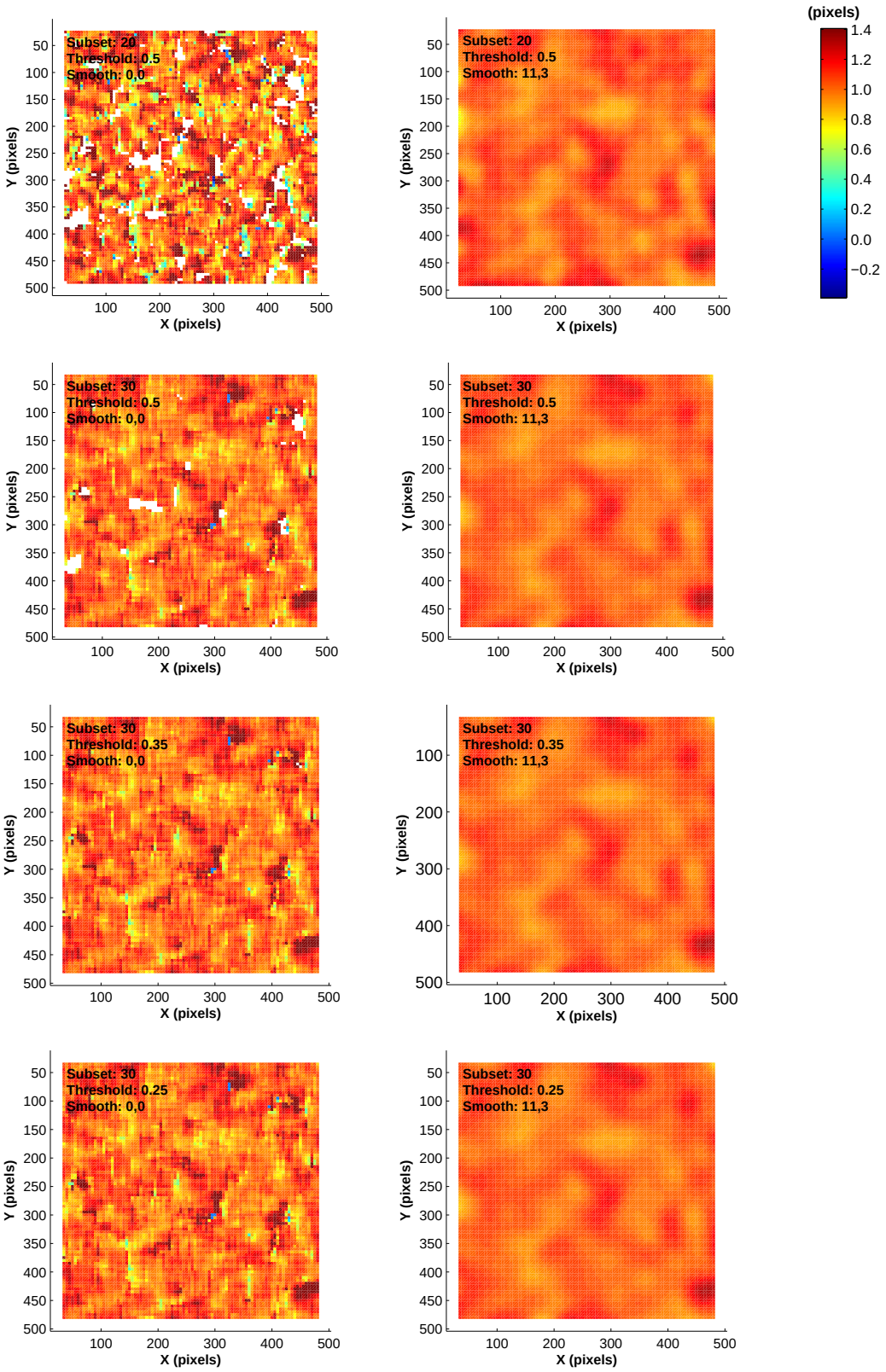

Figure G.7: Select contour plots of the horizontal displacement, U, at the applied displacement of 1.00 pixel.

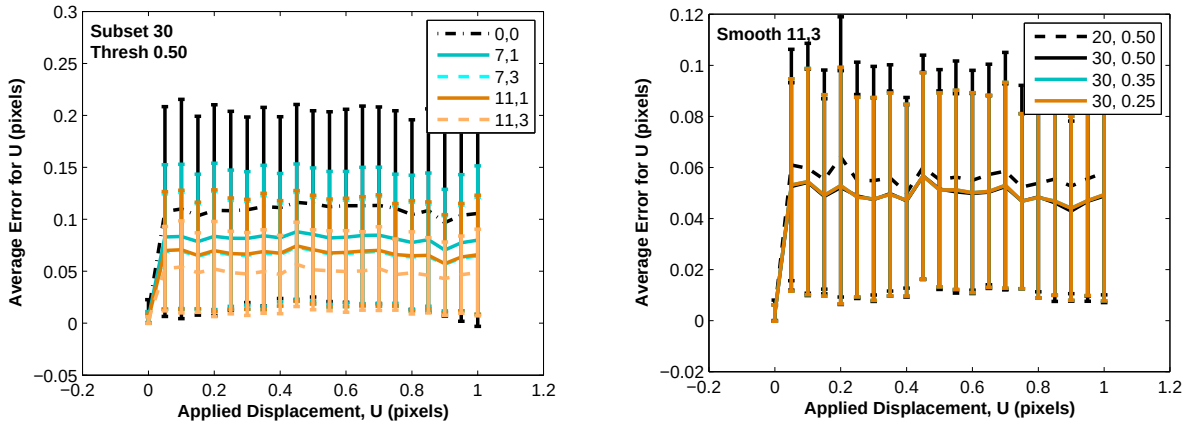

(a) **(b)**

Figure G.8: Error, averaged over the entire image, of the horizontal displacement, U, as a function of the applied horizontal displacement. The legend in (a) indicates different smoothing parameters as [smooth kernel size, number of smoothing passes]. The legend in (b) indicates [subset size, threshold value]. The error bars represent one standard deviation.

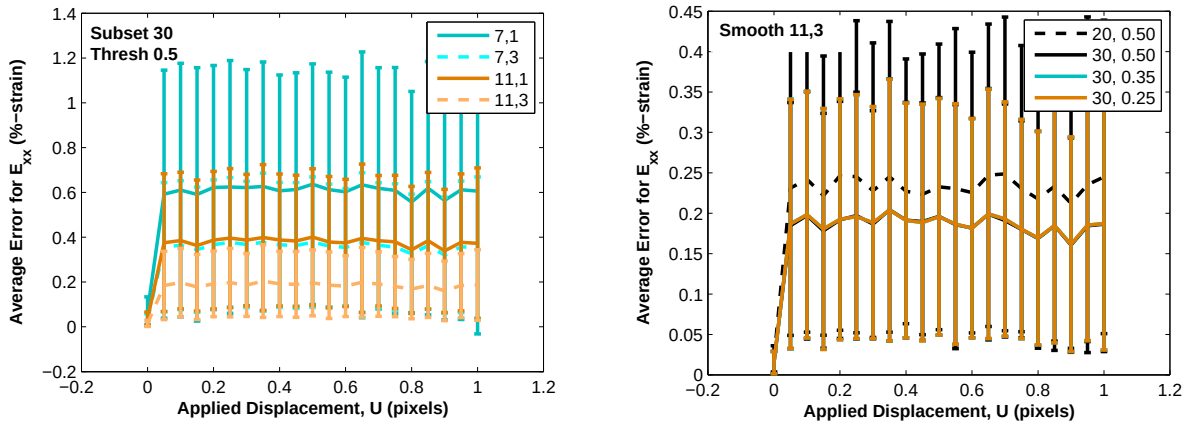

(a) **(b)**

Figure G.9: Error, averaged over the entire image, of the horizontal normal strain, E_{xx}, as a function of the applied horizontal displacement. The legend in (a) indicates different smoothing parameters as [smooth kernel size, number of smoothing passes]. The legend in (b) indicates [subset size, threshold value]. The error bars represent one standard deviation.

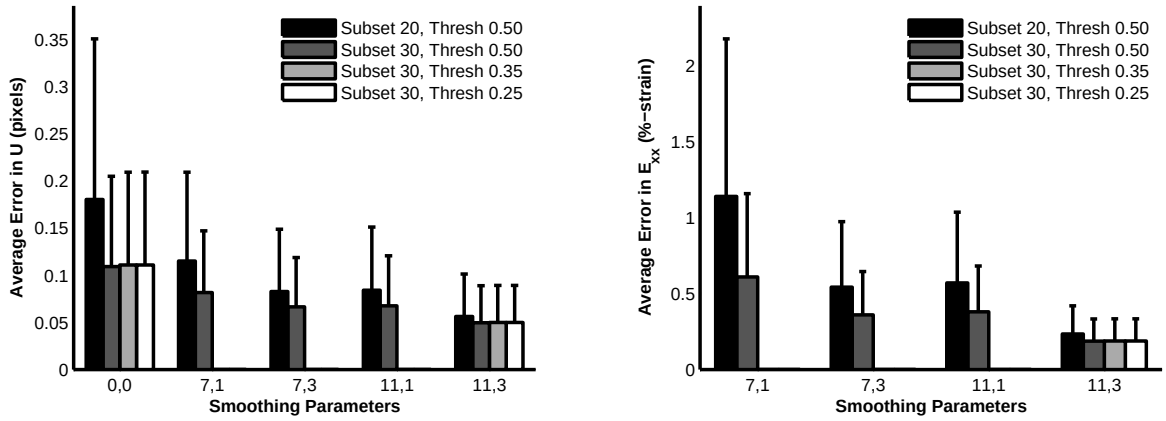

Figure G.10: Error, averaged over all the images except for the self-correlation of the reference image, of the horizontal displacement, U, and the horizontal normal strain, E_{xx}, as a function of subset size, threshold value, and smoothing parameters. The smoothing parameters labeled on the x-axis are [smooth kernel size, number of smoothing passes]. The error bars represent one standard deviation.

Sample 3 (FFT Shift in X, Y)

Deformation: Rigid translation in both X and Y directions, with a step size of 0.10 pixels.

Images: 512 x 512 pixels. Constant and relatively good speckle pattern for all images.

Results:

The results of Sample 3 are similar to those of Sample 1.

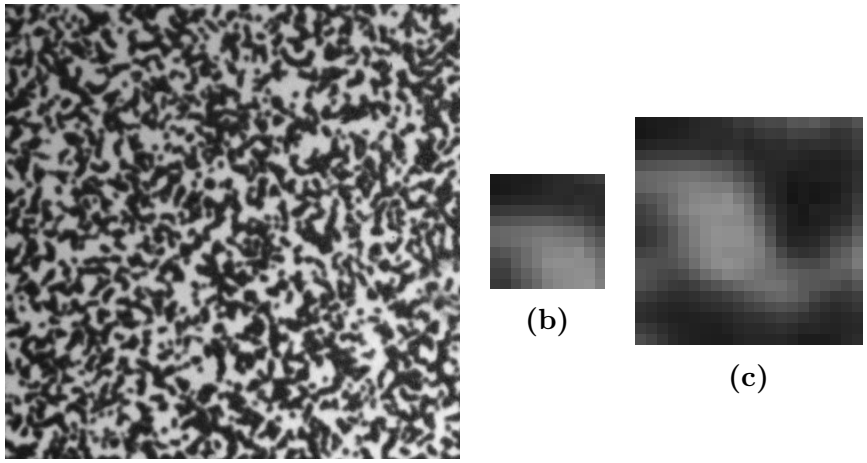

(a) **(b)** **(c)**

Figure G.11: (a) Reference image. (b-c) Representative subsets for subset size 10 and 20 respectively.

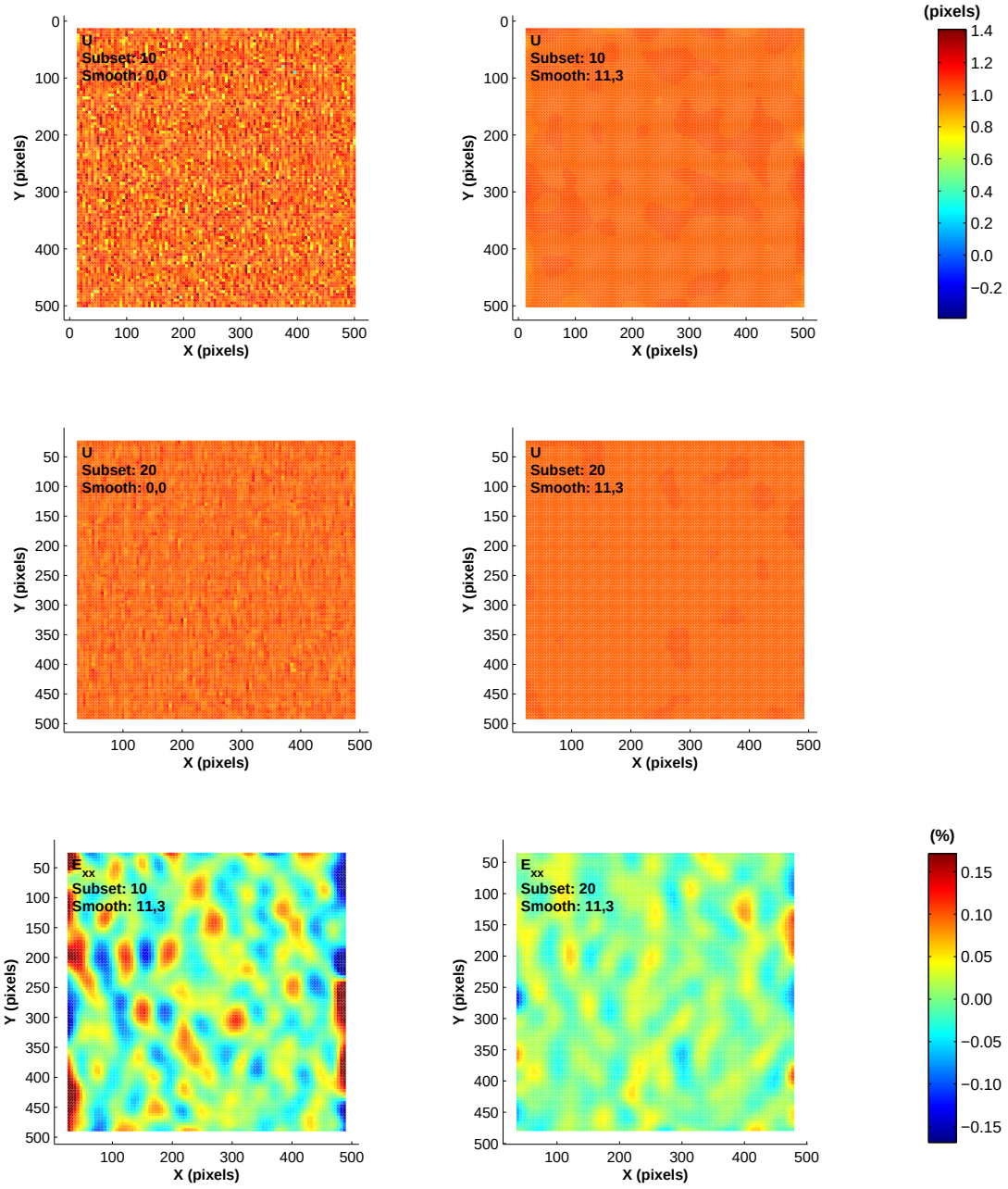

Figure G.12: Select contour plots of the horizontal displacement, U, and horizontal normal strain, E_{xx}, at the applied horizontal displacement of 1.00 pixel.

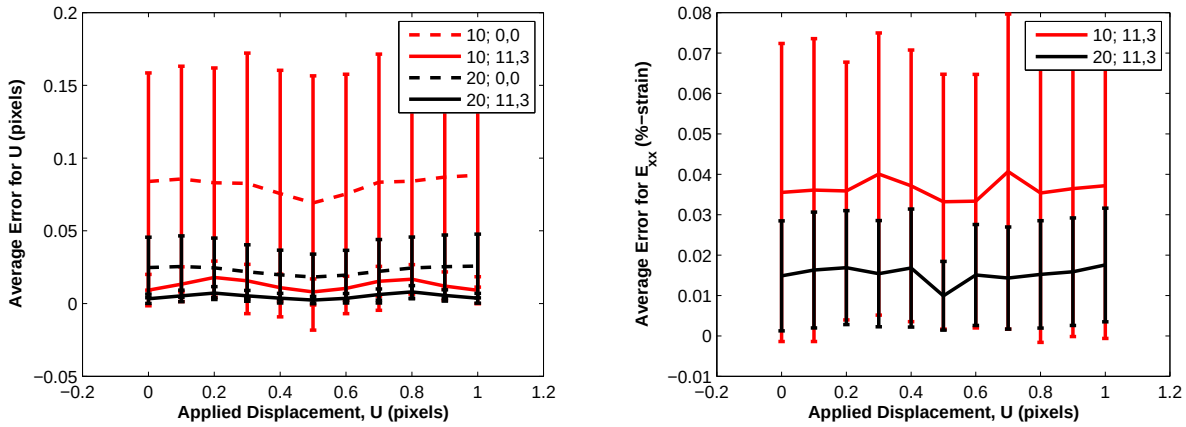

Figure G.13: Error, averaged over the entire image, of the horizontal displacement, U, and the horizontal normal strain, E_{xx}, as a function of the applied horizontal displacement. The legend indicates correlation and smoothing parameters as [subset size; smooth kernel size, number of smoothing passes]. The error bars represent one standard deviation.

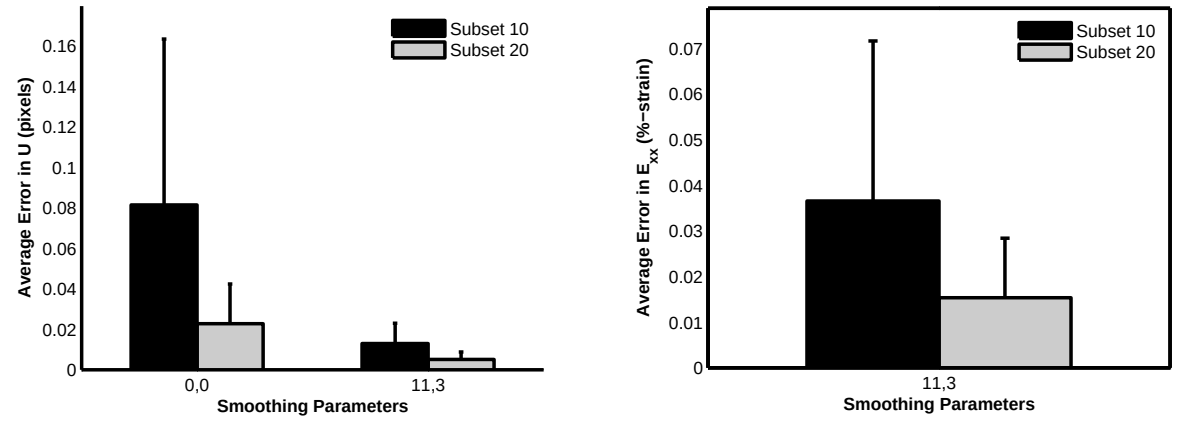

Figure G.14: Error, averaged over all the images except for the self-correlation of the reference image, of the horizontal displacement, U, and the horizontal normal strain, E_{xx}, as a function of subset size and smoothing parameters. The smoothing parameters labeled on the x-axis are [smooth kernel size, number of smoothing passes]. The error bars represent one standard deviation.

Sample 4 (FFT Shift in X, Y with low contrast)

Deformation: Rigid translation in both X and Y directions, with a step size of 0.10 pixels.

Images: 512 x 512 pixels. Poor speckle pattern; low contrast.

Results:

The results of Sample 4 are similar to those of Sample 2, which also had a poor quality speckle pattern.

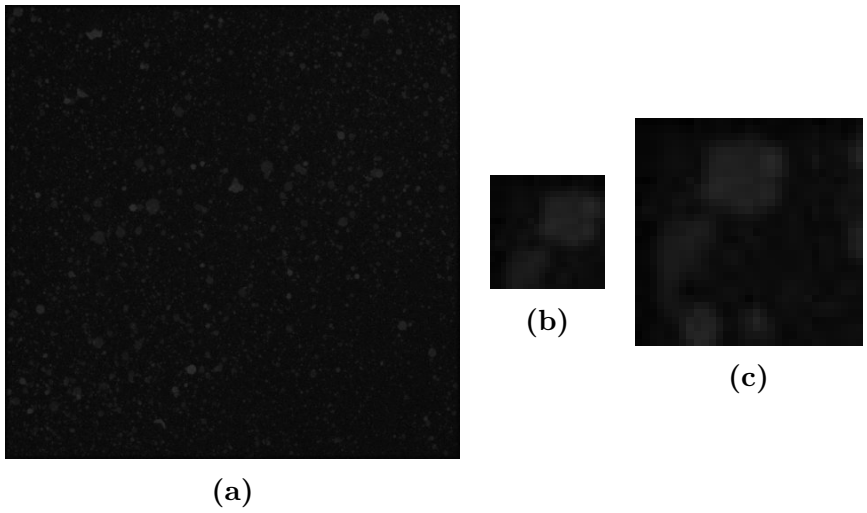

Figure G.15: (a) Reference image. Representative subsets for (b) subset size 20 (b) and (c) subset size 30.

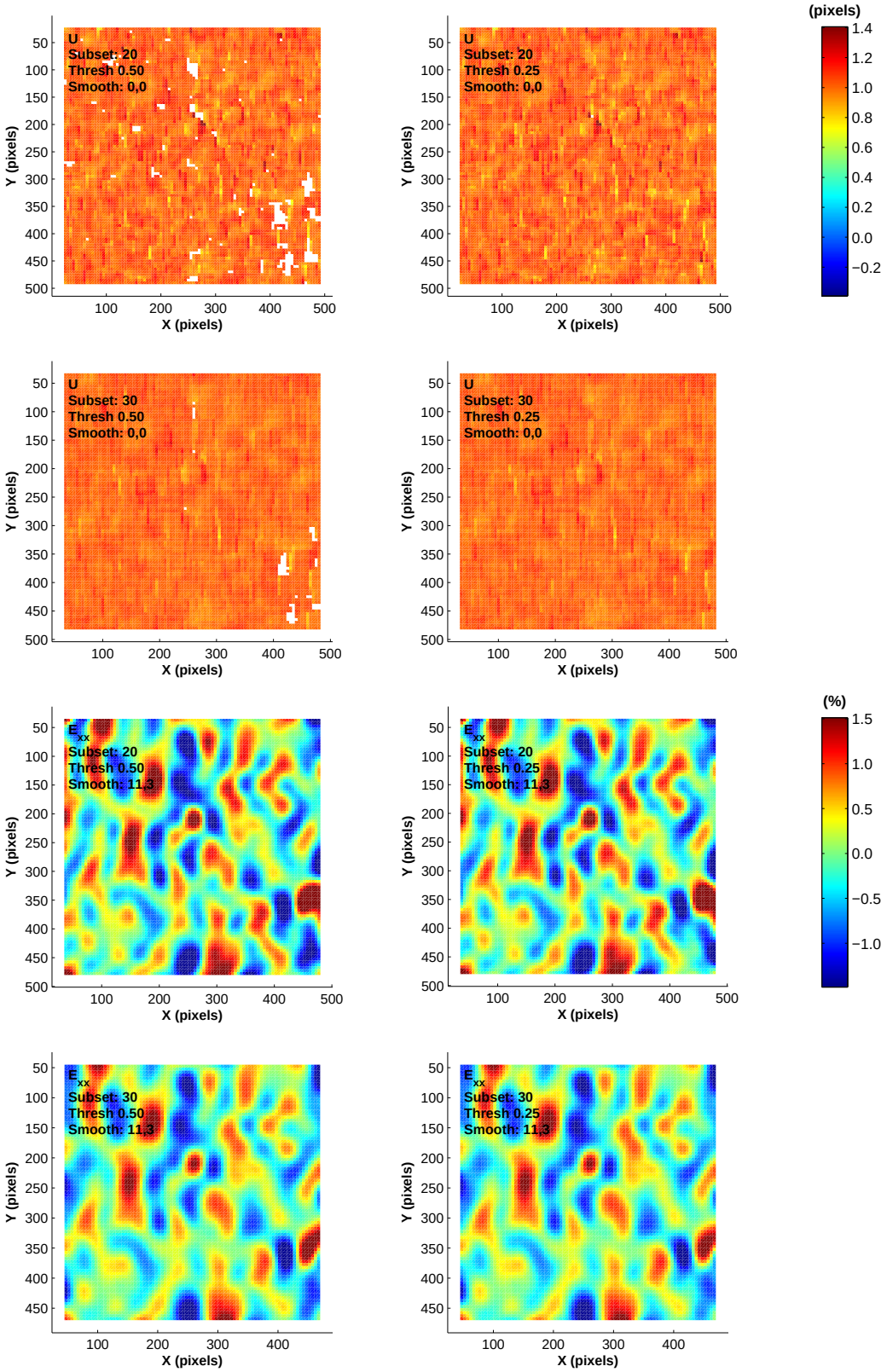

Figure G.16: Select contour plots of the horizontal displacement, U, and the horizontal normal strain, E_{xx}, at the applied displacement of 1.00 pixel.

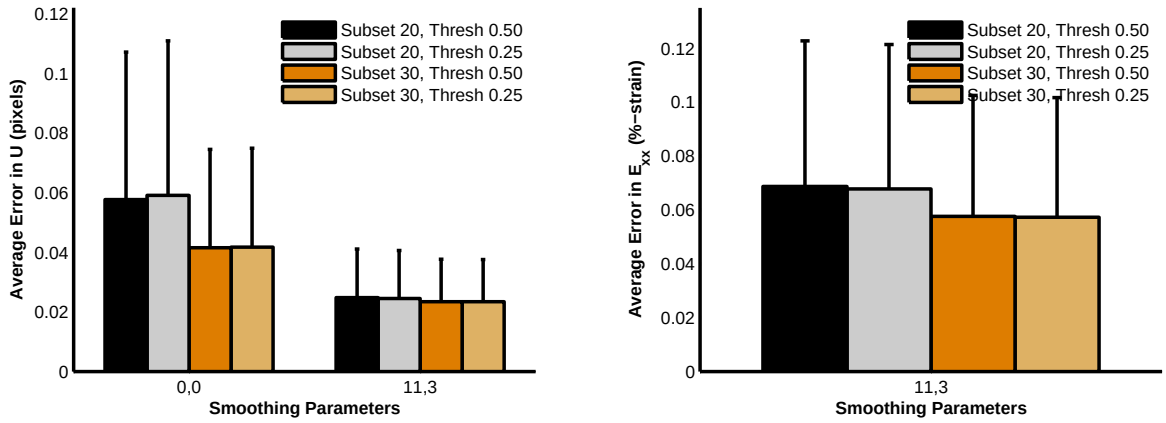

Figure G.17: Error, averaged over all the images except for the self-correlation of the reference image, of the horizontal displacement, U, and the horizontal normal strain, E_{xx}, as a function of subset size, threshold value, and smoothing parameters. The smoothing parameters labeled on the x-axis are [smooth kernel size, number of smoothing passes]. The error bars represent one standard deviation.

Sample 5 (FFT Shift in X, Y with varying contrast)

Deformation: Rigid translation in both X and Y directions, with a step size of 0.1 pixels.

Images: 512 x 512 pixels. Varying contrast of images, but all images have a relatively good speckle pattern.

Results:

The results of Sample 5 are similar to those of Samples 1 and 3.

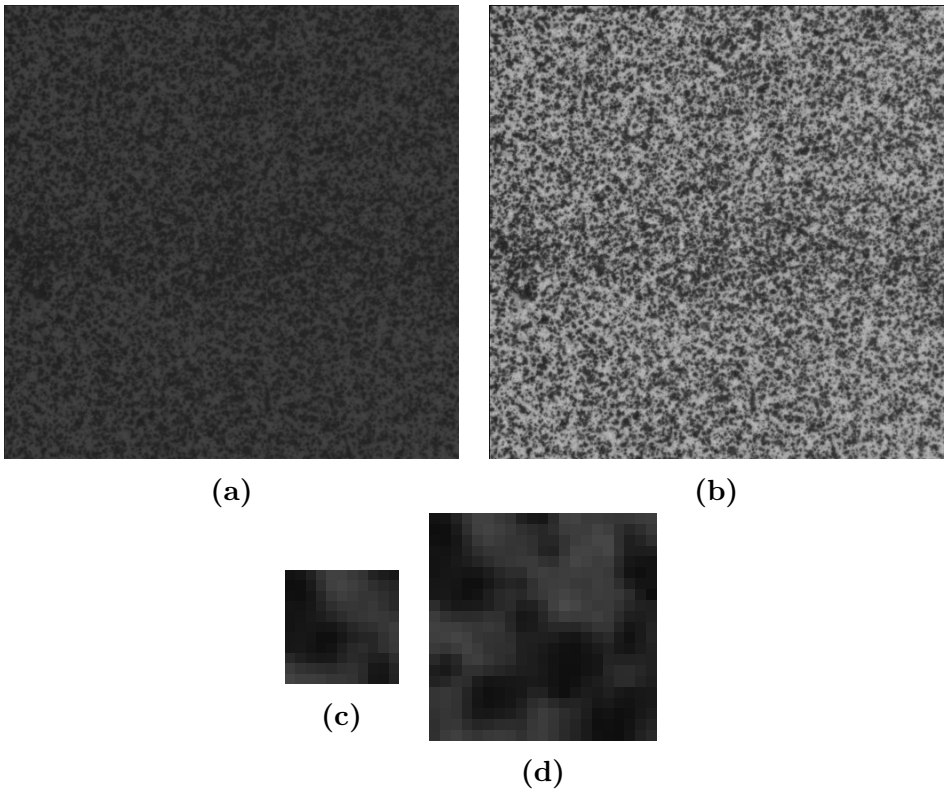

Figure G.18: (a) Image with the poorest contrast (image 8), (b) image with the best contrast (image 11), (c-d) reference image (image 1) with subset size of 10 and 20 respectively.

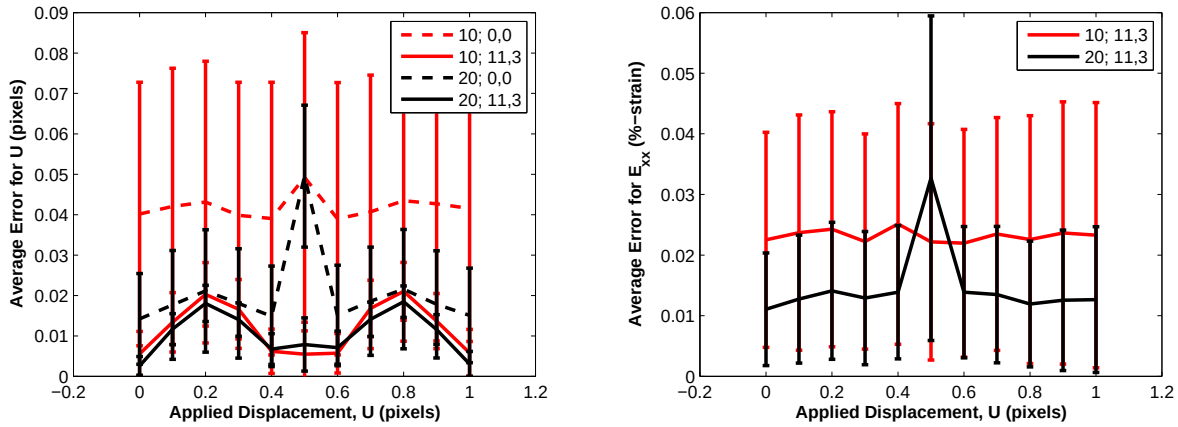

Figure G.19: Error, averaged over the entire image, of the horizontal displacement, U, and the horizontal normal strain, E_{xx}, as a function of the applied horizontal displacement. The legend indicates correlation and smoothing parameters as [subset size; smooth kernel size, number of smoothing passes]. The error bars represent one standard deviation.

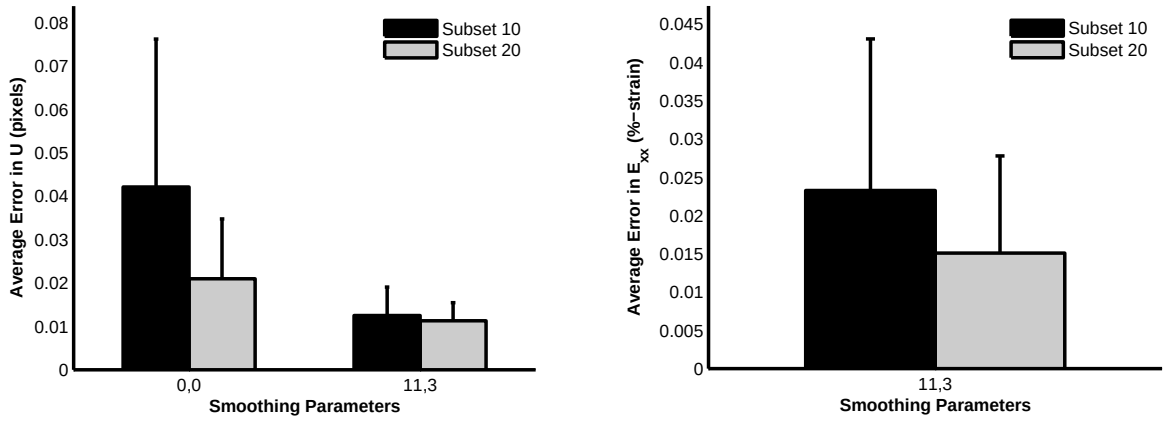

Figure G.20: Error, averaged over all the images except for the self-correlation of the reference image, of the horizontal displacement, U, and the horizontal normal strain, E_{xx}, as a function of subset size and smoothing parameters. The smoothing parameters labeled on the x-axis are [smooth kernel size, number of smoothing passes]. The error bars represent one standard deviation.

Sample 6 (Prosilica Bin Shift in X, Y)

Deformation: Rigid translation in both X and Y directions, with a step size of 0.1 pixels.

Images: 487 x 325 pixels. Isolated dot speckle pattern.

Results:

The results of Sample 6 are similar to those of Samples 1, 3, and 5.

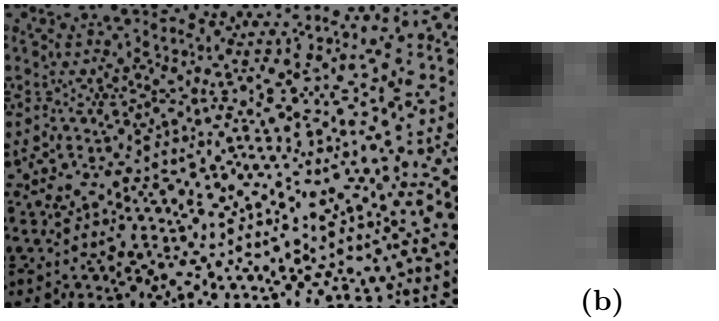

(a) (b)

Figure G.21: (a) Reference image. (b) Representative subset for subset size 20.

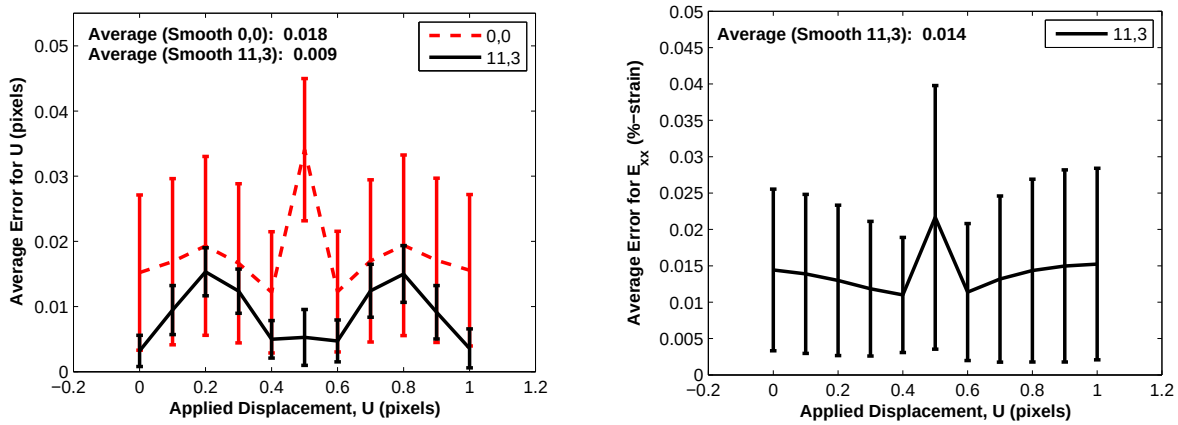

Figure G.22: Error, averaged over the entire image, of the horizontal displacement, U, and the horizontal normal strain, E_{xx}, as a function of the applied horizontal displacement. A subset size of 20 was used for these correlations. The legend indicates smoothing parameters as [subset size; smooth kernel size, number of smoothing passes]. The note in the top-left corner gives the error averaged over all images except for the self-correlation of the reference image. The error bars represent one standard deviation.

Sample 7 (Prosilica Bin Shift in X, Y)

Deformation: Rigid translation in both X and Y directions, with a step size of 0.1 pixels.

Images: 487 x 325 pixels. Good speckle pattern.

Results:

The results of Sample 7 are similar to those of Samples 1, 3, 5, and 6.

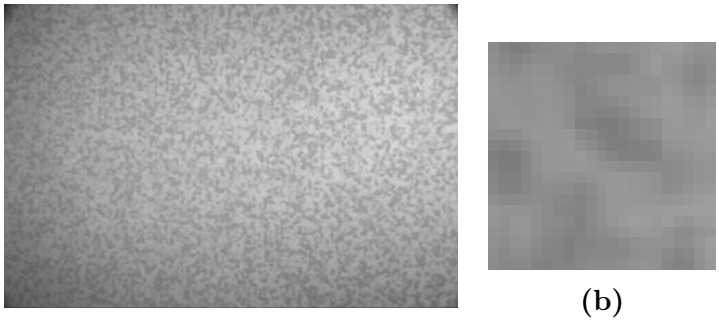

(a) (b)

Figure G.23: (a) Reference image. (b) Representative subset for subset size 20.

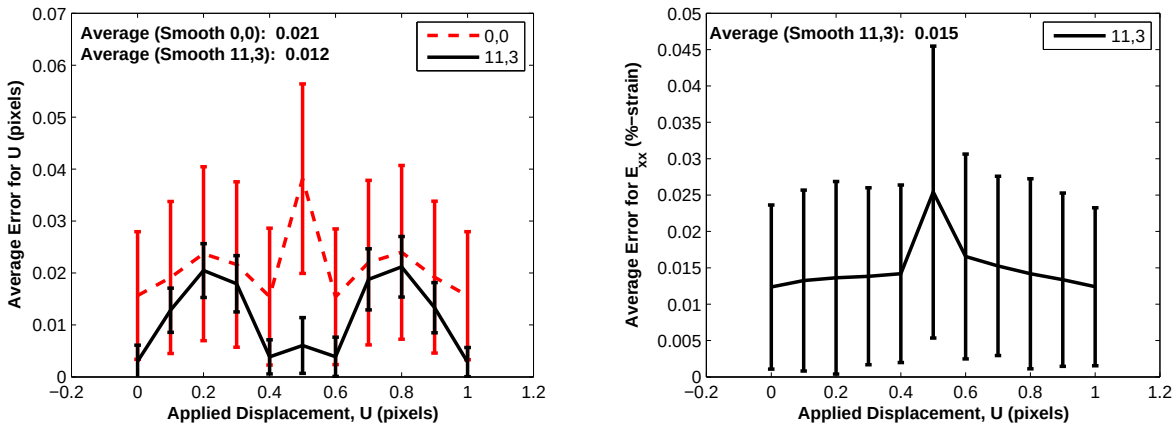

Figure G.24: Error, averaged over the entire image, of the horizontal displacement, U, and the horizontal normal strain, E_{xx}, as a function of the applied horizontal displacement. A subset size of 20 was used for these correlations. The legend indicates smoothing parameters as [subset size; smooth kernel size, number of smoothing passes]. The note in the top-left corner gives the error averaged over all images except for the self-correlation of the reference image. The error bars represent one standard deviation.

Sample 8 (TexGen Rotation)

Deformation: Rigid body rotation about the center of the image in 1 deg increments from 0 deg to 9 deg.

Images: 512 x 512 pixels. Constant speckle pattern.

Results:

Because the rotations induce large displacements (compared to the rigid body translations in image sets 1-4), the reduced images were correlated first to provide initial guesses for the full correlation. For all the analyses presented in this section, the same reduced correlation results were used, with the following parameters: reduction of 3, one reduced correlation, subset of 20 and threshold of 0.25. The effect of using initial guesses is seen most clearly in the contour plots of the difference between the analytic and raw correlated displacements for the largest rotation (Figs. G.27 - G.27); in these contour plots, the error follows a block pattern that relates to the location of the the grid points used for the reduced correlation.

For all applied rotations, the edges of the images rotate out of the field of view. For rotations smaller than approximately 6 deg, the border between the grid points closest to the image edge and the image edge itself is sufficient that all of the grid points are correlated. For larger rotations, however, grid points near the image edge leave the field of view and cannot be correlated (Figs. G.27 - G.27). The error of the smoothed correlated displacements are largest where the grid points did not correlate, because of the large area over which displacements were extrapolated (Figs. G.27 - G.27).

For a more accurate picture of the error associate purely with the rotations (ignoring error associated with grid points leaving the field of view and not correlating), the error is averaged over the center of the field of view, where $100 < X < 412$ and $100 < Y < 412$ (i.e. discounting any grid points that are within 100 pixels from the image edges). The average error for both the displacements and the strains increases monotonically with applied rotation (Fig. G.29). Therefore, caution must be exercised when using this DIC code in situations in which the test sample undergoes large rotations.

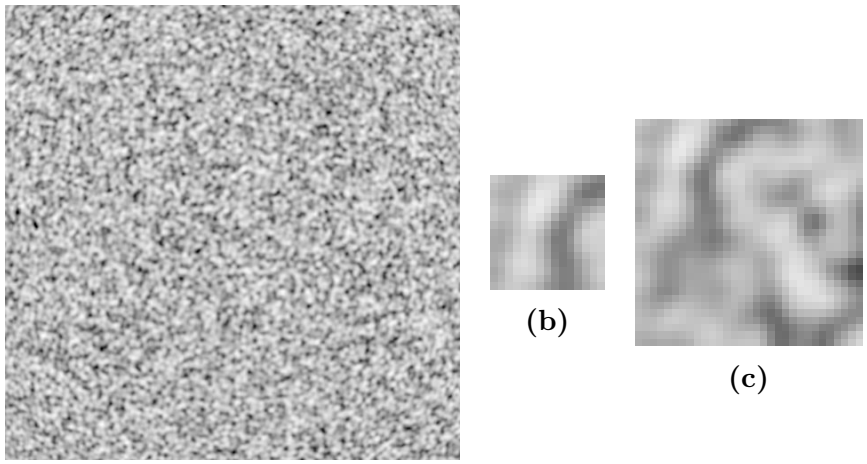

Figure G.25: (a) Reference image. (b-c) Representative subsets for subset size 20 and subset size 30 respectively.

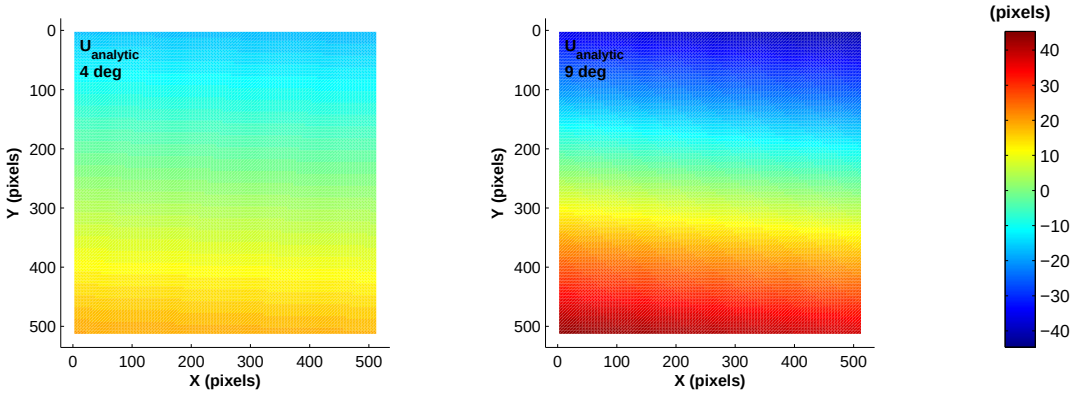

Figure G.26: Contour plots of the analytical horizontal displacement, U, at 4 deg and 9 deg rotations.

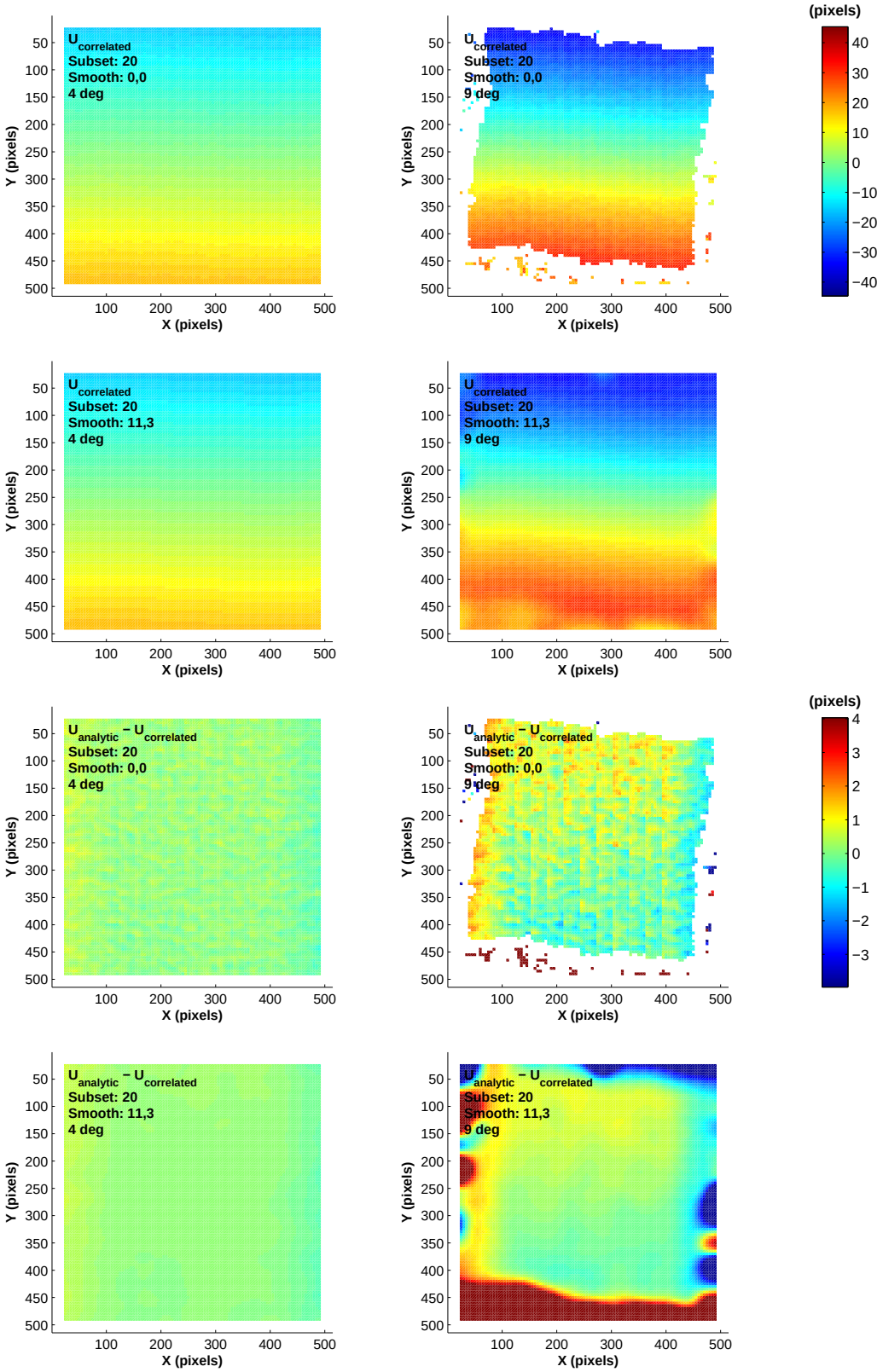

Figure G.27: Select contour plots of the correlated horizontal displacement, $U_{correlated}$, (subset 20) and the difference between the correlated displacement and the analytic displacement, $U_{analytic}$ - $U_{correlated}$, at applied rotations of 4 deg and 5 deg.

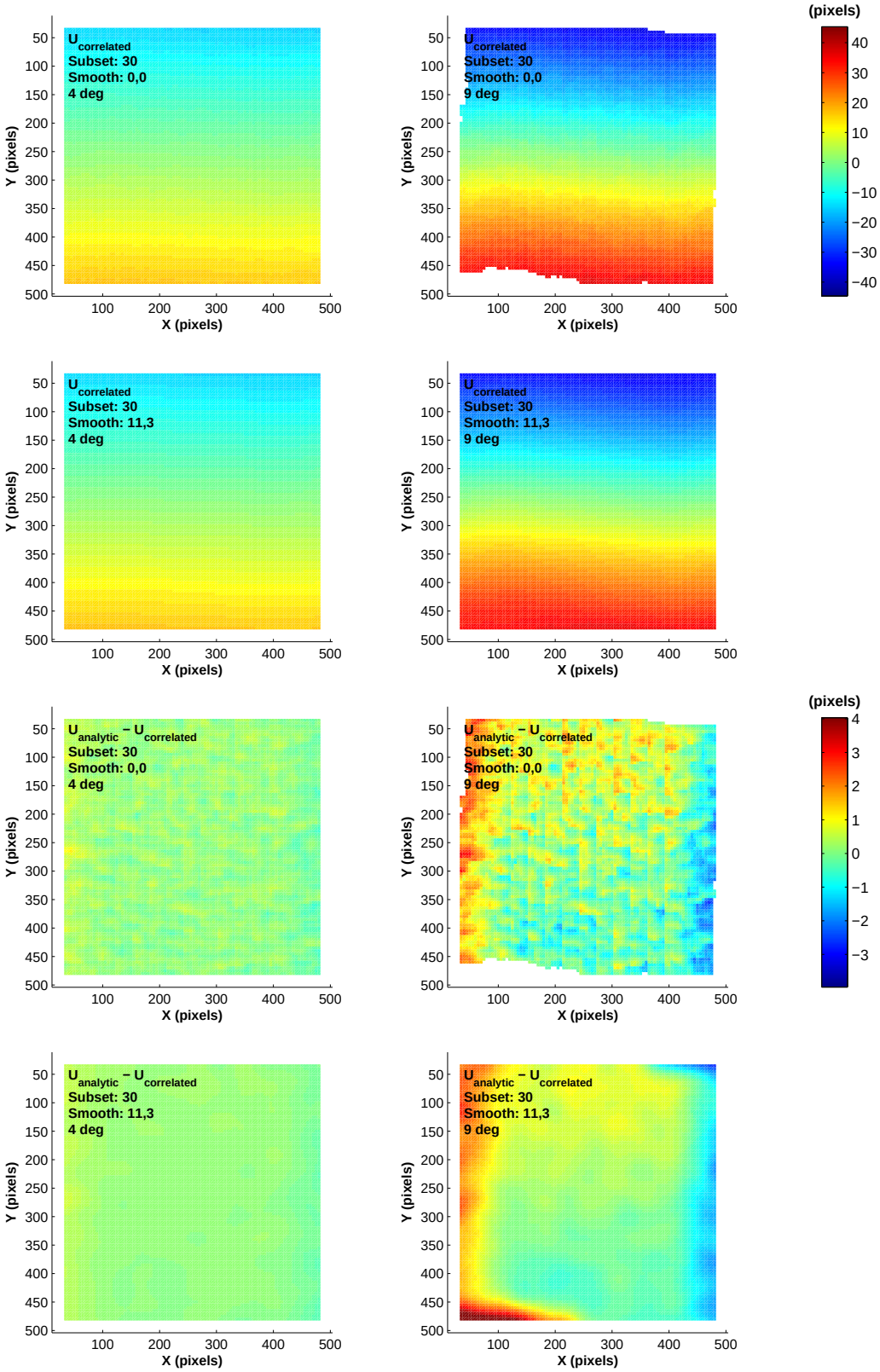

Figure G.28: Select contour plots of the correlated horizontal displacement, $U_{correlated}$, (subset 30) and the difference between the correlated displacement and the analytic displacement, $U_{analytic}$ - $U_{correlated}$, at applied rotations of 4 deg and 5 deg.

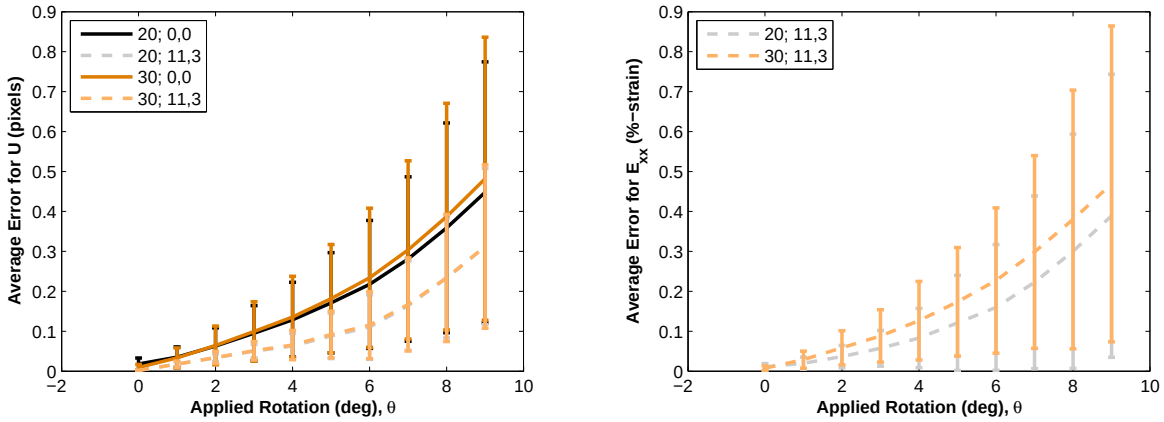

Figure G.29: Error of horizontal displacement, U, and horizontal normal strain, E_{xx}, as a function of applied rotation. The error was averaged over the center of the field of view, where $100 < X < 412$ and $100 < Y < 412$, to avoid contribution to the error from grid points that rotated out of the field of view. The legend indicates the correlation and smoothing parameters as [subset size; smooth kernel size, number of smoothing passes]. The error bars represent one standard deviation.

Sample 9 (FFT Rotation)

Deformation: Rigid body rotation about the center of the image in 1 deg increments from 0 deg to 9 deg.

Images: 512 x 512 pixels. Constant speckle pattern.

Results:

The correlation results of Sample 9 are similar to those from Sample 8.

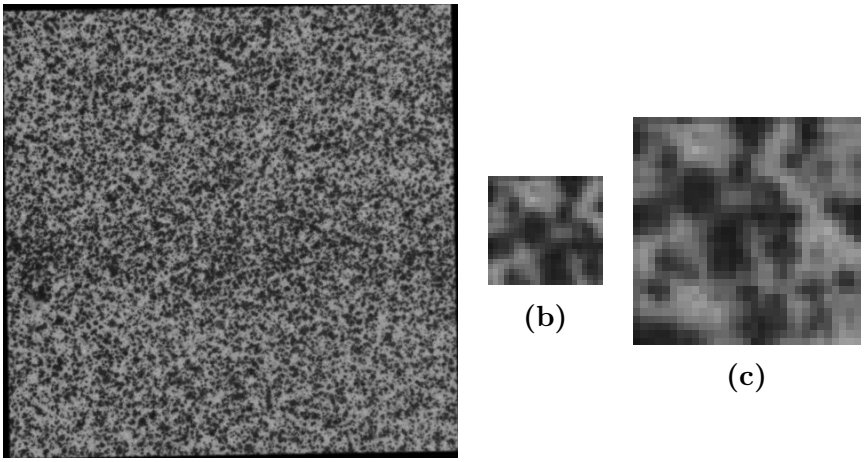

(a) **(b)** **(c)**

Figure G.30: (a) Reference image. (b-c) Representative subsets for subset size 20 and 30 respectively.

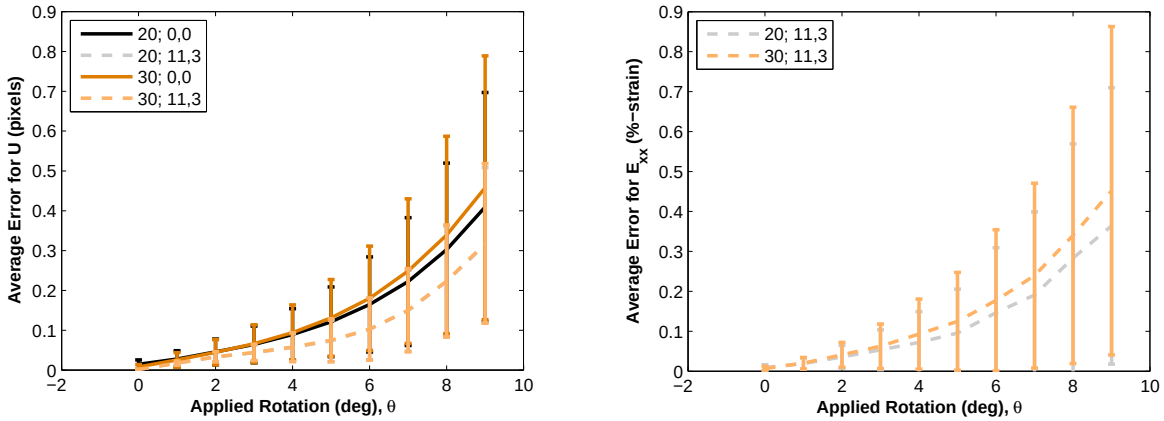

Figure G.31: Error of horizontal displacement, U, and horizontal normal strain, E_{xx}, as a function of applied rotation. The error was averaged over the center of the field of view, where $100 < X < 412$ and $100 < Y < 412$, to avoid contribution to the error from grid points that rotated out of the field of view. The legend indicates the correlation and smoothing parameters as [subset size; smooth kernel size, number of smoothing passes]. The error bars represent one standard deviation.

Sample 10 (Large Strain)

Deformation: Large displacements and strains in the vertical direction. Exact analytic solution is unknown.

Images: 512 x 512 pixels. Good speckle pattern initially but large strain stretches speckle pattern significantly in the vertical direction.

Results:

This image set has two challenges: large displacements and a stretched speckle pattern. The first challenge of large displacements is addressed by correlating the reduced images to provide initial guesses for the correlation of the full images. The second challenge of a stretched speckle pattern is addressed by performing incremental correlations in which the preceding image, instead of the first image, is used as the reference image; changing the reference image for each image minimizes the distortion of the speckle pattern between the reference image and the image being correlated. Typically, using initial guesses and using the preceding image as a reference image would provide satisfactory correlation results. For this particular image set, however, there are still many points that are not correlated for the last image. Reducing the threshold value has no effect, as the points that did not correlate have a correlation coefficient of either 0 (because the control points moved out of the image) or -1 (because the correlated displacement is greater than the maximum allowed by the code). To address the latter set of control points, the search zone was increased from 2 to 4. Increasing the search zone allowed more control points in the center of the image to be successfully correlated, but at the expense of requiring a larger border between the edge control points and the edge of the image. The contour plots in Figs. G.33 - G.35 demonstrate the effect on the correlation results of changing the reference image, using (or not using) initial guesses, and changing the search zone.

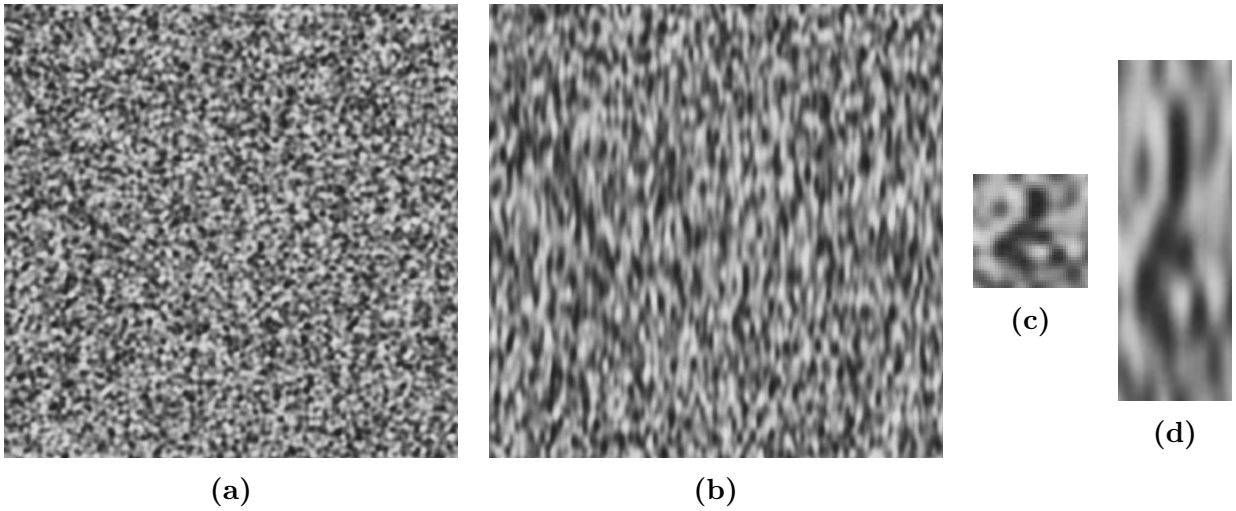

Figure G.32: (a) Reference image and (b) final image. The speckle pattern is stretched significantly in the vertical direction moving from the reference to the final image. (c) Representative subset in the reference image for a subset size of 41 x 41 pixels. (d) Approximately the same subset in the final image; the height of the subset is 123 pixels instead of 41 pixels to emphasize the distortion in the speckle pattern.

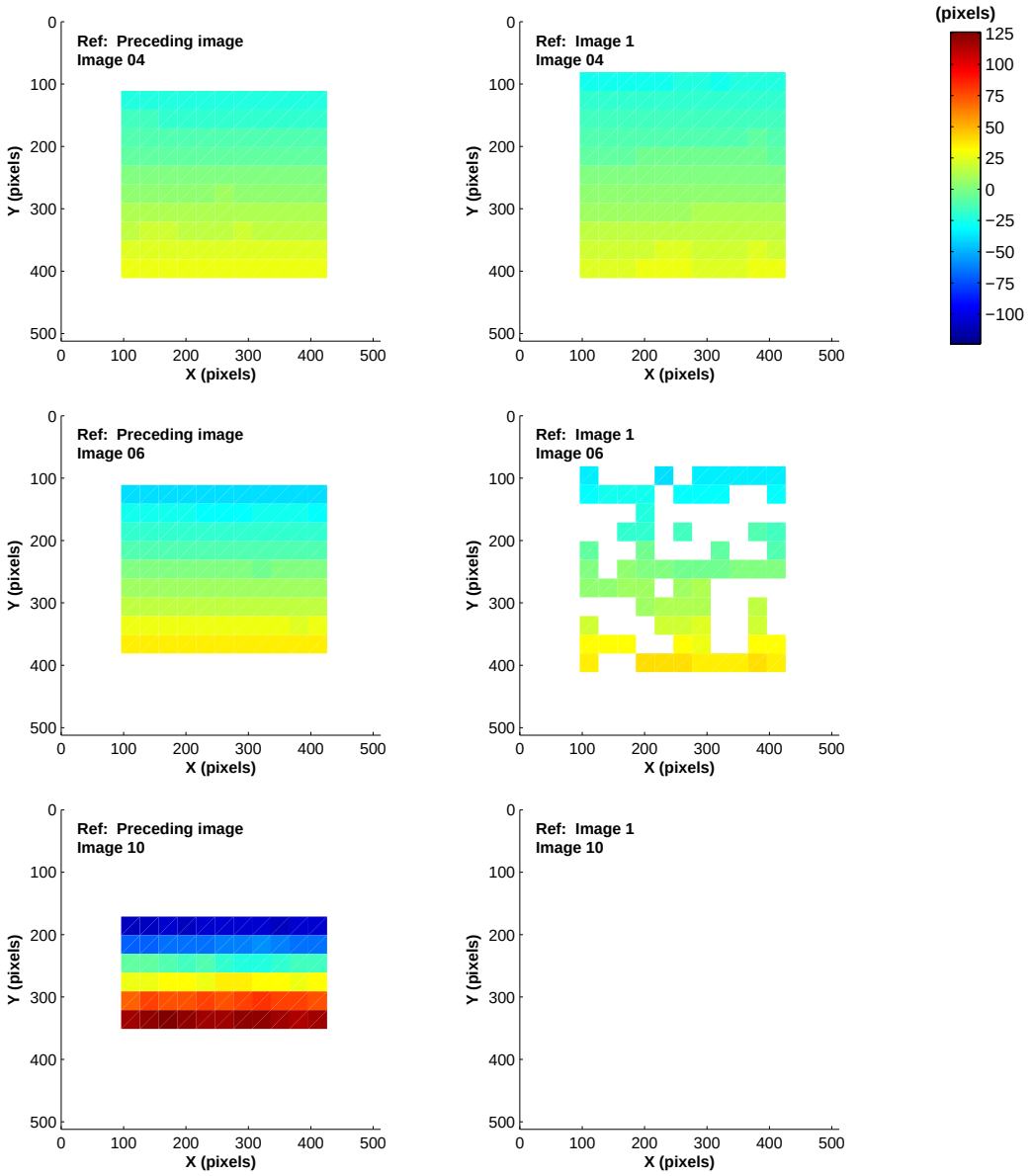

Figure G.33: Select contour plots of the vertical displacement, V, from the correlation of the reduced images. The left column represents the correlation results when the preceding image was used as a reference image and the right column represents the correlation results when the first image was used as a reference image.

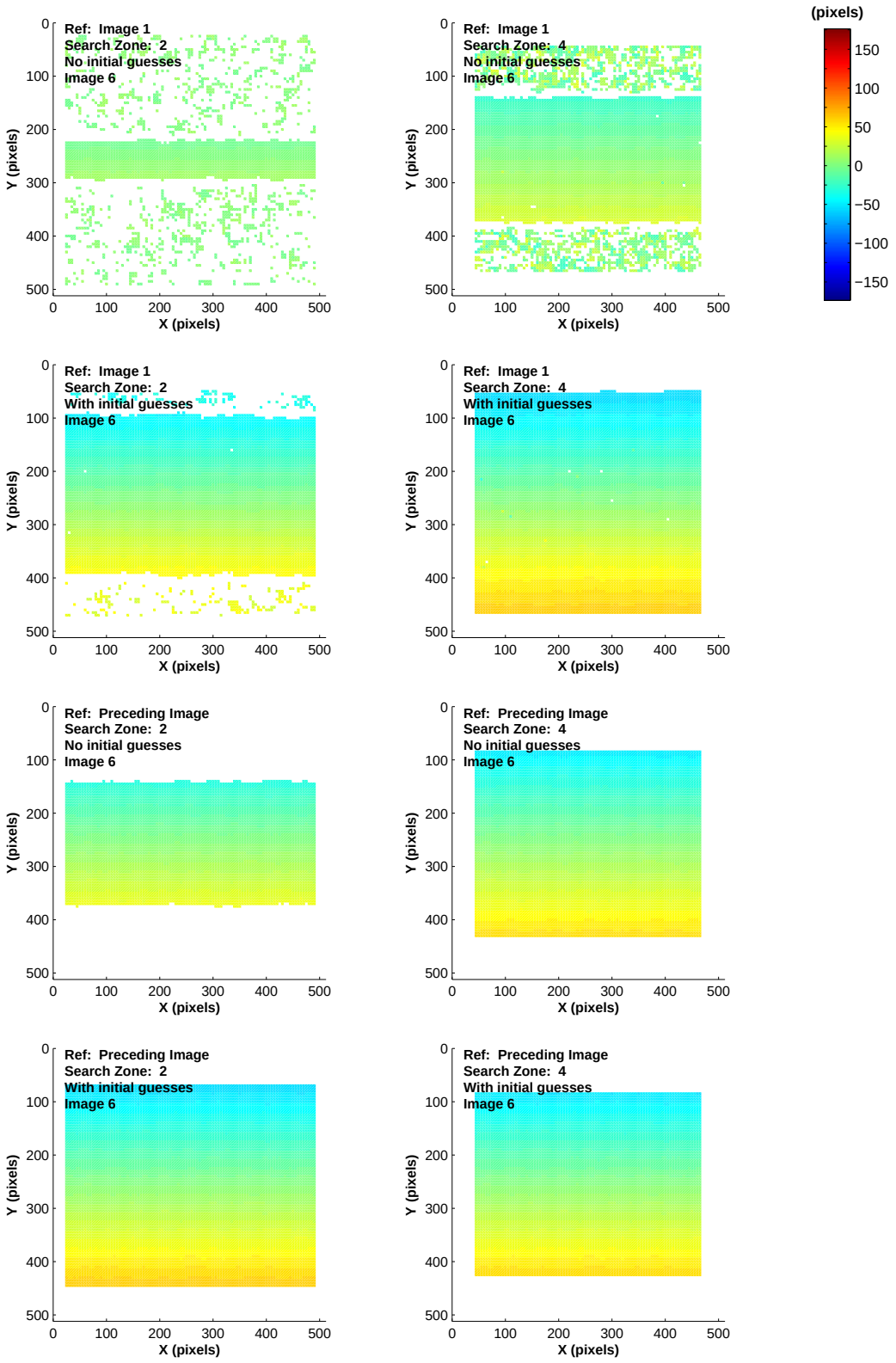

Figure G.34: Select contour plots of the vertical displacement, V, for image 6 under different correlation parameters. Initial guesses were obtained by correlating the reduced images using the preceding image as the reference image. For all correlations, a subset of 21 and a threshold of 0.5 were used.

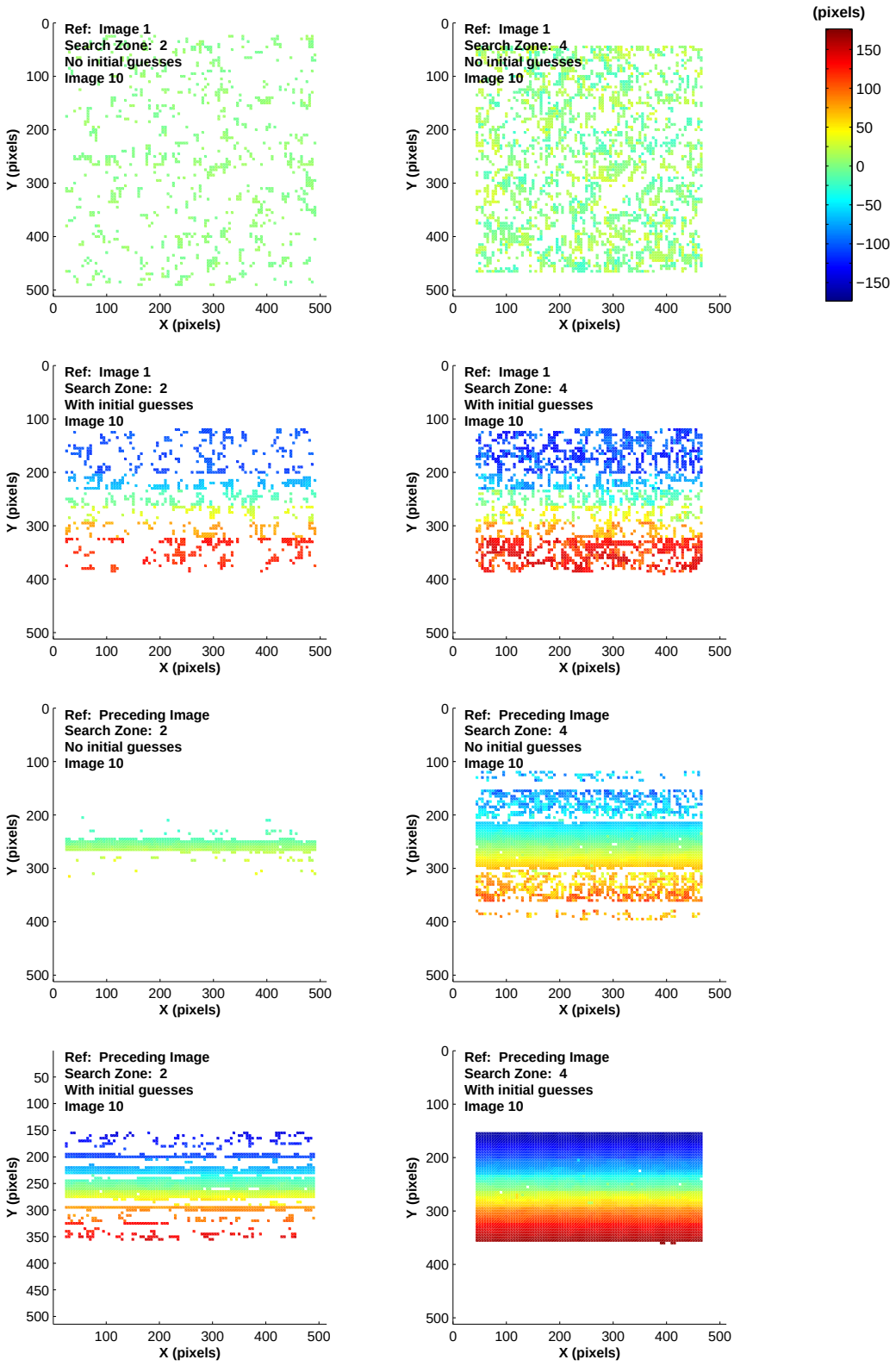

Figure G.35: Select contour plots of the vertical displacement, V, for image 10 under different correlation parameters. Initial guesses were obtained by correlating the reduced images using the preceding image as the reference image. For all correlations, a subset of 20 and a threshold of 0.5 were used.

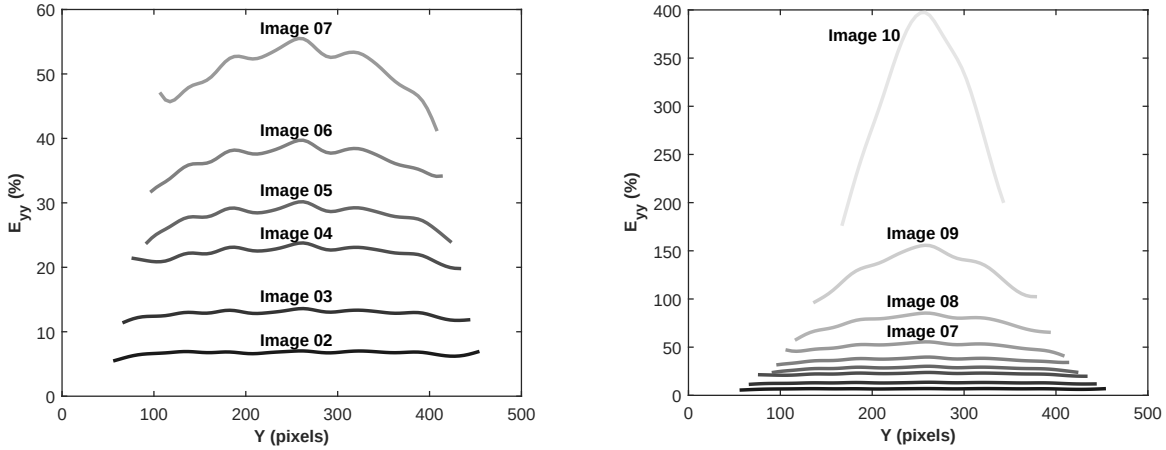

Figure G.36: Line scans of the vertical normal strain, E_{yy}, along a vertical line in the center of the image. The smooth kernel size was 11 control points, and three smoothing passes were used.

Sample 11b (Strain Discontinuity)

Deformation: Constant horizontal normal strain on the left (positive strain) and right (negative strain) sides of the image, with a strain discontinuity in the center of the image. Constant strain values for images 2-6: 0.004 %, 0.020 %, 0.039 %, 0.195 % and 0.397 %. the vertical displacements and normal strains are uniformly zero.

Images: 512 x 512 pixels. Same speckle pattern as Sample 09 (rigid rotation).

Results:

The strain values of the constant-strain portions of the first three images (0.004 %, 0.020 %, 0.039 %) are within the noise associated with the strain calculations. Therefore, the ability of the DIC code to capture the strain discontinuity in these images cannot be evaluated. As the displacements are smoothed over the strain discontinuity, the effective width of the discontinuity increases (Fig. G.40). These results emphasize the trade-off between obtaining smoother strains in the constant-strain region versus clearly seeing strain discontinuities.

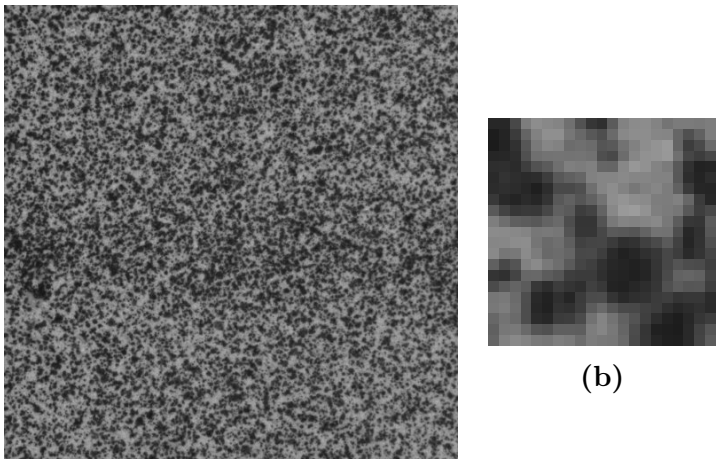

(a) **(b)**

Figure G.37: (a) Reference image. (b) Representative subset for subset size 20.

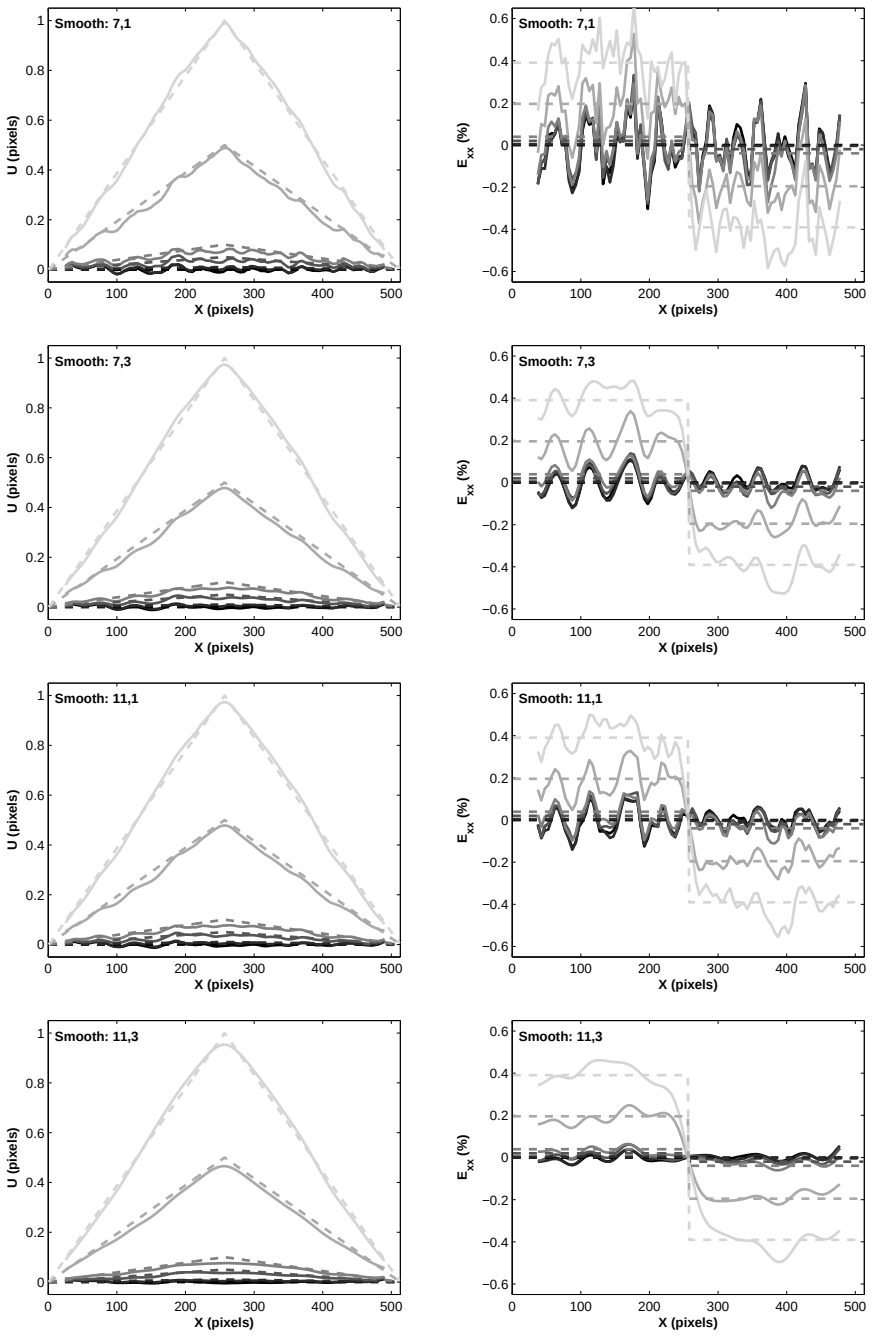

Figure G.38: Select line scans of the correlated vertical displacement, V, and vertical normal strain, E_{yy} (solid curves), and the analytic vertical displacement and vertical normal strain (dashed curves) along a vertical line in the center of the image for image 2 (dark curves), image 4 (medium curves), and image 9 (light curves). The subset size for the correlations was 20, and the different smoothing parameters are listed in the figures as [smooth kernel size, number of smoothing passes].

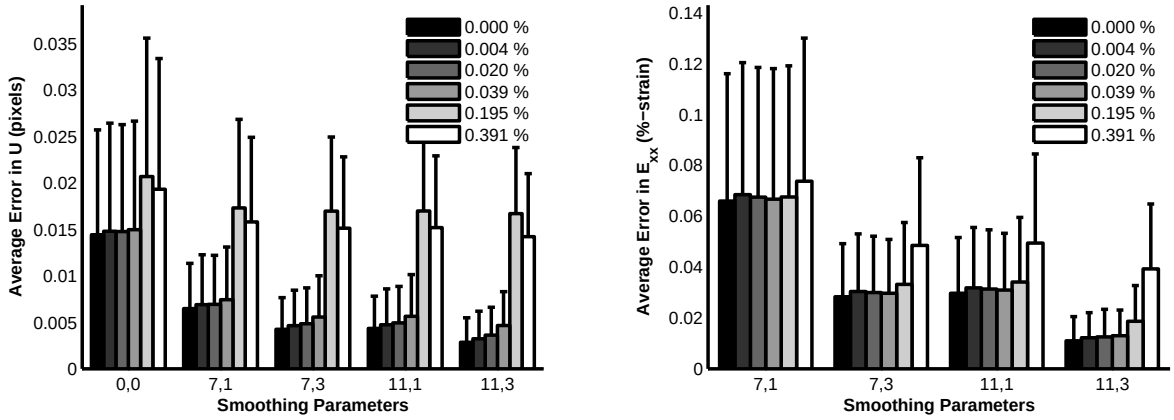

Figure G.39: Error, averaged over the left and right regions of the image ($1 \leq x \leq 152$ and $362 \leq x \leq 512$), where the strain is constant, avoiding the strain discontinuity in the center of the image, of horizontal displacement, U, and horizontal normal strain, E_{xx}. The smoothing parameters labeled on the x-axis are [smooth kernel size, number of smoothing passes]. The legend indicates the theoretical value of the strain in the constant-strain portions of the image. The error bars represent one standard deviation.

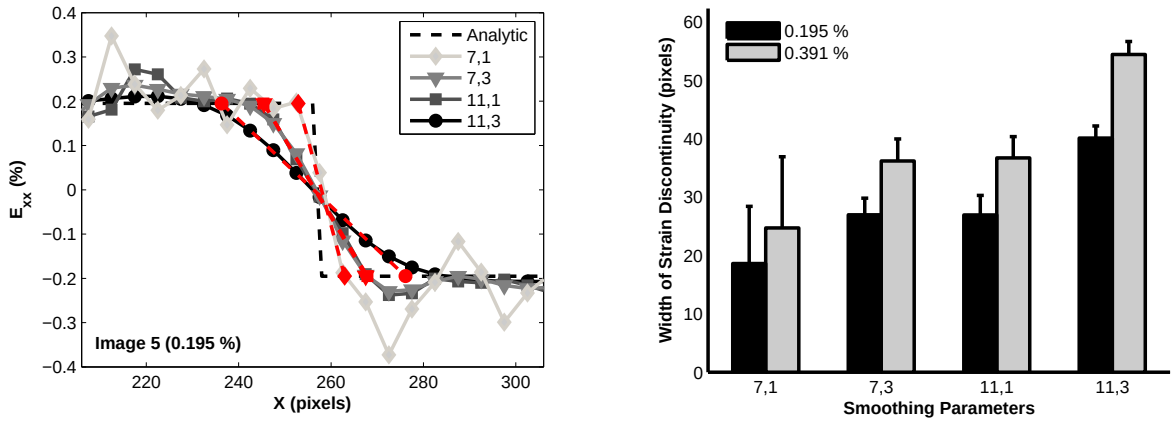

Figure G.40: (a) Line scans of image 5 (0.195 % strain) across the center of the image at approximately $y = 256$. The red lines represent the fitting lines used to calculate the width of the strain discontinuity. (b) Average widths of the strain discontinuity for image 5 (0.195 % strain) and image 6 (0.391 % strain). The widths were calculated by fitting a line to the strain data moving across the strain discontinuity. The applied strains for the first four images were smaller than the error in the correlated strains, so the width of the strain discontinuity was not computed for these images. The error bars represent one standard deviation in the calculated widths along the vertical dimension of the images.

Sample 14 (Varying Strain, FFT)

Deformation: Sinusoidal variation in horizontal normal strain with increasing frequency. The vertical displacements are uniformly zero. The horizontal displacements varying only in the horizontal direction and are constant in the vertical direction.

Images: 2048 x 588 pixels. More contrast towards the left side of the image compared to the right side of the image. Speckle pattern constant for all images.

Results:

The spatially-varying strain fields in this image set emphasize the trade-off that occurs when smoothing displacements. One must smooth the displacements sufficiently to have reasonable strain calculations but not so much that the spatial information of the strains is lost. Smoothing with a kernel of 11 grid points and one smoothing pass results in fairly noisy strains. Increasing the number of smoothing passes results in smoother strains but at the expense of computing a lower strain amplitude than the analytic solution, particularly for the higher frequencies of the sinusoidal variation (Fig. G.42). Though the amplitude of the strain response suffers in accuracy, the frequency of the strain variation is captured well.

The error in the displacements and strains is fairly constant with increasing frequency of the sinusoidal variations when the displacements are smoothed with a kernel of 11 grid points and 1 smoothing pass (Fig. G.43). As the smoothing is increased, the error of the low-frequency variations (i.e. image 2) decreases while the error of the high-frequency variations (i.e. the right portion of image 4) increases. The error averaged over the entire image (Fig. G.44) is a competition between less error in the low-frequency regimes and larger area in the high-frequency regimes.

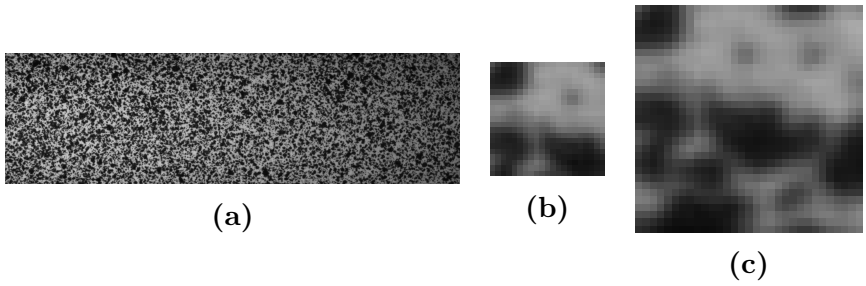

Figure G.41: (a) Reference image. (b-c) Representative subsets for subset size 20 and 30 respectively.

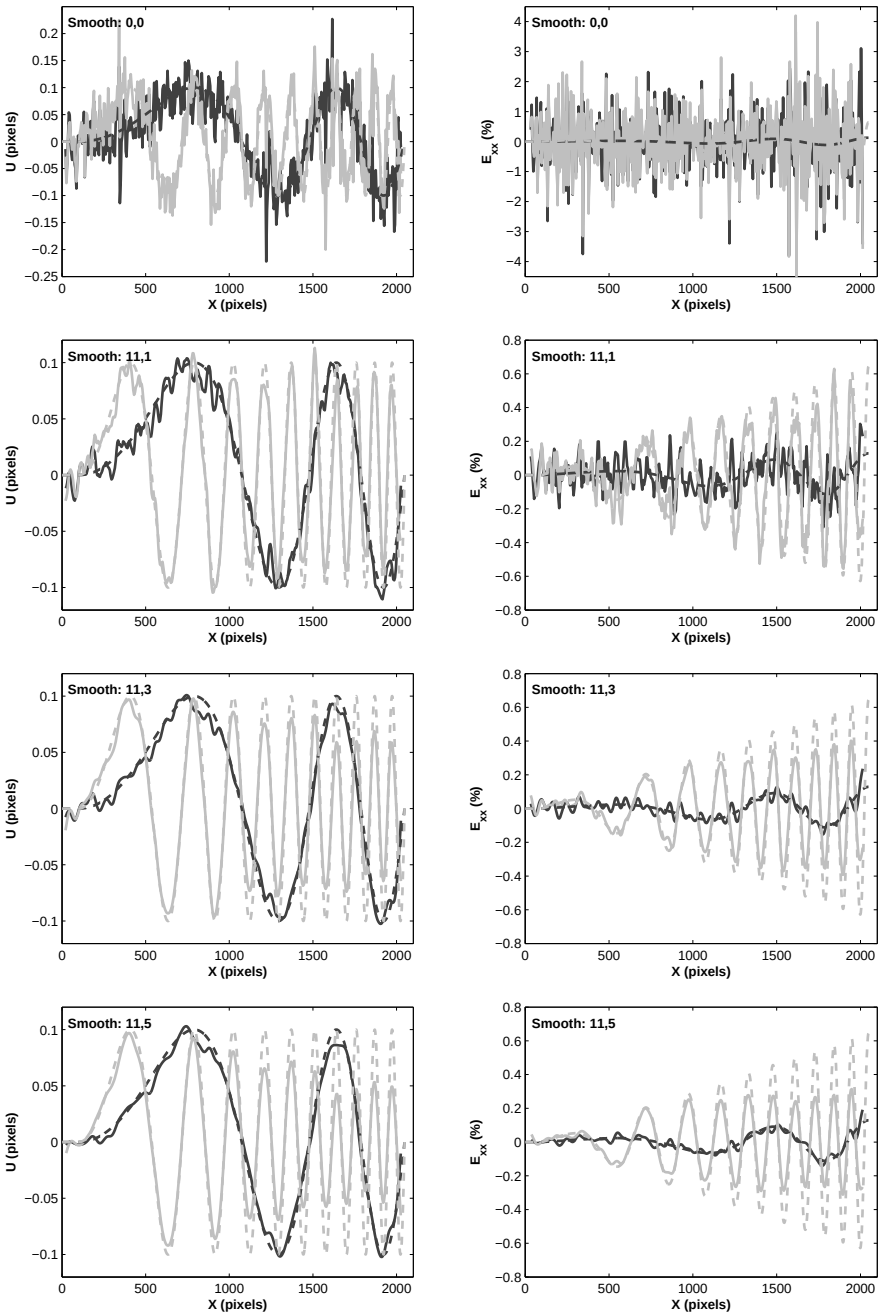

Figure G.42: Select line scans of the correlated horizontal displacement, U, and horizontal normal strain, E_{xx} (solid curves), and the analytic horizontal displacement and horizontal normal strain (dashed curves) along a horizontal line in the center of the image for image 2 (dark curves) and image 4 (light curves). The subset size for the correlations was 20, and the different smoothing parameters are listed in the figures as [smooth kernel size, number of smoothing passes].

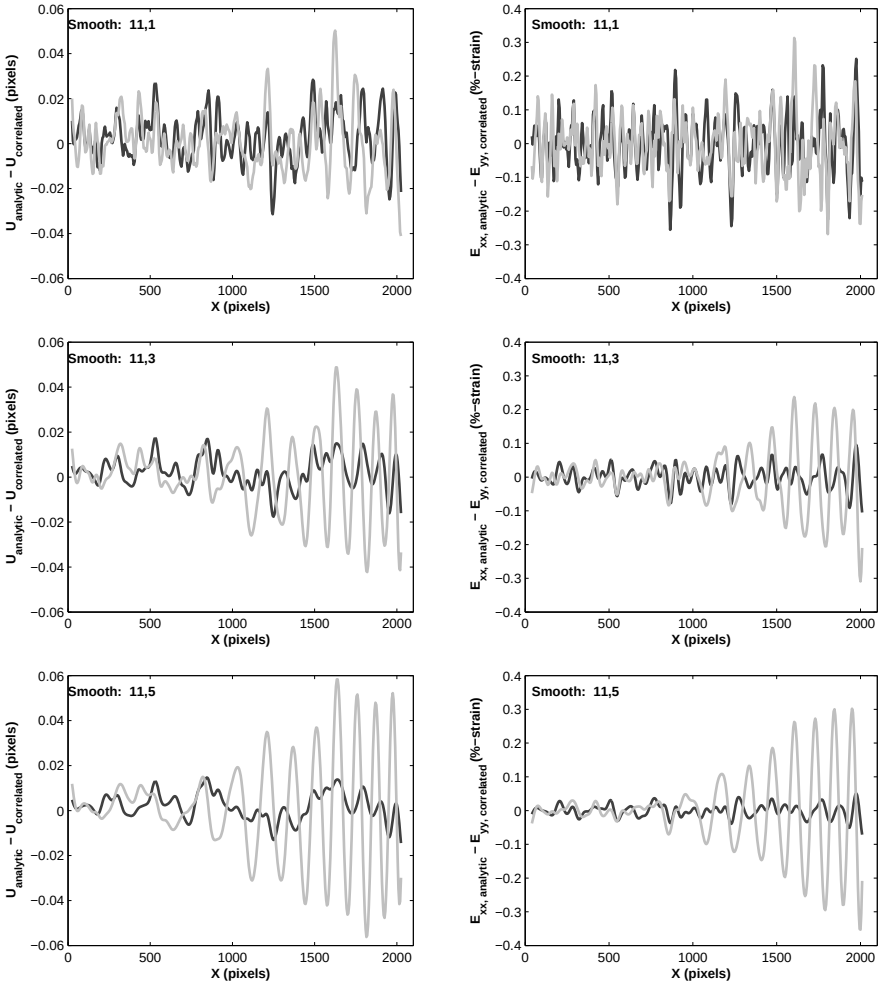

Figure G.43: Select line scans of the error of the horizontal displacement, $U_{analytic}$ - $U_{correlated}$, and horizontal normal strain, $E_{xx,\ analytic}$ - $E_{xx,\ correlated}$, along a horizontal line in the center of the image for image 2 (dark curves) and image 4 (light curves). The subset size for the correlations was 20, and the different smoothing parameters are listed in the figures as [smooth kernel size, number of smoothing passes].

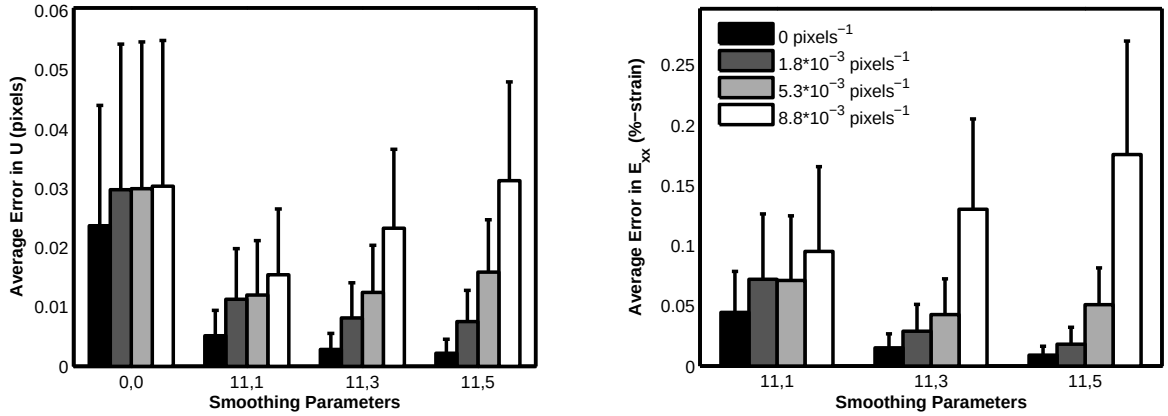

Figure G.44: Error, averaged over the right portion of the image where $X \geq 1478$, of the horizontal displacement, U, and horizontal normal strain, E_{xx}. The smoothing parameters labeled on the x-axis are [smooth kernel size, number of smoothing passes]. The legend indicates the average frequency of the applied horizontal normal strain in the right portion of the image where $X \geq 1478$. The error bars represent one standard deviation.

Sample 15 (Varying Strain, TexGen)

Deformation: Modulations of the horizontal normal strain, E_{xx}, with increasing distance between peaks. The horizontal displacements, U, and the horizontal normal strains, E_{xx}, vary only in the horizontal direction and are constant along the vertical direction. The vertical displacements, V, and vertical normal strains, E_{yy}, are uniformly zero.

Images: 2000 x 1000 pixels. Speckle pattern constant for all images.

Results:

The relatively large displacements at the top and bottom of the field of view required the correlation of reduced images to provide initial guesses for the correlation of the full images. The following parameters were used for the reduced image correlation: subset size 20, reduction 3, threshold 0.5.

Similar to the results from Sample 14, the most error is found at the sharpest strain gradients, where the error in the strain can reach 2-3 % strain. Similar to the results from rigid translations, the error in the regions with no strain are approximately 0.03-0.05 % strain. As the ratio of the strain peak spacing to the strain peak width increases, the error of the strain (averaged over the portion of the images with non-zero applied strain) decreases until the ratio is greater than 1 (Fig. G.48). For ratios greater than 1, the error increases slightly, but this is due likely to the full width of the outermost strain peaks falling outside of the image.

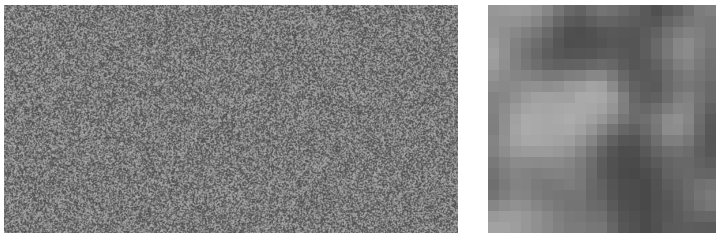

(a) **(b)**

Figure G.45: (a) Reference image. (b) Representative subset for subset size 20.

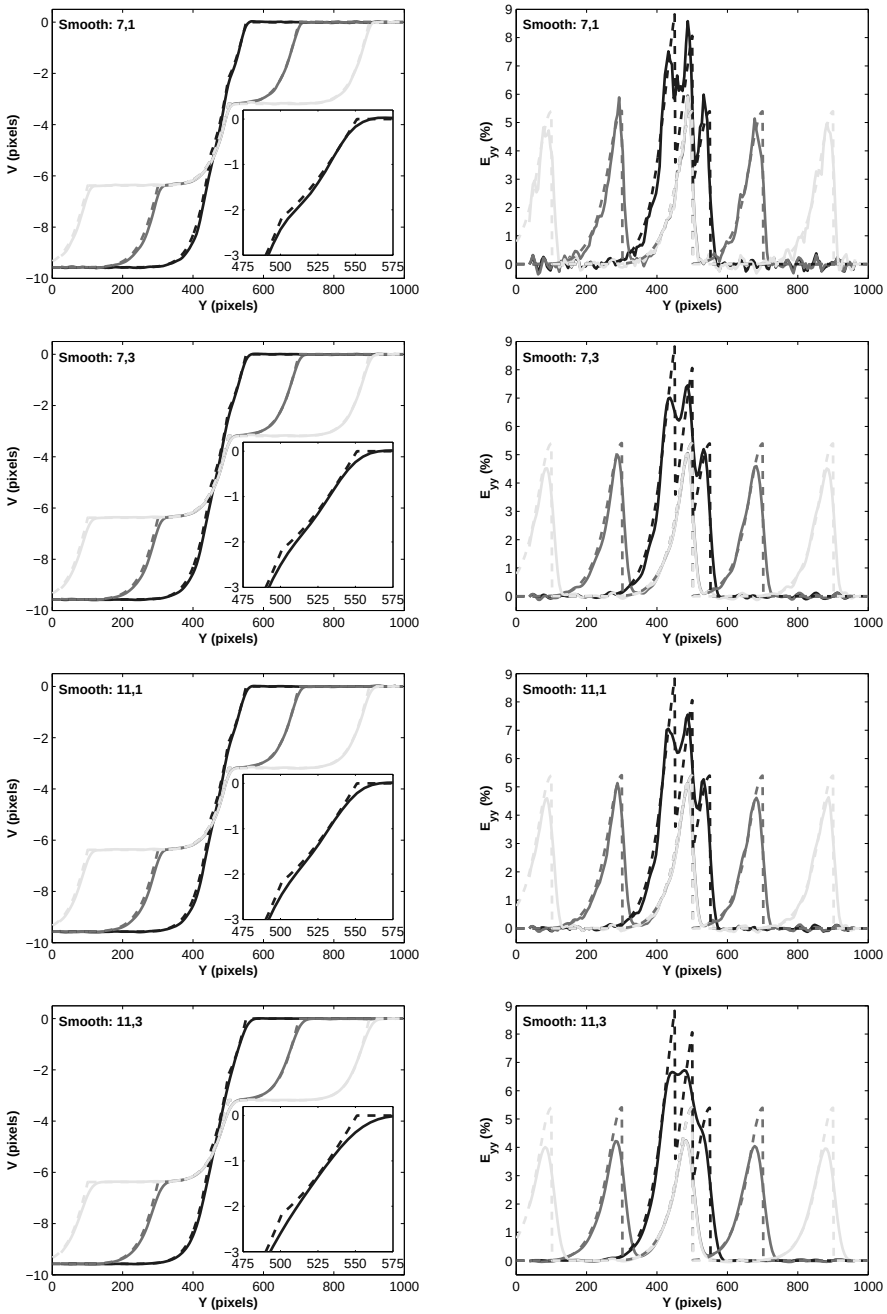

Figure G.46: Select line scans of the correlated vertical displacement, V, and vertical normal strain, E_{yy} (solid curves), and the analytic vertical displacement and vertical normal strain (dashed curves) along a vertical line in the center of the image for image 2 (dark curves), image 4 (medium curves), and image 9 (light curves). The subset size for the correlations was 20, and the different smoothing parameters are listed in the figures as [smooth kernel size, number of smoothing passes].

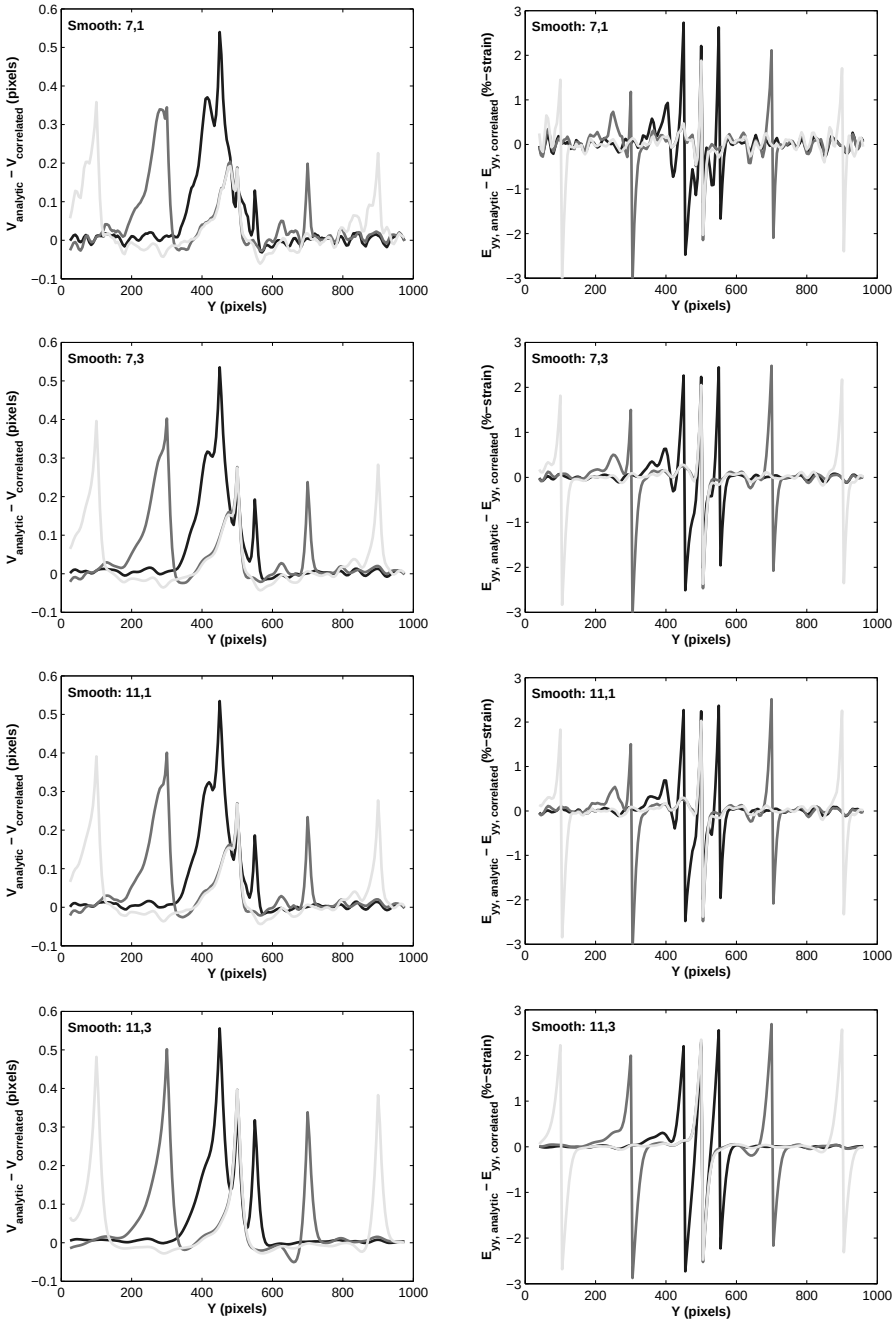

Figure G.47: Select line scans of the error of the vertical displacement, $V_{analytic}$ - $V_{correlated}$ and vertical normal strain, $E_{yy,\ analytic}$ - $E_{yy,\ correlated}$, along a vertical line in the center of the image for image 2 (dark curves), image 4 (medium curves), and image 9 (light curves). The subset size for the correlations was 20, and the different smoothing parameters are listed in the figures as [smooth kernel size, number of smoothing passes].

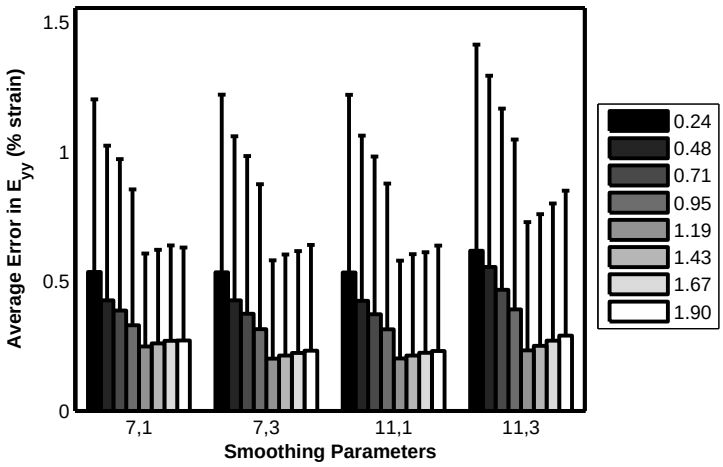

Figure G.48: Error, averaged over the portions of the image with non-zero applied vertical normal strain, of the vertical normal strain, E_{yy}. The smoothing parameters labeled on the x-axis are [smooth kernel size, number of smoothing passes]. The legend indicates the ratio of the strain peak spacing (50-450 in 50 pixel increments for images 2-9 respectively) to the strain peak width (estimated as 210 pixels for strains greater than 0.01 %). The error bars represent one standard deviation.

Appendix H

Synthesis of Fluorescent Silica Nanoparticles

This appendix presents a generalized procedure for the synthesis of fluorescent silica nanoparticles, summarized from several references in the literature [52, 53, 118].

H.1 Materials

- Rhodamine isothiocyanate (RITC) dye
- 3-aminopropyltriethoxysilane (APES)
- tetraethoxysilance (TEOS)
- 30 % ammonium hydroxide
- ethanol
- ultra pure water

H.2 Equipment

- 100 mL round-bottom flask
- 1 L round-bottom flask
- glass funnel
- two (2) septa

H.3 Preparation

1. Clean all glassware in a fresh base bath (e.g. potassium hydroxide dissolved in isopropanol) overnight.
2. Rinse thoroughly with ultra high purity water.
3. Dry thoroughtly (in oven).
4. Rinse thoroughly with ethanol.
5. Allow ethanol to evaporate.

H.4 Recipe

H.4.1 Core

1. Use the Eqn. H.1 to determine the quantity of ethanol (core), TEOS (core), water, and ammonium hydroxide required to produce cores with the desired diameter, d_c. Note that these equations are valid for 0.1 - 0.5 M TEOS, 0.5 - 17.0 M H_2O and 0.5 - 3.0 M NH_3.

$$d_c = A\left[H_2O\right]^2 \exp\left(-B\left[H_2O\right]^{1/2}\right) \tag{H.1a}$$

$$A = \left[TEOS\right]^{1/2}\left(82 - 151\left[NH_3\right] + 1200\left[NH_3\right]^2 - 366\left[NH_3\right]^3\right) \tag{H.1b}$$

$$B = 1.05 + 0.523\left[NH_3\right] - 0.128\left[NH_3\right]^2 \tag{H.1c}$$

2. To determine the quantity of APES, keep the molar ratio of APES:TEOS (core) the same as Ref. [52].

$$\frac{0.127 \text{ mol TEOS}}{0.0938 \text{ g APES}\frac{1 \text{ mol}}{221.37 \text{ g}}} \rightarrow 320 \text{ mol TEOS} : 1 \text{ mol APES} \tag{H.2}$$

3. To determine the quantity of RITC dye, keep the molar ratio of APES:RITC the same as Ref. [52].

$$\frac{0.0938 \text{ g APES}\frac{1 \text{ mol}}{221.37 \text{ g}}}{0.1178 \text{ g RITC}\frac{1 \text{ mol}}{536.08 \text{ g}}} \rightarrow 1.928 \text{ mol APES} : 1 \text{ mol RITC} \tag{H.3}$$

4. Split the ethanol into three quantities:

   - 10 mL (7.9 g), for step (1) in core procedure
   - Same mass as TEOS (core), for step (6) in core procedure
   - Remainder from Eqn. H.1

H.4.2 Shell

1. Use Eqn. H.4 to determine the quantity of TEOS (shell) to add to produce particles with a final desired diameter of d_f, where M denotes the mass of TEOS, V denotes the volume of the particle, d denotes the diameter of the particle, the subscript f refers to the final particle (core plus shell), the subscript c refers to the particle core, and the subscript s refers to the particle shell.

$$\frac{M_f}{M_c} = \frac{V_f}{V_c} = \left(\frac{d_f}{d_c}\right)^3 \tag{H.4a}$$

$$M_s = M_f - M_c = M_c\left(\left(\frac{d_f}{d_c}\right)^3 - 1\right) \tag{H.4b}$$

2. Divide the TEos into five or more quantities:

   - 0.5 g TEOS for first shell growth
   - Remainder of TEOS divided into four or more equal amounts. Each addition should be less than about 1 g total. Adding smaller amounts of TEOS, with more total additions, will lead to smaller dispersion in the final particle size.

H.5 Procedure

H.5.1 Core

1. In clean, dry 100 mL round bottom flask, mix RITC, APS, and 10 mL (7.9 g) ethanol. Cap with a septum. Stir 12-17 hours, slowly, in the dark. (Wrap aluminum foil around the flask.)

2. In a clean, dry 1 L round bottom flask, add remaining ethanol (core). This will be the total ethanol (core) amount determined in the recipe for the core, minus the 10 mL from the above step, minus the amount used to dilute the TEOS in step (6).

3. Mix ammonium hydroxide (30 %) with ultra high pure water in a centrifuge. Shake well by hand.

4. Add ammonium hydroxide and water solution from step (3) to ethanol in 1 L flask and stir for several minutes.

5. Add RITC solution from step (1) to ethanol and ammonium hydroxide in 1 L flask.

6. In a 20 mL scint vial, dilute TEOS (core) in ethanol in a 1:1 mass ratio. Shake well by hand.

7. Set stir rate of 1 L flask so the resulting vortex in the liquid is about 1/3 total liquid height. Do not stir so vigorously that the stir rod is bouncing around.

8. Add diluted TEOS to the 1 L flask using a funnel. Add the TEOS quickly! Do not try to shake extra drops out of the vial or the funnel. This is the key step that determines the quality of the particles.

9. Cap the 1 L flask with a septum and let stir overnight, in the dark.

H.5.2 Shell

1. Dilute 0.5 g TEOS (shell) with ethanol in a 1:5 or 1:10 mass ratio (i.e. 5 g ethanol) in a 20 mL scint vial. Shake by hand to mix thoroughly.
2. Add diluted TEOS to reaction flask with a funnel while solution continues to stir with a stir rod. Add TEOS quickly!
3. Stir in the dark for at least 2 hours.
4. Repeat steps 1-3 (with appropriate amount of TEOS addition determined in the shell recipe) four or more times until all the TEOS (shell) has been added.

H.5.3 Cleaning and Storage

1. Centrifuge solution until particles settle to bottom of centrifuge tube(s).
2. Pour excess reaction liquid into a waste container.
3. Disperse particles in fresh ethanol via sonication.
4. Repeat steps 1-3 three times in order to thoroughly rinse particles from reaction vessel.
5. Store particles in ethanol in a dark freezer. (Wrap container in aluminum foil.) The dark and cold temperature will help to prevent particles from bleaching over time.

H.6 Notes

- The original Van Blaaderen procedure calls for purging with nitrogen after each addition step [52]. However, this seems to be unnecessary. Additionally, it may reduce ammonium hydroxide concentration.
- The original Van Blaaderen procedure calls for the addition of water along with TEOS during the growth of the shell [52]. However, this is called for when using 25 % ammonium hydroxide with no additional water. If one adds water in the initial core step, then no additional water must be added during the shell growth steps.
- 3-aminopropyltrimethoxysilane (APMS) can be used instead of APES with no modification to the recipe or procedure.
- Any dye with an isothiocyanate functional group, i.e. fluorescein isothiocyanate (FITC), can be used in place of RITC.

References

[1] B. J. Landi, M. J. Ganter, C. D. Cress, R. a. DiLeo, R. P. Raffaelle, Carbon nanotubes for lithium ion batteries, Energy Environ. Sci. 2 (2009) 638.

[2] K. E. Aifantis, S. A. Hackney, R. V. Kumar, Current and potential applications of secondary Li batteries, in: High Energy Density Lithium Batteries, Wiley-VCH, Weinheim, Germany, 2010, Ch. 4, pp. 81–89.

[3] J. Vetter, P. Novák, M. Wagner, C. Veit, K. Möller, J. Besenhard, M. Winter, M. Wohlfahrt-Mehrens, C. Vogler, A. Hammouche, Ageing mechanisms in lithium-ion batteries, J. Power Sources 147 (2005) 269–281.

[4] J. R. Dahn, R. Fong, M. J. Spoon, Suppression of staging in lithium-intercalated carbon by disorder in the host, Phys. Rev. B 42 (10) (1990) 6424–6432.

[5] J. R. Dahn, Phase Diagram of LixC6, Phys. Rev. B 44 (17) (1991) 9170–9177.

[6] S. Safran, Cooperative effects and staging in graphite intercalation compounds, Synthetic Met. 2 (1980) 1–15.

[7] N. Daumas, A. Hérold, Sur les relations entre la notion de stade et les mécanismes réactionnels dans les composés d'insertion du graphite, C.R. Acad. Sc. Série C Feb. (1969) 373–375.

[8] Y. Qi, H. Guo, L. G. Hector, A. Timmons, Threefold increase in the Young's modulus of graphite negative electrode during lithium intercalation, J. Electrochem. Soc. 157 (5) (2010) A558–A566.

[9] N. Takami, A. Satoh, M. Hara, T. Ohsaki, Structural and kinetic characterization of lithium intercalation into carbon anodes for secondary lithium batteries, J. Electrochem. Soc. 142 (2) (1995) 371–379.

[10] E. M. C. Jones, M. N. Silberstein, S. R. White, N. R. Sottos, In situ measurements of strains in composite battery electrodes during electrochemical cycling, Exp. Mech. 54 (6) (2014) 971–985.

[11] Y. Qi, S. J. Harris, In situ observation of strains during lithiation of a graphite electrode, J. Electrochem. Soc. 157 (6) (2010) A741–A747.

[12] J. Chen, A. K. Thapa, T. A. Berfield, In-situ characterization of strain in lithium ion battery anodes, J. Power Sources 271 (2014) 406–413.

[13] L. Y. Beaulieu, K. W. Eberman, R. L. Turner, L. J. Krause, J. R. Dahn, Colossal reversible volume changes in lithium alloys, Electrochem. Solid-State Lett. 4 (9) (2001) A137–A140.

[14] X. H. Liu, J. Y. Huang, In situ TEM electrochemistry of anode materials in lithium ion batteries, Energy Environ. Sci. 4 (2011) 3844–3860.

[15] A. Timmons, J. R. Dahn, In situ optical observations of particle motion in alloy negative electrodes for Li-ion batteries, J. Electrochem. Soc. 153 (6) (2006) A1206–A1210.

[16] J. Gonzalez, K. Sun, M. Huang, J. Lambros, S. Dillon, I. Chasiotis, Three dimensional studies of particle failure in silicon based composite electrodes for lithium ion batteries, J. Power Sources 269 (2014) 334–343.

[17] V. A. Sethuraman, M. J. Chon, M. Shimshak, V. Srinivasan, P. R. Guduru, In situ measurements of stress evolution in silicon thin films during electrochemical lithiation and delithiation, J. Power Sources 195 (2010) 5062–5066.

[18] V. A. Sethuraman, N. Van Winkle, D. P. Abraham, A. F. Bower, P. R. Guduru, Real-time stress measurements in lithium-ion battery negative-electrodes, J. Power Sources 206 (2012) 334–342.

[19] V. A. Sethuraman, A. Nguyen, M. J. Chon, S. P. V. Nadimpalli, H. Wang, D. P. Abraham, A. F. Bower, V. B. Shenoy, P. R. Guduru, Stress evolution in composite silicon electrodes during lithiation/delithiation, J. Electrochem. Soc. 160 (4) (2013) A739–A746.

[20] A. Mukhopadhyay, A. Tokranov, K. Sena, X. Xiao, B. W. Sheldon, Thin film graphite electrodes with low stress generation during Li-intercalation, Carbon 49 (8) (2011) 2742–2749.

[21] A. Mukhopadhyay, F. Guo, A. Tokranov, X. Xiao, R. H. Hurt, B. W. Sheldon, Engineering of graphene layer orientation to attain high rate capability and anisotropic properties in li-ion battery electrodes, Adv. Funct. Mater. 23 (2013) 2397–2404.

[22] A. F. Bower, P. R. Guduru, V. A. Sethuraman, A finite strain model of stress, diffusion, plastic flow, and electrochemical reactions in a lithium-ion half-cell, J. Mech. Phys. Solids 59 (2011) 804–828.

[23] R. Deshpande, Y.-T. Cheng, M. W. Verbrugge, Modeling diffusion-induced stress in nanowire electrode structures, J. Power Sources 195 (2010) 5081–5088.

[24] G. Ning, B. Haran, B. Popov, Capacity fade study of lithium-ion batteries cycled at high discharge rates, J. Power Sources 117 (2003) 160–169.

[25] H. Buqa, D. Goers, M. Holzapfel, M. E. Spahr, P. Novak, High rate capability of graphite negative electrodes for lithium-ion batteries, J. Electrochem. Soc. 152 (2) (2005) A474.

[26] J. Li, E. Murphy, J. Winnick, P. a. Kohl, The effects of pulse charging on cycling characteristics of commercial lithium-ion batteries, J. Power Sources 102 (1-2) (2001) 302–309.

[27] M. Ebner, F. Marone, M. Stampanoni, V. Wood, Visualization and quantification of electrochemical and mechanical degradation in Li-ion batteries, Science 342 (2013) 716–720.

[28] Y. Li, F. El Gabaly, T. R. Ferguson, R. B. Smith, N. C. Bartelt, J. D. Sugar, K. R. Fenton, D. A. Cogswell, A. D. Kilcoyne, T. Tyliszczak, M. Z. Bazant, W. C. Chueh, Current-induced transition from particle-by-particle to concurrent intercalation in phase-separating battery electrodes, Nat. Mater. 13 (2014) 1149–1156.

[29] A. Mukhopadhyay, B. W. Sheldon, Deformation and stress in electrode materials for Li-ion batteries, Progress Mater. Sci. 63 (2014) 58–116.

[30] V. A. Sethuraman, L. J. Hardwick, V. Srinivasan, R. Kostecki, Surface structural disordering in graphite upon lithium intercalation/deintercalation, J. Power Sources 195 (11) (2010) 3655–3660.

[31] L. J. Hardwick, H. Buqa, P. Novak, Graphite surface disorder detection using in situ Raman microscopy, Solid State Ionics 177 (2006) 2801–2806.

[32] P. Verma, P. Maire, P. Novák, A review of the features and analyses of the solid electrolyte interphase in Li-ion batteries, Electrochim. Acta 55 (2010) 6332–6341.

[33] E. Peled, D. Golodnitsky, J. Penciner, The Anode / Electrolyte Interface, in: Handbook of Battery Materials, 2nd Edition, Wiley, 2011, Ch. 16, pp. 479–523.

[34] A. Andersson, A. Henningson, H. Siegbahn, U. Jansson, K. Edström, Electrochemically lithiated graphite characterised by photoelectron spectroscopy, J. Power Sources 119-121 (2003) 522–527.

[35] E. Markervich, G. Salitra, M. Levi, D. Aurbach, Capacity fading of lithiated graphite electrodes studied by a combination of electroanalytical methods, Raman spectroscopy and SEM, J. Power Sources 146 (1-2) (2005) 146–150.

[36] R. Kostecki, F. McLarnon, Microprobe study of the effect of Li intercalation on the structure of graphite, J. Power Sources 119-121 (2003) 550–554.

[37] L. J. Hardwick, M. Marcinek, L. Beer, J. B. Kerr, R. Kostecki, An investigation of the effect of graphite degradation on irreversible capacity in lithium-ion cells, J. Electrochem. Soc. 155 (6) (2008) A442.

[38] P. Liu, J. Wang, J. Hicks-Garner, E. Sherman, S. Soukiazian, M. Verbrugge, H. Tataria, J. Musser, P. Finamore, Aging mechanisms of LiFePO4 batteries deduced by electrochemical and structural analyses, J. Electrochem. Soc. 157 (4) (2010) A499.

[39] S. Bhattacharya, A. R. Riahi, A. T. Alpas, A transmission electron microscopy study of crack formation and propagation in electrochemically cycled graphite electrode in lithium-ion cells, J. Power Sources 196 (20) (2011) 8719–8727.

[40] V. Agubra, J. Fergus, Lithium ion battery anode aging mechanisms, Mater. 6 (4) (2013) 1310–1325.

[41] V. A. Agubra, J. W. Fergus, The formation and stability of the solid electrolyte interface on the graphite anode, J. Power Sources 268 (2014) 153–162.

[42] X. Su, Q. Wu, J. Li, X. Xiao, A. Lott, W. Lu, B. W. Sheldon, J. Wu, Silicon-based nanomaterials for lithium-ion batteries: a review, Adv. Energy Mater. 4 (2014) 1–23.

[43] H. Wu, Y. Cui, Designing nanostructured Si anodes for high energy lithium ion batteries, Nano Today 7 (2012) 414–429.

[44] W. J. Zhang, A review of the electrochemical performance of alloy anodes for lithium-ion batteries, J. Power Sources 196 (1) (2011) 13–24.

[45] A. Mukhopadhyay, A. Tokranov, X. Xiao, B. W. Sheldon, Stress development due to surface processes in graphite electrodes for Li-ion batteries: A first report, Electrochim. Acta 66 (2012) 28–37.

[46] A. Tokranov, B. W. Sheldon, P. Lu, X. Xiao, A. Mukhopadhyay, The origin of stress in the solid electrolyte interphase on carbon electrodes for Li ion batteries, J. Electrochem. Soc. 161 (1) (2013) A58–A65.

[47] H. Tavassol, M. K. Y. Chan, M. G. Catarello, J. Greeley, D. G. Cahill, A. A. Gewirth, Surface coverage and SEI induced electrochemical surface stress changes during Li deposition in a model system for Li-ion battery anodes, J. Electrochem. Soc. 160 (6) (2013) A888–A896.

[48] P. Maire, A. Evans, H. Kaiser, W. Scheifele, P. Novak, Colorimetric determination of lithium content in electrodes of lithium-ion batteries, J. Electrochem. Soc. 155 (11) (2008) A862.

[49] T. A. Berfield, J. K. Patel, R. G. Shimmin, P. V. Braun, J. Lambros, N. R. Sottos, Fluorescent image correlation for nanoscale deformation measurements., Small 2 (5) (2006) 631–635.

[50] T. A. Berfield, J. K. Patel, R. G. Shimmin, P. V. Braun, J. Lambros, N. R. Sottos, Micro- and nanoscale deformation measurement of surface and internal planes via digital image correlation, Exp. Mech. 47 (2007) 51–62.

[51] A. R. Hamilton, N. R. Sottos, S. R. White, Local strain concentrations in a microvascular network, Exp. Mech. 50 (2010) 255–263.

[52] A. Van Blaaderen, A. Vrij, Synthesis and characterization of colloidal dispersions of fluorescent, monodisperse silica spheres, Langmuir 8 (12) (1992) 2921–2931.

[53] N. A. M. Verhaegh, A. Van Blaaderen, Dispersions of rhodamine-labeled silica spheres: synthesis, characterization, and fluorescence confocal scanning laser microscopy, Langmuir 10 (1994) 1427–1438.

[54] Chemical Book, Carboxymethyl cellulose (2010).
URL http://www.chemicalbook.com/ChemicalProductProperty_EN_CB5209844.htm

[55] International Programme on Chemical Safety, Carbon black (2012).
URL http://www.inchem.org/documents/icsc/icsc/eics0471.htm

[56] J. Li, R. B. Lewis, J. R. Dahn, Sodium carboxymethyl cellulose: a potential binder for Si negative electrodes for Li-ion batteries, Electrochem. Solid-State Lett. 10 (2) (2007) A17–A20.

[57] Matweb, Graphite (Carbon, C) (2013).
URL www.matweb.com

[58] J. M. Whitney, R. L. McCullough, Micromechanical materials modeling, Technomic Publishing Company, Inc., Lancaster, PA, 1990.

[59] L. J. Gibson, M. F. Ashby, Cellular solids, Pergamon Press, New York 10523, USA, 1988.

[60] B. W. Rosen, Z. Hashin, Effective thermal expansion coefficients and specific heats of composite materials, Int. J. Engng. Sci. 8 (1970) 157–173.

[61] D. Guerard, A. Hérold, Intercalation of lithium into graphite and other carbons, Carbon 13 (1975) 337–345.

[62] R. A. Sharma, R. N. Seefurth, Thermodynamic properties of the lithium-silicon system, J. Electrochem. Soc.: Electrochem. Sci. Tech. 123 (12) (1976) 1763–1768.

[63] B. Boukamp, G. Lesh, R. Huggins, All-solid lithium electrodes with mixed-conductor matrix, J. Electrochem. Soc.: Electrochem. Sci. Tech. 128 (4) (1981) 725–729.

[64] C. Eberl, Digital image correlation and tracking (2010).
URL http://www.mathworks.com/matlabcentral/fileexchange/12413-digital-image-correlation-and-tracking

[65] E. M. C. Jones, Improved Digital Image Correlation (DIC), Matlab Central File Exchange #43073.
URL http://www.mathworks.com/matlabcentral/fileexchange/43073-improved-digital-image-correlation--dic-

[66] L. Freund, S. Suresh, Thin film materials, Cambridge University Press, Cambridge, UK, 2003.

[67] L. Chai, Q. Qu, L. Zhang, M. Shen, L. Zhang, H. Zheng, Chitosan, a new and environmental benign electrode binder for use with graphite anode in lithium-ion batteries, Electrochim. Acta 105 (2013) 378–383.

[68] L. Gong, M. H. T. Nguyen, E.-S. Oh, High polar polyacrylonitrile as a potential binder for negative electrodes in lithium ion batteries, Electrochem. Commun. 29 (2013) 45–47.

[69] K. Ui, D. Fujii, Y. Niwata, T. Karouji, Y. Shibata, Y. Kadoma, K. Shimada, N. Kumagai, Analysis of solid electrolyte interface formation reaction and surface deposit of natural graphite negative electrode employing polyacrylic acid as a binder, J. Power Sources 247 (2014) 981–990.

[70] H. Buqa, M. Holzapfel, F. Krumeich, C. Veit, P. Novák, Study of styrene butadiene rubber and sodium methyl cellulose as binder for negative electrodes in lithium-ion batteries, J. Power Sources 161 (1) (2006) 617–622.

[71] J.-P. Yen, C.-M. Lee, T.-L. Wu, H.-C. Wu, C.-Y. Su, N.-L. Wu, J.-L. Hong, Enhanced High-Temperature Cycle-Life of Mesophase Graphite Anode with Styrene-Butadiene Rubber/Carboxymethyl Cellulose Binder, ECS Electrochem. Lett. 1 (6) (2012) A80–A82.

[72] T. Utsunomiya, O. Hatozaki, N. Yoshimoto, M. Egashira, M. Morita, Influence of particle size on the self-discharge behavior of graphite electrodes in lithium-ion batteries, J. Power Sources 196 (20) (2011) 8675–8682.

[73] K. Zaghib, X. Song, A. Guerfi, R. Kostecki, K. Kinoshita, Effect of particle morphology on lithium intercalation rates in natural graphite, J. Power Sources 124 (2003) 505–512.

[74] A. J. Smith, J. C. Burns, X. Zhao, D. Xiong, J. R. Dahn, A high precision coulometry study of the SEI growth in Li/graphite cells, J. Electrochem. Soc. 158 (5) (2011) A447.

[75] J. C. Burns, R. Petibon, K. J. Nelson, N. N. Sinha, A. Kassam, B. M. Way, J. R. Dahn, Studies of the effect of varying vinylene carbonate (VC) content in lithium-ion cells on cycling performance and cell impedance, J. Electrochem. Soc. 160 (10) (2013) A1668–A1674.

[76] L. El Ouatani, R. Dedryvere, C. Siret, P. Biensan, S. Reynaud, P. Iratcabal, D. Gonbeau, The Effect of vinylene carbonate additive on surface film formation on both electrodes in Li-ion batteries, J. Electrochem. Soc. 156 (2) (2009) A103.

[77] R. Petibon, E. C. Henry, J. C. Burns, N. N. Sinha, J. R. Dahn, Comparative study of vinyl ethylene carbonate (VEC) and vinylene carbonate (VC) in LiCoO2/graphite pouch cells using high precision coulometry and electrochemical impedance spectroscopy measurements on symmetric cells, J. Electrochem. Soc. 161 (1) (2013) A66–A74.

[78] L. El Ouatani, R. Dedryvere, C. Siret, P. Biensan, D. Gonbeau, Effect of vinylene carbonate additive in Li-ion batteries: comparison of LiCoO2/C, LiFePO4/C, and LiCoO2/Li4Ti5O12 systems, J. Electrochem. Soc. 156 (2009) A468.

[79] Y. Wang, S. Nakamura, K. Tasaki, P. B. Balbuena, Theoretical studies to understand surface chemistry on carbon anodes for lithium-ion batteries: How does vinylene carbonate play its role as an electrolyte additive?, J. Am. Chem. Soc. 124 (16) (2002) 4408–4421.

[80] K. Ushirogata, K. Sodeyama, Y. Okuno, Y. Tateyama, Additive effects on reductive decomposition of carbonate-based solvent toward solid electrolyte interphase formation, J. Am. Chem. Soc. 135 (2013) 11967–11974.

[81] K. Leung, Electronic Structure Modeling of Electrochemical Reactions at Electrode/Electrolyte Interfaces in Lithium Ion Batteries, J. Phys. Chem. C 117 (2013) 1539–1547.

[82] H. Tavassol, J. W. Buthker, G. A. Ferguson, L. A. Curtiss, A. A. Gewirth, Solvent oligomerization during SEI Formation on model systems for Li-ion battery anodes, J. Electrochem. Soc. 159 (6) (2012) A730.

[83] K. Xu, Electrolytes and interphases in Li-ion batteries and beyond, Chem. Rev. 114.

[84] D. Aurbach, M. Levi, E. Levi, A. Schechter, Failure and stabilization mechanisms of graphite electrodes, J. Phys. Chem. 101 (1997) 2195–2206.

[85] D. Aurbach, B. Markovsky, I. Weissman, E. Levi, Y. Ein-Eli, On the correlation between surface chemistry and performance of graphite negative electrodes for Li-ion batteries, Electrochim. Acta 45 (1999) 67–86.

[86] D. Aurbach, M. D. Levi, E. Levi, H. Teller, B. Markovsky, G. Salitra, U. Heider, L. Heider, Common electroanalytical behavior of Li intercalation processes into graphite and transition metal oxides, J. Electrochem. Soc. 145 (1998) 3024–3034.

[87] A. M. Dimiev, G. Ceriotti, N. Behabtu, D. Zakhidov, M. Pasquali, R. Saito, J. M. Tour, Direct real-time monitoring of stage transitions in graphite intercalation compounds, ACS Nano 7 (2013) 2773–2780.

[88] J. B. Goodenough, K.-S. Park, The Li-ion rechargeable battery : a perspective, JACS 135 (2013) 1167–1176.

[89] M. Levi, D. Aurbach, Simultaneous Measurements and Modeling of the Electrochemical Impedance and the Cyclic Voltammetric Characteristics of Graphite Electrodes Doped with Lithium, J. Phys. Chem. B 101 (1997) 4630–4640.

[90] K. Persson, V. A. Sethuraman, L. J. Hardwick, Y. Hinuma, Y. S. Meng, A. van der Ven, V. Srinivasan, R. Kostecki, G. Ceder, Lithium diffusion in graphitic carbon, J. Phys. Chem. Lett. 1 (2010) 1176–1180.

[91] B. Liang, Y. Liu, Y. Xu, Silicon-based materials as high capacity anodes for next generation lithium ion batteries, J. Power Sources 267 (2014) 469–490.

[92] W. Xu, S. S. S. Vegunta, J. C. Flake, Surface-modified silicon nanowire anodes for lithium-ion batteries, J. Power Sources 196 (20) (2011) 8583–8589.

[93] J. Zhang, R. Wang, X. Yang, W. Lu, X. Wu, X. Wang, H. Li, L. Chen, Direct observation of inhomogeneous solid electrolyte interphase on MnO anode with atomic force microscopy and spectroscopy, Nano Lett. 12 (2012) 2153–2157.

[94] J. Zhang, X. Yang, R. Wang, W. Dong, W. Lu, X. Wu, X. Wang, H. Li, L. Chen, Influences of Additives on the Formation of a Solid Electrolyte Interphase on MnO Electrode Studied by Atomic Force Microscopy and Force Spectroscopy, J. Phys. Chem. C 118 (2014) 20756–20762.

[95] J. Zheng, H. Zheng, R. Wang, L. Ben, W. Lu, L. Chen, L. Chen, H. Li, 3D visualization of inhomogeneous multi-layered structure and Young's modulus of the solid electrolyte interphase (SEI) on silicon anodes for lithium ion batteries, Phys. Chem. Chem. Phys. 16 (2014) 13229–13238.

[96] X.-R. Liu, X. Deng, R.-R. Liu, H.-J. Yan, Y.-G. Guo, D. Wang, L.-J. Wan, Single Nanowire Electrode Electrochemistry of Silicon Anode by in Situ Atomic Force Microscopy: Solid Electrolyte Interphase Growth and Mechanical Properties, ACS Appl. Mater. Interfaces 6 (2014) 20317–20323.

[97] X. Deng, X. Liu, H. Yan, D. Wang, L. Wan, Morphology and modulus evolution of graphite anode in lithium ion battery: An in situ AFM investigation, Sci. China Chem. 57 (1) (2014) 178–183.

[98] N. Weadock, N. Varongchayakul, J. Wan, S. Lee, J. Seog, L. Hu, Determination of mechanical properties of the SEI in sodium ion batteries via colloidal probe microscopy, Nano Energy 2 (5) (2013) 713–719.

[99] K. Xu, Whether EC and PC differ in interphasial chemistry on graphitic anode and how, J. Electrochem. Soc. 156 (9) (2009) A751–A755.

[100] M. Nishizawa, H. Koshika, T. Itoh, M. Mohamedi, T. Abe, I. Uchida, In situ conductance measurement to investigate roles of conductive additives in lithium ion battery electrodes, Electrochem. Commun. 1 (1999) 375–378.

[101] T. Takamura, M. Saito, A. Shimokawa, C. Nakahara, K. Sekine, S. Maeno, N. Kibayashi, Charge/discharge efficiency improvement by the incorporation of conductive carbons in the carbon anode of Li-ion batteries, J. Power Sources 90 (2000) 45–51.

[102] L. Valdes, Resistivity measurements on germanium for transistors, Pro. I.R.E. February (1954) 420–427.

[103] A. Uhlir (Jr.), The potentials of infinite systems of sources and numerical solutions of problems in semiconductor engineering, Bell Sys. Tech. J. January (1955) 105–128.

[104] F. Smits, Measurement of sheet resistivities with the four-point probe, Bell Sys. Tech. J. May (1958) 711–718.

[105] K. Striebel, A. Sierra, J. Shim, C.-W. Wang, A. Sastry, The effect of compression on natural graphite anode performance and matrix conductivity, J. Power Sources 134 (2) (2004) 241–251.

[106] Z. Shu, R. Mcmillan, J. Murray, Electrochemical intercalation of lithium into graphite, J. Electrochem. Soc. 140 (4) (1993) 922–927.

[107] W. Primak, L. Fuchs, Electrical conductivities of natural graphite crystals, Phys. Rev. 95 (1) (1954) 22–31.

[108] A. Celzard, J. Mareche, F. Payot, G. Furdin, Electrical conductivity of carbonaceous powders, Carbon 40 (2002) 2801–2815.

[109] B. Marinho, M. Ghislandi, E. Tkalya, C. E. Koning, G. de With, Electrical conductivity of compacts of graphene, multi-wall carbon nanotubes, carbon black, and graphite powder, Powder Tech. 221 (2012) 351–358.

[110] Z. Chen, L. Christensen, J. Dahn, Large-volume-change electrodes for Li-ion batteries of amorphous alloy particles held by elastomeric tethers, Electrochem. Commun. 5 (11) (2003) 919–923.

[111] W.-R. Liu, M.-H. Yang, H.-C. Wu, S. M. Chiao, N.-L. Wu, Enhanced cycle life of Si anode for Li-ion batteries by using modified elastomeric binder, Electrochem. Solid-State Lett. 8 (2) (2005) A100.

[112] T. Yim, S. J. Choi, Y. N. Jo, T.-H. Kim, K. J. Kim, G. Jeong, Y.-J. Kim, Effect of binder properties on electrochemical performance for silicon-graphite anode: Method and application of binder screening, Electrochim. Acta 136 (2014) 112–120.

[113] S. Kang, Self-healing strategies for lithium-ion battery anodes, Ph.D. thesis, University of Illinois at Urbana-Champaign (2015).

[114] Mathworks, Normalized 2-D cross-correlation (normxcorr2) (2012).
URL http://www.mathworks.com/help/images/ref/normxcorr2.html

[115] J. Barlow, Optimal stress locations in finite element models, Int. J. Num. Methods Eng. 10 (1976) 243–251.

[116] D. A. Tortorelli, Solid mechanics : analysis and design with the finite element method, Electronic Publication, Urbana, IL USA, 2010.

[117] P. Reu, B. Wattrisse, W.-C. Wang, L. Robert, H. Bruck, S. Daly, R. Rodriguez-Vera, F. Bugarian, Digital Image Correlation (DIC) Challenge (2015).
URL http://sem.org/dic-challenge/

[118] G. Bogush, M. Tracy, C. Zukoski IV, Preparation of Monodisperse Silica Particles: Control of Size and Mass Fraction, J. Non-Crystalline Solids 104 (1988) 95–106.